Non-Newtonian polymeric fluid transport through porous media

A thesis submitted to the University of Manchester for the degree of
Doctor of Philosophy
in the Faculty of Science and Engineering

2021

Takshak Bhimrao Shende
Department of Chemical Engineering and Analytical Science
School of Engineering

Contents

List of Figures

List of Tables

List of Publications

- **T. Shende,** V. J. Niasar, and M. Babaei. Effective viscosity and Reynolds number of non-newtonian fluids using Meter model. *Rheologica Acta*, 60 (1):11–21, 2021.
- **T. Shende,** V. J. Niasar, and M. Babaei. An empirical equation for shear viscosity of shear thickening fluids. *Journal of Molecular Liquids*, 325:115220, 2021.
- **T. Shende,** V. Niasar, and M. Babaei. Upscaling non-Newtonian rheological fluid properties from pore-scale to Darcy's scale. *Chemical Engineering Science*, 239:116638, 2021.
- **T. Shende,** V. Niasar, and M. Babaei. Pore-scale simulation of viscous instability for non-Newtonian two-phase flow in porous media. *Journal of Non-Newtonian Fluid Mechanics*, 296:104628, 2021.

Conference Presentations

- **T. Shende,** V. Niasar, and M. Babaei. Capillary bundle-Meter model for non-Newtonian fluid flow in porous media, *InterPore Conference 2020 (online)*, Qingdao, China, 31 Aug-4 Sept 2020.
- **T. Shende,** V. J. Niasar, and M. Babaei. The Reynolds number of shear-thinning fluid flow in a circular geometry, *18th International Congress on rheology (online),* Rio de Janeiro, Brazil, 14-18 Dec 2020.
- **T. Shende,** V. J. Niasar, and M. Babaei. Pore-scale two-phase simulation of viscous fingering of non-Newtonian fluids, *InterPore Conference 2021 (online)*, Edinburgh, United Kingdom 31 May-4 June 2021.

Abstract

The non-Newtonian rheology of polymer solutions makes it challenging to understand the pore-scale behaviour of polymer solutions in porous media, and therefore, it also presents challenges to upscale their pore-scale properties to the Darcy scale. An analytical and numerical approach are adopted in the thesis to evaluate the effect of non-Newtonian rheology on polymeric fluid flow in porous media. In an analytical approach, Darcy viscosity is upscaled from pore-scale shear viscosity using the Bundle-of-Capillaries model modified with a pore-correction coefficient and a fluid-correction coefficient. This approach is based on an exact analytical solution derived in the present work for the flow of non-Newtonian fluids described by a shear stress-dependent Meter model and a viscoelastic Phan-Thien-Tanner model. An OpenFOAM-based method has been developed for numerically simulating single-phase and two-phase flow in 2D and 3D porous media, involving Meter model fluids to gain pore-scale insight. The results suggest that the effective viscosity and Reynolds numbers defined in this work correctly describe non-Newtonian fluid flow as laminar, turbulent, and transition flow. Pore-scale single-phase simulation in 2D and 3D porous media indicates that the fluid's Darcy viscosity is associated with the fluid's viscosity in the active mobile zone of porous media only. The viscoelastic fluid flow simulation shows elastic instability at low Reynolds number flow in a 2D and 3D porous medium. The volume-of-fluid method-based two-phase simulation indicates that pore-scale micro-heterogeneity and wettability govern non-Newtonian fluid flow front stability while displacing Newtonian fluid. Simulations based on the Euler-Lagrangian approach (discrete particle modelling) show that nanoparticle transport in porous media exhibits non-Fickian behaviour due to heterogeneity-dependent confinement. The generalised Newtonian fluid equation proposed for shear thickening fluids captures all typical shear thickening fluid regimes and can be used to do single-phase simulations.

Declaration of originality

I hereby confirm that no portion of the work referred to in the thesis has been submitted in support of an application for another degree or qualification of this or any other university or other institute of learning.

Copyright statement

Acknowledgements

First of all, I must express my sincere thanks to my supervisors, Dr. Masoud Babaei and Dr. Vahid Niasar, who introduced me to the complex and beautiful world of non-Newtonian fluids. Now, I am in love with non-Newtonian fluids. This work could not have been initiated and completed in such a short time without the constant support, encouragement, guidance, and selfless dedication from my supervisor, Dr. Masoud Babaei. I feel incredibly pleased and honoured to express my deep gratitude and indebtedness to Dr. Masoud, who has helped me comprehensively understand porous media research. I am lucky to have you. Thank you so much.

I would like to thank my co-supervisor, Dr. Vahid Niasar, for his incredible support and commitment to the work. He always furnished valuable and constructive feedback that changed the course of the research, which helped me improve the work and gave me more insight into how to conduct constructive research. You are a gem, and you make others into gems.

The constructive feedback provided by Dr. Claudio Da Fonte and Dr. Steven Lind in the first and second year examinations (viva) helped significantly improve the thesis work. A special thanks to both of you.

I would like to thank Dr. Amer Syed, from the University of Aberdeen, for his help in neutron tomography experiments and fruitful discussions. A big thanks to Dr. Genoveva Burca, ISIS Facility, Harwell, Oxford, for initial image processing training and neutron tomography. I would like to thank Dr. Omar E. Godinez-Brizuela and Dr. Daniel Niblett for their initial guidance in learning OpenFOAM and ParaView. Thanks to Dr. Arash Rabbani and Dr. Morteza Aminnaji for being helpful throughout this journey. Senyou An deserves special recognition for his contributions to the Meter model-based thermal transport. Thanks to Mohammadjavad Shokriafra for his bits of help in conducting microfluidic experiments. The government of Maharashtra, India, funded the research outcome presented in this thesis. I sincerely thank the government of Maharashtra for providing financial support.

Personally, this journey would not have been possible without my wife Priyanka's generous love and support. Words are not enough to express it. Thank you for giving me a beautiful daughter, 'Metta', as a gift. Finally, I must thank my beloved parents, brother Shubham and sister Shruti, for their selfless love and motivation.

Chapter 1

Introduction

This thesis examines the flow of non-Newtonian fluids (shear thinning, shear thickening, and viscoelastic) through porous media using analytical and numerical simulation approaches. This thesis is written in an alternative format, consisting of five articles in a journal format. Each chapter (article) examines a specific goal in detail. The thesis covers a broad range of non-Newtonian fluid flow aspects within porous media, including single-phase flow, two-phase flow, and nanoparticle dispersion within non-Newtonian fluids and porous media. In summary, Chapter 2 provides an exact analytical solution, similar to the Hagen-Poiseuille equation, for an inelastic Meter model fluid flowing through a circular capillary. Chapter 3 describes the proposed generalised non-Newtonian fluid equations that accurately capture the complex rheology of typical shear thickening fluids and their usefulness in performing single-phase numerical simulations through porous media. The method to upscale pore-scale properties of inelastic and viscoelastic non-Newtonian fluids to the Darcy scale is proposed in Chapter 4. The effect of the pore-scale heterogeneity and wettability of porous media on viscous fingering during the two-phase flow of an inelastic non-Newtonian fluid displacing oil is discussed in Chapter 5. In Chapter 6, the Euler-Lagrangian simulation approach is used to evaluate the migration and dispersion of nanoparticles (suspended in an inelastic Meter fluid) in heterogeneous porous media. Finally, Chapter 7 presents the summary and future work.

1.1 Motivation

Almost all the natural materials that surround us are porous. Porous media are solid materials with void spaces, complex pore geometry, and interconnected networks [64, 218]. The void spaces of the porous medium are always filled with fluids, i.e. either with gases or liquids. Although fluid transport in a porous medium occurs at the pore scale, the fluid flow measurements are performed at a length scale several orders of magnitude larger than the void space of the porous medium [25]. This macroscopic measurement usually fails to depict the microscopic displacement of the fluid and its interaction with complex geometry. Thus, upscaling pore-scale property to macroscale is essential to describe flow behaviour in a porous medium correctly [184]. If the fluid has non-Newtonian properties, modelling and upscaling become challenging.

The addition of solutes (e.g. polymers or colloidal/non-colloidal particles) in the solvent gives the fluid non-Newtonian characteristics. Non-Newtonian fluids can have shear thinning, shear thickening, or viscoelastic properties [21, 22]. Polymers are macromolecules with repetitive structural units of a mesoscopic length scale ($10-100$ nm) [21, 155, 200]. The bond interaction between polymers can form a complex structure with a high molecular weight of up to thousands of g/mol. The flow-induced evolution of molecular structure (i.e. orientation and stretching) along a streamline governs polymeric non-Newtonian fluids' rheological properties [21, 39, 155, 200]. In addition to the shear-thinning characteristics, the stress caused by local deformation and the rearrangement of the microstructure in the fluid element endows certain polymeric fluids with viscoelastic properties [52, 165]. Colloidal or non-colloidal particles based non-Newtonian fluids show shear thickening properties after the critical value of shear stress [28, 31, 214]. These distinct properties of shear-thinning, shear-thickening and viscoelastic fluids have been utilised in many industrial, consumer and commercial settings [14, 21, 184, 196, 214, 218, 221]. The shear-thinning (drop-in viscosity at high shear) and shear thickening (increase in viscosity at high shear) features of these fluids are specifically of engineering interest [21, 200]. The normal stress of viscoelastic non-Newtonian fluids that induces the rod climbing effect (i.e. the Weissenberg effect) has also been utilised in many industrial applications [39]. For example, xanthan gum and polyacrylamide polymer mixed in water have been used extensively for enhanced

oil recovery and subsurface remediation [32, 145, 200, 207, 238]. These polymeric liquids show non-Newtonian shear-thinning or viscoelastic characteristics, depending on polymer concentration, temperature, salinity and hardness of the liquid [32, 33, 200].

The challenging aspect of rheology is developing a physically realistic mathematical model that predicts the non-Newtonian fluid's flow behaviour in complex geometry. Several constitutive equations [8, 21, 39, 43, 78, 134, 214] and numerical schemes [7, 8, 53, 54, 56, 75, 162, 163] have been developed to model rheology and fluid flow through void spaces. Most of the generalised Newtonian fluid models (e.g. power-law [21], Carreau [222], Cross [43], and Meter [134]) or viscoelastic fluid models (e.g. Maxwell, Oldroyd-B, Giesekus, and Phan–Thien—Tanner) [8, 20] that describe the rheology of inelastic and viscoelastic non-Newtonian fluids are empirical. Thus, each model has its own limitations and cannot be universally applied to all types of non-Newtonian fluids [20]. Most shear thinning and viscoelastic fluids show an S-shaped type of viscosity curve over a range of shear values (see Fig 1.1a).

On the contrary, modelling the rheology of shear thickening fluid is much more complex, as it shows Newtonian, shear thinning, shear thickening, and extreme shear-thinning regimes with an increase in shear values (see Fig 1.1b) [78]. An equation that describes all shear thickening fluid regimes and can be used for pore-scale fluid flow simulation is absent in the literature. The complex behaviour of shear thinning and shear thickening non-Newtonian fluids in complex pore-space geometry makes modelling their flow behaviour challenging.

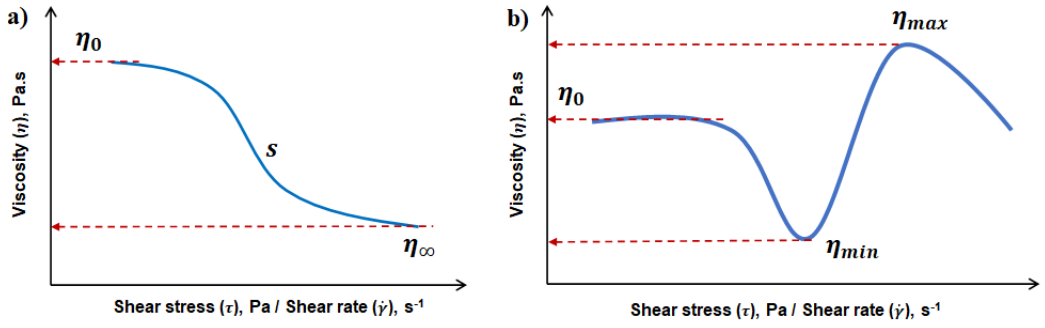

FIGURE 1.1: a) Typical S-shaped viscosity curve of a shear thinning non-Newtonian fluids b) typical viscosity curve of a shear thickening non-Newtonian fluids. Note: figure not to the scale.

The flow of non-Newtonian fluids (shear thinning, shear thickening or viscoelastic) through a circular tube/capillary has applications in the engineering field [21, 184, 196].

Many theories and models for Newtonian fluids have been developed based on the Hagen-Poseuille equation, such as the Lucas-Washburn equation [123, 215] (the commercial tensiometer uses it to measure surface tension), the capillary bundle model [184], and the pore-network models [198]. However, the exact analytical solution is not available in the literature for a) fluids that show S-shaped shear-dependent viscosity variations (e.g. Carreau, Cross, and Meter models, Fig 1.1a) and b) shear thickening fluids (Fig 1.1b). The lack of an analytical solution makes it difficult to define the flow's effective viscosity and Reynolds number. The analytical solution is specifically crucial to upscale pore-scale properties to Darcy's scale [184].

The continuity and momentum equations govern the pore-scale flow properties of the fluid in porous media, whereas Darcy's law governs the Darcy scale properties of the fluid transport in porous media. Upscaling non-Newtonian rheology from pore-scale to Darcy scale requires a correct way to estimate the shift factor. The empirical shift factor relates the steady shear-dependent viscosity of non-Newtonian fluids to the Darcy viscosity in porous media. [18, 65, 177, 200, 226]. The reported values of the empirical shift factor cover three orders of magnitude, depending on the considered fluid-medium configurations [18, 194, 200]. This variation creates a challenge in upscaling non-Newtonian rheology from pore-scale to Darcy scale.

Most of the recent work in the literature is focused on evaluating the relationship between shift factor and physical properties of porous media and non-Newtonian fluids [18, 65, 177, 200, 226]. Both analytical [65], and numerical approaches (e.g., [18]) have been used to identify a correlation between shift factor and various physical parameters of fluids and porous media. The power-law model has been historically used to upscale pore-scale properties to Darcy's scale and to conduct pore-scale direct numerical simulations [184, 196, 200]. Although the power-law model does not capture the Newtonian regime of non-Newtonian fluids at low and high shear rates (see Fig. 1.1) [21], most numerical simulations of the flow of polymer solutions through porous media were carried out using a power-law model [196, 200]. Thus, to numerically and analytically upscale pore-scale properties to Darcy's scale, there is a need for a rheological model that: a) captures the S-shaped rheology of a typical non-Newtonian fluid; b) has an analytical solution; c) can numerically simulate the flow of a non-Newtonian fluid through heterogeneous porous media.

Upscaling pore-scale properties require correct evaluation of a non-Newtonian fluid flow behaviour at the pore scale. This can be done by simulating non-Newtonian fluid flow through 3D porous media. The Meter model captures the S-shaped rheology of shear-thinning fluids [134]. Viscoelastic linear Phan-Thien-Tanner (PTT) has an analytical solution for flow through the tube [147]. Thus, it will be helpful to simulate Meter model fluid and PTT fluid through porous media for upscaling pore-scale properties. However, no attempts have been made to simulate inelastic shear stress-dependent Meter model fluid, inelastic shear thickening fluid, or viscoelastic linear Phan-Thien-Tanner fluid flow through realistic 3D porous media due to the complexity of solving the momentum equation coupled with the continuity equation. The present thesis has made an attempt to derive an analytical solution and simulates a single-phase flow of shear thinning, shear thickening, and viscoelastic fluid through porous media. The properly averaged values obtained after simulations could be considered as an upscaled value linked to single-phase Darcy's law [170].

Fluid flow in a subsurface porous medium is a multiphase flow. Upscaling multiphase flow from pore-scale to Darcy's scale requires realistic modelling of the dynamic behaviour of each phase and its interaction amongst different phases and solid boundaries of heterogeneous porous media. A two-phase pore-scale simulation would be a helpful first step towards understanding multiphase flow behaviours of non-Newtonian fluids in heterogeneous porous media. An Euler-Euler or Euler-Lagrangian simulation approach can be adopted to study two-phase flow in porous media. In light of its use in oil recovery and soil remediation, this thesis looked at: a) the two-phase transport of a non-Newtonian fluid that displaces oil using the Euler-Euler method; and b) the dispersion of nanoparticles suspended in a non-Newtonian fluid using the Euler-Lagrangian method.

Understanding the pore-scale two-phase displacement of non-Newtonian fluid displacing Newtonian fluid such as oil or non-aqueous phase liquid (NAPL) contaminants is of paramount importance for enhanced oil recovery and soil remediation, respectively [145, 200, 207, 238]. Most of the previous studies on pore-scale two-phase flow involving non-Newtonian fluid were carried out in a simple homogeneous porous medium [9, 56, 70, 95, 137, 145]. This geometry is highly unlikely to account for the microscopic heterogeneity and true complexity observed in porous media. Only a few studies [56, 59, 152, 212, 220] considered the effects of micro-heterogeneity on polymeric fluid-induced oil displacement.

The pore size in porous media can vary by up to two orders of magnitude, which leads to spatial variation of viscosity and velocity in porous media over several orders of magnitude. This spatial change in viscosity and velocity in pore space and capillarity governs flow stability and fingering. Wettability, the ability of polymer solutions to adhere to porous materials in the presence of other fluids, affects the displacement of non-Newtonian fluids on a pore scale [25]. No attempt has yet been made to numerically evaluate the effect of micro-heterogeneity and wettability on viscous fingering during non-Newtonian fluid's two-phase displacement.

Nanoparticles mixed with polymer solutions have been used to enhance oil recovery and soil treatment because they change the properties of liquids [14, 60, 89, 93, 164, 239]. Spatial heterogeneity of porous media, non-Newtonian behavior of polymer solutions and Brownian motion of nanoparticles influence pore-scale transport and dispersion of nanoparticles in porous materials. The dispersion of nanoparticles in porous materials is of considerable importance because it makes many regions of the porous medium accessible to the injected polymer [218]. By tracking the movement of individual particles on the pore scale, the microscopic mass transport can be upscaled to the macroscale [15]. The transport of nanoparticles is a 3D phenomenon, but previous experimental monitoring of nanoparticles in porous media was still performed in 2D (i.e. no z-direction) [15, 141, 160, 171, 218]. Therefore, the dispersion of nanoparticles in the transverse direction could not be truly evaluated. In addition, no attempt has yet been made to simulate the transport of nanoparticles within non-Newtonian fluid and 3D heterogeneous porous media, such as sandstone, and to use particle tracking to determine the coefficients of longitudinal and transverse dispersion.

1.2 Objectives

This thesis addresses the issues mentioned above through the following objectives:

1. Derive an analytical solution for the radial velocity profile and volumetric flow rate of the steady-state laminar flow of Meter model fluid through a circular geometry.

2. Formulate a generalised Newtonian fluid equation that describes the rheology of typical shear thickening fluid.

3. Develop and validate a computational framework that simulates the flow of non-Newtonian fluids described using the proposed shear thickening fluid equation, the Meter model equation and the viscoelastic Phan-Thien-Tanner equation in heterogeneous 2D and 3D porous media.

4. Upscale pore-scale rheological properties of inelastic Meter model fluid and viscoelastic linear Phan-Thien-Tanner fluid to macroscopic Darcy scale.

5. Determine how microscale heterogeneity and wettability of the porous medium govern the stability of inelastic polymeric fluid flow even for favourable viscosity ratios.

6. Develop an Euler-Lagrangian framework that simulates the transport of nanoparticles in non-Newtonian fluids and 3D porous media incorporating particle-fluid, particle-particle, particle-wall interactions and Brownian motion.

7. Determine the transverse and longitudinal dispersion coefficients by tracking nanoparticles in 3D space.

1.3 Thesis outline

The topics mentioned in the objectives are addressed in five separate manuscripts. Four manuscripts (Chapters 2-5) are published, and one manuscript (Chapter 6) is submitted to peer-reviewed journals at the time of submission of the thesis. The OpenFOAM C++ library [98, 99] was used and modified to perform numerical simulations.

The paper [190] published in *Rheologica Acta* is presented in Chapter 2, which addresses objective 1 of the thesis. The literature extensively uses shear rate-dependent models such as power-law, Carreau and Cross to describe the inelastic rheology of non-Newtonian fluids [21, 39, 196, 198]. On the contrary, the Meter model [134] describes viscosity as a function of shear stress and captures S-shaped rheology (i.e. a Newtonian plateau at low and high shear stress and a slope at intermediate shear stress) of most shear-thinning fluids well as a purely shear-thickening regime of shear thickening fluids (see Fig 1.1a). An equation similar to the Hagen-Poiseuille equation for non-Newtonian fluids was absent in the literature, except for power-law [21, 39], the Elis model [130] and the linear PTT model [147] fluids. Thus, we derived an analytical solution for the

flow of Meter model fluid in a circular capillary. This helped correctly describe the Reynolds number for non-Newtonian fluid flow and characterised the non-Newtonian fluid's laminar, transition and turbulent flow. The radial velocity profile estimated using the analytical solution of the Meter model agrees with the experimental observations of xanthan gum fluid flow in a microcapillary (diameter 320 μm) by Campagnolo *et al.* [34] and of polyacrylamide fluid flow in a tube (diameter 0.1 m) by Escudier *et al.* [69]. The Meter model described in Chapter 2 helped develop a rheological model for shear thickening fluid as described in Chapter 3. The analytical solution of the Meter model could help develop a bundle-of-capillary model for non-Newtonian fluid as described in Chapter 4 for upscaling pore-scale properties to Darcy's scale.

The paper [191] published in the *Journal of Molecular Liquids* is presented in Chapter 3. This chapter addresses objective 2 of the thesis. Typical shear thickening non-Newtonian fluids show complex viscosity behaviour as shown in Fig 1.1b. The shear stress dependent Meter model equation (presented in Chapter 2) was modified to describe the typical viscosity curve of shear thickening fluids. Empirical equations are proposed to describe the relative free volume-dependent viscosity, the shear stress-dependent viscosity, the shear rate-dependent viscosity and the dimensionless Péclet number-dependent relative viscosity of shear thickening fluids adopting Doolittle's free volume theory approach [62]. The proposed formulae predict all rheologically different behaving Newtonian, intermediate shear thinning, shear thickening and extreme shear-thinning regimes of shear-thickening fluids. The pimpleFoam solver of the OpenFOAM C++ library was modified to incorporate the proposed shear thickening fluid model and simulate the single phase flow of shear thickening fluid in 2D porous media. The proposed formulae have been validated against the experimental rheological data of various shear thickening fluids over a range of pH, volume fraction, electrolyte concentration, temperature and magnetic field. The results suggest that the predicted threshold material parameters of shear thickening fluids help to quantitatively evaluate the effect of varying physicochemical conditions on the rheology of shear thickening fluids. The simulated flow of a shear thickening fluid, modelled using the proposed shear rate-dependent equation, showed a bimodal distribution of pore-scale shear rate, shear viscosity and velocity in a 2D staggered porous medium. The pimpleFoam solver modified for shear thickening fluid was utilised in Chapter 4, Chapter 5 and Chapter 6 to simulate the single-phase flow and two-phase flow involving inelastic Meter model fluids. Grid dependent convergence of the simulation carried out

using a modified pimpleFoam solver is presented in Appendix A.

The paper [189] published in the *Chemical Engineering Science* journal is presented in Chapter 4. This chapter addresses objectives 3 and 4 of the thesis. Spatiotemporal variations of velocity and viscosity in pore-space create a challenge to upscale pore-scale flow to the Darcy scale [18]. Meter model and its analytical solution (described in chapter 2) were used to develop a bundle-of-capillary model to upscale pore-scale flow to Darcy scale. The bundle-of-capillaries model with a pore-correction coefficient and fluid-correction coefficient was developed to upscale pore-scale rheological properties to the Darcy scale based on the analytical solution of the Meter model (inelastic fluid) and the linear Phan-Thien-Tanner (viscoelastic fluid) model. The pore-correction coefficient and fluid-correction coefficient take into account pore-scale variation due to pore-geometry and fluid rheology, respectively. The pimpleFoam solver modified for shear thickening fluid (described in chapter 3) was utilised for Meter model fluid flow simulation, whereas, the RheoTool developed by [163] was utilised to simulate the viscoelastic Phan-Thien-Tanner model fluid flow. The flow of Meter model fluid and linear Phan-Thien-Tanner fluid in 2D and 3D porous media is simulated using the OpenFOAM C++ library and validated using the experimental observations of Galindo-Rosales *et al.* [80]. The results depict that the viscoelastic linear Phan-Thien-Tanner model shows viscoelastic instability at low Reynolds number flow. A similar viscoelastic instability was also observed during the simulation of linear PTT flow in a heterogeneous sandstone porous medium in 3D. The results showed that immobile and mobile zones in porous media affect rheology. Thus, Darcy's viscosity, estimated using Darcy's law, is associated with the fluid's viscosity in the mobile zone of a heterogeneous porous medium. This result implies that the heterogeneity of porous media significantly affects the pore-scale and Darcy-scale single-phase flow of non-Newtonian fluid. As subsurface flow is largely multi-phase flow, the Meter model was used to conduct a two-phase flow simulation involving non-Newtonian fluid to evaluate the effect of pore-scale heterogeneity on a) two-phase displacement in chapter 5 and b) the dispersion of nanoparticles suspended in non-Newtonian fluid in longitudinal and transverse directions in chapter 6.

The paper [188] published in the *Journal of Non-Newtonian Fluid Mechanics* is presented in Chapter 5. This chapter deals with objective 5 of the thesis. The applicability of the Meter model described in Chapter 2 and 4 is extended to simulate two-phase flow of a non-Newtonian fluid using the interFoam solver of OpenFOAM. The impact

of micro-heterogeneity on non-Newtonian two-phase flow is the focus of Chapter 5. The direct numerical simulation of non-Newtonian fluids (modelled using the shear stress-dependent Meter model) displacing oil in 3D Mt. Simon sandstone and 2D heterogeneous porous media were considered over a range of wettabilities (strong imbibition to strong drainage), capillary numbers and viscosity ratios. This result suggests that the heterogeneity of the porous medium can potentially lead to an unstable fluid flow front (even after the use of polymer). Therefore, along with capillary number and viscosity ratio, heterogeneity is the governing factor for controlling viscous and capillary fingering, and it is crucial to account for the microscale heterogeneity of porous media to design polymer solution injection. The addition of nanoparticles can modify the physicochemical properties of polymeric non-Newtonian fluids, which might help recover more oil from the subsurface. First, however, it is essential to understand how nanoparticles suspended in non-Newtonian fluid access the pores through diffusion and dispersion in a heterogeneous porous medium. Thus, to evaluate the effect of heterogeneity on nanoparticle dispersion in porous media, two-phase simulations involving nanoparticles and an inelastic Meter model fluid were carried out in Chapter 6.

The paper submitted to the *Physical Review E* is presented in Chapter 6. This chapter focuses on objectives 6 and 7 of the thesis. The applicability of the Meter model (described in Chapter 2 and 4) is extended to simulate the flow of nanoparticles suspended in an inelastic Meter model fluid. In this work, an Euler-Lagrangian method is adopted to simulate the flow of nanoparticles and inelastic non-Newtonian fluids in a simple convergent and divergent microchannel, 2D homogeneous porous media, and 3D heterogeneous Mt. Simon sandstone over a range of injection rates. The results indicate that the spatial heterogeneity of the porous medium forms a shear stress gradient in the pore space, which controls the temporal and spatial position and migration of nanoparticles in porous media. The velocity distribution of nanoparticles in the porous medium is non-Gaussian, leading to the nanoparticle dispersion's non-Fickian behaviour. Due to pore space confinement, nanoparticles' long-time mean square displacement exhibits nonlinear behaviour.

In Chapter 7, the important findings of this thesis are summarised. In addition, possible next steps for this research are suggested.

Chapter 2

Effective viscosity and Reynolds number of non-Newtonian fluids using Meter model

This chapter is published in the '*Rheologica Acta*'. Supplementary information of the published article is added to the main text of the chapter.

Authors: **T. Shende,** V. J. Niasar, and M. Babaei. Effective viscosity and Reynolds number of non-newtonian fluids using Meter model. *Rheologica Acta*, 60 (1):11–21, 2021.

2.1 Introduction

The laminar flow of a non-Newtonian fluid (described using a generalised Newtonian fluid model) through a circular capillary/tube has broader engineering application (e.g. polymer fluid flow through pipes in an industrial settings [21], capillary bundle model of a porous medium [184], pore-Network model [198]). Amongst generalised Newtonian fluid models [223], Cross [43], Carreau [222], Carreau-Yasuda [222], Meter [133, 134, 184, 207–209], and Steller-Ivako model [201] can predict S-shaped rheological properties (i.e. constant viscosity at low and high shear values and decreasing viscosity at intermediate shear values) of many shear-thinning fluids (see Fig 2.1).

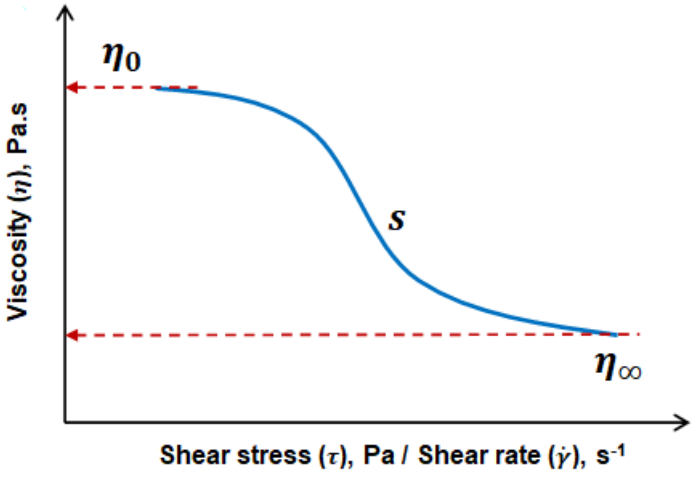

FIGURE 2.1: Typical S-shaped type behaviour of a shear thinning non-Newtonian fluids.[Note: figure not to the scale]

Many attempts have been made by many investigators to obtain an analytical solution for the flow of non-Newtonian fluid through a circular tube. Matsuhisa *et al.* [130] derived an analytical solution for the laminar flow of a fluid obeying the shear stress-dependent Ellis model. Meter and Bird [134] proposed the analytical solution for the flow of shear stress-dependent Meter model fluid in a circular capillary if $\frac{\eta_\infty}{\eta_0}$ is very small. Here, η_0 and η_∞ are zero and infinite shear viscosity, respectively. Although Sochi [197] and Kim [109] proposed an analytical solutions for Carreau and Cross fluid flow through a circular tube and Peralta [156, 157] proposed analytical solution for flow over a free-draining vertical plate, the exact analytical solution is absent for estimation of the radial velocity profile, average velocity and volumetric flow rate of fluid flow in a circular tube/micro-capillary obeying the Cross, Carreau, Meter, or Steller-Ivako model.

The Reynolds number of non-Newtonian fluids in a circular tube/capillary is commonly defined using the viscosity of the fluid at the wall [69, 109], the zero-shear viscosity [75], or the Metzner and Reeds equation [135]. The shear viscosity of non-Newtonian fluids vary along the radial direction in a fully developed circular capillary. Thus, zero shear viscosity, or the viscosity of the fluid at the wall, is not the representative viscosity or the effective viscosity of fluid flow. The Metzner and Reeds' equation is applicable to purely power-law fluids.

The effective viscosity of the fluid is analogous to the average velocity of the fluid. Both velocity and viscosity vary spatially during fluid flow in the circular capillary. Thus, similar to the average velocity value, the effective viscosity value is a single representative viscosity value for fluid flow under a given set of conditions. Sadowski and Bird [183] defined the effective viscosity of the Ellis model fluid, as in Eq. 2.1, based on the exact analytical solution for the flow of the Ellis model fluid in the circular capillary:

$$\frac{1}{\eta_{\text{eff}}} = \frac{1}{\eta_0}\left(1 + \frac{4}{\alpha+3}\left(\frac{\tau_{\text{w}}}{\tau_{\frac{1}{2}}}\right)^{\alpha-1}\right) \tag{2.1}$$

here η_{eff} is the effective viscosity of the fluid, η_0 is the zero shear viscosity, α is an exponent, $\tau_{\frac{1}{2}}$ is the critical shear stress parameter, and τ_{w} is the wall shear stress. The effective viscosity helps to define the Reynolds number and Darcy's friction factor. Further, effective viscosity helps to upscale shear viscosity from pore-scale to Darcy scale [17, 63, 65, 183, 184] during polymeric fluid flow in the porous medium. Effective viscosity and the exact analytical solution are useful in developing pore-network models for the flow of non-Newtonian fluids in porous media [198]. The pore-network model for non-Newtonian fluids has wider engineering and industrial applications, e.g. it helps understand the complex interaction of non-Newtonian fluids with tortuous and heterogeneous porous media at pore-scale. Effective viscosity is usually used in a porous media community to describe the flow at Darcy's scale [65, 184]. However, the present work determines effective viscosity based on an exact analytical solution for non-Newtonian fluid flow through a circular capillary and correlates it with the Hagen-Poiseuille equation.

A formulation to define the effective viscosity (η_{eff}) of non-Newtonian fluids (having S-shape type rheology) for a given flow condition using measurable parameters is absent in the literature. The absence of an analytical solution to estimate the average velocity

of Cross and Carreau fluid makes correlating the Reynolds number with Darcy's friction factor arduous.

To address the above discrepancy, we obtain an exact analytical solution for the flow of a Meter model fluid through a circular geometry. The analytical solution of the Meter model (MM) helps to define the effective viscosity, Reynolds number, and friction factor of non-Newtonian fluid flow using measurable parameters.

2.2 Mathematical Formulation

The Cauchy's momentum equation describes momentum transfer in any continuum. The state of stress at any point in the continuum (i.e. normal stresses, σ_n, and shear stresses, τ) is defined using Cauchy's stress tensor ($\boldsymbol{\sigma}$). For an incompressible fluid, a divergence of Cauchy's stress tensor is $\nabla \cdot \boldsymbol{\sigma} = -\nabla P + \nabla \cdot \boldsymbol{\tau}$, where ∇P is the pressure gradient and $\boldsymbol{\tau}$ is the deviatoric stress tensor. The constitutive equation of generalised Newtonian fluid (GNF) defines viscosity of the fluid as a non-linear function of second invariant of either rate-of-deformation tensor (i.e. $\boldsymbol{\tau} = 2\,\eta(\dot{\gamma})\,\boldsymbol{D}$) [22] or deviatoric stress tensor (i.e. $\boldsymbol{\tau} = 2\,\eta(\tau)\,\boldsymbol{D}$) [130, 134, 159, 201]. Here, $\boldsymbol{D} = \frac{1}{2}\dot{\boldsymbol{\gamma}} = \frac{1}{2}(\nabla \mathbf{u} + (\nabla \mathbf{u})^T)$, the magnitude of shear-rate is $|\dot{\gamma}| = \sqrt{\frac{\dot{\boldsymbol{\gamma}} : \dot{\boldsymbol{\gamma}}}{2}}$ [22], the magnitude of shear stress is $|\tau| = \sqrt{\frac{\boldsymbol{\tau} : \boldsymbol{\tau}}{2}}$ [134], and $\mathbf{u}$ is the velocity vector. The constitutive equations for commonly used shear rate-dependent and shear stress-dependent GNF models are given in Table 2.1.

The intermolecular and inter-particle interactions in the fluid generate stresses (i.e. normal and shear stresses). These stresses govern the flow properties of non-Newtonian fluids, including the viscosity of fluids. Thus, the stress-based model shall be adopted to describe the physics behind non-Newtonian fluid flow through void spaces. Meter [134] proposed his model in 1964 to describe the S-shape type rheology of a non-Newtonian fluid. The Meter model is a modified version of the Ellis model [20], Reiner-Philippoff model [161, 173] which were independently proposed in 1927, 1930, 1935 respectively; thus, it could also be renamed as the 'truncated Ellis-Reiner-Philippoff model'.

The Meter model (Eq. 2.2) gives the viscosity of a non-Newtonian fluid in terms of shear stress as follows [134]

TABLE 2.1: Empirical model for time independent non-Newtonian fluids

Model	**No. of parameters**	**Equation**
Power-law [148]	2	$\eta = m\,\dot{\gamma}^{n-1}$
Cross [43]	4	$\eta = \eta_\infty + \dfrac{(\eta_0 - \eta_\infty)}{1 + C\,\dot{\gamma}^n}$
Carreau [222]	4	$\eta = \eta_\infty + (\eta_0 - \eta_\infty)\left(1 + (K\,\dot{\gamma})^2\right)^{\frac{n-1}{2}}$
Carreau-Yasuda [222]	5	$\eta = \eta_\infty + (\eta_0 - \eta_\infty)\,(1 + (K\,\dot{\gamma})^a)^{\frac{n-1}{a}}$
Bingham [19]	2	$\tau = \tau_0^B + \eta_0^B\,\dot{\gamma}$
Herschel-Bulkley [90]	3	$\tau = \tau_0^H + m\,\dot{\gamma}^n$
Casson [23]	3	$\sqrt{(\tau)} = \sqrt{(\tau_0^C)} + \sqrt{(\eta_C\,\dot{\gamma})}$
Reiner-Philippoff [161, 173]	3	$\eta = \eta_\infty + \dfrac{\eta_0 - \eta_\infty}{1 + \left(\dfrac{\tau}{\tau_0}\right)^2}$
Ellis [130]	3	$\eta = \dfrac{\eta_0}{1 + \left(\dfrac{\tau}{\tau_{\frac{1}{2}}}\right)^{(\alpha_E - 1)}}$
Meter [134]	4	$\eta = \eta_\infty + \dfrac{\eta_0 - \eta_\infty}{1 + \left(\dfrac{\tau}{\tau_m}\right)^{(\alpha-1)}}$
Steller and Ivako [201]	4	$\eta = \eta_0\, e^{\left(-\dfrac{\delta\,\tau^n}{1 + \alpha_s\,\tau^n}\right)}$

$$\eta = \eta_\infty + \frac{\eta_0 - \eta_\infty}{1 + \left(\dfrac{\tau}{\tau_{\mathrm{m}}}\right)^{\alpha-1}} \tag{2.2}$$

here, η [Pa·s] is the shear viscosity at a given shear stress (τ); η_0 [Pa·s] is the viscosity at the zero shear stress (i.e. zero shear viscosity); η_∞ [Pa·s] is the viscosity at the infinite shear stress (i.e. infinite shear viscosity); τ_{m} [Pa] is the critical shear stress of the non-Newtonian fluid at which viscosity of the solution drops to $\frac{\eta_0+\eta_\infty}{2}$; α is the shear stress-dependent exponent of a Meter model. η_0, η_∞, and τ_{m} are measurable quantities of the non-Newtonian fluid. Here we slightly modify the denotation of the Meter model by replacing $\alpha - 1$ with S. Where, S is the shear stress-dependent exponent of the Meter model (MM). The characteristic time (λ) of the MM (Eq. 2.3) is the time at which the fluid transition from Newtonian behaviour (zero shear viscosity) to shear thinning or shear thickening behaviour (i.e. at τ_{m}) occurs.

$$\lambda = \frac{\eta_0 + \eta_\infty}{2\,\tau_{\mathrm{m}}} \tag{2.3}$$

The shear rate of MM is

$$\dot{\gamma} = \frac{\tau}{\eta_\infty + \frac{\eta_0 - \eta_\infty}{1 + \left(\frac{\tau}{\tau_\mathrm{m}}\right)^S}} \tag{2.4}$$

We note that Eq. 2.4 applies to the Newtonian fluid (if $\eta_0 = \eta_\infty$, $S = 1$, $\tau_\mathrm{m} = 1$), shear-thinning fluid (if $\eta_0 > \eta_\infty$, $S > 0$, $\tau_\mathrm{m} > 0$), and shear-thickening fluid (if $\eta_0 < \eta_\infty$, $S > 0$, $\tau_\mathrm{m} > 0$).

2.2.1 Analytical solution

Adopting the Hagen-Poiseuille framework, the analytical solution is derived for a fully developed, incompressible, isothermal, laminar, steady, unidirectional flow of shear stress-dependent time-independent non-Newtonian fluid through a circular tube of radius (R) under constant pressure gradient of $\left(\frac{dP}{dx}\right)$.

The shear rate $\dot{\gamma}(r)$ along radial direction r is defined as,

$$\dot{\gamma}(r) = \frac{\tau}{\eta}, \tag{2.5}$$

Substituting Eq. 2.2 in Eq. 2.5, we obtain

$$\dot{\gamma}(r) = \frac{\tau}{\eta_\infty + \frac{\eta_0 - \eta_\infty}{1 + \left(\frac{\tau}{\tau_\mathrm{m}}\right)^S}}, \tag{2.6}$$

The shear rate $\dot{\gamma}(r)$ in terms of velocity $u(r)$ along radial position r is as defined in Eq. 2.7,

$$\dot{\gamma}(r) = -\frac{du(r)}{dr}, \tag{2.7}$$

The shear stress (τ) in a circular tube under a constant pressure gradient of $\frac{dP}{dx}$ in the x-direction is as defined in Eq. 2.8,

$$\tau = -\frac{dP}{dx}\frac{r}{2}, \tag{2.8}$$

Now, substituting Eq. 2.7 and Eq. 2.8 in Eq. 2.6 we obtain,

$$-\frac{du(r)}{dr} = \frac{(-\frac{dP}{dx}\frac{r}{2})}{\eta_\infty + \frac{\eta_0 - \eta_\infty}{1 + \left(-\frac{dP}{dx}\frac{r}{2\,\tau_\mathrm{m}}\right)^S}}, \tag{2.9}$$

The velocity profile along the radial direction can be obtained as follows by integrating Eq. 2.9,

$$\begin{aligned} u(r) =& \frac{dP}{dx}\frac{r^2}{4\,\eta_0\,\eta_\infty}\left(\eta_0 + (\eta_\infty - \eta_0)\,{}_2\mathrm{F}_1\left(1, \frac{2}{S}; \frac{S+2}{S}; -\frac{\eta_\infty}{\eta_0}\left(-\frac{dP}{dx}\frac{r}{2\,\tau_\mathrm{m}}\right)^S\right)\right) \\ &+ \text{Constant}, \end{aligned} \tag{2.10}$$

here, ${}_2F_1$ is the hypergeometric function as defined in Eq. 2.17. At the wall of a circular tube, i.e. at $r = R$, by imposing the no-slip boundary condition, $u(R) = 0$, Eq. 2.10 becomes,

$$\text{Constant} = -\frac{dP}{dx}\frac{R^2}{4\,\eta_0\,\eta_\infty}\left(\eta_0 + (\eta_\infty - \eta_0)\,{}_2\mathrm{F}_1\left(1, \frac{2}{S}; \frac{S+2}{S}; -\frac{\eta_\infty}{\eta_0}\left(-\frac{dP}{dx}\frac{R}{2\,\tau_\mathrm{m}}\right)^S\right)\right), \tag{2.11}$$

Substituting Eq. 2.11 in Eq. 2.10, we obtain velocity profile in a circular tube for the Meter model fluid as,

$$\begin{aligned} u(r) = -\frac{dP}{dx}\frac{1}{4\,\eta_0\,\eta_\infty}\Bigg[& R^2\left(\eta_0 + (\eta_\infty - \eta_0)\,{}_2\mathrm{F}_1\left(1, \frac{2}{S}; \frac{S+2}{S}; -\frac{\eta_\infty}{\eta_0}\left(-\frac{dP}{dx}\frac{R}{2\,\tau_\mathrm{m}}\right)^S\right)\right) \\ &- r^2\left(\eta_0 + (\eta_\infty - \eta_0)\,{}_2\mathrm{F}_1\left(1, \frac{2}{S}; \frac{S+2}{S}; -\frac{\eta_\infty}{\eta_0}\left(-\frac{dP}{dx}\frac{r}{2\,\tau_\mathrm{m}}\right)^S\right)\right)\Bigg], \end{aligned} \tag{2.12}$$

The maximum velocity of the Meter model fluid in a circular tube will be at the center of the tube. On substituting $r = 0$ in Eq 2.12, we obtain maximum velocity as follows

$$U_{\max} = -\frac{dP}{dx}\frac{R^2}{4\,\eta_0\,\eta_\infty}\left(\eta_0 + (\eta_\infty - \eta_0)\,{}_2\mathrm{F}_1\left(1, \frac{2}{S}; \frac{S+2}{S}; -\frac{\eta_\infty}{\eta_0}\left(-\frac{dP}{dx}\frac{R}{2\,\tau_{\mathrm{m}}}\right)^S\right)\right), \tag{2.13}$$

Considering Q as the volumetric flow rate, the average velocity in a circular tube is given by

$$U_{\mathrm{avg}} = \frac{Q}{\pi R^2} = \frac{1}{\pi R^2}\int_0^R 2\pi\, r\, u(r)\, dr, \tag{2.14}$$

Substituting Eq. 2.12 in Eq. 2.14, and integration and simplification, we obtain average velocity during flow of a non-Newtonian Meter model fluid as,

$$\begin{aligned} U_{\mathrm{avg}} = -\frac{dP}{dx}\frac{R^2}{8\,\eta_0\,\eta_\infty}\Bigg((\eta_\infty - \eta_0)\,{}_3\mathrm{F}_2\left(1, \frac{2}{S}, \frac{4}{S}; \frac{S+2}{S}, \frac{S+4}{S}; -\frac{\eta_\infty}{\eta_0}\left(-\frac{dP}{dx}\frac{R}{2\,\tau_{\mathrm{m}}}\right)^S\right) \\ + 2\,(\eta_0 - \eta_\infty)\,{}_2\mathrm{F}_1\left(1, \frac{2}{S}; \frac{S+2}{S}; -\frac{\eta_\infty}{\eta_0}\left(-\frac{dP}{dx}\frac{R}{2\,\tau_{\mathrm{m}}}\right)^S\right) - \eta_0\Bigg), \end{aligned} \tag{2.15}$$

The analytical solution to estimate the volumetric flow rate (Q) of fluid in a circular tube/micro-capillary obeying the Meter model is given as

$$\begin{aligned} Q = -\frac{dP}{dx}\frac{\pi\, R^4}{8\,\eta_0\,\eta_\infty}\Bigg((\eta_\infty - \eta_0)\,{}_3\mathrm{F}_2\left(1, \frac{2}{S}, \frac{4}{S}; \frac{S+2}{S}, \frac{S+4}{S}; -\frac{\eta_\infty}{\eta_0}\left(-\frac{dP}{dx}\frac{R}{2\,\tau_{\mathrm{m}}}\right)^S\right) \\ + 2\,(\eta_0 - \eta_\infty)\,{}_2\mathrm{F}_1\left(1, \frac{2}{S}; \frac{S+2}{S}; -\frac{\eta_\infty}{\eta_0}\left(-\frac{dP}{dx}\frac{R}{2\,\tau_{\mathrm{m}}}\right)^S\right) - \eta_0\Bigg), \end{aligned} \tag{2.16}$$

here, the hypergeometric function ${}_2F_1(a,b;c;z)$ is defined as in the Eq. 2.17 and the hypergeometric function ${}_3F_2(a,b,c;d,e;z)$ is defined as in the Eq. 2.18

$$ {}_2F_1(a,b;c;z) = \sum_{n=1}^{\infty} \frac{(a)_n\,(b)_n\,z^n}{(c)_n\,n!}, \tag{2.17} $$

$$ {}_3F_2(a,b,c;d,e;z) = \sum_{n=1}^{\infty} \frac{(a)_n\,(b)_n\,(c)_n\,z^n}{(d)_n\,(e)_n\,n!}, \tag{2.18} $$

The `hypergeom` function of MATLAB was used to solve a generalised hypergeometric function of the analytical solution of the Meter model. The solution of the generalised hypergeometric function ${}_2F_1(a,b;c;z)$ and ${}_3F_2(a,b,c;d,e;z)$ are series as in Eq. 2.19 and 2.20 which converge for $|z|<1$ [16]. Since, all parameters of hypergeometric function of the Meter model are constant values, the series of the generalised hypergeometric function of the Meter model can be solved using `hypergeom` function of MATLAB without error over a range of pressure gradient, radius and Meter model parameters.

$$ \begin{aligned} {}_2F_1(a,b;c;z) &= \sum_{n=1}^{\infty} \frac{(a)_n\,(b)_n\,z^n}{(c)_n\,n!} \\ &= 1 + \frac{a\,b\,z}{c} + \frac{a\,(a+1)\,b\,(b+1)\,z^2}{c(c+1)\,2!} + \frac{a(a+1)\,(a+2)\,b\,(b+1)\,(b+2)\,z^3}{c\,(c+1)\,(c+2)\,3!} + ..., \end{aligned} \tag{2.19} $$

$$ \begin{aligned} {}_3F_2(a,b,c;d,e;z) &= \sum_{n=1}^{\infty} \frac{(a)_n\,(b)_n\,(c)_n\,z^n}{(d)_n\,(e)_n\,n!} \\ &= 1 + \frac{a\,b\,c\,z}{d\,e} + \frac{a\,(a+1)\,b\,(b+1)\,c\,(c+1)\,z^2}{d(d+1)\,e(e+1)\,2!} + \\ &\frac{a(a+1)\,(a+2)\,b\,(b+1)\,(b+2)\,c\,(c+1)\,(c+2)\,z^3}{d\,(d+1)\,(d+2)\,e\,(e+1)\,(e+2)\,3!} + ..., \end{aligned} \tag{2.20} $$

2.2.2 Analytical solution for existing rheological model

Table 2.2 lists the criteria for converting Meter model to Reiner-Philippoff model and Ellis model. The Table 2.2 suggests that the Meter model captures the properties of

existing shear stress-dependent rheological models.

TABLE 2.2: Criteria for converting Meter model (Eq. 2.2) to existing shear stress-dependent rheological model

Rheological model	Conversion criteria	Equation
Newtonian	$\eta_0 = \eta_\infty,\ S = 1,\ \tau_m = 1$	η
Reiner-Philippoff	$S = 2,\ \tau_m = \tau_0$	$\eta = \eta_\infty + \dfrac{\eta_0 - \eta_\infty}{1 + \left(\dfrac{\tau}{\tau_0}\right)^2}$
Ellis	$\eta_\infty = 0,\ S = \alpha - 1,\ \tau_m = \tau_{\frac{1}{2}}$	$\eta = \dfrac{\eta_0}{1 + \left(\dfrac{\tau}{\tau_{\frac{1}{2}}}\right)^{(\alpha-1)}}$

The analytical solution for Newtonian fluid and Reiner-Philippoff model fluid can be derived using the analytical solution of the Meter model.

2.2.2.1 Hagen-Poiseuille equation

The Meter model converts to Newtonian fluid case on substituting $\eta_0 = \eta_\infty$, $S = 1$, $\tau_m = 1$ in Eq. 2.2. Thus, the shear viscosity of the fluid becomes

$$\eta = \eta_\infty \tag{2.21}$$

On substituting $\eta_0 = \eta_\infty$ in Eq. 2.12 and Eq. 2.16, we obtain radial velocity profile ($u(r)$) and volumetric flow rate (Q) for a Newtonian fluid as,

$$u(r) = -\frac{dP}{dx}\frac{1}{4\,\eta}\left(R^2 - r^2\right), \tag{2.22}$$

$$Q = \frac{\pi\,R^4}{8\,\eta}\frac{dP}{dx} \tag{2.23}$$

Eq. 2.22 and Eq. 2.23 are Hagen-Poiseuille equations for radial velocity profile and volumetric flow rate derived from the analytical solution of the Meter model.

2.2.2.2 Reiner-Philippoff model

The analytical solution for Reiner-Philippoff model fluid through a circular capillary can be obtained by replacing $S = 2$ and $\tau_m = \tau_0$ in the analytical solution of the Meter model. Thus, the radial velocity profile $u(r)$ and a volumetric flow rate (Q) of the Reiner-Philippoff model will be as given in the Eq. 2.24 and Eq. 2.25, respectively,

$$u(r) = -\frac{dP}{dx}\frac{1}{4\,\eta_0\,\eta_\infty}\Bigg[R^2\left(\eta_0 + (\eta_\infty - \eta_0)\,{}_2\mathrm{F}_1\left(1,\,1;\,2;\,-\frac{\eta_\infty}{\eta_0}\left(-\frac{dP}{dx}\frac{R}{2\,\tau_0}\right)^2\right)\right) - r^2\left(\eta_0 + (\eta_\infty - \eta_0)\,{}_2\mathrm{F}_1\left(1,\,1;\,2;\,-\frac{\eta_\infty}{\eta_0}\left(-\frac{dP}{dx}\frac{r}{2\,\tau_0}\right)^2\right)\right)\Bigg], \tag{2.24}$$

$$Q = -\frac{dP}{dx}\frac{\pi\,R^4}{8\,\eta_0\,\eta_\infty}\Bigg((\eta_\infty - \eta_0)\,{}_3\mathrm{F}_2\left(1,\,1,\,2;\,2,\,3;\,-\frac{\eta_\infty}{\eta_0}\left(-\frac{dP}{dx}\frac{R}{2\,\tau_0}\right)^2\right) + 2\,(\eta_0 - \eta_\infty)\,{}_2\mathrm{F}_1\left(1,\,1;\,2;\,-\frac{\eta_\infty}{\eta_0}\left(-\frac{dP}{dx}\frac{R}{2\,\tau_0}\right)^2\right) - \eta_0\Bigg), \tag{2.25}$$

2.2.3 Effective viscosity of Meter model fluid

On equating Eq. 2.16 with Hagen-Poiseuille equation ($Q = \frac{\pi\,R^4}{8\,\eta}\frac{dP}{dx}$) and substituting $\frac{dP}{dx}\frac{R}{2} = \tau_\mathrm{w}$ in Eq. 2.16, we obtain an equation for an effective viscosity (η_eff) of fluid in terms of wall shear stress (τ_w) as follows,

$$\frac{1}{\eta_{\text{eff}}} = \frac{1}{\eta_0\,\eta_\infty}\left((\eta_\infty-\eta_0)\,{}_3\text{F}_2\left(1,\frac{2}{S},\frac{4}{S};\frac{S+2}{S},\frac{S+4}{S};-\frac{\eta_\infty}{\eta_0}\left(\frac{\tau_\text{w}}{\tau_\text{m}}\right)^S\right)\right.$$
$$\left.+\,2\,(\eta_0-\eta_\infty)\,{}_2\text{F}_1\left(1,\frac{2}{S};\frac{S+2}{S};-\frac{\eta_\infty}{\eta_0}\left(\frac{\tau_\text{w}}{\tau_\text{m}}\right)^S\right)-\eta_0\right), \tag{2.26}$$

Eq. 2.26 helps determine the effective viscosity (η_{eff}) of a non-Newtonian fluid from measurable parameters η_0, η_∞, τ_m, S, τ_w, R and $\frac{dP}{dx}$. On comparing Eq. 2.16 with Darcy's law ($Q_\text{darcy} = \frac{k\,A}{\eta}\,\frac{dP}{dx}$), we obtain an effective viscosity value as given in Eq. 2.26 and permeability (k) of the porous medium as ($k = \frac{r_\text{eff}^2}{8}$). Here r_eff is the hydraulic radius of a porous medium. Thus, the effective viscosity determined using Eq. 2.26 could be advantageous in determining the Darcy scale flow rate and velocity of a non-Newtonian fluid in a porous medium.

We observed that the effective viscosity value obtained using Eq. 2.26 consistently appears at a distance of ($0.8R$) from the centre of a capillary for all experimental flow data utilised in the present work. This suggests that the value of effective viscosity is equal to the viscosity value at a distance of $\beta\,R$ from the centre of the tube, where $0 < \beta < 1$. Thus, the approximate effective viscosity of the MM fluid for a given flow condition will be as in Eq. 2.27

$$\eta_\text{eff} = \eta_\infty + \frac{\eta_0-\eta_\infty}{1+\left(\frac{\beta\,R}{2\,\tau_\text{m}}\frac{dP}{dx}\right)^S} \tag{2.27}$$

Here, $\beta = 0.8$ for flow through a circular geometry. We note that different geometric shape will have different β value. Eq. 2.27 is an easy-to-use equation for estimation of the effective viscosity of the fluid for a given fluid flow condition compared to Eq. 2.26. The advanced mathematical tool is required to estimate effective viscosity value using Eq. 2.26 due to the presence of hypergeometric function in the equation. We obtain a semi-analytical solution for the flow rate of MM fluid by substituting Eq. 2.27 in Hagen-Poiseuille equation as,

$$Q = \frac{dP}{dx} \frac{\pi R^4}{8 \left(\eta_\infty + \frac{\eta_0 - \eta_\infty}{1 + \left(\frac{\beta R}{2 \tau_\mathrm{m}} \frac{dP}{dx} \right)^S} \right)} \tag{2.28}$$

We define the effective Reynolds number ($\mathrm{Re}_{\mathrm{eff}}$) of MM fluid as

$$\mathrm{Re}_{\mathrm{eff}} = \frac{2 \rho U_{\mathrm{avg}} R}{\eta_{\mathrm{eff}}} \tag{2.29}$$

The Darcy's friction factor (f_D) during any type of a fluid flow is $f_D = \frac{dP}{dx} \frac{4R}{\rho U_{\mathrm{avg}}^2}$. We obtain effective friction factor (f_{eff}) for laminar flow of MM fluid (Eq. 2.30) by substituting the MM analytical solution for average velocity (Eq. 2.15) in Darcy's friction factor equation.

$$f_{\mathrm{eff}} = \frac{256}{\rho R^3 \left(\frac{dP}{dx} \right)} \eta_{\mathrm{eff}}^2 = \frac{128}{\rho R^2 \tau_\mathrm{w}} \eta_{\mathrm{eff}}^2 \tag{2.30}$$

2.3 Results and Discussion

2.3.1 Meter model for shear thinning and shear thickening fluids

Fig 2.2 shows a statistically good fit of experimental and MM predicted (Eq. 2.2) viscosity-shear stress and shear rate-shear stress data of a shear-thinning fluid (xanthan gum fluid of [34] over a range of concentration, polyacrylamide (PAA) fluid of [69]) and a shear-thickening fluid (cornstarch fluid in a glycerol-water mixture of [30]). The model parameters are estimated using Excel-Solver methods that use the GRG nonlinear algorithm [107]. Fig. 2.2 shows that cornstarch fluid has a shear-thinning region at lower shear stresses and high shear stresses. The literature reports similar behaviour for most of shear thickening fluids; thus, an application of MM for shear thickening fluids should be restricted to the shear thickening region of the viscosity-shear stress curve.

The material parameters of MM (Table 2.3) imply that the zero shear viscosity (η_0) and critical shear stress (τ_m) increases exponentially and the shear-thinning property of xanthan gum fluid (i.e. exponent S) increases linearly with an increase in the concentration

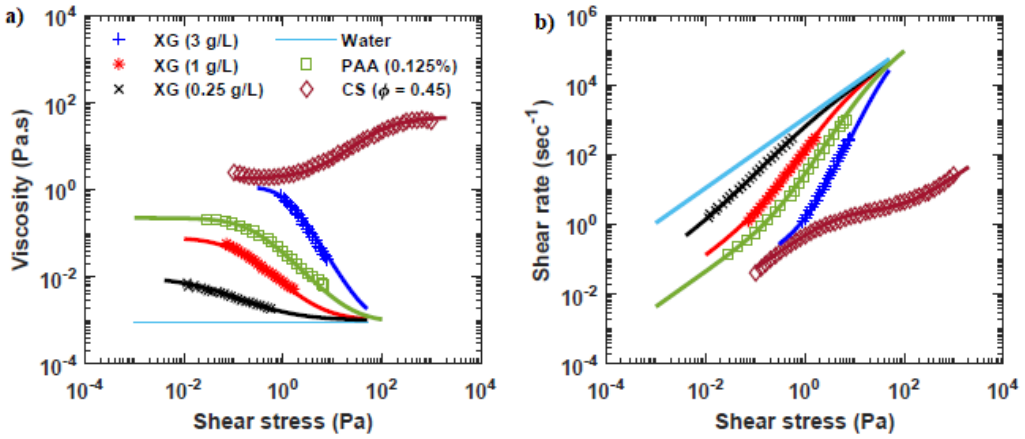

FIGURE 2.2: (a) Shear viscosity as a function of shear stress (Eq. 2.2), (b) shear rate as a function of shear stress (Eq. 2.4) modelled using MM. An experimental rheological data of xanthan gum (XG) fluid over range of concentration (3 g/L, 1 g/L, 0.25 g/L, water) [34]; 0.125% polyacrylamide (PAA) fluid [69], cornstarch (CS) fluid having volume fraction of 0.45 [30] modelled using MM. Continuous line shows MM predications. The material parameters of MM are given Table 2.3. The root means square error (RMSE) range from 3.4×10^{-3} to 1.6×10^{-1}.

TABLE 2.3: MM parameters of [30, 34, 69]

Parameter	Shear thinning fluid					shear thickening fluid
	Xanthan gum (XG) concentration (g/L) [34]				PAA [69]	Cornstarch (CS) [30]
	3 g/L	1 g/L	0.25 g/L	0	0.125%	$\phi = 0.45$
η_0 [Pa.s]	1.2	0.08	0.01	0.000896	0.2257	1.8
η_∞ [Pa.s]	0.000896	0.000896	0.000896	0.000896	0.000896	46
τ_m [Pa]	1.1	0.105	0.028	1	0.24	100
S	1.87	1.11	0.75	1	1.124	1.1
$\lambda\,[s]$	0.546	0.385	0.195		0.47	0.24

of the xanthan gum fluid. This implies that MM helps to quantitatively correlate the effect of physico-chemical parameters (e.g. XG concentration in the present case) on the rheology of shear thinning and shear thickening fluids using measurable parameters.

2.3.2 The factor β

To determine β over a range of pressure gradient, radius and Meter model parameters, we substitute Eq. 2.27 in Eq. 2.26 and solve the resultant equation for β. Fig 2.3 shows that the factor β values ranged from 0.73 to 0.82 over a range of pressure-gradient, radius and Meter model parameters. The average value of the $\beta = 0.8$ suggests that an effective viscosity of the fluid measured at a distance of $0.8R$ from the centre of the capillary can be considered as an approximate effective viscosity of the fluid.

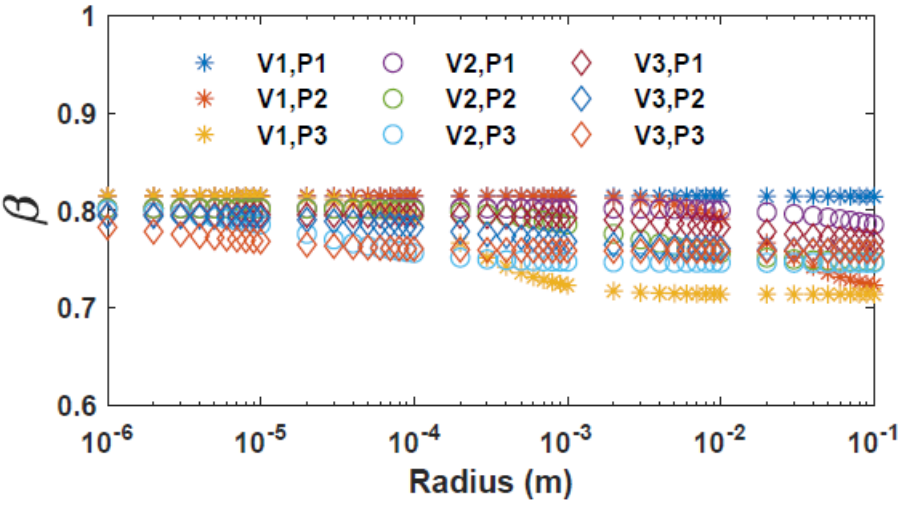

FIGURE 2.3: The factor β over a range of a pressure gradient, radius and Meter model parameters. V1, V2, and V3 represents viscosity of the 3g/L, 1 g/L and 0.25 g/L xanthan gum fluid, respectively, as given in the Table 2.3. P1 = 10^2 Pa/m, P2=10^4 Pa/m and P3 = 10^6 Pa/m.

2.3.3 Validation of the analytical solution of the Meter model

a) Flow-through a micro-capillary

An experimental velocity profile of [34] gave a good fit with the analytical solution of the MM for radial velocity profile (Eq. 2.12) at the pressure gradients of 92,000 Pa/m, 16,500 Pa/m, 4,900 Pa/m and 2,000 Pa/m during flow of 3 g/L, 1 g/L, 0.25 g/L xanthan gum fluid and water (0.4 % milk), respectively (see Fig. 2.4a). Moreover, the analytical (Eq. 2.16) and semi-analytical (Eq. 2.28) solutions of the MM for flow rate could correctly determine the experimental flow rate of 30 μL/min through a circular microfluidic channel of radius 160 μm. Fig. 2.4b suggests that the viscosity profile of the non-Newtonian shear-thinning fluid is bell-shaped in a circular geometry. The viscosity increases gradually near the wall and drastically in the central region of the micro-capillary. The effective viscosity estimated using Eq. 2.26 and Eq. 2.27, for flow of a 3 g/L, 1 g/L and 0.25 g/L xanthan gum fluid through a micro-capillary is 0.041 Pa.s, 0.0075 Pa.s and 0.0022 Pa.s, respectively. We note that the analytical solution of the Meter model fluids is applicable for shear thickening fluids and needs validation using experimental data.

b) Flow-through a tube

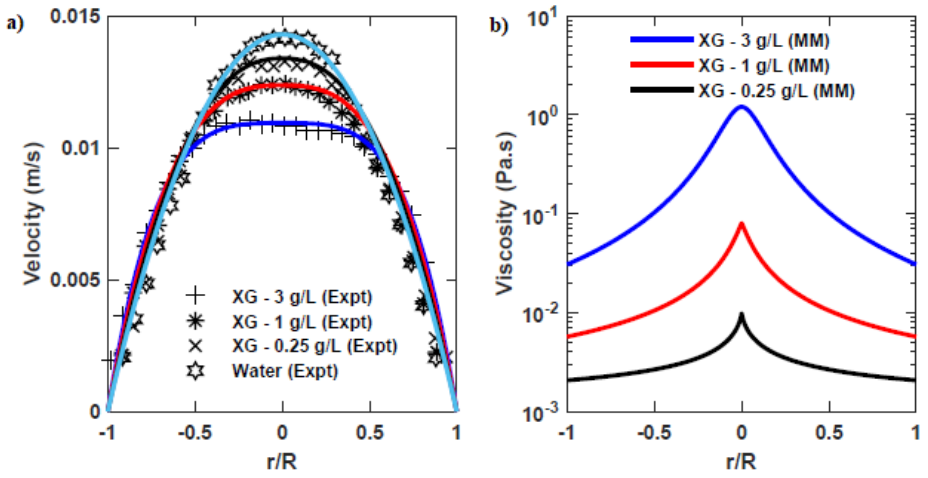

FIGURE 2.4: Comparison of experimental [34] and MM analytical solution predicated by Eq. 2.12, (a) radial velocity profile, and (b) radial viscosity profile during flow of a xanthan gum (XG) through a circular micro-capillary (radius 160 μm) over a range of XG concentrations. The material parameters of MM are given Table 2.3. The root means square error (RMSE) range from 3.4×10^{-4} to 6.3×10^{-2}.

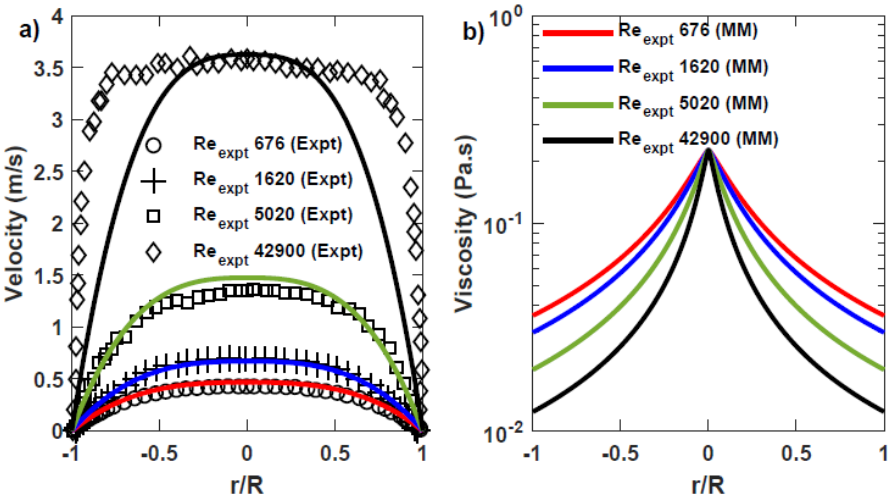

FIGURE 2.5: Comparison of experimental [69] and MM analytical solution predicated by Eq. 2.12, (a) radial velocity profile, and (b) radial viscosity profile during flow of a 0.125% polyacrylamide (PAA) fluid through a circular tube (radius 0.05 m) over a range of Reynolds numbers. The material parameters of MM are given Table 2.3. The root means square error (RMSE) range from 3.4×10^{-4} to 8.5×10^{-3} for $\mathrm{Re}_{\mathrm{eff}} < 1620$.

TABLE 2.4: Validation of the analytical solution of MM for flow through a circular tube

Experimental observation [69]					MM Estimate				
$\mathrm{Re}_{\mathrm{expt}}$	$\frac{dP}{dx}$ (Pa/m)	U_{expt} (m/s)	η_{w} (Pa.s)	f_{D}	η_{eff} (Pa.s)	Q (m^3/s)	U_{Avg} (m/s)	$\mathrm{Re}_{\mathrm{eff}}$	f_{eff}
676	38.5	0.256	0.0376	0.1135	0.0467	0.002	0.2578	552	0.1158
1620	51	0.447	0.0276	0.0510	0.0358	0.0035	0.448	1241	0.0516
5020	70	0.939	0.0187	0.0159	0.0262	0.0065	0.8339	3178	0.0201
42900	109	3.36	0.0078	0.0019	0.0156	0.0172	2.184	14007	0.0046

Escudier *et al.* [69] measured the radial velocity profile of 0.125% polyacrylamide (PAA) fluid flow in a circular tube (radius 5 cm) over a range of Reynolds numbers ($\mathrm{Re}_{\mathrm{expt}}$), wherein the authors defined Reynolds numbers ($\mathrm{Re}_{\mathrm{expt}}$) using shear viscosity at the wall of the pipe. Fig 2.5a depicts that the analytical solution of the MM for the velocity profile (Eq. 2.12) could correctly predict the experimentally observed radial velocity profile at $\mathrm{Re}_{\mathrm{expt}} = 676$ and $\mathrm{Re}_{\mathrm{expt}} = 1620$. The analytical solution of MM is restricted to laminar flow and Fig 2.5a suggests that at $\mathrm{Re}_{\mathrm{expt}} = 5020$ PAA flow is in transition phase and at $\mathrm{Re}_{\mathrm{expt}} = 42900$ is in turbulent phase. Fig 2.5b shows that the shape of the viscosity profile becomes more acute at the centre of the circular tube with an increase in Reynolds number or pressure gradient.

The effective Reynolds number ($\mathrm{Re}_{\mathrm{eff}}$) values calculated using Eq. 2.29 are drastically different from $\mathrm{Re}_{\mathrm{expt}}$ estimated by [69] (see Table 2.4). The analytical solution of the MM could correctly estimate the velocity profile, flow rate, average velocity and friction factor within the error range ($\pm$ 5%), when $\mathrm{Re}_{\mathrm{eff}}$ of PAA is less than 1241 (at $\frac{dP}{dx} < 51$ Pa/m). On the contrary, when $\mathrm{Re}_{\mathrm{eff}}$ was 3178 (at $\frac{dP}{dx} = 70$ Pa/m) and 14007 (at $\frac{dP}{dx} = 109$ Pa/m), flow becomes turbulent, and velocity profile could not be matched with the experimental data. This result suggests that the Reynolds number determined using Eq. 2.29 gives comparable results to the Reynolds number of a Newtonian fluid in a circular tube. Thus, it is convenient to define a non-Newtonian fluid flow as (i) laminar if $\mathrm{Re}_{\mathrm{eff}} < 2300$, (ii) turbulent if $\mathrm{Re}_{\mathrm{eff}} > 2900$, and (iii) transition zone if $2300 < \mathrm{Re}_{\mathrm{eff}} < 2900$.

As given in Table 2.4, the friction factor of the MM determined using Eq. 2.30 and the experimental friction factor (f_{D}) determined using Darcy's law give approximately same result for a laminar flow ($\mathrm{Re}_{\mathrm{eff}} < 1241$). As expected for the turbulent flow, the friction factor estimate has a difference of 26% at $\frac{dP}{dx} = 70$ Pa/m and 142% at $\frac{dP}{dx} = 109$ Pa/m. For a Newtonian fluid, the relationship between the Reynolds number and the friction factor for laminar flow through a circular tube is given as $\mathrm{Re} = \frac{64}{f_{\mathrm{D}}}$.

The same relationship applies to the non-Newtonian fluid described by the MM. The $\mathrm{Re}_{\mathrm{eff}}$ estimated using Eq. 2.29 is equivalent to the Reynolds number estimated using $\mathrm{Re}_{\mathrm{eff}} = \frac{64}{f_{\mathrm{D}}}$, if an experimental error of up to 5% is taken into account for laminar flow of [69].

2.3.4 The effective friction factor

A simple algebraic formula for the effective friction factor as a function of pressure gradient, radius and Meter model parameters (η_∞, η_0, τ_{m}, S), as presented in Eq. 2.31, can be obtained on substituting Eq. 2.27 in Eq. 2.30. This is a semi-analytical formula for the effective friction factor of the Meter model fluid.

$$f_{\mathrm{eff}} = \frac{256}{\rho\, R^3 \left(\frac{dP}{dx}\right)} \left(\eta_\infty + \frac{\eta_0 - \eta_\infty}{1 + \left(\frac{0.8\, R}{2\, \tau_{\mathrm{m}}} \frac{dP}{dx} \right)^S} \right)^2 \tag{2.31}$$

Fig 2.6 shows that the effective friction factor estimated using Eq. 2.30 closely matches with the f_{eff} estimated using Eq. 2.31 over a range of xanthan gum concentrations. Fig 2.6 also shows a non-linear relationship between the pressure gradient and the effective friction factor. An increase in the radius of the circular capillary/pipe decreases the friction factor. Moreover, increase in the polymeric concentration of xanthan gum fluid shows increase in f_{eff} over a range of pressure gradients and radii. The results suggest that the Eq. 2.31 can be utilised to determine f_{eff} of a non-Newtonian fluid using measurable parameters (i.e. radius, pressure gradient, and Meter model parameters).

2.3.5 Radial viscosity variation

We determined radial viscosity variation (%) during flow of an MM fluid through a circular tube/micro-capillary using Eq. 2.32.

$$\text{Radial viscosity variation}\,(\%) = \frac{(\eta_{\mathrm{center}} - \eta_{\mathrm{w}})}{\eta_{\mathrm{center}}} \times 100, \tag{2.32}$$

here, η_{center} and η_{w} is the viscosity at the centre and wall of a circular tube, respectively. The variation of viscosity along the radial direction in a circular tube/capillary depends

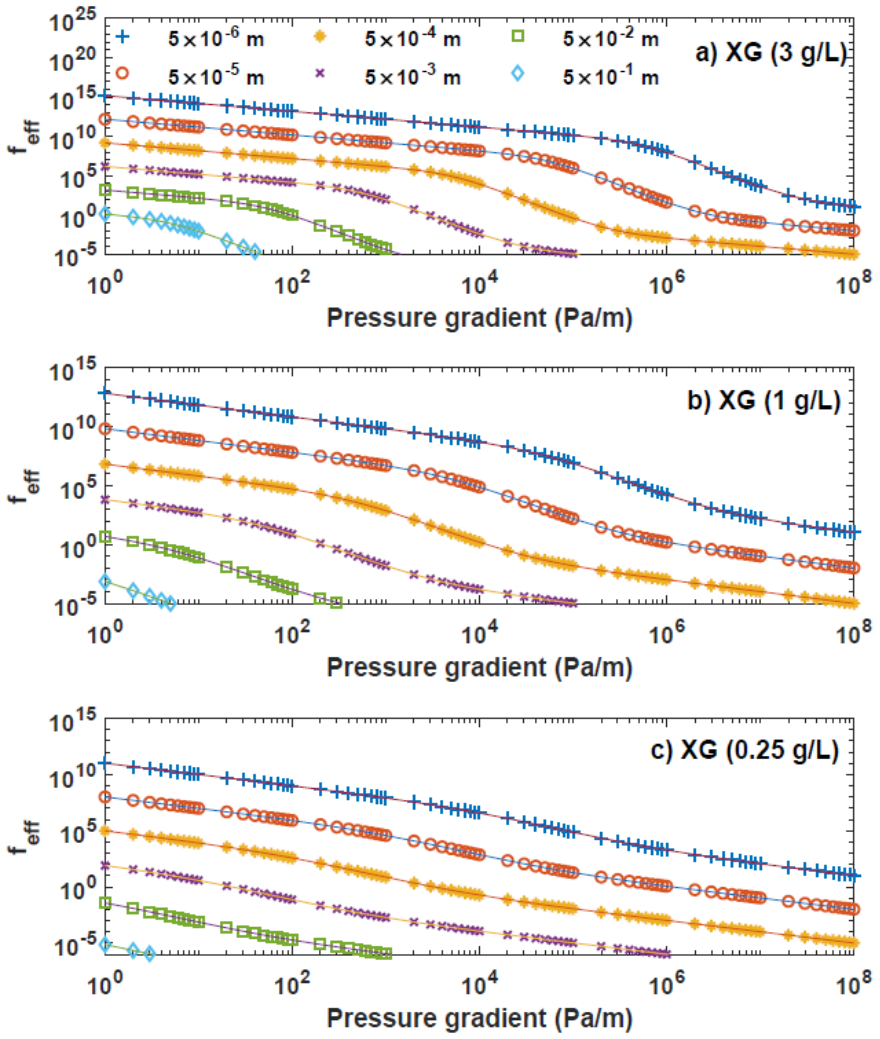

FIGURE 2.6: The effective friction factor as a function of pressure gradient over a range of radii (5 μm to 0.5 m) and xanthan gum (XG) concentrations. (a) XG: 3 g/L, (b) XG: 1 g/L, and (c) XG: 0.25 g/L. Symbols show f_{eff} estimated using Eq. 2.30 and continuous solid lines show f_{eff} estimated using Eq. 2.31 for radius (R) of capillary/tube. Meter model parameters are given in Table 2.3.

on radius and pressure gradient, i.e. on the shear stress. Fig. 2.7a shows estimated radial viscosity variation (%) at a various pressure gradients (1 Pa/m to 10^8 Pa/m) and a radius (0.05 μm – 500 mm) during XG-3 g/L fluid flow of [34] in a circular tube/capillary. Similarly, Fig. 2.7b elucidates radial viscosity variation (%) at various Reynolds number (10^{-9} to 10^7) and pressure gradient ($10^{-1} - 10^6$ Pa/m).

It appears from Fig. 2.7a that for each radius, there exists a critical pressure gradient value below which the viscosity variation is insignificant. If radial viscosity variation of 10^{-1}% is considered as an insignificant variation, then 10^6 Pa/m, 10^5 Pa/m, 10^4 Pa/m, 10^3 Pa/m, 10^2 Pa/m, 10^1 Pa/m will be the critical/threshold pressure gradient values

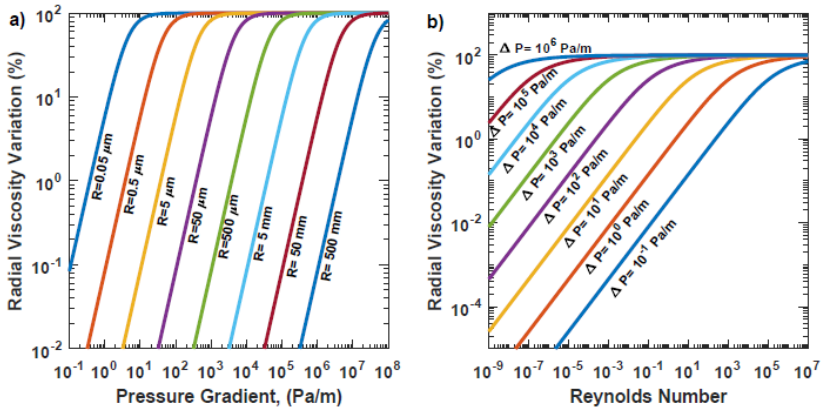

FIGURE 2.7: (a) Effect of pressure gradient and radius (R) on the radial viscosity variation (%) during flow of a xanthan gum (XG, 3 g/L) fluid of [34] in a circular capillary/tube, (b) effect of Reynolds number and pressure gradient on the radial viscosity variation (%) during flow of a xanthan gum (XG, 3 g/L) fluid of [34] in a circular capillary/tube.

for capillaries of radius 0.05 μm, 0.5 μm, 5 μm, 50 μm, 500 μm, and 5 mm, respectively. Below these thresholds the viscosity variation could be considered as insignificant or effectively constant. The choice of viscosity variation as "an insignificant" might depend on the viscosity at a zero shear stress (η_0), and effect of the viscosity variation on the output of work. Fig. 2.7a also suggests that with an increase in the radius of a capillary, magnitude of the critical pressure gradient decreases.

Similarly, Fig. 2.7b shows that, for each pressure gradient, there exists a critical Reynolds number below which the viscosity variation is insignificant. Fig. 2.7b shows that if the pressure gradient of the XG-3 g/L fluid through a circular tube/micro-capillary is lower than 100 Pa/m and Reynolds number is below 0.001, the radial viscosity variation is insignificant. Overall, Fig. 2.7 illustrates that if applied pressure gradient or Reynolds number are below their threshold/critical values, the non-Newtonian fluid flow can be modelled as a Newtonian fluid with a zero shear stress viscosity as its constant viscosity. This means that the fluid flow through a capillary can be modelled using the Hagen-Poiseuille equation.

2.4 Conclusions

The Meter model was validated against experimental rheological data of cornstarch fluid, polyacrylamide fluid and xanthan gum fluid. The analytical solution of the MM was

validated against the experimentally measured velocity profile during the flow of non-Newtonian fluids (xanthan gum and polyacrylamide) through a circular micro-capillary of radius 160 μm and a circular tube of radius 0.05 m. An easy-to-use semi-analytical solution (similar to the Hagen-Posseuille equation) is formulated for the computation of an effective viscosity and a flow rate. The effective Reynolds number estimated using the formulation presented in this work helps to correctly characterise fluid flow in laminar, turbulent and transition flow. The Darcy's friction factor computed using the formulation given in the current work, and the experimental friction factor gave equivalent results for laminar flow. Finally, this work suggests that there exists a threshold pressure gradient for a given radius and a critical effective Reynolds number below which the radial viscosity variation is insignificant, and it will be convenient to assume a constant viscosity for such flows.

The method proposed in the present work to compute effective viscosity, average velocity, radial velocity profile, flow rate, effective Reynolds number, and effective friction factor using measurable flow parameters will help to understand the behaviour of non-Newtonian fluids comprehensively. In the future, we will apply the proposed model for the flow of non-Newtonian fluids in heterogeneous porous media using OpenFOAM and the pore-Network model and compare our results to similar recent publications, for example, [228].

Chapter 3

An empirical equation for shear viscosity of shear thickening fluids

This chapter is published in the '*Journal of Molecular Liquids*'

Authors: **T. Shende,** V. J. Niasar, and M. Babaei. An empirical equation for shear viscosity of shear thickening fluids. *Journal of Molecular Liquids*, 325:115220, 2021.

3.1 Introduction

The suspension shear-thickening behaviour (i.e. increase in the shear viscosity with an increase in the shear stress/rate showed by colloidal/non-colloidal suspension) [193] has wide applications starting from cement [47], woven fabrics [114], chocolates [74], cornstarch [72] to ceramics [214]. The shear-thickening fluids are excellent for a shock-absorption due to their high elastic modulus and high dissipation energy [87, 214]. Smart materials are being developed, such as magnetorheological shear thickening fluids [221], which act as actuating fluids to maintain variable flow rate or force transfer scenario in many engineering applications such as artificial joints and breaks [87, 182].

Mixing colloidal particles or polymers (i.e. solutes) in a solvent (e.g. water) leads to an increase in the viscosity of the solution, and a further increase in the concentration of solute/colloids makes the fluid behave like a non-Newtonian fluid. At lower stress, shear thickening fluids show Newtonian behaviour [214]. The fluid shows shear-thinning characteristics once critical stress exceeded, i.e. the viscosity of the fluid drops with an increase in stress. The fluid can flow under weak stress and still be able to behave like a gel at rest. The viscosity of the fluid suddenly rises once it reaches critical stress at higher stresses [214]. This behaviour of a fluid is defined as shear thickening, which mostly depends on the properties of solutes and colloids (shape and size of molecules, volume fraction, etc.) and solvents (viscosity, deformation, etc.) [31, 87, 143, 214]. Figure 3.1 shows the typical rheological behaviour of a shear thickening fluid under varying shear stress or shear rate. The typical shear thickening behavior can also be observed at low temperatures (i.e. temperature $> -40°C$) [38].

Interparticle and intermolecular contact forces and hydrodynamic forces significantly contribute towards shear thickening of the suspension in the fluid [40, 118, 129, 143, 205, 229]. The external or internal forces in solution cause displacement of suspended colloid particles/solute. The force transmits from one colloid particle/solute molecule to the neighbouring colloid particle/solute molecule through the intervening fluid. The hydrodynamic interaction between colloid particles/solute and solvent disturb the local flow field of all colloids particles/solute molecules [223, 229]. We note that the intervening fluid (solvent) acts as a lubricant between neighbouring colloids particles/solutes [31, 193]. Hydrophobic or hydrophilic properties of the colloidal particles/polymer

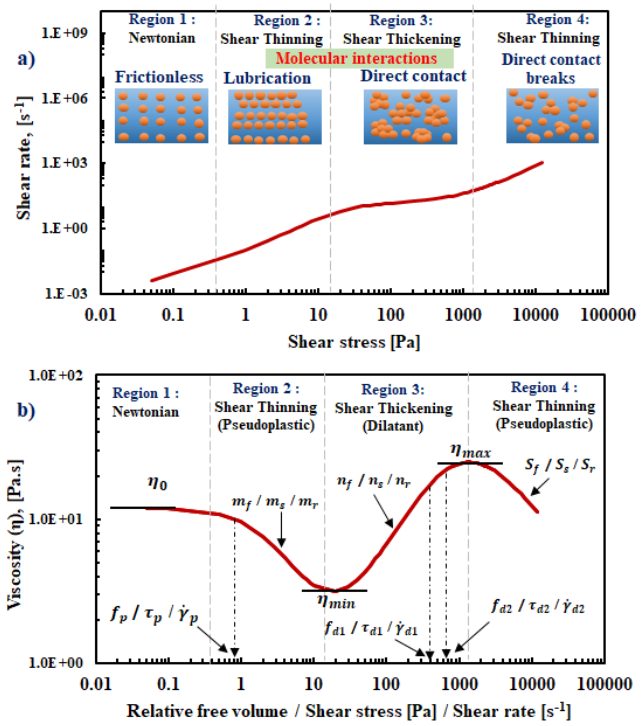

FIGURE 3.1: Typical rheological behaviour of a shear thickening fluid under varying relative free volume or shear stress or shear rate. (a) Shear rate - stress relationship, and (b) viscosity as a function of shear stress or shear rate. Typical shear thickening fluid shows Newtonian, shear thinning, shear thickening and second shear thinning regimes. We note that the image is representative and not to scale.

molecules along with hydrodynamic interaction between colloid/solute and solvent determines the relative motion of the particles and effectiveness of the solvent to act as a lubricant. The electrostatics [103, 233] and van der Waals forces play a significant role in maintaining the viscosity of the solution [87, 143, 193]. Interparticle forces are dominant at lower stresses; on the contrary, hydrodynamic forces play a vital role at high stresses. Alteration of particles' surface chemistry, ionic strength, shape, and size affect the interparticle or intermolecular forces, thus the viscosity of the solution. The shear induced particle migration and shear banding also affect the shear thinning or thickening of the fluid [72].

Although many empirical models have been developed to characterise the shear thinning behaviour of non-Newtonian fluids [223], a single equation which could completely characterise the rheological behaviour of shear thickening fluids (see Fig. 3.1) is meagre. Previously, Gopalakrishnan and Zukoski [83] proposed an empirical equation for the shear viscosity based on thermodynamics and hydrodynamic interaction of shear thickening fluids. The constitutive relation proposed by Wyart and Cates [219] for

shear thickening suspension is a well accepted constitutive model for shear thickening suspension. Galindo-Rosales *et al.* [78, 79] developed shear rate-dependent branch of equations based on Cross model [43] to capture first shear thinning, shear thickening and second shear thinning region of shear thickening fluids. Recently, Steller and Iwko [201] proposed an empirical shear stress-dependent and shear-rate dependent model for the non-Newtonian fluids based on the free volume theory. The Steller-Iwko multi-model rheological equation [201] captures the complicated viscosity curve of non-Newtonian fluids. Steller-Iwko [201] modified an empirical equation developed by Doolittle [62] to relate viscosity of the fluid with shear stress and shear rate. Free volume theory proposed by [62] is being extensively used to explain temperature-dependent viscosity variations observed in amorphous polymers and glass-forming liquids. Williams-Landel-Ferry (WLF) equation [217] developed based on the free volume theory of Doolittle [62] has been employed to model time temperature-dependent rheology of polymeric solutions (e.g. polystyrene melts [150], supra-macromolecular polymers [26]).

Free volume theory assumes that the viscosity of the fluid depends on the free space available for molecules to move in a total volume. The relative free-space available for molecules or particles depends on the stresses generated in the fluids [62]. Adopting the Doolittle approach, the interlink between relative free space, viscosity, and stress can be established to empirically define viscosity as a function of the relative free volume of shear thickening fluids.

The absence of a single rheological equation, which could characterise all regimes of shear thickening fluids (see Fig 3.1) and could be utilised for the pore-scale fluid flow numerical simulation, motivated us to develop an empirical equation based on the free volume theory that models rheological characteristics of shear thickening fluids using measurable parameters and identifies threshold parameters of shear thickening fluids. We propose an empirical equation that relates the shear viscosity of a shear thickening fluid with a relative free volume. The proposed free volume-based equation is then utilised to develop a shear stress-dependent rheological equation and a shear rate-dependent rheological equation for shear thickening fluids. The proposed equations are validated against experimental data. Further, we simulate the flow of shear thickening fluid, using the proposed equation, through a 2D micromodel of a porous medium.

3.2 Mathematical Formulations

The shear viscosity of non-Newtonian fluids can be defined using a constitutive equation of generalised Newtonian fluids (GNF) [21, 22]. The shear stress-dependent viscosity functions ($\eta(\tau)$) define viscosity as a function of the magnitude of deviatoric stress tensor (i.e. $\boldsymbol{\tau} = 2\,\eta(\tau)\,\boldsymbol{D}$) [130, 134, 159, 201]. The shear rate-dependent viscosity function ($\eta(\dot{\gamma})$) defines viscosity as a function of second invariant of rate-of-deformation tensor (i.e. $\boldsymbol{\tau} = 2\,\eta(\dot{\gamma})\,\boldsymbol{D}$) [21, 22]. Here, the magnitude of shear stress is $|\tau| = \sqrt{\frac{\boldsymbol{\tau} : \boldsymbol{\tau}}{2}}$ [134], the magnitude of shear-rate is $|\dot{\gamma}| = \sqrt{\frac{\dot{\boldsymbol{\gamma}} : \dot{\boldsymbol{\gamma}}}{2}}$ [22], $\boldsymbol{D} = \frac{1}{2}\dot{\boldsymbol{\gamma}} = \frac{1}{2}(\nabla\mathbf{u} + (\nabla\mathbf{u})^T)$, and $\mathbf{u}$ is the velocity vector. Most of the GNF model equations are empirical equations and have their limitations [21, 22]. Amongst commonly used GNF equations (i.e. power-law, Bingham, Herschel–Bulkley, Carreau, Cross [21, 22]) in the literature, Cross equation [43] is considered to be deduced from a physical basis (i.e. the rate kinetics of rupture and formation of linkage between the particles of the polymers) [43, 78, 79]

The shear stress-dependent Meter model equation (Eq. 3.1, Eq. 2.2 of Chapter 2) [134, 190] is a logistic equation that describes the S-shape type curve (i.e. Newtonian plateau at high and low shear values and slope at intermediate shear values) of many shear-thinning fluids.

$$\eta = \eta_\infty + \frac{\eta_0 - \eta_\infty}{1 + \left(\frac{\tau}{\tau_p}\right)^{\alpha-1}} \tag{3.1}$$

here, η [Pa·s] is the shear viscosity; η_0 [Pa·s] is the zero shear viscosity of the Newtonian region of fluid; η_∞ [Pa·s] is the infinite shear viscosity. α is a Meter model exponent which represents the slope. τ_p is the threshold shear stress at which viscosity value is $\frac{\eta_0+\eta_\infty}{2}$.

We modified the equation proposed by Meter as follows that captures the typical viscosity curve of the shear thickening fluid over a range of shear stress values (see Fig 3.1). We note that the proposed equation follows a similar type of approach as adopted by Galindo-Rosales *et al.* [78, 79],

$$\eta = \eta_{min} + \frac{\eta_0 - \eta_{min}}{1 + \left(\frac{\tau}{\tau_p}\right)^{m_s}} + \frac{(\eta_{max} - \eta_{min})\left(\frac{\tau}{\tau_{d1}}\right)^{n_s}}{\left(1 + \left(\frac{\tau}{\tau_{d2}}\right)^{n_s}\right)^{S_s}}, \tag{3.2}$$

here, η [Pa·s] is the shear viscosity; η_0 [Pa·s] is the zero shear viscosity of the Newtonian region of fluid (region 1); η_{min} [Pa·s] is the minimum viscosity of the intermediate shear thinning region (region 2) of fluid (i.e. minimum shear viscosity); η_{max} [Pa·s] is the maximum viscosity of the shear thickening region of fluid (i.e. maximum shear viscosity). m_s is an exponent which represents the slope of the intermediate shear thinning region of fluid (region 2). n_s is an exponent which represents the slope of the shear thickening region of fluid; S_s is an exponent which represents the slope of the extreme shear thinning region of fluid (region 4). τ_p [Pa] is the shear stress at which the viscosity of the solution drops to $\frac{\eta_0+\eta_{min}}{2}$ in the intermediate shear thinning region (region 2). τ_{d1} [Pa] and τ_{d2} [Pa] are shear stresses at which the viscosity of the solution drops to intermediate values between η_{min} and η_{max} in the shear thickening region (region 3). The viscosity at τ_{d1} is $\eta_{min} + \frac{\eta_0 - \eta_{min}}{1 + \left(\frac{\tau_{d1}}{\tau_P}\right)^{m_s}} + \frac{(\eta_{max} - \eta_{min})}{\left(1 + \left(\frac{\tau_{d1}}{\tau_{d2}}\right)^{n_s}\right)^{S_s}}$ and the viscosity at τ_{d2} is $\eta_{min} + \frac{\eta_0 - \eta_{min}}{1 + \left(\frac{\tau_{d2}}{\tau_P}\right)^{m_s}} + \frac{(\eta_{max} - \eta_{min})\left(\frac{\tau_{d2}}{\tau_{d1}}\right)^{n_s}}{2^{S_s}}$. Fig. 3.1b shows the rheological material parameters of the shear stress-dependent viscosity.

3.3 Free-Volume Theory

Most of the non-Newtonian fluid solutions are a mixture of solute or colloidal particles (e.g. cornstarch, xanthan-gum) in a solvent (e.g. water). Note that colloids (e.g. silica nano-particles) are phase separated and insoluble molecules in the solution, whereas solute (e.g. polymers) dissolve in the solvent. The small molecular size of the solvent in the solution helps the solvent to act as a lubricant between solute/colloid molecules of larger size. The shear thinning or shear thickening behaviour observed in the non-Newtonian fluid depend highly on the thickness of the solvent's lubricant layer between solute/colloid particles molecules [27, 31, 214]. Interaction between solute or colloid molecules is relatively frictionless (i.e. in equilibrium) at lower stress [214], and this may be the reason for Newtonian behaviour at a lower shear rate or shear stress (as in

Region 1, Fig 3.1). An increase in the stress decreases frictionless interaction between solute/colloids molecules [129, 193, 214]; and the solvent effectively acts as a lubricant between solute/colloids molecules. The solvent, being a lubricant, resists direct interaction between solute/colloids molecules. The viscous nature of the solvent streamlines solute/-colloids molecules and increases the efficient transport of a solute/colloids in the solvent [143, 214]. The flow of a solvent is mostly laminar between solute/colloids molecules. This causes a drop in the viscosity of a solution with an increase in shear stress (see Region 2 in Fig 3.1). The effectiveness of a solvent to act as a lubricant ceases at sufficiently higher shear stresses. Coagulation of solute/colloids molecules forms a hydro cluster [27, 31, 36, 143, 214] in the solution due to direct contact between solute/colloids molecules. The viscosity of the fluid increases abruptly at high stresses due to the larger size of the coagulated hydro cluster (see Region 3 in Fig 3.1). However, at very high shear stresses direct contact between coagulated solute/colloids molecules breaks [77]. This leads to smaller size hydro clusters and separated solute/colloids molecules which decrease the viscosity of the solution (see Region 4 in Fig 3.1). The viscosity of the fluid could also decrease due to rupture or erosion of the hydro-clusters or particles. The presence of artefact in the suspension may lead to the slipping of the particles if the colloidal suspension is solid-like. This may cause shear thinning at high shear values. We note that hydrodynamic and interparticle (intermolecular) interactions between solute/colloids and solvent strongly affect the relative free volume of solute/colloids and solvent and, in turn, viscosity of the solution is changed.

Macleod (1923) [124] was first to postulate that the viscosity of a fluid is influenced by the free space available for molecules to move in a total volume. He suggested that the crowding of more molecules in a small space will increase the viscosity of the fluid as it will increase the cohesive force between molecules and decrease the required time for molecules to move out of contact. The free space theory proposed by Macleod was further developed by Doolittle [62] in which he defined free-space in a liquid as space arises due to the liquid's total thermal expansion without phase change. Doolittle defined relative free space as in Eq. 3.3,

$$\frac{V_f}{V_0} = \frac{V - V_0}{V_0} \tag{3.3}$$

Where $\frac{V_f}{V_0}$ is a relative free space for a single substance; V_f is a volume of free space per gram at any temperature; V_0 is a volume of one gram of liquid extrapolated to absolute zero temperature without change of phase; V is a volume of one gram of liquid at any temperature. Doolittle [62] proposed an empirical equation to relate the viscosity of the solution with the free volume space as in Eq. 3.4,

$$\eta = A\, e^{\left(\frac{B}{V_f/V_0}\right)} \tag{3.4}$$

Here, A and B are material constants for a single substance. Although Doolittle validated Eq. 3.4 for the temperature-dependent decrease in viscosity of a Newtonian fluid, he noted that pressure and temperature could change relative free space in the liquid. Although Doolittle equation (i.e. Eq. 3.4) can not define the rheology of shear thickening fluids, we could extend the free volume theory of Doolittle to model the rheology of non-Newtonian fluids, specifically shear thickening fluids.

3.3.1 Relative free-volume dependent viscosity

Extending Doolittle free volume theory [62], we propose an empirical equation (Eq. 3.5) that relates the relative free volume (f) with the shear viscosity (η) of shear thickening fluids. We assume that (a) relative free volume of the solution changes due to hydrodynamic and inter molecular (or particle) forces; (b) fluid flow and deformation, thermal variation, external and internal pressure, molecular movement due to chemical reactions generate these hydrodynamic and inter molecular (or particle) forces in a solution; (c) the change in relative free volume is proportional to the local stresses (shear, normal, or thermal); (d) V_f is the free volume at any stress, V_0 is the volume of liquid at a zero stress and absolute zero temperature without phase change, V is the volume of liquid at any stress, and the relative free volume is $f = \frac{V-V_0}{V_0} = \frac{V_f}{V_0}$. Eq. 3.5 has the following form similar to Eq. 3.2:

$$\eta = \eta_{min} + \frac{\eta_0 - \eta_{min}}{1 + \left(\frac{f}{f_p}\right)^{m_f}} + \frac{(\eta_{max} - \eta_{min})\left(\frac{f}{f_{d1}}\right)^{n_f}}{\left(1 + \left(\frac{f}{f_{d2}}\right)^{n_f}\right)^{S_f}} \tag{3.5}$$

here, f_p is a relative free volume of the fluid at which viscosity of the solution drops to $\frac{\eta_0+\eta_{min}}{2}$ in the intermediate shear thinning region (region 2); m_f is an exponent which represents the slope of the intermediate shear thinning region of fluid (region 2). n_f is an exponent which represents the slope of the shear thickening region of fluid; S_f is an exponent which represents the slope of the extreme shear thinning region of fluid (region 4). f_{d1} and f_{d2} are relative free volumes of fluid at which the viscosity of the solution drops to an intermediate value between η_{min} and η_{max} in the shear thickening region (region 3). The viscosity at f_{d1} is $\eta_{min} + \frac{\eta_0 - \eta_{min}}{1 + \left(\frac{f_{d1}}{f_p}\right)^{m_f}} + \frac{(\eta_{max} - \eta_{min})}{\left(1 + \left(\frac{f_{d1}}{f_{d2}}\right)^{n_f}\right)^{S_f}}$ and the viscosity at f_{d2} is $\eta_{min} + \frac{\eta_0 - \eta_{min}}{1 + \left(\frac{f_{d2}}{f_p}\right)^{m_f}} + \frac{(\eta_{max} - \eta_{min})\left(\frac{f_{d2}}{f_{d1}}\right)^{n_f}}{2^{S_f}}$. Fig. 3.1b shows the rheological material parameters of a relative free volume-dependent viscosity.

3.3.2 Shear stress-dependent viscosity

The relative free volume in the liquid depends on the mobility of the molecules [201] (i.e. colloids or solutes and solvents). The size and shape of molecules, interaction amongst fluid molecules, spatial arrangement and intermolecular forces between molecules, and nature of bulk fluid flow determines the rheology of the fluid [31, 129, 143, 214]. An interaction amongst molecules (i.e. colloids, solute, solvent etc.) during fluid flow, thermal changes, and external/internal pressure generate stresses in the liquid. The relative free space in the liquid changes under the influence of these stresses. We propose a non-linear empirical relationship between stresses in the liquid with a relative free volume as in Eq. 3.6,

$$f = \left(\frac{\tau}{\tau_0}\right)^m \tag{3.6}$$

Here, τ_0 [Pa] and m are material constants of the fluid. By substituting Eq. 3.6 in Eq. 3.5, we obtain the shear stress-dependent rheological model (Eq. 3.2) for a shear thickening fluid. The shear rate of the fluid will be as in Eq. 3.7

$$\dot{\gamma} = \frac{\tau}{\left(\eta_{min} + \frac{\eta_0 - \eta_{min}}{1 + \left(\frac{\tau}{\tau_p} \right)^{m_s}} + \frac{(\eta_{max} - \eta_{min}) \left(\frac{\tau}{\tau_{d1}} \right)^{n_s}}{\left(1 + \left(\frac{\tau}{\tau_{d2}} \right)^{n_s} \right)^{S_s}} \right)} \tag{3.7}$$

here, $\tau_p = \tau_0 \left(f_p\right)^{\frac{1}{m}}$, $\tau_{d1} = \tau_0 \left(f_{d1}\right)^{\frac{1}{m}}$, $\tau_{d2} = \tau_0 \left(f_{d2}\right)^{\frac{1}{m}}$, $m_s = m \left(m_f\right)$, and $n_s = m \left(n_f\right)$.

3.3.3 Shear rate-dependent viscosity

We note that the deformation of fluid under stress alter the relative free volume of the fluid. We propose a non-linear [223] empirical relationship between shear rate and relative free volume as in Eq. 3.8

$$f = \left(\frac{\dot{\gamma}}{\dot{\gamma}_0} \right)^n, \tag{3.8}$$

here, $\dot{\gamma}_0$ [s^{-1}] and n are material constants of the fluid. By substituting Eq. 3.8 in Eq. 3.5, we obtain a shear rate-dependent rheological model (Eq. 3.9) for shear thickening fluids,

$$\eta = \eta_{min} + \frac{\eta_0 - \eta_{min}}{1 + \left(\frac{\dot{\gamma}}{\dot{\gamma}_p} \right)^{m_r}} + \frac{(\eta_{max} - \eta_{min}) \left(\frac{\dot{\gamma}}{\dot{\gamma}_{d1}} \right)^{n_r}}{\left(1 + \left(\frac{\dot{\gamma}}{\dot{\gamma}_{d2}} \right)^{n_r} \right)^{S_r}}, \tag{3.9}$$

here, $\dot{\gamma}_p = \dot{\gamma}_0 \left(f_p\right)^{\frac{1}{n}}$, $\dot{\gamma}_{d1} = \dot{\gamma}_0 \left(f_{d1}\right)^{\frac{1}{n}}$, $\dot{\gamma}_{d2} = \dot{\gamma}_0 \left(f_{d2}\right)^{\frac{1}{n}}$, $m_r = n \left(m_f\right)$, and $n_r = n \left(n_f\right)$; $\dot{\gamma}_p$ [s^{-1}] is a shear rate at which the viscosity of the solution drops to $\frac{\eta_0 + \eta_{min}}{2}$ in the intermediate shear thinning region (region 2). m_r is an exponent which represents the slope of the intermediate shear thinning region of fluid (region 2). n_r is an exponent which represents the slope of the shear thickening region of fluid; S_r is an exponent which represents the slope of the extreme shear thinning region of fluid (region 4). $\dot{\gamma}_{d1}$ [s^{-1}] and $\dot{\gamma}_{d2}$ [s^{-1}] are shear rate at which the viscosity of the solution drops to an intermediate values between η_{min} and η_{max} in the shear thickening region (region 3). The viscosity at $\dot{\gamma}_{d1}$ is $\eta_{min} + \frac{\eta_0 - \eta_{min}}{1 + \left(\frac{\dot{\gamma}_{d1}}{\dot{\gamma}_p} \right)^{m_r}} + \frac{(\eta_{max} - \eta_{min})}{\left(1 + \left(\frac{\dot{\gamma}_{d1}}{\dot{\gamma}_{d2}} \right)^{n_r} \right)^{S_r}}$ and the viscosity at $\dot{\gamma}_{d2}$

is $\eta_{min} + \dfrac{\eta_0 - \eta_{min}}{1 + \left(\dfrac{\dot{\gamma}_{d2}}{\dot{\gamma}_p}\right)^{m_r}} + \dfrac{(\eta_{max} - \eta_{min})\left(\frac{\dot{\gamma}_{d2}}{\dot{\gamma}_{d1}}\right)^{n_r}}{2^{S_r}}$. Fig. 3.1b shows rheological material parameters of a shear rate-dependent viscosity.

3.3.4 Péclet number-dependent relative viscosity

Stokes-Einstein-Sutherland equation (Eq. 3.10) defines diffusivity (D) of the molecules/-particles with a thermal energy k_BT in a solvent of viscosity η_s [136, 211] as

$$D = \frac{k_B\, T}{6\,\pi\,\eta_s\, a} \tag{3.10}$$

where, k_B [J/K] is the Boltzmann's constant, T [K] is the absolute temperature, a [m] is the radius of the molecules/particles. Péclet number (Pe), also known as the dimensionless shear rate [136], relates the magnitude of thermal motion of molecules with a motion caused by shear. Péclet number as defined in Eq. 3.11 quantifies the strength of the shear force compared to the Brownian forces in the fluid [136],

$$\mathrm{Pe} = \frac{\dot{\gamma}}{\frac{D}{a^2}} = \frac{6\,\pi\,\eta_s\,\dot{\gamma}\,a^3}{k_B\,T} \tag{3.11}$$

We obtain the dimensionless Péclet number-dependent relative viscosity of the shear thickening fluid (Eq. 3.12) by diving Eq. 3.9 over η_s and substituting Eq. 3.11 for the shear rate in Eq. 3.9,

$$\frac{\eta}{\eta_s} = \frac{\eta_{min}}{\eta_s} + \frac{\frac{\eta_0}{\eta_s} - \frac{\eta_{min}}{\eta_s}}{1 + \left(\dfrac{\mathrm{Pe}}{\mathrm{Pe}_p}\right)^{m_r}} + \frac{\left(\frac{\eta_{max}}{\eta_s} - \frac{\eta_{min}}{\eta_s}\right)\left(\dfrac{\mathrm{Pe}}{\mathrm{Pe}_{d1}}\right)^{n_r}}{\left(1 + \left(\dfrac{\mathrm{Pe}}{\mathrm{Pe}_{d2}}\right)^{n_r}\right)^{S_r}} \tag{3.12}$$

here, Pe_p is a Péclet number at which the relative viscosity of the solution drops to $\frac{1}{2}(\frac{\eta_0}{\eta_s} + \frac{\eta_{min}}{\eta_s})$ in the intermediate shear thinning region (region 2). Pe_{d1} and Pe_{d2} are Péclet number at which the relative viscosity of the solution drops to an intermediate values between $\frac{\eta_{min}}{\eta_s}$ and $\frac{\eta_{max}}{\eta_s}$ in the shear thickening region (region 3). $\mathrm{Pe} << 1$ shows domination of the Brownian motion in the fluid while $\mathrm{Pe} >> 1$ suggests that the microstructure is distorted by flow forces [28, 136]. Thus, the arrangement of the

molecules is highly dependent on Péclet number and by that the viscosity of the fluid [28].

3.3.5 Conversion to an existing model

Eq. 3.2 converts to the shear stress-dependent Meter model (Eq. 3.1, Eq. 2.2 of Chapter 2) [134, 190] by substituting $\eta_\infty = \eta_{min} = \eta_{max}$ and $m_s = \alpha - 1$. Similarly, Eq. 3.9 converts to the shear rate-dependent Cross model equation [43] (Eq. 3.13), by substituting $\eta_\infty = \eta_{min} = \eta_{max}$ and $(\frac{1}{\dot{\gamma}_p})^{m_r} = C$.

$$\eta = \eta_\infty + \frac{\eta_0 - \eta_\infty}{1 + C\,\dot{\gamma}^{m_r}} \tag{3.13}$$

This suggests that the free-volume theory based equations proposed in the present work capture the properties of existing shear stress-dependent (Meter model) and shear rate-dependent rheological models (Cross model). Thus, a free-volume theory based equation could be utilised to model the purely shear-thinning rheology of the polymeric fluid along with the rheology of the colloidal suspensions.

3.3.6 Numerical simulation

3.3.6.1 Governing equation for a shear rate-dependent rheological model

The laminar flow of an incompressible, single-phase shear thickening fluid through a void space is defined using governing continuity equation (Eq. 3.14) and momentum equation (Eq. 3.15):

$$\nabla \cdot \mathbf{u} = 0, \tag{3.14}$$

$$\rho\left(\frac{\partial \mathbf{u}}{\partial t} + \mathbf{u} \cdot \nabla \mathbf{u}\right) = -\nabla P + \nabla \cdot \boldsymbol{\tau} + \mathbf{f}, \tag{3.15}$$

here, P is the pressure, $\mathbf{f}$ is any external body force, $\mathbf{u}$ is the velocity vector, t is the time, and $\boldsymbol{\tau}$ is the stress tensor as defined in Eq. 3.16

$$\boldsymbol{\tau} = \eta(\dot{\gamma})\,(\nabla \mathbf{u} + (\nabla \mathbf{u})^T), \tag{3.16}$$

where $\eta(\dot{\gamma})$ is the shear viscosity of a shear thickening fluid, which is a function of shear rate. The magnitude of the rate of strain tensor for shear-dominated flow is as follows,

$$\dot{\gamma} = \sqrt{\frac{\dot{\boldsymbol{\gamma}} : \dot{\boldsymbol{\gamma}}}{2}} = \sqrt{2\mathbf{D} : \mathbf{D}}, \tag{3.17}$$

here, $\dot{\boldsymbol{\gamma}} = (\nabla \mathbf{u} + (\nabla \mathbf{u})^T)$ and $\mathbf{D} = \frac{1}{2}\dot{\gamma}$

The shear viscosity ($\eta(\dot{\gamma})$) of a shear rate-dependent model is as defined in Eq. 3.9.

3.3.6.2 Numerical domain, boundary condition and solver

We utilised finite volume method based OpenFOAM C++ libraries [84, 99] for solving Eq. 3.14 and Eq. 3.15 in conjunction with a shear rate-dependent model equation (Eq. 3.9). We simulated the flow of a shear thickening fluid through a 2D circular staggered micromodel porous medium over a range of constant injection velocity (10^{-7} m/s - 0.1 m/s). The constant injection velocity was applied at the right boundary. The numerical domain had a uniform velocity of zero at the beginning of the simulation. The no-slip condition was deployed at the boundary wall of the micromodel. The snappyHexMesh module and blockMesh module of OpenFOAM were employed to generate a fine hexagonal mesh in a porous medium domain.

The PIMPLE algorithm with nOuterCorrectors of 5 was employed to maintain the stability and accuracy of a shear thickening fluid flow simulations. The Gauss linear uncorrected scheme of OpenFOAM was employed to discretise the Laplacian term of governing equations. Gauss linear scheme was used to discretise the gradient term and the divergence term. The Gauss linear scheme uses standard finite volume Gaussian integration. The time scheme of the momentum equation was discretised using the second-order implicit backward method. SmoothSolver with a Gauss-Seidel smoother was used to determine the velocity profile and Generalised Geometric-Algebraic Multi Grid (GAMG) solver with diagonal incomplete-Cholesky (symmetric) smoother was employed to estimate the pressure field. The Courant number was maintained below 0.1

using time-step of 10^{-6} s. The convergence criteria were set to 10^{-6} for both the velocity and pressure fields. We used Paraview 5.7.0 software to visualise and post process the shear thickening fluid flow simulation data.

3.4 Results and Discussion

3.4.1 Validation of the shear-stress dependent equation

We utilised a rheological data of Cwalina *et al.* [48] and Laun [111] to validate the proposed shear stress-dependent model (Eq. 3.2). Cwalina *et al.* [48] investigated shear stress-dependent rheological characteristics of silica nanoparticles (diameter 520 nm) plus cubic aluminosilicate zeolites dispersed in a polyethylene glycol suspending fluid at colloidal volume fraction (ϕ) of 0.445, 0.518 and 0.507. Laun [111] scrutinized the shear stress-dependent viscosity of a styrene-ethyl-acrylate-copolymer-latex of diameter 250 nm dispersed in the water over a range of pH and NaCl concentration. We used Excel Solver-GRG nonlinear algorithm [107] to determine the material parameters of the proposed rheological equations. The estimated material parameters of the shear thickening fluids of [48] and [111] are as given in Table 3.1.

Fig 3.2 and Fig 3.3 show good fit of the viscosity-shear stress data using Eq. 3.2 and shear rate-shear stress data using Eq. 3.7 with experimental measurements of Cwalina *et al.* [48] (ϕ: 0.445 - 0.518) and Laun [111] (pH: 5.1 - 7; NaCl Conc.: 0 - 1.14 g/L). The root means square error (RMSE) of Eq. 3.2 and Eq. 3.7 with respect to the experimental data ranged from 5.4×10^{-4} to 1.6×10^{-2} in Fig 3.2 and Fig 3.3, respectively, which suggest statistically good fits of the shear stress-dependent equation with the experiment.

Eq. 3.2 could capture the Newtonian, shear thinning and shear thickening region of the silica nanoparticles based shear thickening fluid of [48] at ϕ of 0.445. At $\phi = 0.507$, Eq. 3.2 could capture the shear thinning, shear thickening and extreme shear thinning at high shear values (see Fig 3.2a and 3.2b) of the shear thickening fluid of [48]. Fig 3.3 shows that Eq. 3.2 correctly depicts the effects of the pH and NaCl concentration on the rheological behaviour of the styrene-ethyl-acrylate-copolymer-latex fluid. Charge on the particle and degree of dissociation change due to pH variation in the solution. The addition of NaCl-salt in the solution increases total ion concentration in the fluid.

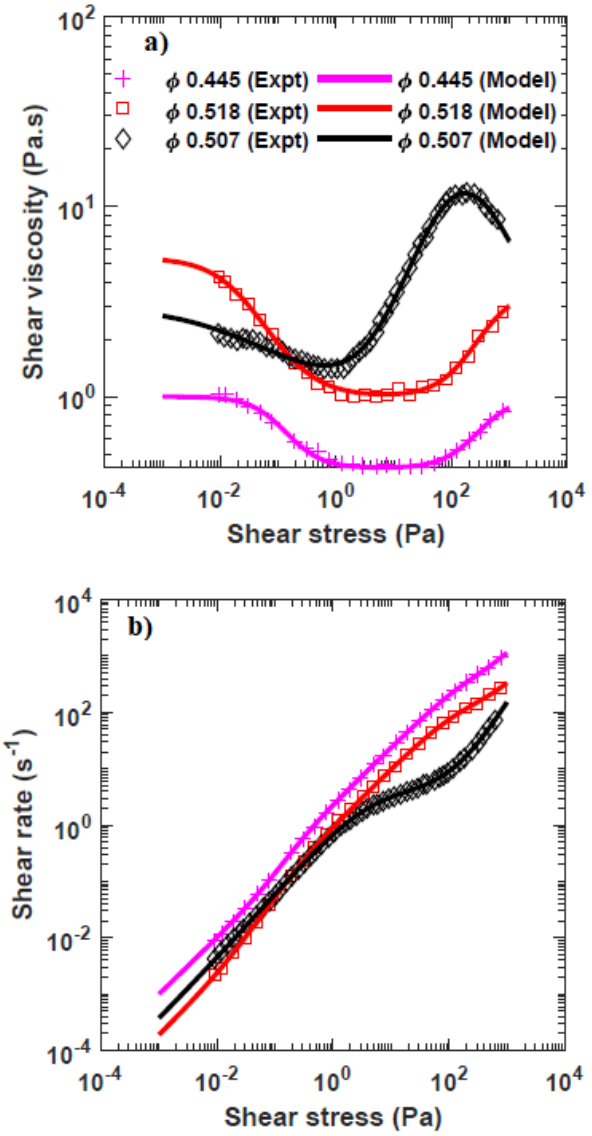

FIGURE 3.2: An experimental rheological data of a silica nanoparticles and cubic aluminosilicate zeolites -based shear thickening fluid of [48] over a range of volume fraction (ϕ) modelled using a proposed shear stress-dependent model. (a) shear viscosity as a function of shear stress modelled using shear stress-dependent equation (Eq. 3.2), and (b) shear rate as a function of shear stress modelled using shear stress dependent equation (Eq. 3.7). The material parameters are given in Table 3.1.

TABLE 3.1: Estimated material parameters for shear thickening silica nanoparticles-cubic aluminosilicate zeolites based fluid of [48] over range of volume fraction and shear thickening styrene-ethylacrylatecopolymer latex fluid of [111] over a range of pH and NaCl concentration.

Parameter	Volume fraction (ϕ) [48]			pH of solution [111]				NaCl conc (g/L) [111]		
	0.445	0.507	0.518	5.1	5.7	6.2	7	0	0.287	1.14
η_0 [Pa·s]	1	3	5.4	0.787	11.84	83.408	200	120.2	50	0.2
η_{min} [Pa·s]	0.42	1	1	0.034	0.034	0.034	0.034	0.034	0.034	0.034
η_{max} [Pa·s]	2	12	4	0.72	0.260	0.170	0.09	0.15	0.23	0.52
τ_p [Pa]	0.1	0.024	0.026	0.05	0.033	0.029	0.04	0.02	0.02	0.304
τ_{d1} [Pa]	815	44	490	604.6	2567	6700	12847	8398	3476	1120
τ_{d2} [Pa]	393	146	445	939	3629	10196	21474	14000	3041	4621
m_s	1.37	0.5	1	1.344	2.02	2.3	2.1	2	1.9	2.845
n_s	1.4	1.04	1.29	1.389	1.462	1.354	1.3	1.804	1.172	0.969
S_s	1	1.85	1	1.261	1.194	1.255	1.004	1.347	0.9	2.005

These parameters strongly affect the intermolecular interactions (due to van der Waals and electrostatic forces) between colloids and solvents. The relative free volume in the solution changes due to the combined effect of these intermolecular interactions and hydrodynamic forces. Table 3.1 shows a decrease in η_{max} and an increase in η_0, τ_{d1} and τ_{d2} with an increase in the pH. On the contrary, Table 3.1 reports an increase in η_{max} and a decrease in τ_{d1} and τ_{d2} with an increase in the electrolyte (NaCl) concentration. We note that the proposed model predicted Newtonian viscosity (η_0) of [111] shear thickening fluid solution, which would not have been possible to identify by observation of the rheological data or graph. The predicted minimum shear-thinning viscosity (η_{min}) of 0.034 Pa·s over a range of pH, and NaCl concentrations of [111] indicate that varying hydrogen concentrations and ionic strength did not significantly affect the η_{min} of a latex fluid. This suggests that the proposed rheological equation helps to quantitatively correlate the rheological behaviour of the shear thickening fluid under varying physiochemical conditions.

3.4.2 Validation of the shear-rate dependent equation

We utilised rheological data of Kalman *et al.* [102], Maus *et al.* [131] and Zhang *et al.* [232] to validate the proposed shear rate-dependent model (Eq. 3.9). Kalman *et al.* [102] investigated shear rate-dependent rheological characteristics of monodisperse polymethylmethacrylate (PMMA) particles dispersed in polyethylene glycol fluid at colloidal volume fraction (ϕ) of 0.40, 0.45, 0.48 and 0.49. Maus *et al.* [131] measured shear viscosity of the α, ω-Mg carboxylato-polyisoprene (MCPI) in decahydronaphthalene over a range of temperature (25 °C, 30 °C, 35 °C). Zhang *et al.* [232] scrutinized the

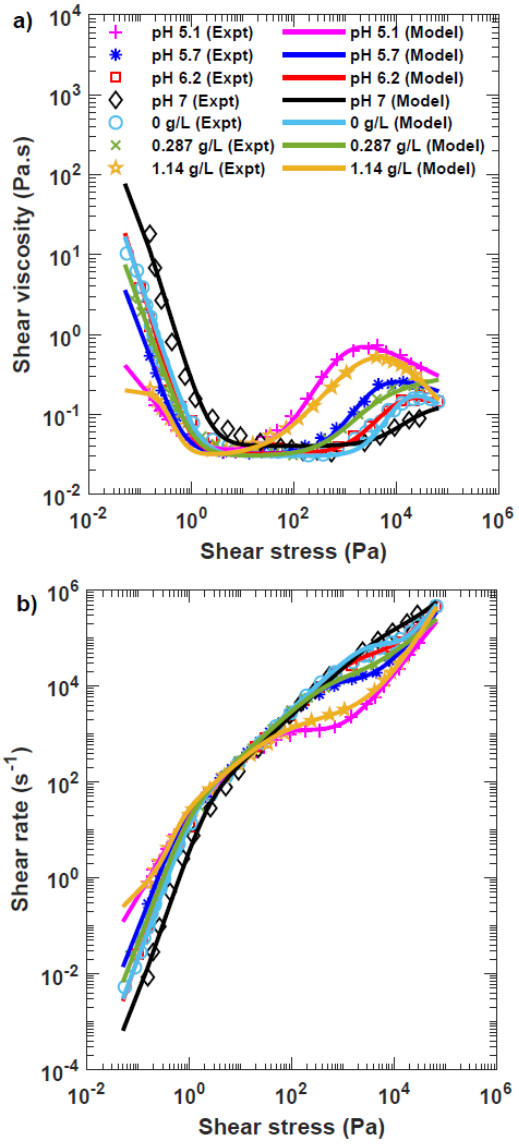

FIGURE 3.3: The experimental rheological data of styrene-ethyl-acrylate-copolymer-latex based shear thickening fluid of [111] over a range of pH and NaCl concentrations modelled using proposed shear stress-dependent model. (a) shear viscosity as a function of shear stress modelled using shear stress-dependent equation (Eq. 3.2), and (b) shear rate as a function of shear stress modelled using shear stress dependent equation (Eq. 3.7). The material parameters are given Table 3.1.

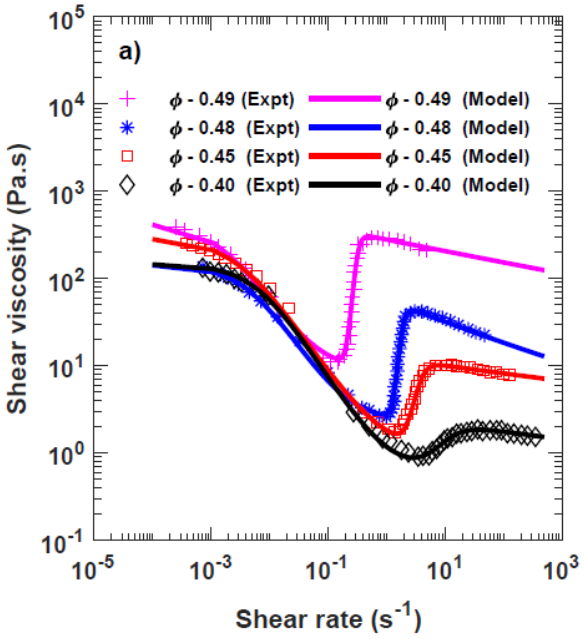

FIGURE 3.4: Shear viscosity of monodisprsed polymethylmethacrylate (PMMA) particles based shear thickening fluid of [102] over a range of volume fraction (ϕ) modelled using the proposed shear rate-dependent equation (Eq. 3.9). The material parameters are given Table 3.2.

TABLE 3.2: Estimated material parameters for the shear thickening PMMA particles-based fluid of [102] over a range of volume fraction, the MCPI fluid of [131] over a range of temperature, and the carbonyl iron and silica particles-based fluids of [232] over a range of magnetic field

Parameter	Volume fraction (ϕ) [102]				Temperature (°C) [131]			Magnetic field (kA/m) [232]			
	0.49	0.48	0.45	0.40	25	30	35	0	100	200	300
η_0 [Pa·s]	437	143	292	146	477	239	140	20	300	500	800
η_{min} [Pa·s]	8.34	2.3	1	0.60	10	10	10	1.5	2.0	10	11
η_{max} [Pa·s]	293	42	10	1.82	1770	520	213	25	29	32	45
$\dot{\gamma}_p$ [s^{-1}]	0.00146	0.0044	0.0028	0.0065	0.9	1.8	5	2.2	0.7	1.8	1.5
$\dot{\gamma}_{d1}$ [s^{-1}]	0.3	1.8	4	10	3	5.5	11	961	522	415	420
$\dot{\gamma}_{d2}$ [s^{-1}]	0.3	1.82	3.61	10	7.8	11	18.52	1095	557	467	442
m_r	1.1	1.1	1	1.1	2.1	1.9	1.5	0.9	0.82	1.3	1.3
n_r	10.6	8.88	4.27	2.04	1.46	1.24	1.59	6.46	7.09	5.31	7.69
S_r	1.01	1.03	1.03	1.07	1.95	1.42	1.49	1.43	1.13	1.21	1.16

shear rate-dependent viscosity of a carbonyl iron particles of 5 μm mean size and fumed silica particles dispersed in ethylene glycol over a range of magnetic field (kA/m). The estimated material parameters of the shear thickening fluids of [102], [131], and [232] are as given in Table 3.2.

Fig 3.4, Fig 3.5 and Fig 3.6 show good fit of the viscosity-shear rate data using Eq. 3.9 with experimental measurements of Kalman *et al.* [102] (ϕ: 0.4 - 0.49), Maus *et al.* (Temp: 25-35 °C) [131], and Zhang *et al.* [232] (Magnetic field: 0 - 300 kA/m). The root means square error (RMSE) of Eq. 3.9 with respect to the experimental data is ranged

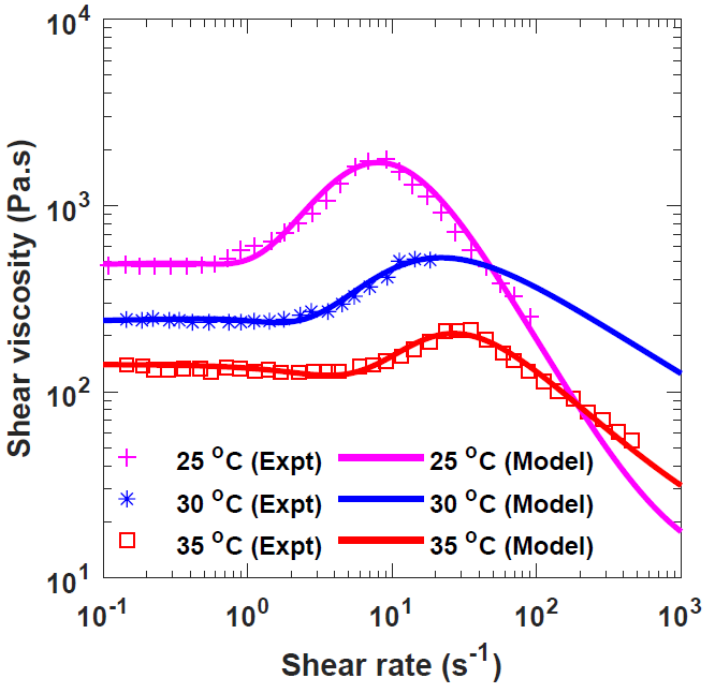

FIGURE 3.5: Shear viscosity of α,ω-Mg carboxylato-polyisoprene (MCPI)-based shear thickening fluid of [131] over a range of temperatures modelled using the proposed shear rate-dependent equation (Eq. 3.9). The material parameters are given Table 3.2.

from 2×10^{-1} to 3×10^{1} in Fig 3.4, Fig 3.5, and Fig 3.6 respectively, which suggests a statistically good fit of the shear rate-dependent equation with experiments.

Fig 3.4 illustrates that the Eq. 3.9 can encompass all four regions (Newtonian, intermediate shear thinning, shear thickening, and extreme shear thinning) of the PMMA shear thickening fluid over a range of ϕ values. On the contrary, as depicted in Fig 3.5, intermediate shear-thinning region is absent in the rheological data of [131]. Yet, Eq. 3.9 is able to correctly capture Newtonian followed by shear thickening and extreme shear-thinning regions of the fluid over a range of temperature values. Further, Table 3.2 shows a constant minimum viscosity (η_{min}) of the fluid at high shear rate values in the extreme shear thinning region. This suggests that η_{min} also represents the lowest limiting viscosity value of the extreme shear thinning region.

An increase in the ϕ of the particles in the solution increased η_{min} and η_{max}, and decreased $\dot{\gamma}_{d1}$ and $\dot{\gamma}_{d2}$ (see Table 3.2) of [102]. We note that $\dot{\gamma}_{d1}$ and $\dot{\gamma}_{d2}$ have approximately same values for given ϕ values of [102]. The slope (m_r) of the intermediate shear thinning region of [102] has same value of 1.1 over a range of ϕ, except for ϕ=0.45. These results suggest that the shear rate-dependent rheological model helps predict threshold

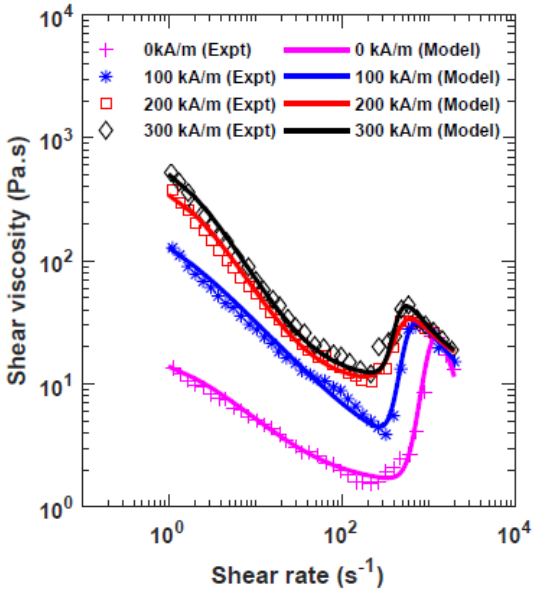

FIGURE 3.6: Shear viscosity of carbonyl iron particles and fumed silica particles-based magnetorheological shear thickening fluid of [232] over a range magnetic field modelled using the proposed shear rate-dependent equation (Eq. 3.9). The material parameters are given in Table 3.2.

shear rate values ($\dot{\gamma}_p$, $\dot{\gamma}_{d1}$, and $\dot{\gamma}_{d2}$). As predicted, the rheological parameters of [131] show a decrease in η_0, η_{max}, m_r and an increase in $\dot{\gamma}_{d1}$, $\dot{\gamma}_{d2}$, n_r with an increase in the temperature of the shear thickening fluid. We note that an increase in the temperature generates thermal stresses, which change the relative free volume in the solution. This leads to a decrease in the viscosity of the solution with an increase in the temperature. An increase in exposure of the magnetic field (0 - 300 kA/m) to the shear thickening fluid of [232] increased η_0, η_{min}, η_{max} and decreased $\dot{\gamma}_{d1}$ and $\dot{\gamma}_{d2}$ (see Table 3.2 and Fig 3.6). The shear-rate dependent model (Eq. 3.9) could estimate η_{min} of the fluid.

These results suggest that the shear stress-dependent equation (Eq. 3.2) and the shear rate dependent equation (Eq. 3.9) capture highly non-linear rheological characteristics of the shear thickening fluid and predict threshold measurable parameters of shear thickening fluids such as threshold shear stress/rate.

3.4.3 Validation of the Péclet number-dependent equation

Fig 3.7 shows a perfect fit of the experimentally determined Péclet number-dependent relative viscosity of the superball silica fluid of [181] with Eq. 3.12. The material

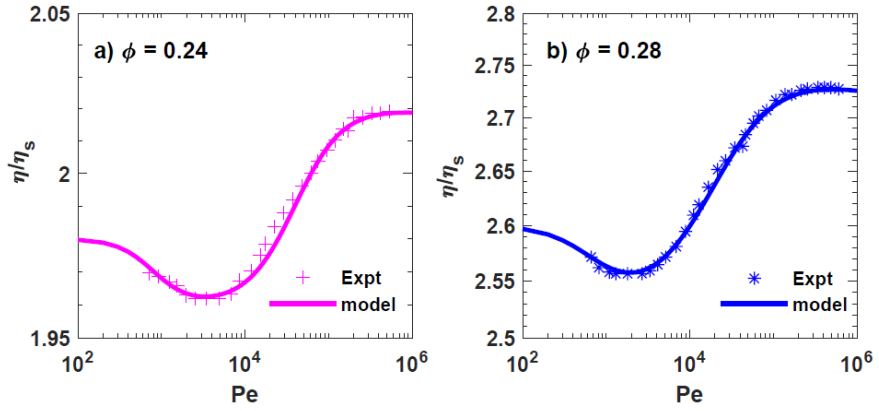

FIGURE 3.7: Comparison of the experimentally measured Péclet number-dependent relative viscosity of the superball silica at volume fraction of (a) $\phi = 0.24$, and (b) $\phi = 0.28$ of [181] with a proposed Péclet Number-dependent equation (Eq. 3.12).

TABLE 3.3: Estimated material parameters for a shear thickening superball silica fluid of [181] over a range of volume fraction

Parameters	Volume fraction (ϕ) [181]	
	0.24	0.28
$\frac{\eta_0}{\eta_s}$	1.98	2.6
$\frac{\eta_s}{\eta_{min}}$	1.96	2.53
$\frac{\eta_s}{\eta_{max}}$	2.02	2.72
Pe_p	800	700
Pe_{d1}	4×10^4	1.8×10^4
Pe_{d2}	4.1×10^4	2.1×10^4
m_r	2	1.5
n_r	1.5	1.1
S_r	1.01	1.03

parameters are given in Table 3.3. Pe in Fig 3.7 corresponds to the shear rate of 10^0 s^{-1} to 10^3 s^{-1}. We note that Pe takes into account the size of the particle (see Eq. 3.11). The observed shear thickening behaviour of the fluid at Pe $> 10^3$ suggests a strong dependence of shear thickening on changes in the microstructural arrangement. The Pe_p, Pe_{d1}, Pe_{d2} values obtained using Eq. 3.12 could be considered as a threshold Pe which helps to modulate shear thinning and shear thickening behaviours in non-Newtonian fluid.

3.4.4 Pore-scale flow simulation

We simulated the flow of a PMMA particles-based fluid of [102] over a range of constant injection velocity (10^{-7} m/s - 0.1 m/s) in a circular staggered porous medium (domain size: 4.2 mm $\times$ 2.4 mm, circle diameter: 262 μm, pore-throat size: 162 μm, channel

depth: 120 μm, porosity: 0.7, see Fig 3.8). The material parameters of PMMA fluid used for simulation are as given in the Table 3.2.

Fig 3.8 shows spatial distribution along with the frequency of the shear rate, shear viscosity and velocity in the 2D porous medium. Fig 3.8d,e,f indicate that the field of shear rate, viscosity and velocity is non-uniformly distributed in the porous medium domain. The bi-modal distribution in Fig 3.8a,d suggest that the shear rate profile at the micromodel boundary is different from the central part of the micromodel. The first tall peak in the fig 3.8d is the shear rate distribution in the central part, and a small peak at high shear values is the shear rate distribution at the boundary. Similar to the shear rate profile, the bi-modal distribution observed in the shear viscosity profile in Fig 3.8e indicate variations in the distribution of viscosities in the central region and boundary region of the porous medium. Fig 3.8c imply that the PMMA fluid has higher velocity along the flow direction; further, there exists a no-flow region with a velocity lower than 10^{-5} m/s before and after circular blocks of the porous medium.

The average shear rate, the average shear viscosity, and the average velocity of the fluid flow in the porous medium for each simulation over a range of injection velocity are estimated using 'integrate variable' filter of the Paraview 5.7.0 software. Fig 3.9a compare the average shear rate of the porous medium with an average viscosity of the porous medium over a range of volume fraction and injection rate. Fig 3.9a depict shear thickening behaviour of the fluid in the porous medium similar to the rheological data. Note that the average values of shear rate and shear viscosity of the porous medium do not overlap with a rheological data of the PMMA fluid measured using a rheometer (i.e. as in Fig 3.4).

Fig 3.9b shows the non-linear relationship between average velocity and pressure gradient during the flow of PMMA based shear thickening fluid in the 2D staggered porous medium. Further, we can deduce from Fig 3.9b that an increase in the volume fraction of the particles in the fluid increases the pressure requirements. The results of direct numerical simulation indicate that the proposed shear rate-dependent rheological model for shear thickening fluid can be utilised to gain pore-scale insight into shear thickening fluid flow. In the future, we will use the proposed rheological model to numerically simulate two-phase shear thickening fluid flow using the volume of fluid method, specifically

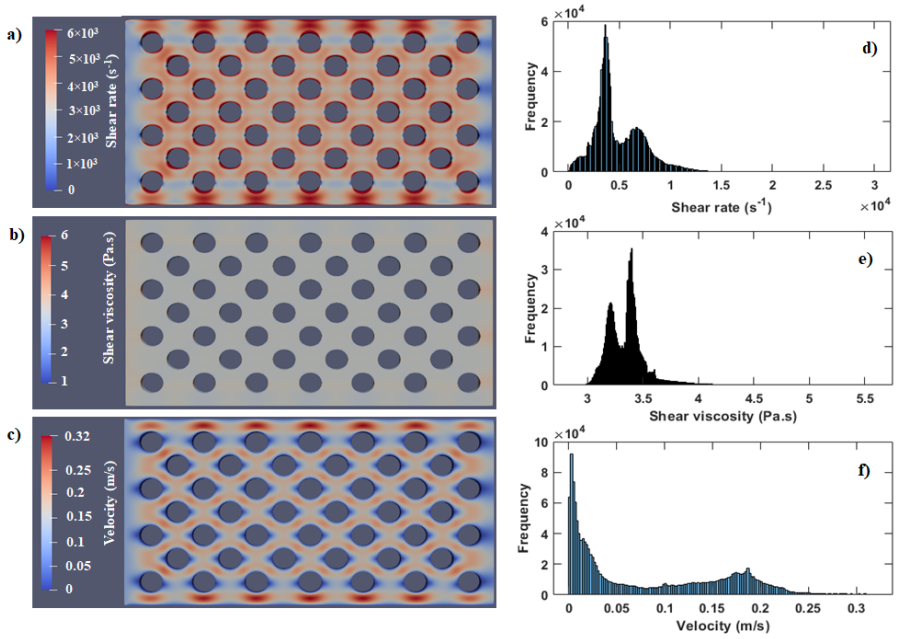

FIGURE 3.8: Spatial distribution of a) shear rate (b) shear viscosity (c) velocity and frequency of d) shear rate e) shear viscosity f) velocity in the porous medium domain during PMMA fluid ($\phi = 0.45$) flow at a constant injection velocity of 0.1 m/s.

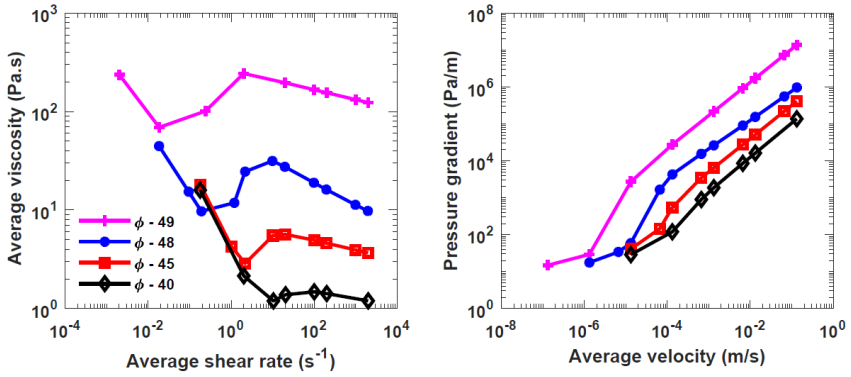

FIGURE 3.9: (a) Average shear viscosity - average shear rate, and (b) average velocity - pressure gradient over a range of volume fraction (ϕ) obtained after simulated flow of PMAA shear thickening fluid of [102] through the 2D staggered porous medium over a range of constant injection rates.

to understand the shear thickening fluid flow behaviour while displacing Newtonian fluid at pore-scale.

3.5 Conclusions

The free volume theory proposed by Doolittle is protracted for a shear thickening fluid. An empirical formula is proposed to relate the shear viscosity of shear thickening fluid

with a relative free volume of the fluid. The stresses generated in the fluid due to intermolecular forces, hydrodynamic forces, and thermal variation cause a change in the relative free volume. The non-linear relationship between stresses and the relative free volume is used to develop a shear stress-dependent rheological equation for shear thickening fluids which captures different behaviours such as Newtonian, intermediate shear thinning, shear thickening, and the extreme shear-thinning regime of a shear thickening fluid. An equation for the shear rate-dependent viscosity is also formulated using a non-linear relationship between the shear rate and the relative free volume. The proposed formulations convert to the existing Meter model and Cross model. We note that the proposed rheological model equations are empirical generalised Newtonian fluid (GNF) models similar to power-law, Carreau, Cross, Meter models.

The perfect fit of the experimental data of various shear thickening fluids (silica nanoparticles, latex, PMMA particles, MCPI, carbonyl iron particles based shear thickening fluid) with the shear stress-dependent equation and the shear rate-dependent equation over a range of physicochemical properties (volume fraction, pH, NaCl concentration, temperature, magnetic field) suggests that the proposed rheological formulations could be used to evaluate the rheological characteristics of the shear thickening fluid using measurable parameters. The nine material parameters of the proposed formulation help to quantitatively analyse the effect of varying physicochemical conditions on the rheology of shear thickening fluids. The proposed equation predicts critical viscosity parameters of shear thickening fluids such as η_0, η_{min}, η_{max}. The threshold shear stress parameters (τ_0, τ_p, τ_{d1}, τ_{d2}), the threshold shear rate parameters ($\dot{\gamma}_0$, $\dot{\gamma}_p$, $\dot{\gamma}_{d1}$, $\dot{\gamma}_{d2}$) and the threshold Péclet number parameters (Pe_p, Pe_{d1}, Pe_{d2}) of the proposed equations are parameters that modulate the effective transmutation of rheological characteristics (i.e. from Newtonian to shear-thinning, followed by shear-thickening regime).

Numerical simulations of PMMA-based fluid (modelled using a shear rate-dependent equation) flow through a 2D circular staggered porous medium show that the proposed shear rate dependent equation can be employed for conducting shear thickening fluid flow studies. We observed shear thinning, shear thickening, followed by again shear thinning of the PMMA-based fluid flow in a 2D porous medium. The shear rate, shear viscosity, and velocity in a 2D porous medium have a bimodal distribution, which indicates that the flow behaviour of the shear thickening fluid at the boundary of the porous medium is different than in the central part of the porous medium. We will extend this work

to a) upscale the pore-scale shear viscosity of the shear thickening fluid to a continuum scale and b) simulate two phase shear thickening fluid flow in porous media..

Chapter 4

Upscaling non-Newtonian rheological fluid properties from pore-scale to Darcy's scale

This chapter is published in the '*Chemical Engineering Science*'.

Authors: **T. Shende,** V. Niasar, and M. Babaei. Upscaling non-Newtonian rheological fluid properties from pore-scale to Darcy's scale. *Chemical Engineering Science*, 239:116638, 2021.

4.1 Introduction

Polymeric fluid flow in a porous medium is of significant importance in many engineering applications such as enhanced oil recovery. Most polymer solutions employed for the enhanced oil recovery applications show non-Newtonian behaviour [21, 184, 200, 220]. The commonly used non-Newtonian fluids (i.e. xanthan gum [155, 199] and polyacrylamide solution [52, 106]) for oil recovery show viscoelastic properties. The rheology of non-Newtonian fluids can be studied considering non-Newtonian fluid as a generalised Newtonian fluid (e.g. power-law, Bingham, Cross, Carreau, Elis, Meter model etc., see section 2.2 of Chapter 2) or viscoelastic fluid (e.g. Maxwell, Oldroyd-B, Giesekus, Phan-Thien-Tanner model etc.) [8, 20]. These models are derived based on an empirical approach with many simplified assumptions; thus, each model has its own limitations and cannot universally be applied to all types of non-Newtonian fluids [20].

The flow of polymeric solution in rheometer is remarkably different from that of the flow in porous media. The reason could be [1] (i) the porous medium has complex geometry compared to rheometers; (ii) the presence of many expansion and contraction in the porous medium expose polymer to the various amount of shear stress [200]; (iii) mechanical retention and adsorption of the polymer change the geometry of the porous medium. To describe polymeric fluid behaviour in a porous medium, apparent viscosity or Darcy viscosity is a commonly used terms in the literature [1, 18, 58, 178, 200]. Darcy viscosity (η_{darcy}) is defined using Darcy's law as [21, 177, 184],

$$\eta_{\text{darcy}} = \frac{Ak}{Q}\frac{dP}{dx} = \frac{k}{U_{\text{darcy}}}\frac{dP}{dx} \tag{4.1}$$

here, A [m^2] is the cross-section area of the porous medium, k [m^2] is the intrinsic permeability, Q [m^3/s] is the volumetric flow rate, and U_{darcy} [m/s] is the Darcy velocity, $\frac{dP}{dx}$ [Pa/m] is the pressure gradient. The Darcy viscosity is generally measured by performing core flood experiments [200]. Darcy viscosity of the polymeric fluid in a porous medium depends on non-Newtonian rheology (measured using rheometer), inaccessible pore volume, degradation of the polymer due to mechanical or chemical forces, adsorption of polymer on a pore surface, elastic stretching of polymeric molecules [59, 106]. Thus, the values of shear viscosity and Darcy viscosity for same non-Newtonian fluid show shift in the viscosity profile [18, 58, 158, 184, 196].

4.1.1 The shift factor

The analytical solution of fluid flow in a circular capillary for the power-law model ($\eta = m\,\dot{\gamma}^n$) is used in a bundle of capillary model along with the Blake-Kozeny equation to determine hydraulic radius (R_h), Darcy viscosity (η_darcy), and Darcy shear rate ($\dot{\gamma}_\mathrm{darcy}$) of the porous medium as [194],

$$R_\mathrm{h} = \sqrt{\frac{8k\psi}{\phi}} \tag{4.2}$$

$$\eta_\mathrm{darcy} = \left(\frac{3n+1}{4n}\right)^{\frac{1}{n-1}} \left(\frac{R_\mathrm{h}}{2\,m}\frac{dP}{dx}\right)^{1/n} \tag{4.3}$$

$$\dot{\gamma}_\mathrm{darcy} = 4\left(\frac{3n+1}{4n}\right)^{\frac{1}{n-1}} \left(\frac{U_\mathrm{darcy}}{\sqrt{8\,k\,\psi\,\phi}}\right) \tag{4.4}$$

here, η [Pa·s] is the shear viscosity, $\dot{\gamma}$ [s^{-1}] is the shear rate, ψ is the tortuosity, ϕ is the porosity, m and n are model parameters of power-law fluid. The correlation between Darcy shear rate and Darcy velocity is defined using shift factor (α) as [18, 58, 177, 184, 206],

$$\dot{\gamma}_\mathrm{darcy} = \alpha\,\frac{U_\mathrm{darcy}}{\sqrt{k\,\phi}} \tag{4.5}$$

here, $\sqrt{k\,\phi}$ is the microscopic characteristic pore length [184]. The empirical shift factors are introduced in the definition of the porous medium's shear rate in order to fit the Darcy viscosity (η_darcy) to the shear viscosity (η) [231].

Balhoff and Thompson [17] developed a macroscopic model to study the effect of fluid rheology and bed morphology on the flow of Ellis model fluids based on a pore-network model. Berg and Wunnik [18] carried out pore-scale simulation in sandstone rock and pointed out the shortcoming of Cannella or Blake–Kozeny equation for correlating shear rate with the Darcy viscosity using empirical shift factor (α). Zami-Pierre *et al.* [227] studied the effect of the depletion layer at pore-boundary on quantification of the Darcy viscosity. Pore network modelling has been used to study the effect of shift factor on in-situ rheology in the porous medium [121, 196].

Rodríguez de Castro and Agnaou [58] numerically studied the effect of shear rheology model (power-law, Carreau model and Herschel-Bulkley model), pore size distribution, and geometrical variability on Darcy shear rate and Darcy velocity in the porous medium. Rodrıguez de Castro and Radilla [177] proposed a framework to relate the shear viscosity of Carreau model fluids with the Darcy viscosity in fractured porous medium. But, the authors neglected the low-shear-viscosity plateau of the Carreau model in the formulations for Darcy viscosity, given that only moderate and high shear rates were involved in their experiments. Zhang *et al.* proposed a correlation for α for the flow of the Cross model fluid in a rough fracture and showed that α depends on geometric tortuosity [231]. Zamani *et al.* [225] showed that α is a function of the porous medium properties (i.e. coordination number, tortuosity, aspect ratio) and rheology of the fluid. The significance of the shift factor is established for non-Newtonian fluid flow in the porous medium [18, 58, 65, 177, 194, 200, 226, 227, 231]. We note that the values of α vary three orders of magnitude in literature [18, 58, 194].

The oversimplified approach to estimate the shear rate (e.g. avoiding pore-size distribution and effect of non-circular cross-sections [225]) and neglecting heterogeneity of porous medium in these models make the estimation of Darcy viscosity and Darcy shear rate of non-Newtonian fluids inconsistent.

Majority of the fluids in porous medium flow at low shear values. The power-law model fails to describe Newtonian behaviour (i.e. constant viscosity plateau) of polymeric solution at low-shear values. Ellis model gives extremely low viscosity values at a high shear rate [130, 198]. Carreau [21], Carreau-Yasuda [222], Cross [43], Meter [134] models correctly depicts S-shape type shear thinning behaviour (i.e. Newtonian plateau at low as well as high shear values and decreasing viscosity at intermediate shear values) of many polymeric solutions [177, 196]. Thus, equations to determine macroscopic (i.e. upscaled) Darcy viscosity, Darcy shear rate, Darcy shear stress using measurable parameters and without the shift factor (α) are needed for the flow of a generalised Newtonian fluid and viscoelastic fluid in a porous medium.

The flow of polymeric fluids through simple geometry (such as a periodic array of cylinders, disorder porous medium) is previously studied by numerically simulating generalised Newtonian fluid (i.e power-law, Carreau, Cross model etc.) and viscoelastic fluid (i.e. FENE, PTT, Oldroyd-B etc.) [4, 6, 39, 42, 51–53, 68, 71, 82, 108, 119, 127, 140, 154,

172, 174, 178, 202, 220, 227, 228, 235]. The experiments, as well as numerical results, have shown viscoelastic instability at low Reynolds number for non-Newtonian fluid flows in porous media [32, 33, 51, 54–59, 67, 80, 106]. However, numerical simulation studies of Meter model fluid (GNF) and Phan-Thien-Tanner model fluid (viscoelastic) flow through a heterogeneous porous medium such as sandstone is absent in the literature.

4.1.2 Present study

To address the above discrepancies, we propose a tortuous Bundle-of-Capillaries model for the flow of non-Newtonian fluids described by the Meter model and the Phan-Thien-Tanner model in Section 4.3. The proposed Bundle-of-Capillaries model (hereafter referred to as BCM) for non-Newtonian fluids takes into account the geometric variability of the porous medium, the pore-size distribution, and the S-shape type rheological behaviour (using the Meter model) and viscoelastic behaviour (using the linear Phan-Thien-Tanner model) of non-Newtonian fluids. We derive upscaled Darcy viscosity, effective Darcy shear rate, effective Darcy shear stress, effective Reynolds number and effective Péclet number from pore-scale shear viscosity. We validate the proposed method using experimental data from the literature and pore-scale direct numerical simulations in Section 4.5.2 and 4.5.3, respectively. We also numerically simulate the flow of shear stress-dependent Meter model fluids and viscoelastic linear Phan-Thien-Tanner (PTT) model fluids in a heterogeneous porous medium using OpenFOAM and validate the numerical simulation approach using experimental microfluidic observations in Section 4.5.3.1. Section 4.5.3.2 compares results obtained by direct numerical simulation with the BCM approach and shows that the BCM captures the contribution of viscosity in the active flow of the polymeric fluid in the pore-space of porous media.

4.2 Mathematical formulation

4.2.1 Governing equations

The continuity equation (Eq. 4.6), momentum equation (Eq. 4.7) and constitutive equation of fluids describe single-phase, incompressible, laminar flow of non-Newtonian fluids through void space [21].

$$\nabla \cdot \mathbf{u} = 0 \tag{4.6}$$

$$\rho \left(\frac{\partial \mathbf{u}}{\partial t} + \mathbf{u} \cdot \nabla \mathbf{u} \right) = -\nabla P + \nabla \cdot \boldsymbol{\tau} \tag{4.7}$$

here, P [Pa] is the pressure, t [s] is the time, $\mathbf{u}$ is the velocity vector, and $\boldsymbol{\tau}$ is the stress tensor. The constitutive equation of the stress tensor of non-Newtonian fluid can be defined considering polymeric fluid as a generalised Newtonian fluid (i.e. power-law, Bingham, Cross, Carreau, Meter model etc.) or viscoelastic fluid (i.e. Oldroyd-B, Giesekus, FENE, PTT etc.) [8, 21]. We note that these constitutive equations of non-Newtonian fluids have been developed based on an empirical approach with simplified assumptions, thus, they have their own limitations [20, 22]. The Meter model (generalised Newtonian fluid) [134] and linear Phan-Thien–Tanner model (viscoelastic fluid) [204] have an analytical solutions for laminar flow through a circular geometry [147, 190]. We used above model in the present work as analytical solutions [147, 190] helped us develop bundle of capillary model for non-Newtonian fluids as described in section 4.3.

4.2.1.1 Meter model

The constitutive equation of a shear stress-dependent generalised Newtonian fluid as described in the section 2.2 of Chapter 2 is [130, 134, 190]

$$\boldsymbol{\tau} = 2\,\eta(\tau)\,\mathbf{D} = \eta(\tau)\,(\nabla \mathbf{u} + (\nabla \mathbf{u})^T) \tag{4.8}$$

Where $\eta(\tau)$ is the shear viscosity of the fluid, which is a function of shear stress. The magnitude of the rate of strain tensor and stress tensor for shear-dominated flow is as follows [22, 130, 134]

$$\dot{\gamma} = \sqrt{\frac{\dot{\boldsymbol{\gamma}} : \dot{\boldsymbol{\gamma}}}{2}} = \sqrt{2\mathbf{D} : \mathbf{D}} \tag{4.9}$$

$$\tau = \sqrt{\frac{\boldsymbol{\tau} : \boldsymbol{\tau}}{2}} = \sqrt{\frac{\eta\,\dot{\boldsymbol{\gamma}} : \eta\,\dot{\boldsymbol{\gamma}}}{2}} = \eta \sqrt{\frac{(\dot{\boldsymbol{\gamma}} : \dot{\boldsymbol{\gamma}})}{2}} = \eta \sqrt{(2\mathbf{D} : \mathbf{D})} \tag{4.10}$$

here, $\dot{\boldsymbol{\gamma}} = (\nabla \mathbf{u} + (\nabla \mathbf{u})^T)$ and $\mathbf{D} = \frac{1}{2}\dot{\boldsymbol{\gamma}}$

We define S-shape type non-Newtonian rheology of the polymeric solution using shear stress-dependent Meter model (Eq. 4.11 and Eq. 2.2 of Chapter 2) [134, 190],

$$\eta = \eta_\infty + \frac{\eta_0 - \eta_\infty}{1 + \left(\frac{\tau}{\tau_m}\right)^S} \tag{4.11}$$

where, η [Pa·s] is the shear viscosity at given shear stress (τ); η_0 [Pa·s] is the zero shear viscosity; η_∞ [Pa·s] is an infinite shear viscosity; τ_m [Pa] is the shear stress of a non-Newtonian fluid at which the viscosity of the solution drops to $\frac{\eta_0+\eta_\infty}{2}$; S is the shear stress-dependent exponent of Meter model which represent the slope of shear thinning or shear thickening fluid. The characteristic time λ [s] of Meter model fluid is $\lambda = \frac{\eta_0+\eta_\infty}{2\,\tau_\mathrm{m}}$. If $\eta_0 = \eta_\infty$, Meter model converts to Newtonian fluid. The Meter model represents a shear thinning fluid (if $\eta_0 > \eta_\infty$), and shear thickening fluid (if $\eta_0 < \eta_\infty$). The analytical solution for radial velocity profile ($u(r)$) and average velocity (U) of a fluid flow obeying Meter model equation in a circular geometry of radius (R) at pressure gradient of $\frac{dP}{dx}$ are derived in section 2.2.1 of chapter 2 and as given in Eq. 4.12 and 4.13, respectively [190].

$$u(r) = -\frac{dP}{dx}\frac{1}{4\,\eta_0\,\eta_\infty}\left[R^2\left(\eta_0 + (\eta_\infty - \eta_0)\,{}_2\mathrm{F}_1\left(1, \frac{2}{S}; \frac{S+2}{S}; -\frac{\eta_\infty}{\eta_0}\left(-\frac{dP}{dx}\frac{R}{2\,\tau_\mathrm{m}}\right)^S\right)\right)\right.$$
$$\left. - r^2\left(\eta_0 + (\eta_\infty - \eta_0)\,{}_2\mathrm{F}_1\left(1, \frac{2}{S}; \frac{S+2}{S}; -\frac{\eta_\infty}{\eta_0}\left(-\frac{dP}{dx}\frac{r}{2\,\tau_\mathrm{m}}\right)^S\right)\right)\right], \tag{4.12}$$

$$U = -\frac{dP}{dx}\frac{R^2}{8\,\eta_\mathrm{eff}} \tag{4.13}$$

Here, η_eff (Eq 4.14, Eq. 2.26 of Chapter 2) is the effective viscosity of the fluid for a given set of fluid flow condition [190].

$$\frac{1}{\eta_{\text{eff}}} = \frac{1}{\eta_0\,\eta_\infty}\left((\eta_\infty-\eta_0)\,{}_3\mathrm{F}_2\left(1,\frac{2}{S},\frac{4}{S};\frac{S+2}{S},\frac{S+4}{S};-\frac{\eta_\infty}{\eta_0}\left(-\frac{dP}{dx}\,\frac{r}{2\,\tau_{\text{m}}}\right)^S\right)\right.$$
$$\left.+\,2\,(\eta_0-\eta_\infty)\,{}_2\mathrm{F}_1\left(1,\frac{2}{S};\frac{S+2}{S};-\frac{\eta_\infty}{\eta_0}\left(-\frac{dP}{dx}\,\frac{r}{2\,\tau_{\text{m}}}\right)^S\right)-\eta_0\right), \tag{4.14}$$

where, ${}_2F_1(a,b;c;z)$ and ${}_3F_2(a,b,c;d,e;z)$ are the hypergeometric function. The `hypergeom` function of MATLAB can be utilised to solve hypergeometric function, which is computationally expensive. Thus, Shende *et al.,* [190] proposed computationally inexpensive Eq. 4.15 in section 2.2.3 of chapter 2 to determine the approximate effective viscosity of the Meter model fluid flow.

$$\eta_{\text{eff}} = \eta_\infty + \frac{\eta_0-\eta_\infty}{1+\left(\dfrac{0.8\,R}{2\,\tau_{\text{m}}}\dfrac{dP}{dx}\right)^S} \tag{4.15}$$

Shende *et al.* [190] in section 2.2.3 of chapter 2 have shown that effective viscosity helps to estimate the Reynolds number of non-Newtonian fluid through a circular geometry correctly.

4.2.1.2 Linear Phan-Thien and Tanner (PTT) model

The constitutive equations of the affine version of the linear PTT viscoelastic model proposed by Phan-Thien and Tanner are [45, 51, 147, 163, 204]

$$f(\mathrm{tr}(\boldsymbol{\tau}))\cdot\boldsymbol{\tau}+\lambda\left(\frac{\partial\boldsymbol{\tau}}{\partial t}+\mathbf{u}\cdot\boldsymbol{\nabla}\boldsymbol{\tau}-\boldsymbol{\tau}\cdot\nabla\mathbf{u}-(\nabla\mathbf{u})^T\cdot\boldsymbol{\tau}\right)=\eta_{\text{p}}(\nabla\mathbf{u}+(\nabla\mathbf{u})^T) \tag{4.16}$$

here, λ is the relaxation time, η_{p} is the polymeric fluid contribution to the zero shear viscosity (η_0). Here, $\eta_0=\eta_{\text{p}}+\eta_{\text{s}}$ and η_{s} is the solvent viscosity [45]. $\boldsymbol{\tau}$ is the polymeric extra-stress tensor. The stress invariants function $f(\mathrm{tr}(\boldsymbol{\tau}))$ in above equation for PTT follows linear form as given in Eq. 4.17 [147, 204],

$$f(\mathrm{tr}(\boldsymbol{\tau})) = \left[1 + \frac{\varepsilon\,\lambda}{\eta_\mathrm{p}}\mathrm{tr}(\boldsymbol{\tau})\right] \tag{4.17}$$

The constant parameter ε $(0 \leq \varepsilon \leq 1)$ represents the extensional properties [45] of the viscoelastic fluid.

Oliveira and Pinho [147] derived an exact analytical solution for radial velocity profile (Eq. 4.18) and average velocity (Eq. 4.19) for linear PTT model fluid flow through a circular pipe.

$$u(r) = -\frac{dP}{dx}\frac{\left(R^2 - r^2\right)}{4\,\eta_\mathrm{p}}\left(1 + \frac{\varepsilon\,\lambda^2\left(\dfrac{dP}{dx}\right)^2}{4\,\eta_\mathrm{p}^2}\left(R^2 + r^2\right)\right) \tag{4.18}$$

$$U = -\frac{dP}{dx}\frac{R^2}{8\,\eta_\mathrm{p}}\left(1 + \frac{\varepsilon\,\lambda^2\,R^2\left(\dfrac{dP}{dx}\right)^2}{3\,\eta_p^2}\right) \tag{4.19}$$

Similar to the approach adopted by [183, 190] and in section 2.2.3 of chapter 2, on equating Eq. 4.19 with Hagen–Poiseuille equation, we obtain the effective viscosity (η_eff) of linear PTT fluid flow as,

$$\frac{1}{\eta_\mathrm{eff}} = \frac{1}{\eta_\mathrm{p}}\left(1 + \frac{\varepsilon\,\lambda^2\,R^2\left(\frac{dP}{dx}\right)^2}{3\,\eta_p^2}\right) \tag{4.20}$$

4.3 Bundle-of-Capillaries model (BCM) for non-Newtonian fluids

We assume that N number of tortuous capillaries of varying radii and length L are kept in parallel in a porous medium of size $(d \times d \times L)$, here, a cross-sectional area of the medium is $A = d^2$. The bundle of circular capillaries consists of a set of different radii and each radius (r_i) appearing N_i times in a porous medium. The relative frequency (n_i) of a radius (r_i) in a bundle of capillaries is $n_i = \frac{N_i}{\sum N_i}$ and $\sum n_i = 1$. Thus, porosity (ϕ) of the porous medium will be,

$$\phi = \frac{V_v}{V} = \frac{\sum n_i \, \pi \, r_i^2}{d^2}, \tag{4.21}$$

where, V_v is the volume of voids, and V is the total volume. We note that due to the heterogeneous nature, pore-size distribution of the porous medium cannot always be defined using a single probability density function (e.g. log-normal distribution, Weibull distribution etc.). Thus, we have not defined pore-size distribution using any functional form.

4.3.1 Pore-correction coefficient (β_{p})

We note that the micro-capillaries in the porous medium follow tortuous paths [178] and the non-circular cross-sectional area of a single micro-capillary varies along its path. To account for this variation, we define hydraulic radius ($r_{\mathrm{h,N}}$) of a single micro-capillary during the flow of Newtonian fluid as $r_{\mathrm{h,N}} = \beta_{\mathrm{p}} \, r$, where, β_{p} is the pore-correction coefficient of a micro-capillary and r [m] is the inscribed pore radius. Adopting Hagen-Poiseuille equation, we define the average pore velocity (U_{N}) of a Newtonian fluid in a bundle of micro-capillaries in parallel as,

$$U_{\mathrm{N}} = \sum n_i \, u_i = \frac{1}{8 \, \mu} \frac{dP}{dx} \sum n_i \, (\beta_{\mathrm{p}} \, r_i)^2, \tag{4.22}$$

here, u_i [m/s] is the average velocity of fluid in a micro-capillary of radius r_i, and μ [Pa·s] is the Newtonian viscosity. The tortuosity (ψ) of the porous medium is $\psi = \frac{L_g}{L_s}$, where, L_g is the average flow path of a porous medium and L_s is the straight line length [81]. Thus, the average velocity of a Newtonian fluid (i.e. Darcy velocity) in the porous medium will be,

$$U_{\mathrm{N,D}} = \phi \, \frac{U_{\mathrm{N}}}{\psi} = \frac{\phi}{8 \, \mu \, \psi} \frac{dP}{dx} \sum n_i \, (\beta_{\mathrm{p}} \, r_i)^2, \tag{4.23}$$

Equating Eq. 4.23 with Darcy's law ($U_{\mathrm{N,D}} = \frac{k}{\mu} \frac{dP}{dx}$) gives the intrinsic permeability (k) as,

$$k = \frac{\phi}{8\,\psi} \sum n_i \left(\beta_{\mathrm{p}}\, r_i\right)^2 \tag{4.24}$$

Eq. 4.24 suggests that β_p of the porous medium can be determined using measurable parameters (i.e. permeability (k), porosity (ϕ), and the pore-size distribution). We note that in the parallel bundle of micro-capillaries, flow through large pore dominates [24, 117]. On the contrary, in reality, the small pores in porous medium control the total flow. The pore-correction coefficient (β_p), which is an averaging parameter of the pore radius, helps balance this variation.

4.3.2 Fluid-correction coefficient (β_{f})

Many non-Newtonian fluids used in industries are polymer solutions. Thus, they are susceptible to adsorption, pore-clogging and deposition in the pore spaces [227]. Adsorption of polymer on the surface of a micro-capillary alters the pore-geometry of the micro-capillary. Also, the elastic properties of non-Newtonian fluids stretch or contract polymeric molecules in the pore space [94, 106]. This creates additional resistance to the non-Newtonian fluid flow through tortuous micro-capillaries. Thus, we define the hydraulic radius of micro-capillary for the flow of non-Newtonian fluids as $r_{\mathrm{h,NN}} = \beta_{\mathrm{f}}\, r_{\mathrm{h,N}} = \beta_{\mathrm{f}}\, \beta_{\mathrm{p}}\, r$, where, β_{f} is the fluid-correction coefficient of micro-capillary due to fluid rheology during non-Newtonian fluid flow.

The analytical solution for average velocity (u_{NN}) of a non-Newtonian fluid in a micro-capillary of the hydraulic radius ($r_{\mathrm{h,\,NN}}$) is,

$$u_{\mathrm{NN}} = \frac{\left(\beta_{\mathrm{f}}\, \beta_{\mathrm{p}}\, r\right)^2}{8\,\eta_{\mathrm{eff}}} \frac{dP}{dx}, \tag{4.25}$$

here, η_{eff} for Meter model fluid will be as in Eq 4.26 and η_{eff} for linear PTT viscoelastic model fluid will be as in Eq. 4.27,

$$\eta_{\mathrm{eff}} = \eta_\infty + \frac{\eta_0 - \eta_\infty}{1 + \left(\dfrac{0.8\,\left(\beta_{\mathrm{f}}\, \beta_{\mathrm{p}}\, r\right)}{2\,\tau_m} \dfrac{dP}{dx}\right)^S} \tag{4.26}$$

$$\frac{1}{\eta_{\text{eff}}} = \frac{1}{\eta_{\text{p}}}\left(1 + \frac{\varepsilon\,\lambda^2\,(\beta_{\text{f}}\,\beta_{\text{p}}\,r)^2\,\left(\frac{dP}{dx}\right)^2}{3\,\eta_p^2}\right) \tag{4.27}$$

Note that η_{eff} is a function of the radius of micro-capillary, thus, an average pore velocity of non-Newtonian fluids (U_{NN}) in a bundle of parallel capillaries is,

$$U_{\text{NN}} = \frac{1}{8}\,\frac{dP}{dx}\sum \frac{n_i\,(\beta_{\text{f}}\,\beta_{\text{p}}\,r_i)^2}{\eta_{\text{eff,i}}}, \tag{4.28}$$

The average velocity (i.e. Darcy velocity) of non-Newtonian fluids in a tortuous porous medium will be,

$$U_{\text{NN,D}} = \phi\,\frac{U_{\text{NN}}}{\psi} = \frac{\phi}{8\,\psi}\,\frac{dP}{dx}\sum \frac{n_i\,(\beta_{\text{f}}\,\beta_{\text{p}}\,r_i)^2}{\eta_{\text{eff,i}}}, \tag{4.29}$$

On equating Eq. 4.1 with Eq. 4.29, we get hydraulic conductivity or conductance (K) of a porous medium as,

$$K = \frac{k}{\eta_{\text{darcy}}} = \frac{\phi}{8\,\psi}\sum \frac{n_i\,(\beta_{\text{f}}\,\beta_{\text{p}}\,r_i)^2}{\eta_{\text{eff,i}}} \tag{4.30}$$

Substituting Eq. 4.24 in Eq. 4.30, we obtain the non-Newtonian fluid's upscaled Darcy viscosity as follow,

$$\eta_{\text{darcy}} = \frac{\sum n_i\,(\beta_{\text{p}}\,r_i)^2}{\sum \frac{n_i\,(\beta_{\text{f}}\,\beta_{\text{p}}\,r_i)^2}{\eta_{\text{eff,i}}}} \tag{4.31}$$

The volumetric flow rate ($Q_{\text{NN,D}}$) of the non-Newtonian fluid in a porous medium is,

$$Q_{\text{NN,D}} = d^2\,U_{\text{NN,D}} = \frac{d^2\,\phi}{8\,\psi}\,\frac{dP}{dx}\sum \frac{n_i\,(\beta_{\text{f}}\,\beta_{\text{p}}\,r_i)^2}{\eta_{\text{eff,i}}}, \tag{4.32}$$

We obtain the volumetric flow rate of the non-Newtonian fluid in terms of the pore radius by substituting Eq. 4.21 in Eq. 4.32

$$Q_{\mathrm{NN,D}} = \frac{1}{8\,\psi}\,\frac{dP}{dx}\sum\frac{n_i\,(\beta_{\mathrm{f}}\,\beta_{\mathrm{p}}\,r_i)^2}{\eta_{\mathrm{eff,i}}}\sum n_i\,\pi\,r_i^2 \tag{4.33}$$

Eq. 4.29 and Eq 4.33 suggest that the β_{f} can be determined using measurable parameters (i.e. Darcy's flow rate/velocity, pore-size distribution, porosity, tortuosity, and model parameters of a non-Newtonian fluid).

4.3.3 Effective (upscaled) parameters

Effective viscosity of the fluid is the representative viscosity (i.e. upscaled viscosity) for a given set of flow conditions in a circular capillary [190]. Similarly, effective shear rate and effective shear stress are representative values (i.e. upscaled Darcy values) for a given set of flow conditions in a porous medium, which take into account pore-size distribution and pore-scale variability. We define the effective shear stress (τ_{eff}) in the porous medium during the non-Newtonian fluid flow as,

$$\tau_{\mathrm{eff}} = \sum n_i\,\tau_i = \frac{1}{2}\,\frac{dP}{dx}\sum n_i\,(\beta_{\mathrm{f}}\,\beta_{\mathrm{p}}\,r_i), \tag{4.34}$$

Here, τ_i is the wall shear stress in the micro-capillary of radius r_i. Similarly, the effective shear rate ($\dot{\gamma}_{\mathrm{eff}}$) in the porous medium is defined as in Eq. 4.35,

$$\dot{\gamma}_{\mathrm{eff}} = \sum n_i\,\frac{\tau_i}{\eta_{\mathrm{eff,i}}} = \frac{1}{2}\,\frac{dP}{dx}\sum\frac{n_i\,(\beta_{\mathrm{f}}\,\beta_{\mathrm{p}}\,r_i)}{\eta_{\mathrm{eff,i}}} \tag{4.35}$$

The Reynolds number of the porous medium is generally defined using particle diameter [151, 184]. It is highly unlikely to correctly define the particle diameter of porous media such as rocks. Furthermore, Reynolds number of fluid flow in a porous medium is a pore-scale property which must be defined using the geometry of the pore-space. Thus, adopting Shende *et al.* [190] approach, we define the effective Reynolds number ($\mathrm{Re}_{\mathrm{eff}}$) and the effective Péclet number ($\mathrm{Pe}_{\mathrm{eff}}$) of a fluid flow in a porous medium as in Eq. 4.36 and Eq. 4.37, respectively,

$$\mathrm{Re}_{\mathrm{eff}} = \sum n_i\,\mathrm{Re}_i = 2\,\rho\sum\frac{n_i\,u_i\,(\beta_{\mathrm{f}}\,\beta_{\mathrm{p}}\,r_i)}{\psi\,\eta_{\mathrm{eff,i}}} \tag{4.36}$$

$$\mathrm{Pe}_{\mathrm{eff}} = \sum n_i \, \mathrm{Pe}_i = \sum \frac{n_i \, u_i \, (\beta_{\mathrm{f}} \, \beta_{\mathrm{p}} \, r_i)}{\psi \, D_{\mathrm{m}}} \tag{4.37}$$

Here, Re_i and Pe_i are the Reynolds number and Péclet number of the flow in micro-capillary of radius r_i, respectively. D_{m} [m^2/s] is the coefficient of molecular diffusion. We note that Eq. 4.34, 4.35, 4.36, and 4.37 can be used to estimate upscaled effective Darcy shear stress, effective Darcy shear rate, effective Reynolds number and effective Péclet number of the Newtonian fluid, respectively, by equating $\eta_{\mathrm{eff,i}} = \mu$ and $\beta_{\mathrm{f}} = 1$. We note that the effective parameters defined above take into account the pore-scale variation in these values due to variation in the pore-size in the porous medium, thus, these values could be considered as representative values (i.e. upscaled values) for a given set of conditions.

4.4 Numerical approach

We simulated the flow of non-Newtonian fluid modelled using Meter model and viscoelastic linear PTT model through void spaces using finite volume method based OpenFOAM C++ libraries [99] and compared the results with a bundle-of-capillary model (BCM) for non-Newtonian fluids. The volume-averaged values over a porous medium domain obtained after numerical simulation are considered as upscaled value for comparison to the Darcy scale.

4.4.1 Meter model

To implement Meter model in OpenFOAM, we convert the Meter model in terms of shear rate by substituting $\tau = \eta_m \, \dot{\gamma}$ in Eq. 4.11, where $\eta_m = \dfrac{\eta_0 + \eta_\infty}{2}$ is the viscosity of the fluid at τ_m. This leads to a corresponding change in the exponent of the Meter model to S^{-1}. The Meter model will be as in Eq. 4.38,

$$\eta = \eta_\infty + \frac{\eta_0 - \eta_\infty}{1 + \left(\dfrac{\eta_0 + \eta_\infty}{2 \, \tau_m} \, \dot{\gamma} \right)^{S^{-1}}} \tag{4.38}$$

Similar to the procedure adopted in section 3.3.6 of chapter 3 to simulate the single phase flow of a shear thickening fluid, the continuity equation (Eq. 4.6), momentum equation (Eq. 4.7) along with Meter model equation (Eq 4.38) was solved using OpenFOAM 7. We used the PIMPLE (i.e. merged PISO-SIMPLE) algorithm of OpenFOAM to solve the pressure-velocity coupling with 8 nOuterCorrectors and to increase the accuracy of the results [142]. The Semi-Implicit Method for Pressure-linked equation (SIMPLE) algorithm [153] can calculate only steady-state solutions, on the contrary, Pressure-Implicit Splitting Operator (PISO) algorithm takes into account velocity correction term which was neglected in SIMPLE algorithm [92, 142]. Readers are refers to the [76, 92, 142, 153] for more details on SIMPLE, PISO and PIMPLE algorithms. The second-order implicit backward method was used to discretise the time scheme of the governing equations. The gradient term and divergence term were discretised using Gauss linear scheme of OpenFOAM, which uses standard finite volume Gaussian integration. The Gauss linear uncorrected scheme of OpenFOAM was employed to discretise the Laplacian term of governing equations. The system of equations obtained after discretisation was solved using iterative matrix solvers. We computed the pressure field using Generalised Geometric-Algebraic Multi Grid (GAMG) solver with diagonal incomplete-Cholesky (symmetric) smoother. The velocity profile was determined using smoothSolver of OpenFOAM with a Gauss-Seidel smoother. We applied the convergence criteria of 10^{-6} for pressure and velocity field. The time-step of 10^{-7} s was applied to maintain a Courant number (C) below 0.01 during the simulation. The Courant number is defined as $C = \frac{u\Delta t}{\Delta x}$, where, Δt is the time step and Δx is the length interval. The magnitude of shear rate and shear stress in flow field was determined using Eq. 4.9 and Eq. 4.10, respectively.

4.4.2 Linear Phan-Thien-Tanner model

We used RheoTool [162], which is implemented in the OpenFOAM, to simulate linear PTT fluid flow. RheoTool uses the Semi-Implicit Method for Pressure-linked equation (SIMPLEC) algorithm for pressure-velocity coupling [163]. Pimenta and Alves [163] developed a new method for stress-velocity coupling which is second-order accurate and implemented in the RheoTool [162]. We used preconditioned conjugate gradient solver to estimate the pressure and velocity field, whereas, preconditioned (bi-) conjugate gradient (PBiCG) solver was utilised to estimate the stress field. The Gauss linear corrected

scheme was used to discretise the Laplacian term and Gauss linear scheme to discretise the gradient and the divergence term of governing equations. Convergent and Universally Bounded Interpolation Scheme for the Treatment of Advection (CUBISTA) scheme was used for the convective term [7, 162, 163] of the governing equation. Readers are referred to [162, 163] for detailed information on available methods to solve linear PTT model using RheoTool.

4.4.3 Numerical domain and boundary conditions

We conducted three sets of numerical experiments. In the first set, we used microfluidic experimental data of Galindo-Rosales *et al.* [80] to validate the numerical simulation approach adopted in the present work. In the second set, we simulated the Meter model fluid flow through a 2D porous medium (Fig 4.1c) over a pressure gradient range and compared it with a BCM. In the third set, we simulated Newtonian fluid, Meter model fluid, and linear PTT fluid flow through heterogeneous Mt. Simon sandstone (Fig 4.1e) and compared them with BCM. Fig 4.1 shows the porous medium domain's geometry along with pore-size distribution and boundary conditions. We applied wall boundary condition at the top, bottom, front, back and solid surface of 3D domain with no-slip velocity and zero fixed flux pressure. The right boundary had total pressure and zero flux corrected velocity boundary conditions.

To validate the numerical simulation approach adopted in the present work for the flow of Meter model fluid and linear PTT fluid in a porous medium, we used experimental data of Galindo-Rosales *et al.* [80]. Similar to Galindo-Rosales *et al.* experiments, we simulated flow of polyacrylamide (PAA, 50 ppm) fluid through symmetric micro-channel (Fig 4.1a.) in 3D over a range of Deborah numbers (0.01 - 5). We applied a constant injection rate boundary condition at the inlet (left boundary). Readers are referred to [80] for more details on experiments. Similar to [80], we defined Deborah number as $De = \lambda \frac{U}{l}$, where, λ is the longest relaxation time and l is the characteristic length scale.

In the second set of numerical experiments, we simulated the flow of the 0.50% PAA fluid of [151] modelled using Meter model through a 2D porous medium ($\phi = 0.38$) over a range of pressure gradient values (10^2 - 10^8 Pa/m). We applied a constant pressure gradient at the left boundary (inlet) of the 2D porous medium (Fig. 4.1c).

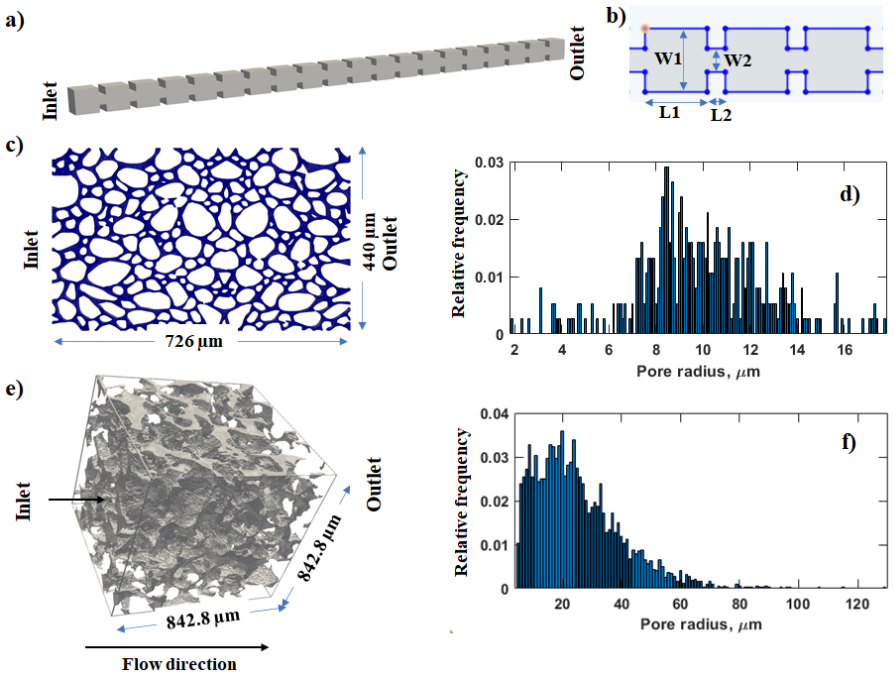

FIGURE 4.1: (a) Symmetric micro-channel with 20 repetitive elements of [80] (b) with size : L1 = 106 μm, L2 = 32 μm, W1 = 108 μm, W2 = 40 μm, H = 103 μm, (c) 2D porous medium of size 726 μm × 440 μm, (d) pore-size distribution of 2D porous medium, (e) segmented Mt. Simon sandstone of size 842.8 μm × 842.8 μm × 842.8 μm, and (f) pore-size distribution of Mt. Simon sandstone. Fluid flows from left to right. No-slip condition at solid surfaces and boundaries (except at inlet and outlet).

In the third set, we simulated the flow of Newtonian fluid (water, $\mu = 0.001$ Pa·s) and 50 ppm PAA fluid of [80] modelled using Meter model and linear PTT model through heterogeneous Mt. Simon sandstone ($\phi = 0.24$) of [110] in 3D. We applied constant injection velocity at the left boundary of Mt. Simon sandstone.

4.4.4 Image processing and visualisation

We used Fiji ImageJ software [185] to process images and Paraview 5.7.0 software to visualise and post-process the fluid flow profile data. We used micro-CT scan data of Mt. Simon sandstone of Kohanpur *et al.* [110] which is available at the Digital Rock portal [166]. The details of the micro-CT scan of Mt. Simon sandstone (original size 3.363 mm^3) is given in Kohanpur *et al.* [110]. The voxel size of the segmented micro-CT sample is 2.8 μm. We took a subsample of size 301×301×301 voxel (i.e. 842.8 μm × 842.8 μm × 842.8 μm) from original Mt. Simson sandstone for present work to minimise computational expenses. The pore-spaces from images were extracted and saved in the required stereolithography (STL) format using the '3D Viewer' plugin [185]

of imageJ. The mesh in the pore-space of the extracted STL file was generated using snappyHexMesh module of OpenFOAM. We determined the pore-size distribution and porosity of the porous medium using the method proposed by Rabbani and Salehi [167].

We computed the fluid flow rate at the right boundary of the porous medium using the SurfaceFlow filter of the Paraview, which integrates the fluid's velocity over the surface at the outlet. We computed average velocity through the porous medium by dividing the estimated flow rate by the total cross-section area of the porous medium at the outlet boundary. We used the "Integrate variable" filter of Paraview to estimate pore-scale volume-averaged velocity, shear rate, shear stress, and viscosity over the porous medium domain. These volume-averaged values can be considered as upscaled values. We simulated the flow of water through porous medium using OpenFOAM to determine the intrinsic permeability of the porous medium (using Eq. $k = \frac{U_N \mu}{\frac{dP}{dx}}$).

4.4.5 Assumptions and limitations

The Meter model is an empirical equation that gives the best fit of shear viscosity-shear stress data. These data are measured using a rheometer and are susceptible to measurement errors. The Meter model equation does not consider viscoelasticity (e.g. relaxation time, normal stress, and shear modulus) of the fluids. The linear PTT model defines the extra stress tensor of the fluid flow theoretically. For instance, the relaxation time of non-Newtonian fluid varies with the applied stress; however, the linear PTT model considers the longest relaxation time in its formulations. The viscoelastic fluid flow simulation modelled using PTT has numerical stability issues. We have used the both-side-diffusion technique implemented in RheoTool to address the stability issue in PTT fluid flow simulations. The readers are referred to [37], which compares different approaches available in the literature to stabilize viscoelastic fluid flow simulation. Readers are also referred to [8, 21, 162, 163] for detailed information on the assumption and limitation of GNF and viscoelastic fluid flow simulations. Although these models are developed based on certain assumptions and have limitations, they provide certain understandings about the fluid dynamics of non-Newtonian fluids.

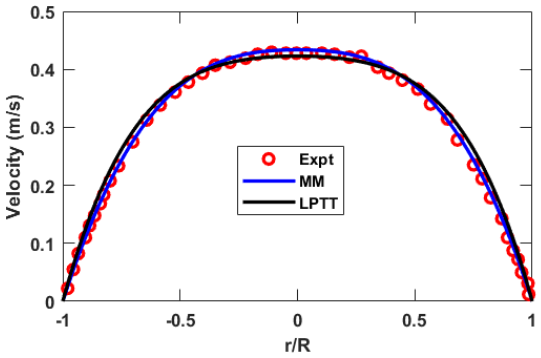

FIGURE 4.2: Comparison of experimental radial velocity profile of [69] with analytical solution of Meter model (Eq. 4.12) and linear Phan-Thien-Tanner (Eq. 4.18) during flow of a 0.125% polyacrylamide (PAA) fluid through a circular tube (radius 0.05 m) [Meter model parameters: $\eta_0 = 0.2257$ Pa·s, $\eta_\infty = 0.000896$ Pa·s, τ_{m}= 0.2381 Pa, $S = 1.2$ [190]; linear PTT model parameters: $\eta_{\mathrm{p}} = 0.2257$ Pa·s, $\lambda = 0.47$ s, $\varepsilon = 0.65$]

4.5 Results and discussion

4.5.1 Analytical solutions

Fig. 4.2 shows that an experimental velocity profile of Escudier *et al.* (2005) [69] gave a good fit with the analytical solution of MM (Eq. 4.12) and linear PTT (Eq. 4.18) models for radial velocity profile at the pressure gradients of 37.5 Pa/m during the flow of 0.125% polyacrylamide through the pipe of radius 5 cm. We note that the rheological parameters of the Phan-Thien-Tanner model were absent in the [69] work; thus, we considered zero-shear viscosity (η_0) of PAA as polymer viscosity of the linear PTT $\eta_{\mathrm{p}} = 0.2257$. The characteristic time of Meter model [190] (i.e. $\lambda = \frac{\eta_0+\eta_\infty}{2\,\tau_{\mathrm{m}}} = 0.47$ s) was considered as the longest relaxation time of PAA fluid. The ε parameter of linear PTT model was considered as the fitting parameter for velocity profile. ε value of 0.65 gave a good fit with an experimentally observed velocity profile of [69] as shown in Fig 4.2.

These results imply that the Meter model parameters and the Meter model's analytical solution for velocity profile can be utilised to determine the unknown parameters of the linear PTT model. Thus, we have adopted the same approach to determine linear PTT model parameters from Meter model parameters of PAA fluid in the subsequent work.

4.5.2 Validation of BCM using experimental observation

We utilised experimental data of 0.5% Separan AP30 (polyacrylamide, PAA) fluid flow in a packed bed of glass beads [151] to validate the Bundle-of-Capillaries model (BCM) for non-Newtonian fluids approach proposed in the present work. Fig. 4.3a shows a perfect fit of shear viscosity data of [151] with the Meter model (Eq. 4.11). The Meter model parameters and linear PTT model parameters are given in the description of the Fig. 4.3. Linear PTT parameters were determined using Meter model parameters and comparing the MM and linear PTT model's analytical solution described in Section 4.5.1. Due to the absence of the packed beds pore-size distribution and tortuosity data in [151], we utilised the sand-pack pore-size distribution of [121] as shown in Fig 4.3b and sand-pack tortuosity value of 1.4 [120] in the present work. We computed $\beta_{\mathrm{p}} = 11.56$ of the sand-pack using Eq. 4.24 and adopting permeability value ($k = 3.57 \times 10^{-9}$ m^2) of [151] packed bed. The estimated $\beta_{\mathrm{f}} = 0.79$ for Meter model fluid and $\beta_{\mathrm{f}} = 0.75$ for linear PTT model implies that the non-Newtonian fluid alters geometry of the pore-structure due to either adsorption, deposition of polymers/colloidal suspension, pore blockage or viscoelastic instability. We note that the β_{p} and β_{f} are pore-scale parameters which take into account the pore-scale variability due to geometry of the pore space and fluid rheology, thus, different porous medium and fluids will have different β values.

Fig. 4.3c and Fig. 4.3d depict that the Darcy velocity estimated using Eq. 4.29 and Darcy viscosity estimated using Eq. 4.31 in the packed bed match closely with the experimentally measured data of Park *et al.* [151]. Furthermore, Fig. 4.3e depicts a good fit of the experimentally measured shear viscosity - shear stress data (measured using rheometer) [151] with the Darcy viscosity-effective shear stress estimated using BCM (Eq. 4.31 and Eq. 4.34). Likewise, Fig. 4.3f shows a good match of the experimental shear rate-shear stress with an effective Darcy shear rate-effective Darcy shear stress estimated using Eq 4.34 and Eq 4.35 of BCM respectively. These results are an improvement to the reported methods in literature (e.g.. [59, 121, 151, 176, 177]) wherein the shift factor α was applied to match the shear rate-dependent viscosity measured using rheometer with the Darcy viscosity in a porous medium. The mismatch observed in the previous works was due to the simplified assumption of a Bundle-of-Capillaries model based Carman–Kozeny equation that does not consider the pore-size distribution

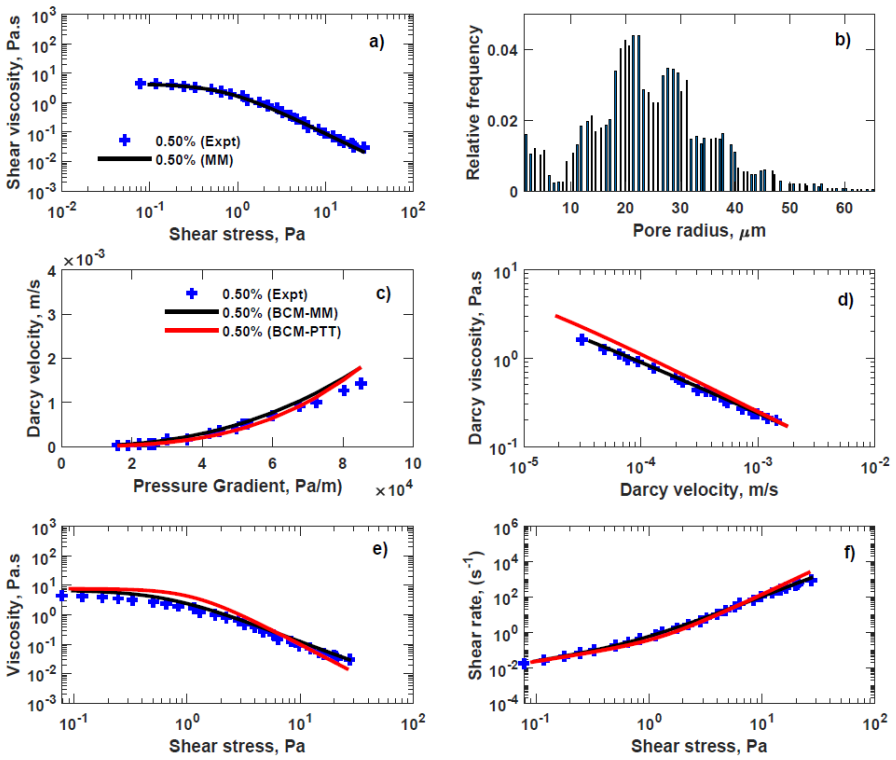

FIGURE 4.3: (a) Experimental shear viscosity-shear stress of 0.5% Separan AP30 fluid of [151] modelled using Meter model (MM, Eq. 4.11), (b) sandpack network pore size distribution of [121], (c) experimentally measured Darcy velocity as a function of pressure gradient [151] compared with velocity estimated using Eq. 4.29, (d) experimental Darcy viscosity compared with Darcy viscosity estimated using Eq. 4.31, (e) experimental shear viscosity as a function of shear stress (measured using rheometer) compared with Darcy viscosity and effective shear rate estimated using Eq. 4.31 and Eq. 4.35, and (f) experimental shear rate as a function of shear stress (measured using rheometer) compared with the effective shear rate and effective shear stress estimated using Eq. 4.34 and Eq. 4.35. BCM-MM: Bundle-of-capillary model for Meter model fluid; BCM-PTT: Bundle-of-capillary model for linear Phan–Thien—Tanner model fluid. Meter model parameters: $\eta_0 = 4.35$ Pa·s, $\eta_\infty = 0.001$ Pa·s, $\tau_{\mathrm{m}} = 0.718$ Pa, $S = 1.471$; linear PTT model parameters: $\eta_{\mathrm{p}} = 4.35$ Pa·s, $\lambda = 3$ s, $\varepsilon = 0.6$.

and alteration in the effective pore radius due to polymeric adsorption, desorption and viscoelasticity.

The analytical solution of linear PTT model derived by [147] does not consider the contribution of solvent viscosity. This could be the reason for the slight deviation of linear PTT based BCM estimate from the experimental observations, as shown in Fig. 4.3. However, Meter model based BCM estimate closely matches with experimental observations.

Fig. 4.4 compares effective Reynolds number estimated using Eq. 4.36 with the volumetric flow rate of MM fluid and linear PTT fluid in a porous medium estimated using

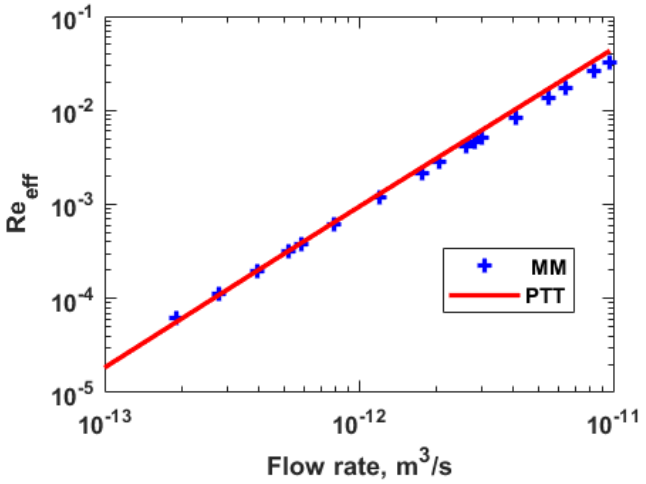

FIGURE 4.4: Effective Reynolds number (Re_{eff}) estimated using BCM (Eq. 4.36) over a range of experimentally observed flow-rate values of [151] during flow of 0.5% PAA fluid through a packed bed.

Eq. 4.33. Fig. 4.4 implies that even though the effective Reynolds number of the non-Newtonian fluid is lower than 1.67, the volumetric flow rate is non-linearly dependent on the effective Reynolds number. This non-linearity is due to the elasticity of non-Newtonian fluids [59, 94, 106]. The proposed BCM correctly captures changes observed during non-Newtonian fluids' flow due to elasticity through β_{f}.

Park *et al.* [151] estimated Reynolds number based on particle diameter ranged from 6×10^{-5} to 0.93 for packed bed, on the contrary effective Reynolds number estimated using Eq 4.36 of BCM for the same experimental data ranged from 7.2×10^{-5} to 1.67 (Fig. 4.4). Park *et al.*'s Reynolds number is based on representative particle diameter; on the contrary, BCM based Reynolds number is an average Reynolds number of the fluid in capillaries. This suggests that Re_{eff} estimated using BCM is representative Re_{eff} for non-Newtonian fluids in porous media compared to the Re formulation developed based on the particle diameter. Rodríguez de Castro and Radilla [176] experimentally observed similar non-linear relationship between Re_{eff} and volumetric flow rate for non-Darcy flow of xanthan gum fluids in the fractured granite and the Vosges sandstone.

4.5.3 Direct numerical simulation (DNS)

4.5.3.1 Validation of numerical simulations

Galindo-Rosales *et al.* experimental measurements [80], during the flow of shear-thinning 50 ppm polyacrylamide (PAA) fluid in symmetric micro-channel, were used to validate the numerical simulation approach adopted in the present work for the flow of Meter model fluids and linear PTT model fluid in the porous medium. Fig. 4.5a shows a statistically good fit of experimental shear viscosity data of [80] with the Meter model (Eq. 4.11). The Meter model parameters and linear PTT parameters are given in the description of Fig. 4.5. The characteristic time of the Meter model (0.054 s) was similar to the relaxation time measured by Galindo-Rasales *et al.* using capillary break-up extensional rheometer (CaBER). The parameter ε was determined using an analytical solution of linear PTT and Meter model.

We adopted a 3D simulation domain similar to Galindo-Rosales *et al.* [80] (see Fig. 4.1a,b). The fine mesh with over 10 million mesh points was generated using snappyHexMesh in the microchannel domain. We applied a constant injection rate at the inlet and allowed the flow to reach statistically steady-state. Fig. 4.5b shows that experimentally observed pressure gradient-Deborah number closely matches the numerical simulations of the Meter model and linear PTT model. However, the Meter model's streamline could not match the experimental observation of Galindo-Rosales *et al.* (see Fig. 4.5). Linear PTT model takes into account the elasticity of the fluid; thus, Fig. 4.5 depicts that streamlines reported by Galindo-Rosales closely match with streamlines of linear PTT model simulations for similar fluid flow conditions. Similar to experimental observation, simulation using linear PTT model shows vortex formation even at lower Deborah numbers. The vortex size increased at the corner with an increase in Deborah number (see Fig 4.5f,g,h).

The linear PTT fluid simulation showed chaotic unsteady flow during the initial few seconds with drastic variations in the shape and size of the vortex. However, after a critical time linear PTT fluid reached a a statistically-steady state with a relatively same vortex pattern (i.e. viscoelastic instability) at the corner. Movie clip 1 of the supporting information (SI) of the published article [189] shows this transition of chaotic viscoelastic instability from unsteady state to statistically-steady state instability using

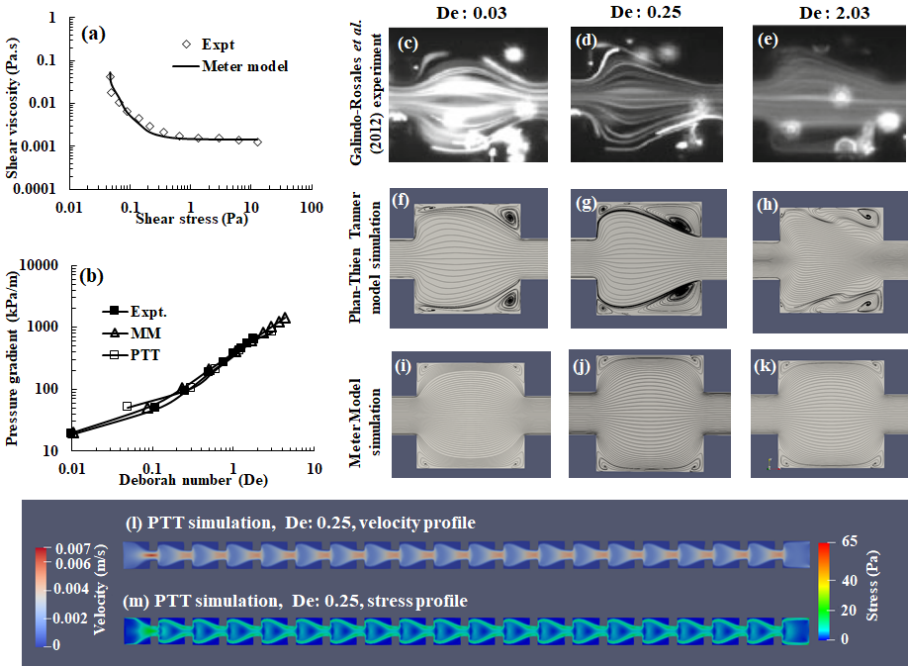

FIGURE 4.5: Comparison of the streamline data obtained after numerical simulation of the flow of 50 ppm PAA fluid (modelled using Meter model and linear PTT model) in symmetric microchannel geometry with the experimental streamline data reported by Galindo-Rasales *et al.* [80] over a range of Deborah numbers. (a) Shear viscosity - shear stress (50 ppm PAA solution, Meter model parameter: $\eta_0 = 0.11$ Pa·s, $\eta_\infty = 0.0014$ Pa·s, $\tau_m = 1.07$ Pa, $S = 1.2$); linear PTT model parameters: $\eta_p = 0.11$ Pa·s, $\eta_s = 0.001$ Pa·s, $\lambda = 0.054$ s, $\varepsilon = 0.3$, $\zeta = 0.02$. (b) Comparison of experimentally observed pressure gradient as a function of Deborah numbers with numerical simulation of PAA fluid modelled using Meter model and linear PTT model. (c,d,e) Experimentally observed streamline snapshot of Galindo-Rosales *et al* [80]. (f,g,h) Streamlines of the flow obtained after linear PTT model numerical simulations. (i,j,k) Streamline of the flow obtained after MM model numerical simulations. (l,m) Velocity profile and magnitude of stress profile at De = 0.25 during linear PTT model fluid.

velocity vector glyphs for linear PTT fluid flow at De of 0.25. Fig. 4.5l,m show the profile of velocity and magnitude of stress at the micro-channel centre over a simulation domain. Fig. 4.5l,m depict that velocity and magnitude of stress at the throat are much larger than the other regions of the micro-channel domain.

These results imply that the linear PTT model gives a more accurate description of pore-scale fluid flow behaviour than the Meter model. However, the average values of the stress, shear rate, velocity, and pressure gradient in the linear PTT model and Meter model's simulation domain are comparable, with slight variation.

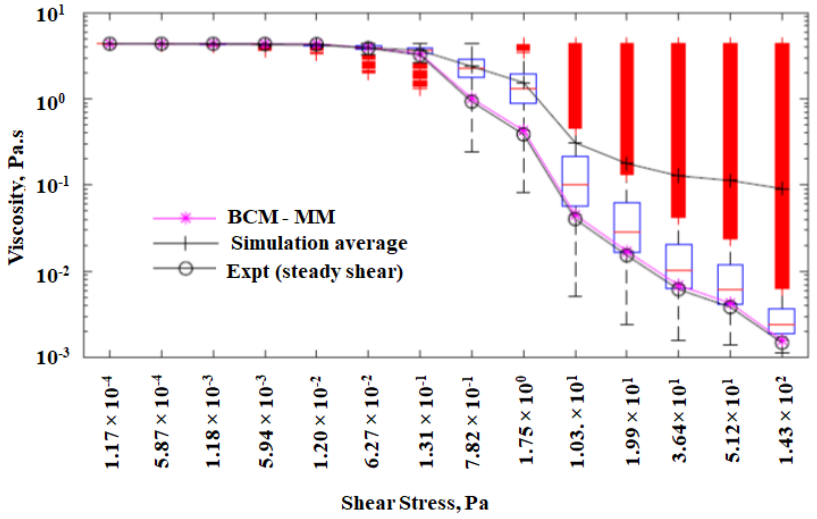

FIGURE 4.6: The boxplot of the viscosity as a function of shear stress during flow of Meter model fluid through 2D porous medium. The boxplot statistics is compared with the values obtained using BCM approach (Eq. 4.31) and experimental shear viscosity values (measured using rheometer). red plus signs indicate outlier values.

4.5.3.2 Polymeric fluid flow in a 2D porous medium

Fig 4.1c shows a pore structure of the 2D micro-porous medium of size 726 μm $\times$ 440 μm [139]. The pore size distribution (Fig 4.1d) and the porosity of 38% are as shown in Fig 4.1d. We simulated the flow of 0.5% PAA fluid of [151] modelled using the Meter model over a range of pressure gradient values (1.38×10^{2} - 1.38×10^{8} Pa/m). The intrinsic permeability of the 2D porous medium estimated using simulation was 1.32 $\times10^{-12}$ m^2. We estimated tortuosity of 1.04 for a 2D porous medium by measuring the length of streamlines. We obtained β_{p} of 0.5215 for the 2D porous medium using pore-size distribution values as given in Fig 4.1d. The BCM-MM approach gave the same volumetric flow rate as obtained using direct numerical simulations over a range of pressure gradient values at the $\beta_{\mathrm{f}} = 1$.

Fig. 4.6 depicts the boxplot statistics observed for the distribution of viscosity values in the 2D porous medium over a range of shear stress values. It also compares the mean viscosity obtained using simulations with a viscosity estimated using BCM approach (Eq. 4.31) and the experimental shear viscosity (measured using rheometer). The experimental shear viscosity of PAA of [151] for a given shear value was estimated using the Meter model. The figure shows many outlier viscosity values (marked in red plus sign) at higher shear values. These values represent the fluid's viscosity in the immobile

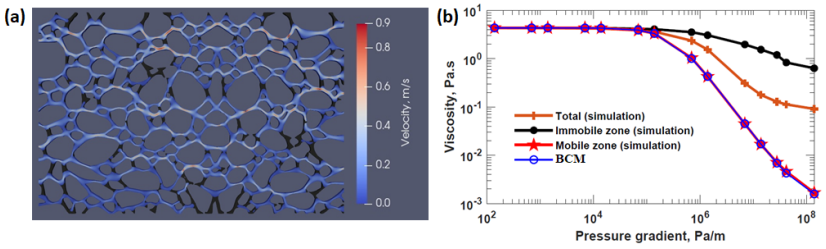

FIGURE 4.7: (a) Immobile zone (marked in a black colour) and velocity profile in a mobile zone (marked in red - white - blue colour) at a pressure gradient of 138 MPa/m, and (b) average viscosity in the total porous medium domain, immobile (stagnant) zone, and mobile zone obtained using BCM and DNS.

(stagnant) zones, which do not contribute to the fluid's active flow in the porous medium. It also shows that average viscosity values lie in the upper outlier region of the boxplot.

To explore further, similar to the approach adopted by de Anna *et al.* [57], we define the immobile zone (or stagnant zone) as the pore space region which has pore-velocity two orders of magnitude lower compared to the average pore-velocity in the porous medium domain and rest of the pore-space region as the mobile zone. We segmented the porous medium domain in the high pore-velocity mobile zone and low pore-velocity immobile (stagnant) zone, as shown in Fig 4.7a. We observed that the immobile zone was 14% of the porous medium domain over a range of pressure gradients (1.38 $\times 10^2$ Pa/m, 1.38 $\times 10^4$ Pa/m, 1.38 $\times 10^6$ Pa/m, and 1.38 $\times 10^8$ Pa/m). Fig 4.7 depicts that most immobile zones are either dead-end of the pore-spaces or perpendicular to the applied pressure gradient and active fluid flow direction. Fig 4.7b shows a comparison of the average viscosity of the fluid in the porous medium domain, its mobile zone, its immobile stagnant zone (obtained after numerical simulation) and the Darcy viscosity (estimated using BCM approach) over a range of pressure gradients. These results show that the average viscosity of the fluid in the immobile zone is very high compared to the mobile zone. Moreover, the viscosity of the fluid in the mobile zones closely matches with the Darcy viscosity of the fluid in the porous medium estimated using a BCM approach. These results imply that the Darcy viscosity of the fluid represents the viscosity of a fluid in the mobile zone of porous medium only.

4.5.3.3 Flow in Mt. Simon sandstone

To explore the effectiveness of the Bundle-of-Capillaries model for non-Newtonian fluids, we simulated the flow of water, and 50 ppm PAA fluid of [80], modelled using Meter

TABLE 4.1: OpenFOAM simulation based estimated parameters during flow of Newtonian (water) and 50 ppm PAA fluid through Mt. Simon sandstone.

Parameter	Water	50 ppm PAA	
		MM	PTT
Average velocity (m/s)	1.47×10^{-4}	1.47×10^{-4}	1.47×10^{-4}
Pressure gradient (MPa/m)	0.035	0.52	0.5
Intrinsic permeability (m^2)	4.2×10^{-12}	-	-

model and linear PTT model, through Mt. Simon sandstone at a constant injection rate of 10^{-4} m/s. Fig. 4.1e shows a segmented 3D subsample of Mt. Simon sandstone utilised in the present work. In total 12,112,242 mesh point was generated in the pore-space of Mt. Simon sandstone's subsample using snappyHexMesh module of OpenFOAM. We determined pore-size distribution (Fig. 4.1f) and porosity of (24 ± 4 %) of the Mt. Simon sandstone. The porosity of 24% and the degree of anisotropy of 0.255 determined using 'BoneJ' plugin of ImageJ suggests that the sandstone subsample is heterogeneous. The average length of streamlines of fluid flow in the Mt. Simon sandstone was 0.001089 m, which gave tortuosity of 1.29.

Table 4.1 shows the estimated average velocity, pressure gradient, and permeability during the flow of water, MM fluid, and linear PTT fluid through Mt. Simon sandstone. The intrinsic permeability of 4.2×10^{-12} m^2 estimated in the present work using OpenFOAM simulation is close to the permeability of 3.8×10^{-12} to 4.15×10^{-12} m^2 estimated by Kohanpur *et al.* [110] using the lattice-Boltzmann method, pore-network method and direct numerical simulations for the subsample of Mt. Simon sandstone. The computed parameters given in the Table 4.1 are close to the field scale values [18].

Fig 4.8 shows the comparison of velocity fields and streamlines in 3D during the fully developed steady-state flow of water, PAA fluid modelled using Meter model and linear PTT model in Mt. Simon sandstone at a constant injection rate of 10^{-4} m/s. Fig 4.8 depicts that the flow paths adopted by Water and PAA fluid modelled using Meter model are similar, on the contrary, the flow path adopted by PAA fluid modelled using linear PTT model shows slight deviation compared to Meter model at same injection rate. This slight deviation in the flow path is due to visco-elasticity of the PAA fluid, which linear PTT could capture. Formation of the vortex in the pore-spaces was observed during the PAA fluid flow modelled using linear PTT model at an applied injection rate of 10^{-4} m/s. However, we did not observe vortex formation during the flow of water and PAA fluid modelled using Meter model. This implies that the variation of

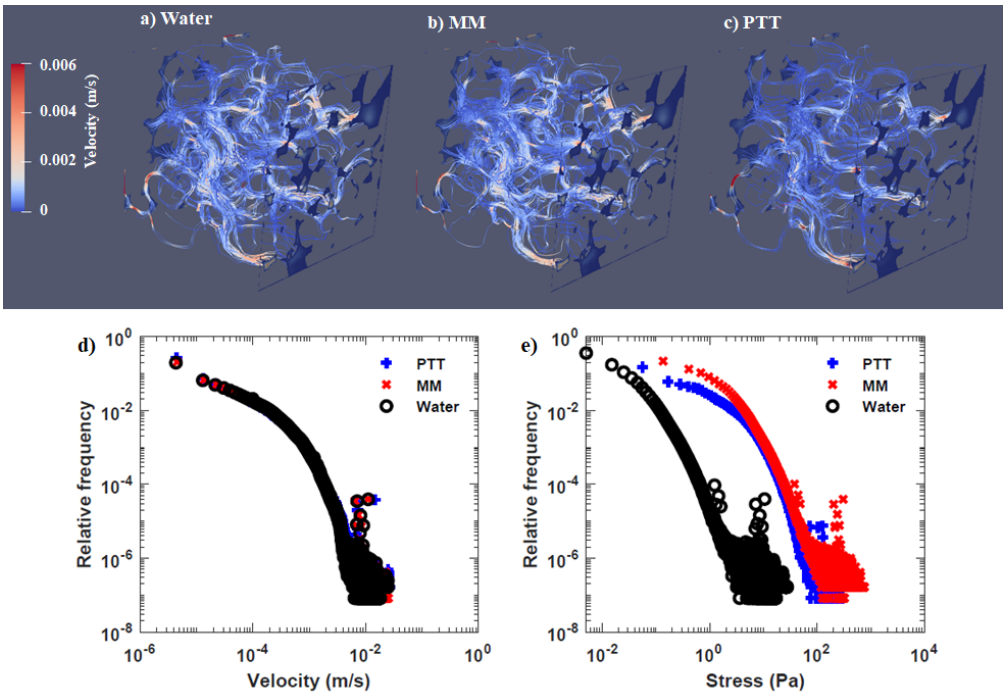

FIGURE 4.8: Comparison of the streamline and velocity fields in the Mt. Simon sandstone during the flow of (a) water, and 50 ppm PAA fluid of [80] model using (b) Meter model (MM), and (c) linear PTT model. (d) Relative frequency of velocity, and (e) relative frequency of shear stress over 12 million mesh points of Mt. Simon sandstone.

pore-space geometry (i.e. converging or diverging) in the heterogeneous Mt. Simon sandstone influences the flow path of a single-phase flow of PAA fluid even if the flow is predominantly laminar. Note that distribution of velocity values over 12 million points in the Mt. simon sandstone's pore-space are similar for Water, MM fluid and linear PTT fluid, due to the same injection rate (see Fig 4.8d).

The relative frequency distribution of velocity profile (Fig 4.8d) of the PAA fluid in the porous medium follows a similar trend as observed by de Anna *et al.* [52] during the flow of viscoelastic fluid through random porous medium. Although a same injection flow rate was applied at inlet during the flow of water and the PAA fluid, the distinct variations in the stress field exist in an Mt. Simon sandstone for water and PAA fluid (Fig 4.8e) flow. Berg and Wunnik [18] observed a similar trend for the shear rate field during Newtonian fluid (water) flow through Berea sandstone.

4.5.3.4 Comparison of BCM approach with DNS

Table 4.2 compares the estimated values using direct numerical simulation and BCM approach during the flow of PAA fluid through Mt. Simon sandstone. We obtained

TABLE 4.2: Comparison of DNS and BCM estimated parameters during flow of a PAA fluid, modelled using Meter model and linear PTT model, through Mt. Simon sandstone.

Parameter	BCM		DNS	
	MM	PTT	MM	PTT
$\beta_{\mathbf{f}}$	1.17	1.286	-	-
Average velocity (m/s)	1.47×10^{-4}	1.47×10^{-4}	1.47×10^{-4}	1.47×10^{-4}
Average viscosity (Pa·s)	0.0143	0.0143	0.058	0.0361
Average stress (Pa)	2.98	3.28	2.01	1.44

β_{p} of 0.4018 for Mt. Simon sandstone using pore-size distribution values as given in Fig 4.1f, porosity of 24%, tortuosity of 1.3 and intrinsic permeability of 4.2×10^{-12} m^2. The β_{f} parameters as given in the Table 4.2 gave volumetric flow rate of 1.6648×10^{-12} m^3/s at the outlet similar to the volumetric flow rate obtained using direct numerical simulations of PAA fluid modelled using Meter model and linear PTT model.

Table 4.2 shows that the estimated values for average viscosity, average shear rate and average stress using BCM are different from those obtained using direct numerical simulations. Since viscosity, shear rate and stress values are distributed in the Mt. Simon sandstone; the average values estimated using DNS may not be representative values for Darcy scale flow as described in Section 4.5.3.2. Thus, effective shear rate, effective shear stress and Darcy viscosity estimated using BCM could be considered the representative values for Mt. Simon sandstone. We note that the average shear stress values of BCM are relatively close to the values estimated using DNS.

The Mt. Simon sandstone's viscosity values vary from 0.009 to 0.11 Pa·s with an average value of 0.058 Pa·s during Meter model fluid flow. On the contrary, Darcy viscosity estimated using BCM is 0.0143 Pa·s. To examine the reason for this drastic variation, we segmented flow zone into the mobile and immobile zone as described in section 4.5.3.2. We obtained mean viscosity of 0.014 Pa·s and 0.09 Pa·s in the mobile zone and immobile (stagnant) zone in the Mt. Simon sandstone. 25% of the volume was an immobile zone in the Mt. Simon sandstone. The average viscosity in the mobile zone closely matches with the Darcy viscosity estimated using BCM. These results further strengthen that the Darcy viscosity is the non-Newtonian fluid's viscosity in the active mobile zone of the porous medium.

4.6 Conclusions

We defined the pore-correction coefficient β_p of a micro-capillary during Newtonian fluid flow and the fluid-correction coefficient β_f for correcting the pore geometry of micro-capillary due to fluid rheology during non-Newtonian fluid flow. The proposed model takes into account the effect of variations in the geometric properties of a porous medium and the effects of non-Newtonian fluids on the hydraulic conductivity of the fluid in porous media. The proposed BCM formulations for upscaled Darcy viscosity, effective Darcy shear rate, and effective Darcy shear stress do not depend on the empirical shift factor (α). Most of the recent works (e.g. [18, 225, 227]) were focused on identifying the relationship between α with pore-morphology and fluid rheology. The BCM model approach differentiates between the effects of pore structure (using β_p) and fluid rheology (using β_f) on the behaviour of the fluid flow in a porous medium. While α is an empirical fitting parameter that is being used to correct the Darcy shear rate value of the porous medium, β_p and β_f are directly related to the physical parameters, i.e. pore morphology, of a porous medium, respectively.

We have also shown that the shear viscosity in the rheometer and the Darcy viscosity in porous media under given shear values are similar. The effective Reynolds number formulation proposed in the present work represents the Reynolds number of non-Newtonian fluids flowing in the porous medium compared to the Reynolds number proposed based on particle diameters and Blake-Kozeny equations.

Moreover, we simulated non-Newtonian fluid flow (modelled using the shear stress-dependent Meter model and linear Phan-Thien Tanner model) through a porous medium using the finite volume method based OpenFOAM C++ libraries. We have shown that the Phan-Thien Tanner model gives a more accurate pore-scale description of the fluid flow than the Meter model. However, the upscaled values of both the Meter model and the linear PTT model are comparable.

The flow fields of viscosity and shear stress obtained after direct numerical simulation of the flow of polymeric PAA fluid and Newtonian fluid show that the pore space geometry of the porous medium affects the fluid flow behaviour. The volume-averaged shear rate, average shear stress, and average velocity obtained after direct numerical simulation closely match the proposed Bundle-of-Capillaries for the non-Newtonian fluids approach

developed for the Meter model and linear PTT viscoelastic model. However, the porous medium's immobile and mobile zones affect rheology, so that the Darcy viscosity of the fluid is associated with the viscosity of the fluid in the active mobile zone of the porous medium only.

Direct numerical simulation is computationally expensive and, consequently, cannot be directly applied to field scale applications, e.g. enhanced oil recovery. The upscaled macroscopic parameters using the BCM approach could be used for Darcy scale simulation. This will be our future interest. Another line of research is two-phase flow modelling at the pore scale using the Meter model and experimental microfluidic data [66], and differentiate the impact of different flow zones on upscaled viscosity from the pore scale.

Chapter 5

Pore-scale simulation of viscous instability for non-Newtonian two-phase flow in porous media

This chapter is published in the '*Journal of Non-Newtonian Fluid Mechanics*'

Authors: **T. Shende,** V. Niasar, and M. Babaei. Pore-scale simulation of viscous instability for non-Newtonian two-phase flow in porous media. *Journal of Non-Newtonian Fluid Mechanics*, 296:104628, 2021.

5.1 Introduction

Immiscible multiphase flow in porous media involving polymeric solutions has many applications specifically for enhanced oil recovery [200, 209, 210], and remediation of subsurface non-aqueous phase liquid (NAPL) contaminants [210, 238]. Polymeric solutions, which have non-Newtonian rheology, is commonly utilised to displace NAPL or crude oil in the subsurface. The heterogeneity of the porous medium and the shear-dependent rheology of non-Newtonian fluids make the multiphase flow more complex. The effectiveness of polymeric solutions to displace oil depends on the physical and chemical parameters of oil, polymeric solutions and subsurface materials that vary spatially with time [145]. Although core-flood experiments on larger samples have been used to study polymeric macroscopic sweep efficiency [200], these experiments can hardly be used to gain pore-scale insights on the microscopic displacement of invading and displacing fluids.

Wettability, which is the fluid's ability to adhere to the solid surface in the presence of another fluid, is one of the key factors in two-phase flow dynamics in the porous medium. The contact angle (θ) between the fluid-fluid interface and the solid surface determines which fluid (displaced or displacing) has a tendency to adhere to the solid surface. For example, in a porous medium wetted by water ($\theta < 90°$), the polymer fluid will adhere to the solid surface, while in a porous medium wetted by oil ($\theta > 90°$), the oil will adhere to the solid surface. Although fluid-fluid interactions during multiphase flow are influenced by the wettability of the solid surface [234], less attention is paid to the multiphase flow involving non-Newtonian fluids. Hatzignatiou *et al.* [88] conducted a polymer flood experiment on water and oil-wet Bentheim and Berea sandstone. They suggested that rock wettability strongly affects the polymer retention in the porous medium and influences the polymer front velocity. The authors postulated that the physical adsorption of polymer to the rock surface causes entrapment of polymer in the sandstone as they observed higher polymer retention in the water-wet Berea sandstone compared to the oil-wet Berea sandstone. Broseta *et al.* [29] reported reduction in the polymer adsorption in an oil-wet micromodel compared to a water-wet one. Jamaloei and Kharrat [96] reported that the displacement front's stability during polymer flooding depends on pore-morphology and wettability in a porous medium. Using magnetic resonance imaging technique, Romero-Zerón *et al.* [180] investigated the

effects of wettability in water-wet and oil-wet rocks and reported higher oil recovery in strongly water-wet rocks using partially hydrolyzed polyacrylamide solution. Ameli *et al.* [9] observed that salinity reduces the efficiency of oil recovery during polymer flooding, and the water-wet system gives favourable oil recovery compared to the oil-wet system. Eslami and Taghavi [70] demonstrated that the wettability affects the viscous fingering pattern formations and flow efficiency of the displacement using two-phase microfluidic experiments wherein Newtonian fluid was used to displace non-Newtonian fluid in a rectangular Hele-Shaw cell. Li *et al.* [116] visualised oil saturation in the oil-wet and water-wet rocks using magnetic resonance imaging and suggested that the polymer stripping mechanism dominates in an oil-wet rock.

Meybodi *et al.* [137] experimentally examined the effect of microscopic heterogeneity on West Paydar crude oil-recovery using polymeric partially hydrolyzed polyacrylamide fluid. They found that water-wet and mixed wet porous medium could recover higher oil compared to oil-wet porous medium in most of the experiments; however, they also reported that the effects of micro-heterogeneity and porous medium's wettability on polymeric fluid-based oil recovery are case dependent [137]. Rodríguez de Castro *et al.* [59] studied the effect of xanthan gum concentration (0 - 2000 ppm) on silicon oil-displacement over a range of capillary numbers and mobility ratios in a heterogeneous hydrophilic 2D micromodel of porosity 60% and pore size distribution of 29 - 160 μm. The authors reported an increase in oil recovery with an increase in polymer concentration; however, they observed heterogeneity dependent viscous fingers in the 2D micromodel porous medium during polymer flooding over a range of xanthan gum concentration [59]. De *et al.* [56] experimentally investigated two-phase displacement of silicon oil using xanthan gum, hydrolyzed polyacrylamide (HPAM) solution and viscoelastic surfactant fluid in a hydrophilic pillared (regularly arranged) micro-channel of porosity 75%. They reported the highest oil recovery using viscoelastic surfactant and HPAM compared to xanthan gum solution over a capillary number range. They suggested that the micro-sweep mechanism plays a vital role in non-Newtonian fluid-based oil displacement in the porous medium. Similarly, Nillson *et al.* [145] found that viscoelastic fluid and shear-thickening nanoparticle fluid displace more oil compared to the shear-thinning fluids. Parasa *et al.* [152], using confocal microscopy visualised HPAM polymer displacing oil in a 3D porous micromodel of porosity 45% and suggested that a non-Newtonian fluid's elastic turbulence leads to the additional oil recovery during

polymer flooding. The recent studies of oil recovery with the aids of microfluidic experiments suggested micro-sweep of oil by polymeric solutions play a crucial role during polymeric flooding [41, 56, 91, 138].

Although pore-scale wettability alteration simulation studies for the flow of Newtonian two-phase flow using Lattice Boltzmann [5] and Volume-of-fluids methods [12] are available in the literature, wettability effects on pore-scale non-Newtonian two-phase flow have not been carefully studied. Shi and Tang [192] carried out a two-phase flow simulation of a Newtonian fluid displacing a power-law fluid using the Lattice Boltzmann method in a porous medium composed of staggered square blocks. This study was carried out using power-law fluids, ignoring the Newtonian plateau at low shear values. Based on numerical simulation, Zhang and Yue [230] reported that visco-elasticity, the flow field, and the stress field determine the sweeping of an oil present in the dead-end by polymeric solutions. Zhong *et al.* [236] conducted two-phase simulations using the volume-of-fluid method in OpenFOAM to study the effects of elasticity on oil recovery. They concluded that elasticity of the non-Newtonian fluid enlarges sweep area and increases displacement efficiency. Using the same approach, Zhong *et al.* [237] investigated the effect of non-Newtonian fluid (based on the cross model) on the displacement of oil and reported that the polymeric solutions increase displacement efficiency by 8-20%. Tsakiroglou [210] developed an inverse modelling numerical scheme to determine macroscopic flow parameters for two-phase flow where non-wetting shear-thinning fluid (modelled using Meter model) displaced Newtonian fluid in a porous medium and validated the same using unsteady two-phase experiments conducted on the pore-network.

5.1.1 This study

Most of the studies reported above were carried out in simple homogeneous porous media; it is unlikely that such geometries will take into account micro-heterogeneity and true complexities as observed realistically. Pore-scale micro-heterogeneity significantly affects the microscopic displacement of fluid in the porous medium. Only a few studies [56, 59, 152, 212, 220] considered the effects of micro-heterogeneity on polymeric fluid-induced oil displacement. The pore size in the real and heterogeneous porous medium can vary by up to 2 orders of magnitude; thus, the pore-scale velocity and viscosity in the porous medium also vary significantly. This spatial variation of viscosity and

velocity in the pore-spaces and capillarity governs the flow's stability. Thus, the main objective of this work is to determine how microscale heterogeneity and wettability of the porous medium govern the stability of polymeric fluid flow, even for favourable viscosity ratios where the flow is stable. For this purpose, we utilise the volume-of-fluid based 'interFoam' solver of OpenFOAM for two-phase flow involving shear-stress dependent Meter model fluids. The Meter model captures S-shaped rheology (i.e. power-law behaviour at intermediate shear values and Newtonian plateau at low and high shear values) of most of the shear thinning and shear thickening polymeric non-Newtonian fluids [190].

We validate the numerical approach adopted in the present work for the two-phase flow of the Meter model fluid using microfluidic experimental observation of air displacing non-Newtonian fluid in the Hele-Shaw cell. We study the effects of wettability alteration on the displacement behaviour of oil and a polymeric non-Newtonian fluid (polyacrylamide) over a range of porosities (with different heterogeneity levels), capillary numbers, polymer concentrations, and viscosity ratios in 2D and 3D porous media. The results substantiate that the complex interplay between pores' geometry, rheology of the fluid, and capillary force regulates the stability of the two-phase fluid transport.

5.2 Numerical simulation

The Volume-of-Fluid (VoF) method, implemented in OpenFOAM [98] using interFoam solver, is used to simulate immiscible and incompressible two-phase fluid flow in a porous medium involving non-Newtonian fluids. The details of the VoF method implemented in OpenFOAM for two-phase flow displacement can be found at [13, 144, 168, 169, 203, 237]. The shear viscosity (η) of the polymeric non-Newtonian fluid is defined using the shear stress-dependent Meter model (Eq. 5.1 also defined at Eq. 2.2 of Chapter 2) [134, 189, 190],

$$\eta = \eta_\infty + \frac{\eta_0 - \eta_\infty}{1 + \left(\frac{\tau}{\tau_\mathrm{m}}\right)^S} \tag{5.1}$$

where, η_0 [Pa·s], η_∞ [Pa·s] and τ_m [Pa] are the zero-shear viscosity, the infinite shear viscosity, and the critical shear stress of the non-Newtonian fluid at which viscosity of

the fluid drops to $\frac{\eta_0+\eta_\infty}{2}$, respectively. S is the shear stress-dependent exponent of Meter model, which represent slope [189, 190]. The characteristic time (i.e. longest relaxation time, λ) of the non-Newtonian fluid is $\lambda = \frac{\eta_0+\eta_\infty}{2\,\tau_\mathrm{m}}$ [134, 190]. For carrying out numerical simulation, Meter model is written as a function of shear rate as described in [189] and section 4.4.1 of chapter 4. This is obtained by substituting $\tau = \eta_m\,\dot{\gamma}$ in Eq. 5.1, where $\eta_m = \frac{\eta_0+\eta_\infty}{2}$ is the viscosity of the fluid at τ_m. The exponent of Meter model changes to S^{-1}:

$$\eta = \eta_\infty + \frac{\eta_0 - \eta_\infty}{1 + \left(\dfrac{\eta_0 + \eta_\infty}{2\,\tau_\mathrm{m}}\,\dot{\gamma}\right)^{S^{-1}}} \tag{5.2}$$

5.2.1 Numerical scheme and the solver

Similar to the procedure adopted in section 3.3.6 of chapter 3 and section 4.4.1 of chapter 4 to simulate the single phase flow of a shear thickening fluid and Meter model fluid, we used the PIMPLE (i.e. merged PISO-SIMPLE) algorithm for coupling of pressure and velocity [142]. Patankar *et al.* [153] proposed the Semi-Implicit Method for Pressure-linked equation (SIMPLE) algorithm to estimate steady-state solution, however, SIMPLE algorithm neglect the velocity correction term. The Pressure-Implicit Splitting Operator (PISO) algorithm proposed by [92] consider the velocity correction term. We refer to [76, 92, 142, 153] for details on PIMPLE, SIMPLE, and PISO algorithms. The second-order implicit backward method was used to discretise the time scheme of the governing equations. The gradient term and the divergence term were discretised using a Gauss linear scheme. The Gauss linear uncorrected scheme was employed to discretise the Laplacian term of governing equations. The pressure field and velocity field were solved using a GAMG solver and smoothSolver of the OpenFOAM. The convergence criterion of 10^{-7} was implemented for pressure and velocity fields. The average time-step was adjustable between 10^{-5} - 10^{-6} s to have a Courant number below 0.5. The Courant number is $C = \frac{u\,\Delta t}{\Delta x}$, here, Δt is the time step and Δx is the length interval.

5.2.2 Initial and boundary conditions

Three sets of two-phase numerical simulations were conducted in the present work.

- Simulation of two-phase flow in square Hele-Shaw cell to validate the model against the experimental data of [216] for air displacing a non-Newtonian polymeric solution (500 ppm polyisobutylene mixed in mineral oil) in a partially saturated square Hele-Shaw cell at a constant pressure.
- Simulation of two-phase flow in three-dimensional Mt. Simon sandstone of [110] (described in section 4.4.3 of chapter 4) to study the effect of wettability on two-phase flow dynamics.
- Simulation of two-phase flow in homogeneous and heterogeneous polydisperse two-dimensional porous media.

SnappyHexMesh utility of OpenFOAM was used to generate meshes on the porous media domain. No-slip boundary conditions were applied to the walls. For the first set of experiment, Hele-Shaw cell (square geometry of 150 mm length and gap spacing of 100 μm, porosity (ϕ) = 1) was partially saturated with 500 ppm polyisobutylene (PIB) fluid at the centre with a volume of 100 μL (diameter of 0.025 m). Air was injected with a constant injection pressure at the centre and allowed to flow along the radial direction. The inlet has an inner diameter of 2.4 mm. We note that White and Ward [216] used a plastic shim to keep the desired spacing between two plates. We could not identify the geometry and exact location of the plastic shim in the experimental Hele-Shaw cell. Furthermore, an initial drop of PIB fluid placed at the centre of the Hele-Shaw fluid by [216] has slightly deviated from the centre; thus, PIB fluid was not uniformly distributed around the centre. Thus, the present simulation is not a replica of the experimental work of [216] as we could not implement the plastic shim spacer geometry and exact spatial saturation of PIB solution in the simulation setup. We modelled shear stress-dependent rheology of 500 ppm polyisobutylene mixed in mineral oil (PIB) using the Meter model (see Fig 5.1 and Table 5.1). We considered density of PIB as ρ = 920 kg/m^3. The interfacial tension (IFT) and contact angle between PIB and air were considered as 0.03 N/m and 60° due to the absence of the same in the work of [216]. The viscosity and density of air were taken as 1.81×10^{-5} Pa·s and 1.225 kg/m^3, respectively.

TABLE 5.1: The Meter model parameters of Separan AP30 fluid of [151] and polyisobutylene mixed in mineral oil (PIB) of [216] used for the numerical experiments.

Parameter	Separan AP30 concentration		PIB
	0.50%	0.05%	500 ppm
η_0 [Pa·s]	4.350	0.260	0.055
η_∞ [Pa·s]	0.001	0.001	0.033
τ_m [Pa]	0.718	0.339	0.079
S	1.471	1.190	3.8
λ [s]	3.030	0.384	0.9

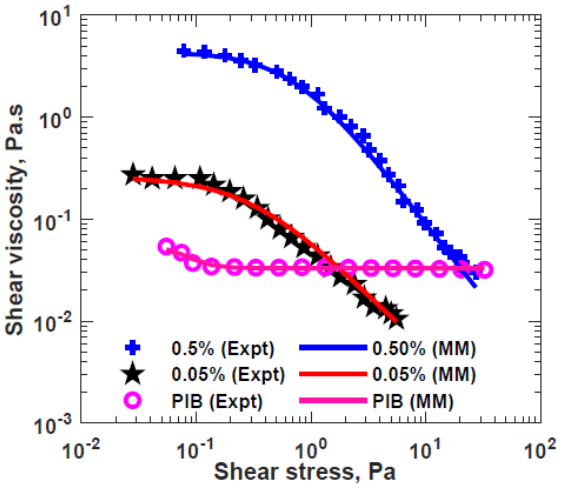

FIGURE 5.1: Experimental shear viscosity-shear stress of 0.5% and 0.05% Separan AP30 fluid of [151] and PIB solution of [216] modelled using Meter model (MM) Eq. 5.1.

For the second and the third sets of numerical experiments, the domain was fully saturated with a silicon oil. Inlet injection velocity and constant pressure with zero gradients were applied to the porous medium domain's left and right boundary. Polyacrylamide solution (Seperan AP30 fluid, see Table 5.1 for Meter model parameter and Fig 5.1) of Park *et al.* [151, 189] was injected into the 3D domain of Mt. Simon sandstone [110, 189], and 2D domain of porous medium saturated with silicon oil (density: 970 kg/m^3, dynamic viscosity: 0.02 Pa·s). The details of 2D and 3D porous media domains used for simulations are given in Figure 5.2 and Table 5.2. The interfacial tension between the polyacrylamide solution and silicon oil is 0.029 N/m [59]. We used ParaView 5.7.0 [3] to post-process the simulation data. Table 5.2 shows an average computation time for each simulation for the 2D and 3D domains along with the number of mesh points in the domain. We used 32 CPU cores in parallel and 16 CPU cores in parallel for the 3D and 2D simulations, respectively. Each CPU cores had a memory of 4GB. The simulations were computationally expensive as the number of grid points were larger than 3 million,

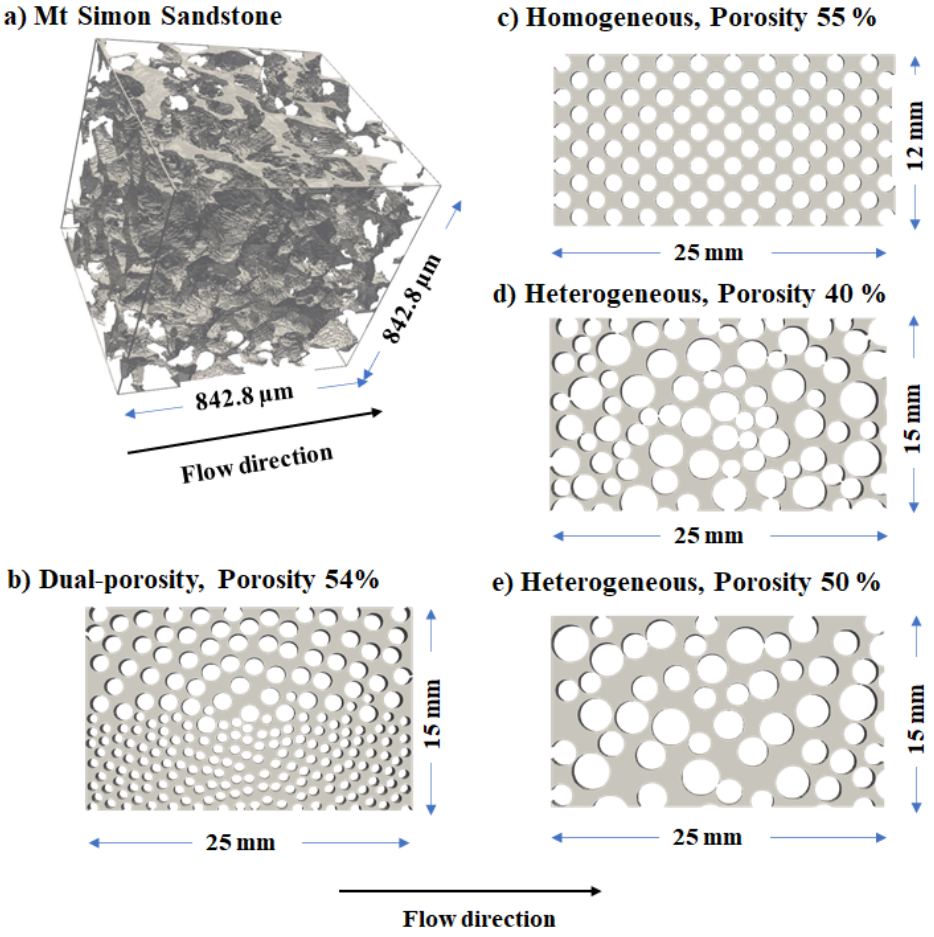

FIGURE 5.2: Geometry of (a) segmented Mt. Simon sandstone of size 842.8 μm $\times$ 842.8μm $\times$ 842.8μm (as described in section 4.4.3 of chapter 4), (b) heterogeneous 2D porous medium having duel-porosity, (c) homogeneous 2D porous medium having porosity 55%, (d) heterogeneous 2D porous medium having porosity 40%, and (e) heterogeneous 2D porous medium having porosity 50%. No-slip condition at solid surfaces and boundaries (except at inlet and outlet).

and the time-step was between 10^{-5} to 10^{-6}s.

TABLE 5.2: Type of porous medium domains and computation time for the second and third numerical experiments.

Type	Porosity (ϕ)	Domain size	Pore size distribution	Mesh points	CPU time (hrs)
Mt. Simon Sandstone (3D)	0.24	842.8 μm $\times$ 842.8 μm $\times$ 842.8 μm	5-120 μm	12,112,247	1176
Homogeneous (2D)	0.55	25 mm $\times$ 12 mm	350 μm	4,319,174	168
Heterogeneous (2D)	0.54	25 mm $\times$ 15 mm	30 - 710 μm	3,319,743	336
Heterogeneous (2D)	0.50	25 mm $\times$ 15 mm	8.1 - 685 μm	3,800,823	168
Heterogeneous (2D)	0.40	25 mm $\times$ 15 mm	6.6 - 418 μm	3,079,048	672

5.2.3 Capillary number, viscosity ratio and Weissenberg number

The capillary number is the ratio of viscous forces to the surface tension forces. Most of the literature uses the Darcy velocity of the injected fluid [12, 49, 169] instead of pore-scale velocity to estimate the Capillary number of a Newtonian fluid flow. The use of Darcy velocity to estimate Capillary number is widespread due to two reasons. Firstly, it is easy to measure experimentally compared to the pore velocity. Secondly, macroscopic properties of fluid flow in a porous medium are easy to analyse using Darcy's law for all practical purpose. However, since the interaction between capillary force and viscous forces during two-phase flow occurs at pore-scale. The capillary number must always be determined using pore-scale fluid flow properties (i.e., velocity, viscosity, interfacial tension) to ensure that the capillary number represents the actual ratio between viscous forces and capillary forces.

In the present work, the capillary number ($\mathrm{Ca_N}$) of a two-phase Newtonian fluid displacing Newtonian fluid flow is estimated using $\mathrm{Ca_N} = \frac{U_\mathrm{i}\,\eta_\mathrm{i}}{\sigma}$ [112, 168]. The viscosity ratio ($\mathrm{M_N}$) for two-phase Newtonian fluids displacement is defined using $\mathrm{M_N} = \frac{\eta_\mathrm{d}}{\eta_\mathrm{i}}$ [112, 168]. Here, η_i [Pa·s] is the viscosity of the invading fluid, η_d [Pa·s] is the viscosity of the displaced fluid, U_i [m/s] is the invading fluid's average velocity in the porous medium domain, σ [N/m] is the interfacial tension between invading fluid and displaced fluid.

The shear viscosity of the non-Newtonian fluid in a porous medium varies spatially, thus, we define capillary number ($\mathrm{Ca_{NN}}$) of non-Newtonian fluid displacing Newtonian fluid as $\mathrm{Ca_{NN}} = \frac{U_\mathrm{i}\,\eta_\mathrm{eff}}{\sigma}$, and the viscosity ratio ($\mathrm{M_{NN}}$) using $\mathrm{M_{NN}} = \frac{\eta_\mathrm{d}}{\eta_\mathrm{eff}}$ [56, 122, 145, 187, 238]. Here, η_eff [Pa·s] is the effective viscosity of the non-Newtonian fluid for a given set of flow conditions [189, 190].

The Weissenberg number (Wi) is the ratio of the elastic forces to the viscous forces. Wi for the flow of non-Newtonian fluid through confined space is defined as the product of the longest relaxation time (λ) of the polymeric solution and the shear rate (i.e. $\mathrm{Wi} = \lambda\,\dot{\gamma}$) [33, 145, 165]. The shear rate of the fluid flow in a porous medium depends on the pore-morphology and fluid rheology, and varies significantly in the porous medium domain. Thus, we defined Weissenberg number (Wi) for the flow of polymeric solution in the porous medium as [32, 33, 105, 145],

$$\mathrm{Wi} = \lambda\,\dot{\gamma}_{\mathrm{avg}} \tag{5.3}$$

here, $\dot{\gamma}_{\mathrm{avg}}$ is the volume-averaged shear rate over a porous medium domain saturated with non-Newtonian fluids. We estimated the volume-averaged velocity (U_{avg}), volume-averaged effective viscosity (η_{eff}), volume-averaged shear rate ($\dot{\gamma}_{\mathrm{avg}}$) of the fluid flow in a porous medium by integrating the pore-scale velocity value (U), viscosity value (η), shear rate value ($\dot{\gamma}$), respectively, over a pore-space filled with a non-Newtonian fluid (V_P) in the porous medium domain during two-phase flow. The representative upscaled value of the fluid properties for a given set of fluid flow condition in a porous medium depends on the pore-scale variation of the property. We have shown in the subsequent section that volume-averaged value can be used as a representative upscaled value of the pore-scale fluid-flow phenomenon.

5.3 Results and discussion

5.3.1 Convergence of numerical simulation

The grid convergence analyses were performed on different grid resolutions (50,000 - 500,000) using the same numerical scheme as given in section 5.2.2. The grid convergence was performed on a subsample (see Figure 5.3) of a porous medium having a porosity of 54% at an injection rate of 0.01 m/s and time-step of 10^{-5} s. Figure 5.3 shows a comparison of average velocity and average viscosity of the polymeric fluid in a saturated domain as a percentage of the high resolution case for each grid size considered. Figure 5.3 shows an insignificant difference in the average velocity and viscosity after grid density 30 cells/μm^2. The Courant number was higher than 1 for a grid size lower than 20 cells/μm^2. Although computationally expensive, all simulations were carried out with a grid density higher than 50 cells/μm^2 to maintain convergence and accuracy. This resolution provided at-least 50 cells in the smallest pore-throat of the heterogeneous porous medium. Appendix A presents more details on the grid-dependent convergence of numerical simulations.

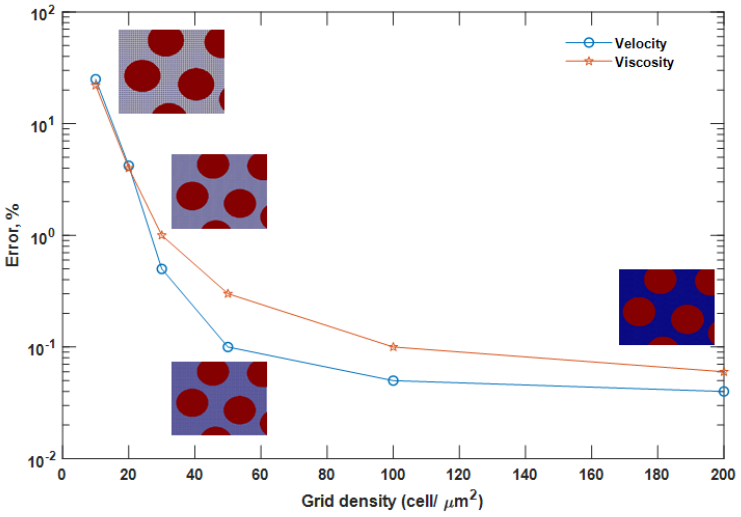

FIGURE 5.3: Average velocity and average viscosity for each grid density. The error shows percentage of the average value attained compared to the zero-grid spacing values determined using Richard extrapolation as described in Appendix A. The average velocity and average viscosity values approach an asymptotic zero-grid spacing value with increase in grid density.

5.3.2 Validation of two-phase numerical modelling

Figure 5.4 shows that the flow paths adopted by a PIB-air interface in the numerical simulation and the Hele-Shaw experiment of [216] are not identical at the injection pressure of 6.9 kPa. This difference in the flow paths is expected due to the difference in the outlet boundary condition of [216] experiment and boundary condition adopted in the simulations described in Section 5.2.2. We note that the PIB fluid location in the Hele-Shaw cell was not uniformly distributed around the inlet during experiment and it was partially deviated from the center as shown by the inner dotted line in Figure 5.4(b). Moreover, fluid material parameters (i.e. interfacial tension, density and contact angle) used in the simulation may not be the same as in the experiments of [216].

Although the interface flow paths of numerical simulation and experiments are not identical, the fluid-fluid interface instability pattern is similar. The branches of the fingers formed during the simulation and the experiment follow the similar pattern. The fingers are formed either by tip splitting or side branching. The thinner fingers with side branches and smooth sides can also be observed in the simulations and the experiment. These results indicate that the Volume of Fluid method based two-phase simulation involving non-Newtonian fluid can be modelled using shear stress-dependent Meter model equation.

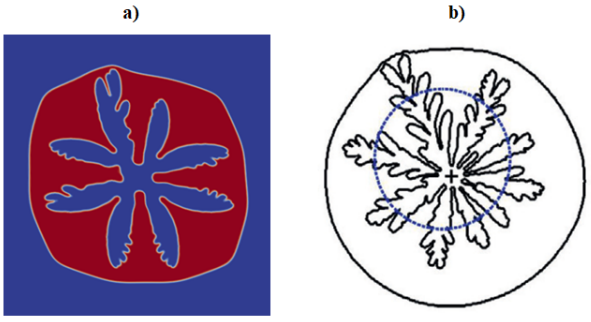

FIGURE 5.4: Comparison of (a) the two-phase simulation of air displacing a non-Newtonian fluid (PIB polymeric fluid modelled using Meter model) in a partially filled radial Hele-Shaw cell, against (b) an experimental observation of White and Ward [216] at inlet pressure of 6900 Pa. Blue and red indicate air and PIB polymeric solution, respectively.

5.3.3 Pore-scale variation of velocity and viscosity

To quantify the variability of the flow of injected fluid within a heterogeneous porous medium (porosity 40%) at an injection rate of 0.01 m/s, we calculated probability density functions (PDF) of the velocity components along the longitudinal and transverse direction, velocity magnitude, and viscosity as shown in Figure 5.5. Similar to the experimental observation of [49] for Newtonian fluid, Figure 5.5c shows exponential decay of velocity magnitude of non-Newtonian fluid. Although flow along the transverse is symmetric about $U_T = 0$, the distribution is non-Gaussian and decays exponentially. Similarly, flow along longitudinal direction U_L shows non-Gaussian distribution with exponential decay. The viscosity of the injected fluid also shows the non-Gaussian distribution. These results imply that flow in the heterogeneous porous medium is non-random and geometry of pore-space governs the distribution of velocity and viscosity.

The probability density function of velocity magnitude could fit into the Beta distribution function. The mean and standard deviation of the velocity magnitude, estimated using the Beta distribution function, were $3\times\ 10^{-2}$ m/s and $4.1\times\ 10^{-2}$ m/s. These results are consistent with a volume-average velocity (2.97×10^{-2} m/s) obtained after integrating the velocity magnitude value over a porous medium domain saturated with injected fluid. Similarly, PDF of viscosity value could fit into Gamma distribution function with a mean of 0.6 Pa·s and standard deviation of 0.165 Pa·s, and these values also agree with volume-averaged viscosity value of 0.61 Pa·s. To take into pore-scale variability in the porous medium, we will report volume-averaged values and the standard deviation of velocity, viscosity, shear rate in the subsequent sections.

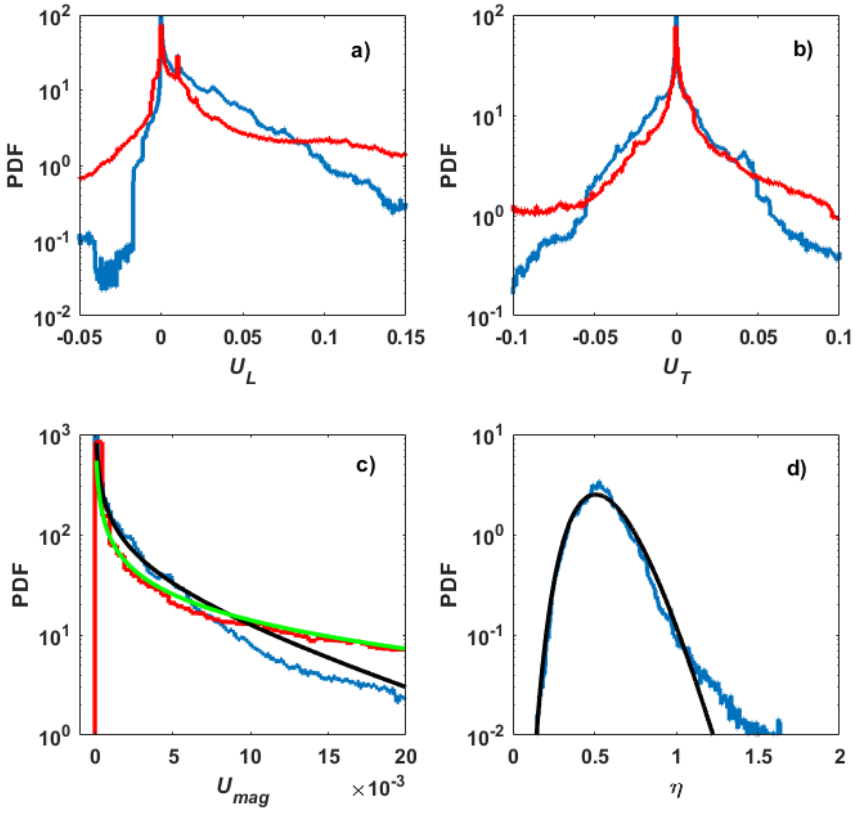

FIGURE 5.5: Probability density function (PDF) of (a) velocity component in longitudinal direction (U_L, m/s), (b) velocity component in transverse direction (U_T, m/s), (c) velocity magnitude (U_{mag}, m/s), and (d) viscosity (η, Pa·s) of injected fluid in the porous medium with porosity 40%. The data is over the domain saturated with injected fluid. Blue line indicates data of PAA fluid and red line indicate data of water. Black and green line in (c) indicate Beta distribution function fitting for PAA fluid and water, respectively. black line in (d) indicate Gamma function fitting with viscosity data. Injection rate is 0.01 m/s.

5.3.4 Mt. Simon sandstone

We simulated the flow of 0.5% PAA polymeric solution displacing silicon oil through Mt. Simon sandstone in the water-wet ($\theta = 30°$), intermediate-wet ($\theta = 90°$) and oil-wet ($\theta = 120°$) conditions. Table 5.3 shows average velocity, effective viscosity, the average shear rate of 0.5% PAA solution flow in the Mt. Simon sandstone and corresponding Ca, M and Wi in water-wet, intermediate-wet and oil-wet domain. The η_{eff} of polymeric solution at an injection rate of 10^{-3} m/s was on average 0.82 Pa·s over a range of contact angles, thus, the estimated Ca on average was 4.19 $\times 10^{-2}$. Generally, for estimation of Ca of polymeric fluid flow, the polymeric solution's zero-shear viscosity has been extensively used in the literature [200]. The estimated value of Ca using zero-shear

viscosity is 2.19 $\times 10^{-1}$ which is one order of magnitude greater than values gives in Table 5.3. We note that the Ca, M and Wi estimated in the present work could be considered as representative values for a given set of fluid flow conditions as these values are determined from direct numerical simulations data instead of unrealistic viscosity values (i.e. zero-shear viscosity) for given fluid flow conditions.

TABLE 5.3: Capillary number (Ca), viscosity ratio (M), Weissenberg number (Wi) of PAA-polymeric fluid flow in 3D Mt. Simon sandstone

θ	U_{avg} (m/s)	η_{eff} (Pa·s)	$\dot{\gamma}_{\text{avg}}$ (s^{-1})	Ca	M	Wi
30°	1.3 $\times 10^{-3}$	0.8	161	3.59 $\times 10^{-2}$	2.5 $\times 10^{-2}$	487
90°	1.5 $\times 10^{-3}$	0.82	153	4.24 $\times 10^{-2}$	2.44 $\times 10^{-2}$	463
120°	1.64 $\times 10^{-3}$	0.83	104	4.75 $\times 10^{-2}$	2.38 $\times 10^{-2}$	315

The PAA polymeric solution saturations (Figure 5.6a,b,c) and simulation movie clip (Clip 1 of the Supporting Information of the published article [188]) over a range of contact angle indicate that the flow path adopted by polymeric solution in water-wet, intermediate-wet and oil-wet porous medium are different. The oil saturation profiles (Figure 5.6d,e,f) and PAA-oil interface profiles (Figure 5.6g,h,i) in the Mt. Simon sandstone indicate that an increase in the contact angles increases the distribution of small trapped oil fragments in the sandstone. The surface area of the PAA-oil interface at a breakthrough was 5.57$\times 10^{-7}$ m^2, 7.76$\times 10^{-7}$ m^2, and 1.51$\times 10^{-6}$ m^2, at $\theta = 30°$, $\theta = 90°$, and $\theta = 120°$, respectively. Figure 5.6j shows 25.71%, 32.44%, and 34.5% remaining oil saturation at breakthrough after injection of 0.5% PAA polymeric solution (injection rate at inlet of 10^{-3} m/s) in water-wet ($\theta = 30°$), intermediate-wet ($\theta = 90°$) and oil-wet ($\theta = 120°$) Mt. Simon sandstone of [110], respectively.

Figure 5.6k shows the pressure gradients during the simulation as a function of oil-saturation at a constant inlet injection rate of 10^{-3} m/s in the Mt. Simon sandstone. These results imply that oil-wet condition requires higher pressure compared to water-wet condition to displace oil from heterogeneous Mt. Simon sandstone. Furthermore, as the oil saturation decreases with time, the pressure required to maintain the constant flow rate increases. The simulation of PAA-solution displacing silicon oil suggests that the water-wet condition is favourable for oil recovery compared to the intermediate-wet or oil-wet conditions. We note that we did not observe a stable fluid flow front in Mt. Simon sandstone at the capillary number of 2.83 $\times 10^{-2}$. Even though PAA polymeric solution with significantly high viscosity value, (i.e. with much lower viscosity ratio) was

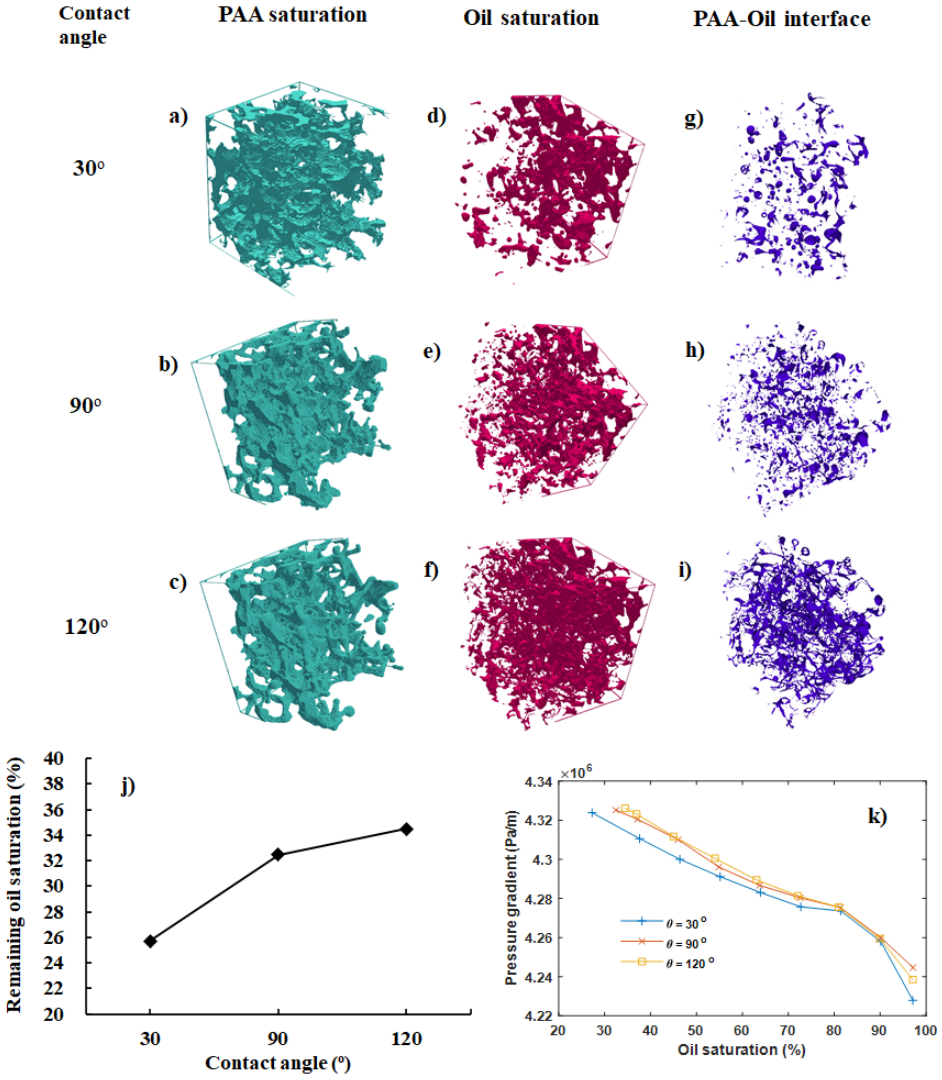

FIGURE 5.6: Effect of contact angle on the remaining oil saturation in Mt. Simon sandstone. Figure (a,b,c) show the distribution of polyacrylamide (PAA) fluid saturation at different contact angles, (d,e,f) silicone oil saturation profiles, and (g,h,i) profile of PAA-oil interface profiles. (j) Remaining oil saturation at breakthrough. (k) Pressure gradient as a function of oil saturation (pressure gradient is the pressure difference between inlet and outlet of Mt. Simon sandstone). Injection rate is 10^{-3} m/s.

used to displace silicon oil, we observed fingers during fluid flow (Figure 5.6a,b,c and simulation movie clip 1 in the SI of the published article [188]). We note that fingers in Mt. Simon sandstone are more visible in simulation movie clip 1 of the SI of the published article [188] as compared to the Figure 5.6a,b,c. These fingers were mostly governed by the heterogeneity of the Mt. Simon sandstone.

TABLE 5.4: Capillary number (Ca) and viscosity ratio (M) of 2D homogeneous and heterogeneous porous medium.

Porous medium	Injection fluid	U_{avg} (m/s)	η_{eff} (Pa·s)	Ca	M
$\phi : 0.40$	Water	0.048 ± 0.101	0.001	1.65×10^{-3}	20
	0.5% PAA	0.030 ± 0.041	0.61 ± 0.17	6.22×10^{-1}	3.3×10^{-2}
$\phi : 0.50$	Water	0.031 ± 0.054	0.001	1.07×10^{-3}	20
	0.5% PAA	0.019 ± 0.022	0.76 ± 0.17	4.87×10^{-1}	2.63×10^{-2}
$\phi : 0.55$	Water	0.017 ± 0.022	0.001	5.80×10^{-4}	20
	0.5% PAA	0.014 ± 0.008	0.53 ± 0.066	2.47×10^{-1}	3.78×10^{-2}
$\phi : 0.54$	Water	0.033 ± 0.030	0.001	1.15×10^{-3}	20
	0.5% PAA	0.019 ± 0.016	0.64 ± 0.23	4.12×10^{-1}	3.12×10^{-2}

5.3.5 Effect of heterogeneity

To explore whether heterogeneity of the porous medium affects the stability of polymeric fluid flow front and oil recovery, we simulated the two-phase flow of 0.5% PAA-polymeric solution displacing silicon oil and water displacing silicon oil in a homogeneous ($\phi : 0.55$) and heterogeneous ($\phi : 0.40$, 0.50, 0.54) porous media domain as shown in Figure 5.7 at the constant injection rate of 0.01 m/s at inlet and contact angle of 30°. Although the injection rate of water and 0.5% PAA polymer was 0.01 m/s during simulation, the average velocity of the injected fluid in the porous medium was higher and varied depending on the porous medium's heterogeneity (see Table 5.4). Average velocity in the porous medium increased with a decrease in the porosity. The capillary number of PAA fluid injection is two orders of magnitude greater than water injection.

Figure 5.7a to d depicts that water injection at an injection rate of 0.01 m/s shows fingers in the porous medium and the fluid front follows preferential flow paths. The width of the fingers in the homogeneous porous medium is much larger than those in the heterogeneous porous medium. Moreover, the width of the fingers becomes thinner with a decrease in the porosity.

The homogeneous or orderly porous medium (circular staggered), as in Figure 5.7e, shows a stable polymeric fluid flow front at an injection rate of 0.01 m/s. On the contrary, the disorderly or heterogeneous porous medium shows instability in the fluid flow front (Figure 5.7f and g) at the same injection rate. The oil-saturation profiles (Figure 5.7f and g) of heterogeneous porous media show that the fragments of residual oil are present in the porous media.

Figure 5.7d and h show fluid flow front of water and PAA fluid in heterogeneous porous medium with two porosities. The upper portion of a porous medium had a porosity of 57% (PSD: 75 μm - 710 μm) and the bottom portion had a porosity of 50% (PSD: 30 μm - 520 μm) with an overall porosity of 54%. Figure 5.7d shows that the length of finger in the upper portion is much larger than in the bottom portion of the medium. Water prefers to flow through areas having higher porosity as compared to low porosity area. On the contrary, polymeric fluid shows a stable fluid flow front in both areas of a porous medium. The fluid flow front of a high porosity area could reach breakthrough early as compared to the fluid flow front in a low porosity area. These results indicate that the porosity variation of the porous medium influences the fluid flow front and preferential path. The remaining oil saturation at breakthrough in a two-porosity porous medium is comparable with the remaining oil saturation in the porous medium with a porosity of 50% at same injection rate. The spatial location of smaller and larger throats in the porous medium governs the porous medium's fingering. Figure 5.7f,g have small throats in between the larger throats, on the contrary, such small throats in between the larger throats are not available in Figure 5.7h. These results imply that fingering in Figure 5.7f and g (visible more in movie clip 2 of the published article [188]) is due to the presence of smaller throats in between the larger throats. The pressure required to displace fluid through smaller throats is much higher than the larger throats/pores. The injected fluid prefers to move through larger throats first and creates an imbalance at the fluid-fluid interface. This leads to an instability at the fluid-fluid interface and fingers appear as the polymeric injected fluid advances towards the outlet.

In water-wet porous media and at the high injection rate, we observed that the silicon oil detaches itself from the porous medium surface, moves into the pore-space centre, and surrounds itself with a polymeric solution (see simulation movie clip 2 in the supporting information of the published article [188]). These small and larger fragments of silicon oil then move along with the polymeric solution toward the outlet. The path of these small oil fragments depends on the pore size and morphology of the porous medium. Oil fragments prefer to move through pores that have large sizes. We note that the mechanism mentioned above helps to recover residual oil using polymeric solutions even after the early breakthrough of a polymeric solution and viscous fingering at a high injection rate.

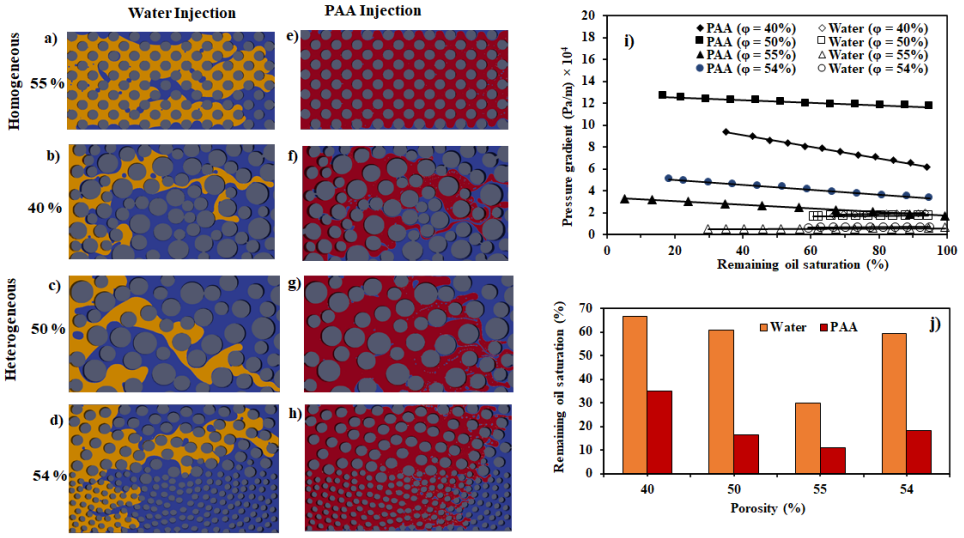

FIGURE 5.7: Effect of heterogeneity on oil recovery during water injection and 0.5% polyacrylamide injection in the 2D porous medium. Figure (a,b,c,d) show distribution of water (in yellow) and silicon oil (in blue) saturation, and (e,f,g,h) distribution of polyacrylamide (PAA) (red) and silicon oil (in blue) saturation at breakthrough over a range of porosity (40%, 50%, 55%, 54%) and heterogeneity. (i) Pressure gradient as a function of oil saturation (pressure gradient is the pressure difference between inlet and outlet). (j) Remaining oil saturation (%) as a function of porosity at the breakthrough. θ is 30°, constant injection rate at inlet is 10^{-2} m/s.

5.3.6 Effect of contact angle and PAA concentration

The effect of viscosity ratio at a constant injection velocity of 10^{-2} m/s on oil displacement was investigated by injecting polymeric fluid, having a PAA concentration of 0, 0.05%, 0.5% in water, in a silicon oil-saturated 2D porous medium of porosity 40% as shown in Figure 5.8a. Similarly, effect of viscosity ratio at a constant injection velocity of 10^{-3} m/s on oil displacement was evaluated over a range of contact angles in a dual-porosity medium as shown in Figure 5.8b. The numerical experiment was carried out by keeping the static contact angle of the fluid interface with the solid surface at 30°, 90°, 120° which represents porous media flow from strong imbibition to strong drainage. The viscosity ratio for a displacement experiment with water, PAA-0.05%, PAA-0.5% were 20, 0.22, 0.032, respectively, over a range of contact angles. Similarly, the capillary number for a displacement was 2.13×10^{-3}, 1.16×10^{-1}, 6×10^{-1} for water, PAA-0.05%, PAA-0.5%, respectively. The Weissenberg number of the fluid flow was higher than 150. Although the injection rate at the inlet was constant (i.e. 10^{-2} m/s), the viscosity ratio decreased, and the capillary number increased with an increase in the

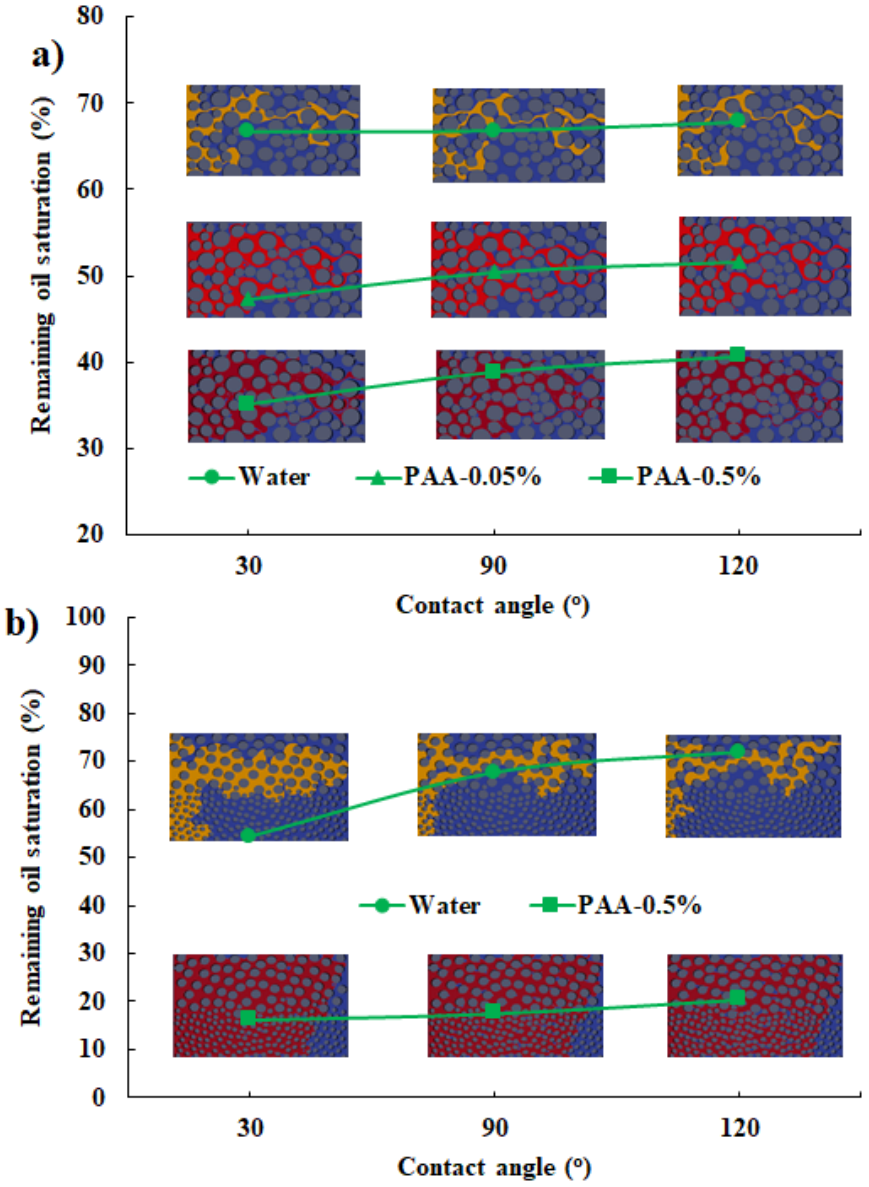

FIGURE 5.8: Effect of contact angle and PAA concentration on oil recovery during water injection and polyacrylamide injection in a 2D porous medium, (a) porosity 40% at an inlet injection rate of 10^{-2} m/s, (b) dual porosity, 54% at inlet injection rate of 10^{-3} m/s. Figure shows distribution of water (in yellow) and silicon oil (in blue) and polyacrylamide (PAA) (red) at breakthrough.

PAA-concentration. These results indicate that the balance of capillary forces and viscous forces in a porous medium varies with variations in the rheology of non-Newtonian fluids.

Figure 5.8a depicts that an increasing concentration of the polymeric solution increases the oil recovery for the $\phi = 40\%$ porous medium. The fluid flow front of water shows

fingers at the capillary number of $2.13\times\ 10^{-3}$, on the contrary, a more stable fluid front (but still with some fingers) can be observed after the addition of PAA-polymeric solution to water. The addition of PAA to water decreased the viscosity ratio and increased the capillary number by 2 to 3 orders of magnitude. Figure 5.8 shows that an increase in the static contact angle decreases the oil recovery over a range of PAA-concentrations. At oil-wet condition ($\theta\ > 120°$), many regions with trapped oil in the polymeric solution were observed in the porous medium. On the contrary, a minimal amount of oil was trapped in the polymeric solution under the water-wet and intermediate-wet conditions ($< 90°$). The average velocity of water in the 2D porous medium was six times (i.e. 6.12×10^{-2} m/s) of the inlet injection velocity (10^{-2} m/s), whereas the average velocity of the polymeric solution ranged from 3.07×10^{-2} to 3.9×10^{-3} m/s over a range of contact angle and PAA concentration. Figure 5.8b shows that the addition of a PAA in water increased the oil recovery over a range of contact angles in the dual-porosity medium at capillary number of 7.5×10^{-2} and injection rate of 10^{-3} m/s. Figure 5.8b shows a stable fluid flow front with PAA fluid over a range of contact angles. On the contrary, water shows fingers in the upper portion of the porous medium over a range of contact angles. Water could not flow through the bottom portion of the porous medium. We note that the flow paths adopted by water and polymeric solutions in the porous medium vary with the contact angle.

The difference between the behaviours of PAA solutions for 40% and dual-porosity media shows the importance of taking into account the heterogeneity at pore scale even for the stable polymeric solutions. Previous work on the continuum scale proposed that the macro-sweep is the primary oil recovery mechanism using the polymeric solution and the micro-sweep plays an insignificant role [200].

5.3.7 Macroscopic representation of the two-phase flow

The macroscopic parameters of fluid flow in a porous medium under steady-state conditions, defined using Darcy's law, depend on the upscalling accuracy over a representative elementary volume [25]. $q = -\frac{K}{\eta}(\nabla P)$. It should be noted that "q" is a volume-averaged fluid flow parameter and does not represent the actual velocity; ∇P is defined over a distance of representative elementary volume (REV), and intrinsic permeability (k) is

a pore-structure property. Darcy's law is extended for multiphase flow involving non-Newtonian fluid as $q = -\frac{k_{rp}K}{\eta_{\text{eff}}}(\nabla P)$, η_{eff} is Darcy's viscosity, k_{rp} is the relative permeability of phase p which is a function of saturation. The amount by which other phases in the pore space restrict the flow is referred to as relative permeability. It is inherently assumed that each phase flows in its own network, and the flow of other phases does not affect it. The impact of the displacement process, displacement history, and viscous stress at fluid-fluid interfaces are ignored during the macroscopic representation of the multiphase flow. This is especially important when fluid flow involves non-Newtonian fluids in porous media. Furthermore, a microscopic fluid configuration in a porous medium is governed by microscopic capillary forces; thus, a steady-state assumption is never achieved [25]. Multiphase flow in porous media is a dynamic process and multi-parameter dependent, which creates a challenge to relating pore-scale flow properties to the macroscopic scale, as it is not evident how to average microscopic flow properties to the Darcy's scale [25, 170]. Note that macroscopic parameters such as relative permeability, pressure gradient, capillary pressure, and saturation are measured at the boundary of the porous medium during core-flood experiments. The complex behaviour of non-Newtonian fluids creates further challenges to upscale pore-scale multiphase properties to Darcy's scale. Thus, in future, we will conduct a two-phase simulation of the inelastic Meter model fluid and the viscoelastic Phan-Thien and Tanner fluid displacing oil to develop a method to upscale pore-scale multiphase properties to Darcy's scale.

5.4 Conclusion

We used a volume-of-fluid-based method to simulate the two-phase flow of non-Newtonian fluid in porous media. To describe the polymeric solution's rheology, we implemented a shear-stress dependent Meter model in the 'interfoam' solver of OpenFOAM. The Meter model-based simulation of Newtonian fluid displacing non-Newtonian fluid in a partially saturated Hele-Shaw cell was compared with a Hele-Shaw experiment of White and Ward [216] for validation. The pattern of the instability of the fluid-fluid interface (i.e. tip-splitting and side branching fingers) observed in the simulation, and the experiments of the White and Ward [216] were similar.

We simulated the displacement of oil by polymeric solution over a range of wettability conditions, heterogeneity, capillary number, and viscosity ratio. The present work

suggests that the heterogeneity of the porous medium governed the fingering during polymeric fluid-oil two phase fluid flow. Increasing the capillary number and viscosity ratio increases the oil recovery over a range of wetting conditions (i.e. strong imbibition to strong drainage). Heterogeneity of the porous medium leads to an unstable fluid flow front (even after use of polymer). This suggests that along with capillary number and viscosity ratio, heterogeneity is the governing factor for controlling viscous and capillary fingering.

Viscoelasticity plays a vital role in the displacement of a polymeric solution. The Weissenberg number (Wi) of more than 140 in the porous medium implies that the micro-sweep of the oil by the polymeric solution depends on the visco-elasticity of the polymeric solution. These results agree with reported experimental observations [56]. In the future, we will study the effect of the wettability of the porous medium and the visco-elasticity of the polymeric solution on the micro-sweep of oil using microfluidic experiments and two-phase simulation using the linear Phan–Thien—Tanner model.

Chapter 6

Nanoparticle transport within non-Newtonian fluid flow in porous media

This chapter is submitted to the '*Physical Review E*'

Authors: **T. Shende,** D. Mangal, J. C. Conrad, V. Niasar, and M. Babaei. Nanoparticle transport within non-Newtonian fluid flow in porous media.

6.1 Introduction

The migration and dispersion of nanoparticles in porous media are of considerable importance in many commercial, industrial, and natural systems [14, 60, 93]. The addition of nanoparticles in the polymer solution improves the liquid's optical, electrical and mechanical properties [164]. Therefore, it has been widely used in various biological and industrial applications. For example, the use of nanoparticles to improve oil recovery has shown promising results for its application in the field [89, 239]. Nanoparticles in polymeric solution improve the wetting properties of pore surfaces [2], modify viscosity, reduce surface tension [146], control mobility, and has the potential to act as a catalyst [2]. Furthermore, pore accessibility is an essential factor for nanoparticle transport in heterogeneous porous media, mainly in applications where nanoparticles are used as catalysts or property modifiers, e.g., soil remediation. However, the fate and transport of nanoparticles within polymeric solutions at the pore scale are still not fully understood due to the Brownian motion of nanoparticles and the non-Newtonian rheology of polymeric fluids.

Understanding the nanoparticle transport in porous materials is challenging due to multiple reasons. (a) The complex geometry of porous media, *viz.* voids accessibility, spatial structure, and connectivity, governs nanoparticles' mobility in porous media [218]. (b) Sizes of particles and pores affect the nanoparticles' dispersion [93, 186, 218]. (c) Confinement in disordered porous media results in a non-Gaussian distribution of nanoparticle displacements [14]. (d) Spatial and temporal variations in the fluid flow path regulate the longitudinal and transverse displacement of nanoparticles. (e) The polymeric fluid's non-Newtonian shear-dependent rheology influences the migration and dispersion of nanoparticles in porous media [61, 93].

Advection and diffusion control the dispersion of nanoparticles in heterogeneous porous media. Few studies in the literature have evaluated the dispersion of nanoparticles in the longitudinal and transverse directions in a porous medium by tracking the movement of nanoparticles of non-Newtonian fluids. Scholz *et al.* observed a non-linear increase in the dispersion coefficient of nanoparticles (size, 3 μm) mixed in the polyacrylamide solution flowing in a square periodic array with a channel width of 500 μm using particle tracking velocimetry [186]. They discovered that as the Weissenberg number increases, the dispersion coefficient increases nonlinearly. Babayekhorasani *et al.* [14] demonstrated that

the long-time dispersion of nanoparticles in a disordered porous medium is independent of polymer rheology. They suggested that fluid rheology-dependent velocity fluctuation could be suppressed by random mixing in a heterogeneous porous medium compared to an ordered porous medium. In another work, Babayekhorasani *et al.* [15] reported that an increase in the confinement of porous medium decreases the diffusive mobility of nanoparticles in both Newtonian and non-Newtonian fluids due to hydrodynamic interactions. In addition, they observed that the diffusive mobility of nanoparticles in polymeric solutions is also controlled by adsorption-desorption-based depletion interaction. The pore-scale trajectories of nanoparticle motion tracked by Jacob *et al.* [93] showed that the elastic turbulence-based velocity fluctuations in hydrolysed polyacrylamide are higher in ordered porous media than they are in disordered porous media. Using microfluidic experiments, Maitri *et al.* [126] found that particle focusing depends on the Weissenberg number in the ordered porous medium; however, nanoparticles could not follow the focusing of nanoparticles in a disordered porous medium. Thus, they suggested that a simplified structure may not always give a realistic overview of mass transport phenomena in a complex porous medium [126].

6.1.1 This study

Tracking the motion of individual particles at the pore-scale helps upscale the microscopic mass transport mechanisms to the macroscopic transport properties. This helps explain the pore-scale mass transport mechanism and provides representative macroscopic transport properties in porous media. Although particle tracking in Newtonian fluids and 2D porous media has been extensively studied [141, 160, 171, 218], there are limited studies on nanoparticle transport in non-Newtonian fluids and a 3D porous medium.

Previous research on nanoparticle tracking was primarily carried out at a significantly small domain in 2D due to instrumental limitations [14, 93, 115, 186]. An exception to this is the work of [15]. Furthermore, the porosity considered in these studies was considerably larger than the natural porous medium. The porous medium's heterogeneity strongly affects the nanoparticle transport of non-Newtonian fluids. Therefore, we

simulated nanoparticle transport of a non-Newtonian fluid flowing through a converging-diverging microchannel in 3D, a homogeneous ordered 2D porous medium, and Mt. Simon sandstone in 3D over a range of injection rates. The objectives of the present work include:

- developing an Euler-Lagrangian framework to simulate nanoparticle transport within non-Newtonian fluid and 3D porous media incorporating particle-fluid, particle-particle, particle-wall interactions, and Brownian motion;
- evaluating pore-accessibility of nanoparticles in a heterogeneous domain;
- determining dispersion coefficient along transverse and longitudinal direction over a range of fluid injection rates and porous media geometries.

6.2 Governing equations

To investigate nanoparticle transport in a polymeric non-Newtonian fluid, we use the Euler-Lagrangian approach. In this approach, nanoparticles are treated as suspended in the solution. We solve the governing equations of the inelastic Meter model fluid. The nanoparticle motions are predicted based on the previously calculated flow field and Newton's second law at each time step. We use the OpenFOAM C++ library to perform Euler-Lagrangian based particle-fluid simulations.

6.2.1 Eulerian frame

We describe the single-phase, laminar flow of non-Newtonian fluids using continuity (Eq. 6.1) and momentum (Eq. 6.2) equations,

$$\nabla \cdot \mathbf{u}_\mathrm{f} = 0 \tag{6.1}$$

$$\rho_\mathrm{f} \left(\frac{\partial \mathbf{u}_\mathrm{f}}{\partial t} + \mathbf{u}_\mathrm{f} \cdot \nabla \mathbf{u}_\mathrm{f} \right) = -\nabla P + \nabla \cdot \boldsymbol{\tau} - \mathbf{S}_\mathrm{p} \tag{6.2}$$

where ρ_f [kg/m^3] is the density of fluid, $\mathbf{u}_f$ [m/s] is the velocity vector of fluid phase, P [Pa] is the pressure, t [s] is the time, $\boldsymbol{\tau}$ [Pa] is the fluid stress tensor and $\mathbf{S}_p$ is the additional source term that considers the effect of particle forces on the fluid motion at each time step. The constitutive equation of the inelastic stress-dependent Meter model (see section 2.2 and Eq. 2.2 of Chapter 2) is defined as, [134, 189, 190]

$$\boldsymbol{\tau} = 2\,\eta(\tau)\,\mathbf{D} = \eta(\tau)\,(\nabla \mathbf{u}_f + (\nabla \mathbf{u}_f)^T) \tag{6.3}$$

We used the Meter model (Eq. 6.4 and Eq. 2.2 of Chapter 2) in the present work that describe the S-shaped rheology of most of the shear thinning and shear thickening fluids. [134, 189, 190],

$$\eta = \eta_\infty + \frac{\eta_0 - \eta_\infty}{1 + \left(\dfrac{\tau}{\tau_m}\right)^S}, \tag{6.4}$$

where η [Pa·s] is the shear viscosity at a given shear stress, η_0 [Pa·s] is the zero-shear viscosity, η_∞ [Pa·s] is an infinite shear viscosity, τ_m [Pa] is the critical shear stress parameter, and S is an exponent representing slope.

6.2.2 Lagrangian frame

Particles interact with each other, with the wall, and with the surrounding fluid while migrating in the porous medium. The Discrete Element Model (DEM) can be used to solve the governing equations of particle motion [73, 85, 97] in porous media. Newton's second law governs the motion of the particle in the Lagrangian framework (Eq. 6.5) [44, 73, 85]

$$m_p \frac{d\mathbf{u}_p}{dt} = \mathbf{F} = (\mathbf{F}_C + \mathbf{F}_F) \tag{6.5}$$

where m_p [kg] is the particle mass, $\mathbf{u}_p$ [m/s] is the particle velocity, $\mathbf{F}$ is the total forces acting on particles, $\mathbf{F}_C$ is the contact forces acting on the particles due to interparticle interaction or particle-wall interactions and $\mathbf{F}_F$ is the particle-fluid interaction forces

acting on particles. Readers are referred to [73] for details on the implementation of DEM in OpenFOAM.

6.2.2.1 Particle-fluid interaction

Several particle-fluid interaction forces can act on the particle during particle migration in the fluid [128]. In the present work, we defined particle-fluid forces as follow,

$$\mathbf{F}_{\mathrm{F}} = \mathbf{F}_{\mathrm{D}} + \mathbf{F}_{\mathrm{G,B}} + \mathbf{F}_{\mathrm{P}} + \mathbf{F}_{\mathrm{B}} \tag{6.6}$$

where $\mathbf{F}_{\mathrm{D}}$, $\mathbf{F}_{\mathrm{G,B}}$, $\mathbf{F}_{\mathrm{P}}$, $\mathbf{F}_{\mathrm{B}}$ are drag force, combined gravity and buoyancy force, pressure force, and Brownian motion forces acting on the particle, respectively. The drag force ($\mathbf{F}_{\mathrm{D}}$) acting on the particle is given by

$$\mathbf{F}_{\mathrm{D}} = \frac{3\, C_{\mathrm{d}}\, \mathrm{Re}_{\mathrm{p}}\, m_{\mathrm{p}}\, \eta\, (\mathbf{u}_{\mathrm{f}} - \mathbf{u}_{\mathrm{p}})}{4\, \rho_{\mathrm{p}}\, d_{\mathrm{p}}^2} \tag{6.7}$$

where C_{d} is the drag coefficient, Re_{p} is the particle Reynolds number, ρ_{p} [kg/m^3] is the density of the particle, d_{p} [m] is the diameter of the particle. The Reynolds number of particles in the flow is below 10 in the present work, thus, $C_{\mathrm{d}}\, \mathrm{Re}_{\mathrm{p}} = 24 \left[1 + \frac{\mathrm{Re}_{\mathrm{p}}^{\frac{2}{3}}}{6}\right]$ [73]. The combined buoyancy and gravity forces ($\mathbf{F}_{\mathrm{G,B}}$) due to gravity g [m/s^2] and the force act on the particle due to local pressure gradient ($\mathbf{F}_{\mathrm{P}}$) are estimated using Eq. 6.8 and Eq. 6.9, respectively [73],

$$\mathbf{F}_{\mathrm{G,B}} = m_{\mathrm{p}}\, g \left(1 - \frac{\rho_{\mathrm{f}}}{\rho_{\mathrm{p}}}\right) \tag{6.8}$$

$$\mathbf{F}_{\mathrm{P}} = \frac{\pi\, d_{\mathrm{p}}^3}{6} \Delta P \tag{6.9}$$

Due to their nanoscopic size, nanoparticles are expected to exhibit Brownian motion. This strongly affects the dispersion of nanoparticles in a porous medium. Thus, we implemented the Brownian force ($\mathbf{F}_{\mathrm{B}}$) as a Gaussian white noise random process as given in Eq 6.10 and in line with the work of Lee and Ahmadi [113],

$$\mathbf{F}_{\mathrm{B}} = \xi_{\mathrm{i}} \left(\frac{\pi}{\Delta t} \delta_{\mathrm{ij}} \frac{216\, \nu\, k_{\mathrm{B}}\, T}{\pi^2\, d_{\mathrm{p}}^5\, \rho_{\mathrm{f}}\, C_{\mathrm{c}} \left(\frac{\rho_{\mathrm{p}}}{\rho_{\mathrm{f}}} \right)^2} \right)^{\frac{1}{2}}, \tag{6.10}$$

where ξ_{i} is the Gaussian random number with zero mean and unit variance, Δt is the time step, δ_{ij} is the Kronecker delta function, k_{B} [J/K] is the Boltzmann constant, T [K] is the temperature, ν [m^2/s] is the kinematic viscosity, and C_{c} is the Stokes-Cunningham slip correction, which is a function of the molecular mean free path (λ_{m}), given as

$$C_{\mathrm{c}} = 1 + \frac{2\lambda_{\mathrm{m}}}{d_{\mathrm{p}}} \left(1.257 + 0.4e^{\frac{1.1 d_{\mathrm{p}}}{2\lambda_{\mathrm{m}}}} \right) \tag{6.11}$$

Note that the time-step (Δt) is assumed to be larger than a successive collision of the particles [35, 86]. However, the time step associated with a significant particle displacement change due to interaction and external force is substantially smaller. For more details, readers are referred to [35, 86].

6.2.2.2 Particle contact forces

We used a simple spring-slider-dashpot model implemented in OpenFOAM to determine contact forces due to particle collisions. The dashpot represents viscous dissipation, whereas the spring represents elastic deformation. This model uses the Hertzian contact theory [44]. Readers are referred to [44, 46, 73, 132, 149] for a detailed description of particle contact forces. In summary, the force $\mathbf{F}_{\mathrm{p,ij}}$ acting during collision between two particles i and j are divided into normal ($\mathbf{F}_{\mathrm{n,ij}}$) and tangential ($\mathbf{F}_{\mathrm{t,ij}}$) components and are given as

$$\mathbf{F}_{\mathrm{p,ij}} = \mathbf{F}_{\mathrm{n,ij}} + \mathbf{F}_{\mathrm{t,ij}} = \left(k_{\mathrm{n}} \delta_{\mathrm{n}}^{b} + \gamma_{\mathrm{n}} \nu_{\mathrm{n}} \right) + \left(k_{\mathrm{t}} \delta_{\mathrm{t}} + \gamma_{\mathrm{t}} \nu_{\mathrm{t}} \right), \tag{6.12}$$

where k_{n} and k_{t} are stiffness coefficients in the normal and tangential directions of particles, δ_{n} and δ_{t} are normal and tangential displacements due to particle-particle interactions, $b = 1.5$ is a collision constant, γ_{n} and γ_{t} are normal and tangential viscous damping constants, and ν_{n} and ν_{t} are the relative velocities between particles in normal

and tangential directions. Similarly, the force $\mathbf{F}_{\mathrm{w,i}}$ acting during a collision between particle i and wall w are decomposed into normal $\mathbf{F}_{\mathrm{n,wi}}$ and tangential $\mathbf{F}_{\mathrm{t,wi}}$ parts. These forces are calculated as

$$\mathbf{F}_{\mathrm{w,i}} = \mathbf{F}_{\mathrm{n,wi}} + \mathbf{F}_{\mathrm{t,wi}} = \left(k_{\mathrm{nw}}\delta_{\mathrm{nw}}^{b} + \gamma_{\mathrm{nw}}\nu_{\mathrm{nw}}\right) + \left(k_{\mathrm{tw}}\delta_{\mathrm{tw}} + \gamma_{\mathrm{tw}}\nu_{\mathrm{tw}}\right) \tag{6.13}$$

where k_{nw} and k_{tw} are stiffness coefficients in the normal and tangential direction of particles-wall interaction, δ_{nw} and δ_{tw} are normal and tangential displacements due to particle-wall interactions, γ_{nw} and γ_{tw} are normal and tangential viscous damping constants for particle-wall interactions, and ν_{nw} and ν_{tw} are the relative velocities between particle and wall in normal and tangential directions. The total force acting on the particle due to particle-particle and particle-wall interaction will be as

$$\mathbf{F}_{\mathrm{C}} = \left(\mathbf{F}_{\mathrm{p,ij}} + \mathbf{F}_{\mathrm{w,i}}\right) \tag{6.14}$$

6.2.3 Numerical scheme and the solver

The DPMFoam solver is a discrete particle modelling solver of OpenFOAM, designed to couple Eulerian and Lagrangian frames. A detailed description of the DPMFoam is presented in [73]. We modified the DPMFoam solver of OpenFOAM to implement the Meter model. For simulating an inelastic Meter model fluid, we used a backward scheme to discretize the time, a Gauss linear upwind to discretize the divergence, a Gauss linear scheme to discretize the gradient, and a Gauss-linear corrected scheme to discretize the Laplacian term. The PIMPLE algorithm, as described in section 4.4.1 of chapter 4, was used for pressure-velocity coupling [76, 142]. We used the Euler scheme to integrate the velocity during a Lagrangian particle transport. The computationally expensive simulations were run in parallel at the University of Manchester's high-performance computing cluster facility.

6.2.4 Numerical domain and boundary conditions

We simulated nanoparticles transport (d_{p} of 400 nm) in a 2D homogeneous porous medium having porosity of 70% as described in section 3.4.4 of chapter 3, in a 3D

converging-diverging microchannel having 20 repetitive elements, and in a 3D Mt. Simon sandstone of [110] having a porosity of 24%, as shown in Figure 6.1 and described in section 4.4.3 of chapter 4. The pore-size of a microchannel, homogeneous medium and sandstone ranged from 32-108 μm, 150 μm, 2-100 μm, respectively. The volume fraction of the nanoparticles was lower than 0.005 during all simulations, which implies that the system is dilute and particle interaction was limited. Therefore, the jamming of the particles was unlikely. The degree of anisotropy of sandstone is 0.255, whereas microchannel and homogeneous 2D porous medium are isotropic, indicating sandstone is highly heterogeneous. No-slip velocity and zero fixed flux pressure boundary conditions were applied at front, back, top, bottom, and solid surfaces of a 3D domain. Zero flux corrected velocity and total pressure boundary conditions were applied to the right boundary (outlet) of the porous medium domain. The constant injection velocity boundary condition was applied at the inlet (left boundary) of the porous medium. We injected 500 (unless otherwise noted) polystyrene nanoparticles per second for one second at the inlet (left boundary) during numerical experiments. The polystyrene nanoparticle had a density of 1050 kg/m^3, a Young modulus of 1.25×10^9 N/m^2, and a Poisson's ratio of 0.33. For Brownian motion force calculation, we kept the polymeric solution at 300 K and the mean free path of the particle in the polymeric solution as 1×10^{-9} m. We investigated the transport of nanoparticles in a 0.125% polyacrylamide (PAA) fluid having a density of 1300 kg/m^3. The Meter model parameters of PAA are $\eta_0 = 2.1$ Pa·s, $\eta_\infty = 0.001$ Pa·s, $\tau_\mathrm{m} = 0.3$ Pa, and $S = 1.8$. We simulated the flow of a polymeric non-Newtonian fluid and a Newtonian fluid ($\eta = 2.1$ Pa·s) over a range of injection rates (10^{-5} - 10^{-2} m/s). The Courant number was maintained below 0.9 during all numerical simulations. The Courant number $C = \frac{u\,\Delta t}{\Delta x}$, where Δt is the time step and Δx is a length interval. A fine mesh of more than 3 million mesh points were generated in the pore-space of porous medium using snappyHexMesh module of OpenFOAM.

6.3 Nanoparticles trajectories analysis

The mean square displacement (MSD) of nanoparticles as a function of a lag time (t') in a porous medium was determined by using Eq 6.15 [218],

$$\mathrm{MSD}(t') = \langle \mathbf{r}(t')^2 \rangle = \langle (\mathbf{r}(t+t') - \mathbf{r}(t'))^2 \rangle \tag{6.15}$$

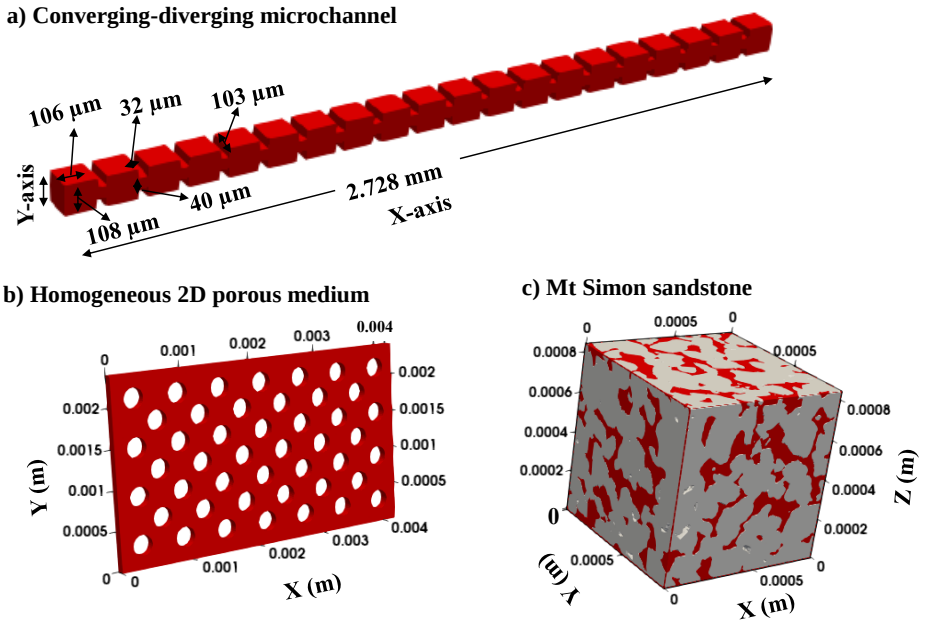

FIGURE 6.1: Geometry of (a) symmetric converging-diverging micro-channel with 20 repetitive elements (3D) (described in section 4.4.3 of chapter 4)), (b) homogeneous ordered porous medium (2D), and (c) Mt. Simon sandstone (3D) (as described in section 4.4.3 of chapter 4)). Red indicates pore spaces. Fluid flows from left to right.

where $\mathbf{r}(t)$ is the position of nanoparticles in a porous medium at time t, $\langle\,\rangle$ is an ensemble or time-averaged value. The MSD was fitted to $\langle r(t')^2\rangle = 2\mathrm{D}_{\mathrm{L,T}}\,t'$ to determine dispersion coefficient [195]. In addition, using particles velocity data, we calculated the longitudinal ($\mathrm{D_L}$, along flow direction) or the transverse ($\mathrm{D_T}$, normal to flow direction) dispersion coefficients using Eq. 6.16 [93, 125].

$$\mathrm{D}_{\mathrm{L,T}} = \frac{1}{2}\frac{d\sigma^2_{\mathrm{L,T}}}{dt^2} = \int C_{\mathrm{L,T}}(t')\,dt' \tag{6.16}$$

where $\sigma^2_{\mathrm{L,T}}(t)$ is the second moment of the particle displacement in a longitudinal or a transverse direction and $C_{\mathrm{L,T}}(t')$ is the autocorelation of velocity $v_{\mathrm{x,y}}(t')$, given by $C_{\mathrm{L,T}}(t') = \langle (v_{\mathrm{x,y}}(t+t') - \langle v_{\mathrm{x,y}}\rangle)\,(v_{\mathrm{x,y}}(t) - \langle v_{\mathrm{x,y}}\rangle)\rangle$. $v_{\mathrm{x,y}}(t)$ and $v_{\mathrm{x,y}}(t+t')$ are the longitudinal or transverse velocity of a particle at the start of trajectory and a lag time t', respectively; and $\langle v_{\mathrm{x,y}}\rangle$ is the average velocity of particles over all time and trajectories [93, 125]. The Stokes-Einstein equation was used to determine the molecular diffusion coefficient of spherical nanoparticles in a non-Newtonian fluid [195],

$$\mathrm{D_{SE}} = \frac{k_\mathrm{B}\, T}{3\pi\, \eta_0\, d_\mathrm{p}} \tag{6.17}$$

where $\mathrm{D_{SE}}$ [$\mathrm{m^2/s}$] is the Stokes-Einstein based molecular diffusion coefficient. The dispersion coefficient was normalised by a Stokes-Einstein diffusion coefficient ($\mathrm{D_{SE}}$). We define the relative variation in the rate of advection and diffusion using Péclet number (Pe), the relative variation of inertial forces and viscous forces using Reynolds number (Re), following,

$$\mathrm{Pe} = \frac{U_\mathrm{avg}\, \delta_\mathrm{L}}{\mathrm{D_{SE}}} \tag{6.18}$$

$$\mathrm{Re} = \frac{\rho_\mathrm{f}\, U_\mathrm{avg}\, \delta_\mathrm{L}}{\eta_\mathrm{eff}} \tag{6.19}$$

Here, U_avg [m/s] is the average pore-scale velocity of the fluid, η_eff [Pa.s] is the effective viscosity of the fluid flow and δ_L [m] is the characteristic length scale. The velocity, viscosity, shear rate, and pore size vary spatially in the porous medium; thus, to estimate the representative dimensionless number of the fluid flow in a porous medium, we use volume-averaged values of velocity, viscosity and shear rate. We integrate the pore-scale velocity, shear rate, and viscosity over a pore-space filled with polymeric non-Newtonian fluids to determine the volume-averaged velocity (U_avg), volume-averaged shear rate ($\dot{\gamma}_\mathrm{avg}$) and volume-averaged effective viscosity (η_eff) [189].

6.4 Results and discussion

6.4.1 Homogeneous porous medium

Tracking nanoparticle transport in 3D provides a realistic insight into its transport compared to 2D. Therefore, we simulated the flow of nanoparticles in Newtonian and non-Newtonian fluids and in 3D converging-diverging microchannels over a range of Pe (10^6 - 10^8). Fig 6.2 shows nanoparticle transport behaviour in Newtonian and non-Newtonian fluids at a Pe of 2.48×10^6. Although fluid flow velocity is low (i.e. 10^{-4} m/s), nanoparticles show channelised motion along a flow direction with time in

both Newtonian and non-Newtonian fluids. We observed that the spatial distribution of nanoparticles after 2 seconds is relatively concentrated or crowded compared to the spatial distribution at 5 seconds and 10 seconds in both Newtonian and non-Newtonian fluids. This is expected as there is axial dispersion even in straight channels. This also suggests that converging-diverging geometry influenced the dispersion of nanoparticles.

The velocity of the nanoparticles depended on the spatial location of the particles. Particles at the centre had a high velocity, whereas particles near the boundaries had a much lower velocity. Fig 6.2c,d,e,f,g shows a spatial profile of the velocity, shear stress, and viscosity of the non-Newtonian fluid and Newtonian fluid at the centre of the micro-channel. Fig 6.2e and f depict that shear stress at the corner and centre of the channel is minimum in both Newtonian and non-Newtonian fluids. This spatial distribution of shear stress imparts resistance to the transport of nanoparticles in those regions, which slows down the velocity of nanoparticles trapped at the corner. Fig 6.2e and f shows that shear stress at the centre of the micro-channel is minimum, and the gradient of shear stress initially increases and then decreases spatially from the centre towards the outer boundaries in both converging and diverging regions of the micro-channel. This spatial distribution of shear stress in fluid flow governs the location of nanoparticles during their transport. Fig 6.2h and i shows that most nanoparticles avoided the regions with lower shear stress, i.e., the centre of the micro-channel. Therefore, most nanoparticles were mostly channelised towards an equilibrium position, i.e. in the region with maximum shear stress. This result agrees with the channelisation of nanoparticles in a non-Newtonian fluid reported by [50, 179, 213, 224]. Fig 6.2e and f show distinct differences in shear stress distributions between the non-Newtonian fluid and the Newtonian fluid due to spatial variation of viscosity in a non-Newtonian fluid (see Fig 6.2g). The slight spatiotemporal variation in nanoparticle distribution in Newtonian and non-Newtonian fluids at the same Pe is due to these viscosity variations.

Fig 6.3 shows the spatial distribution of nanoparticles at dimensionless time 2, 4 and 7 in Newtonian and non-Newtonian fluids in the 2D homogeneous porous medium at Pe of 1.13×10^6. These results indicate that nanoparticles follow a similar type of channelised flow path and spatiotemporal distribution of nanoparticles in both Newtonian and non-Newtonian fluids. The slight variation of the resident concentration of nanoparticles (Fig 6.3i) in both Newtonian and non-Newtonian fluids is due to the shear-thinning property of a non-Newtonian fluid. Fig 6.3j shows an overlap of the mean square displacement

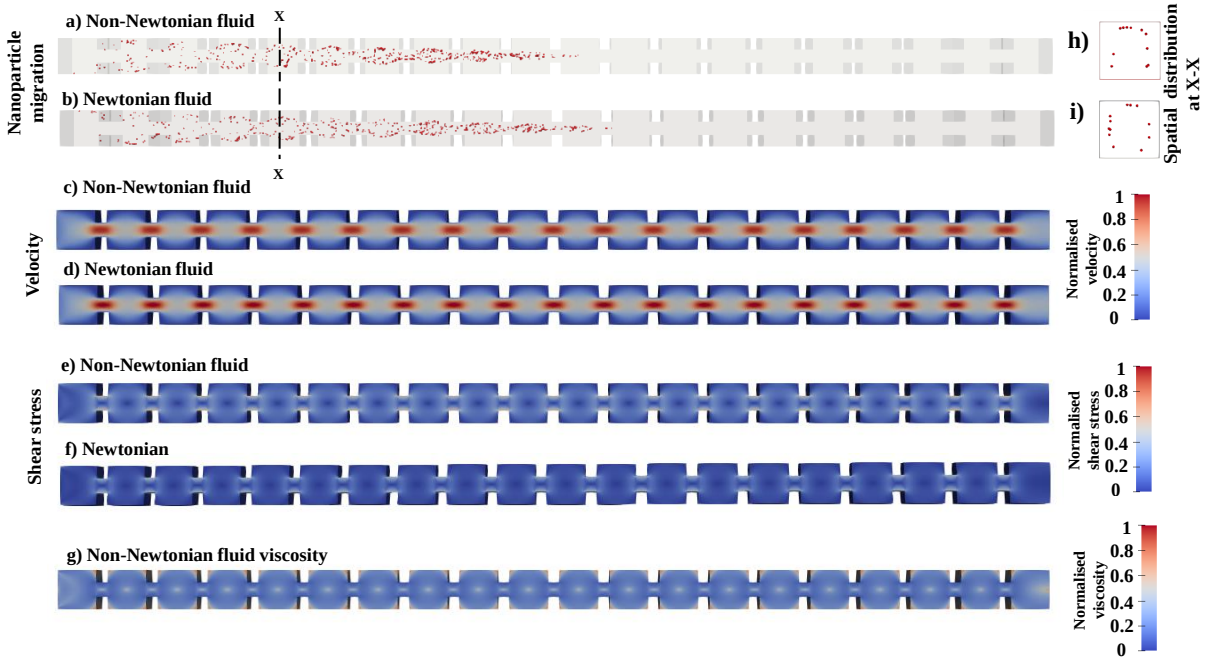

FIGURE 6.2: Spatial distribution of nanoparticles at dimensionless time 12 in converging-diverging micro-channel a) with non-Newtonian fluid b) Newtonian fluid at Pe = 2.48×10^6. Spatial distribution of (c,d) velocity, (e,f) shear stress, and (g) viscosity at the middle section of the micro-channel. The spatial distribution of nanoparticles at section x-x h) non-Newtonian fluid i) Newtonian fluid.

(MSD) profile along the longitudinal and transverse directions for both Newtonian and non-Newtonian fluids. These results imply that the transport of nanoparticles in an inelastic non-Newtonian fluid follows a similar type of nanoparticle transport behaviour as in a Newtonian fluid in a homogeneous porous medium.

We note that we were not able to fit the analytical solution of the advection-dispersion equation (Fickian transport) in Fig 6.3i to estimate the dispersion coefficient. This result indicates that nanoparticles follow non-Fickian transport due to pore-scale confinement-dependent non-linearity in Newtonian and non-Newtonian fluids. Thus, the MSD method, as described in Section 3, was used to determine the dispersion coefficient.

6.4.2 Mt. Simon sandstone

Fig 6.4 depicts the spatial distribution of nanoparticles at dimensionless time of 6 and 45 in Newtonian and non-Newtonian fluids at Pe of 1.26×10^6 along with spatial distribution of shear stress gradient in the Mt. Simon sandstone. At Pe of 1.26×10^6, the spatial

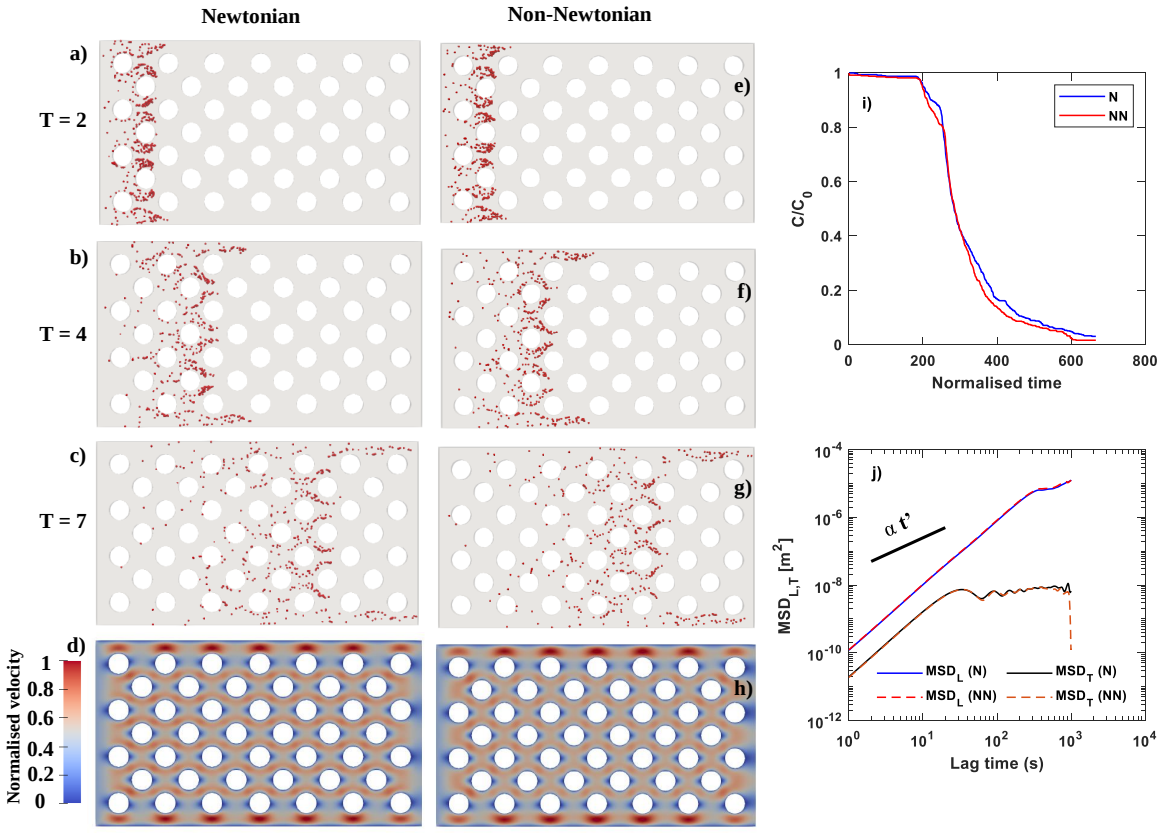

FIGURE 6.3: Spatial distribution of nanoparticles at dimensionless time (T) (a,e) 2 (b,f) 4 (c,g) 7, and (d,h) normalised velocity of fluid in 2D homogeneous porous medium in Newtonian (N) and non-Newtonian (NN) fluids. i) Normalised resident concentration of nanoparticles as a function of dimensionless time. (j) Mean square displacement (MSD) along longitudinal direction and transverse direction in homogeneous 2D porous medium in Newtonian (N) and non-Newtonian (NN) fluids (Pe = 1.13×10^6).

distribution of nanoparticles is scattered (Fig 6.4a, b); on the contrary, due to the channelled migration of nanoparticles, this scattered distribution was not observed at higher Pe (i.e. 1.26×10^7 and 1.26×10^8). Furthermore, there are drastic spatial variations of shear stress gradient values in sandstone for Newtonian and non-Newtonian fluids (Fig 6.4c,f). Fig 6.4g shows that shear stress distributions in Newtonian and non-Newtonian fluid at same Pe are drastically different. Similarly, *gradient* of shear stress in Newtonian and non-Newtonian also show significant difference in its distribution. The shear stress gradient governs the spatiotemporal distribution of nanoparticles in Newtonian and non-Newtonian fluids. Moreover, we observed that 11%, 13%, 18%, 22% , 25% and 27% of pore-space for non-Newtonian fluid and 11%, 13.2%, 17.5%, 20% , 22% and 23% of pore-space for Newtonian fluid was immobile/stagnant (fluid velocity in immobile regions was 3 orders of magnitude lower than the average velocity) at Pe of 6.28×10^5,

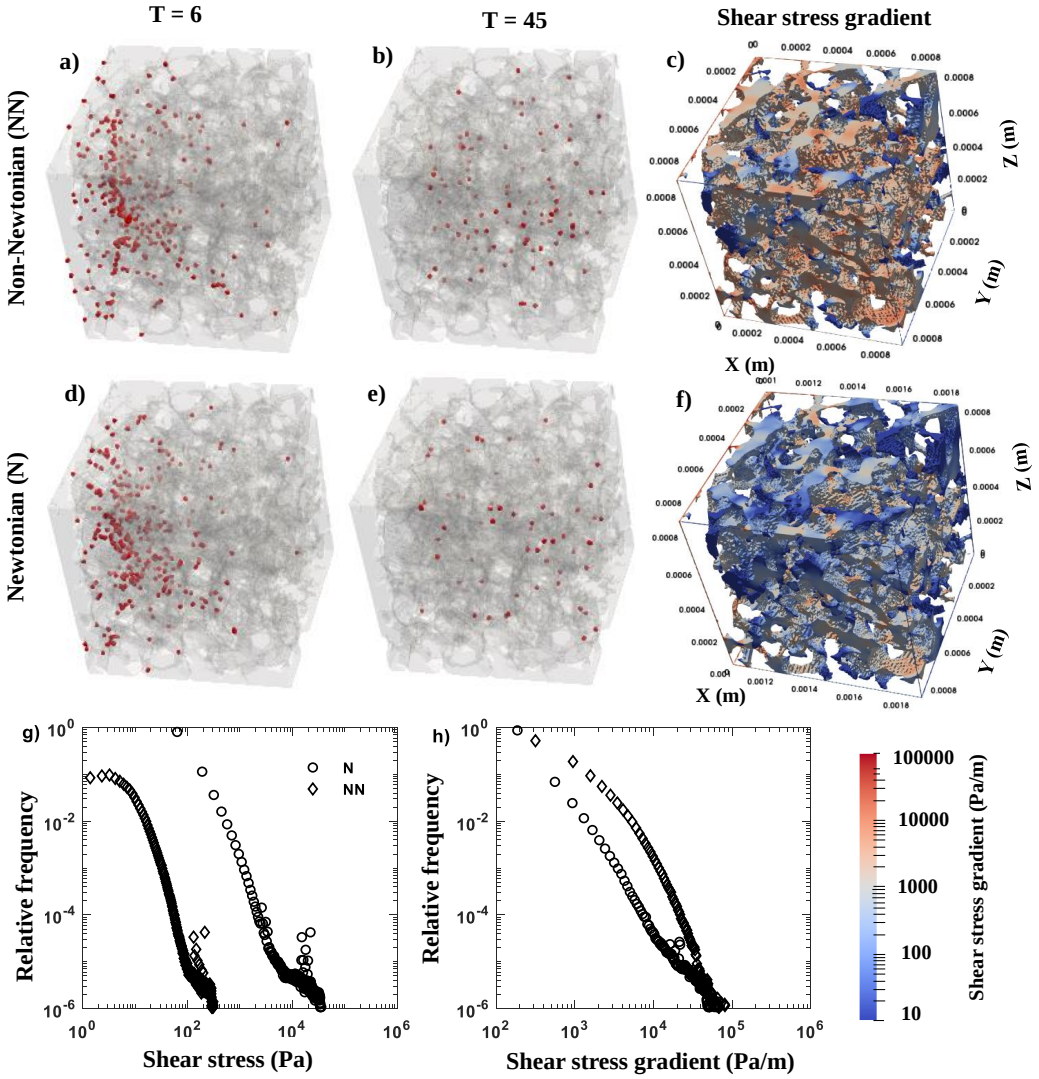

FIGURE 6.4: Spatial distribution of nanoparticles in Mt. Simon sandstone at normalised time (T) 6 and 45 and spatial distribution of shear stress gradient at Péclet number 1.26×10^6 in Newtonian and non-Newtonian fluids. (g,h) Histogram of distribution of shear stress and shear stress gradient in Newtonian (N) and non-Newtonian (NN) fluids. Size of nanoparticles in the images were enlarged for visibility.

1.26×10^6, 6.28×10^6, 2.51×10^7, 6.28×10^7 and 1.26×10^8 respectively. This results indicate that channelised fluid transport at Pe higher than 10^7 in the heterogeneous porous medium leads to a more stagnant region in non-Newtonian fluid than the Newtonian fluid. The migration of nanoparticles in the stagnant zone, due to lower shear stress in those regions, are not observed. Although the pore size (i.e > 3 μm) was much larger than the nanoparticle size (i.e. 0.4 μm), pore accessibility was mostly governed by gradient of shear stress and pore geometry.

We evaluated nanoparticle dispersion using the mean-square displacement and velocity autocorrelation function approach [11, 14, 15, 93, 186]. Fig 6.5 shows that mean square

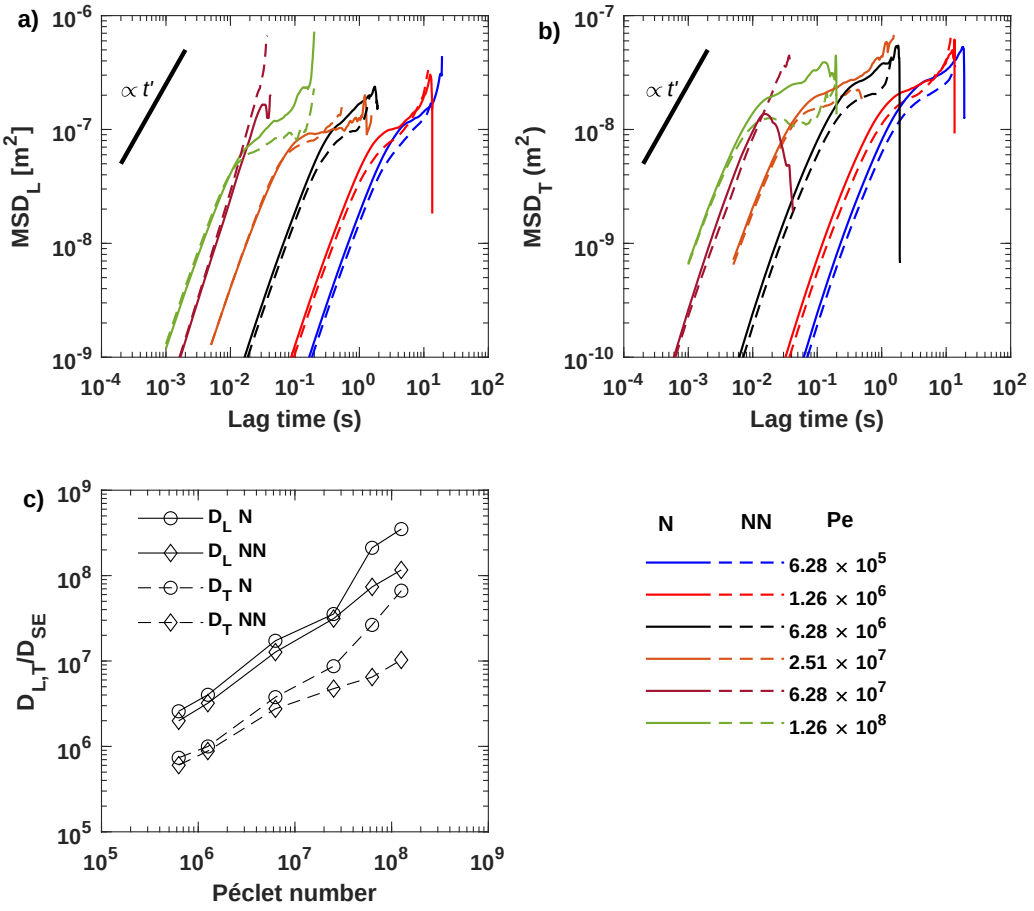

FIGURE 6.5: Mean square displacement (MSD) along (a) longitudinal direction, (b) transverse direction, and (c) normalised longitudinal and transverse dispersion coefficient over a range of Péclet number in Newtonian (N) and non-Newtonian (NN) fluids and Mt. Simon sandstone.

displacement (MSD) is a non-linear function of lag-time along longitudinal and transverse directions in the Mt. Simon sandstone over a range of Péclet number. Fig 6.5 indicates that the pattern of long-time MSD curves at lower Pe of 10^5 deviates from the MSD curves of 10^7 and 10^8. This deviation indicates that nanoparticle migration at lower Pe is different from migration at high Pe. The shear stress in the porous medium at low Pe will be much lower than at high Pe. Furthermore, high viscosity at fluid's low-velocity creates more resistance for the fluid as well as for nanoparticles to migrate in the porous medium. The geometry and shear stress gradient-dependent resistance govern the nanoparticle flow path in the porous medium, which in turn, govern the longitudinal and transverse dispersion.

Fig 6.5c shows that D_L and D_T of Newtonian and non-Newtonian fluids increases linearly with increase in Pe. However, D_L and D_T of Newtonian fluid is consistently higher than

non-Newtonian fluid. Two-sample statistical T-test had a p-value of 0.23-0.62 for Pe less than 10^7, indicating an insignificant difference in dispersion coefficient for Newtonian and non-Newtonian fluid at Pe $< 10^7$. The p-value of 0.007-0.04 at Pe higher than 10^7 indicate a significant difference in dispersion coefficient in a Newtonian and non-Newtonian fluid. The long-time MSD at Pe higher than 10^7 in Fig 6.5a,b shows the significant difference in the MSD curve for Newtonian and non-Newtonian fluid. This considerable difference arises due to spatiotemporal difference in shear stress distribution in Newtonian and non-Newtonian fluids (see Fig 6.4).

Fig 6.6a,b,c show the distribution of the velocities of nanoparticles in longitudinal and transverse directions, normalised by the average velocity of all nanoparticles in the considered domains. The distribution of velocity along the longitudinal direction is skewed non-Gaussian with an exponential stretching in the positive direction. Although velocity distributions of nanoparticles along a transverse Y and Z direction do not overlap, both are symmetric about zero velocity and non-Gaussian. Nanoparticles along the longitudinal direction are channelised along the flow direction, and thus, it has a skewed profile along the positive direction. Whereas, in transverse directions, distributions are non-Gaussian and symmetric. These results are similar to those of [14, 15, 93].

Fig 6.6d and e show the normalised autocorrelation function (VACF) over a range of Pe in a non-Newtonian fluid. We normalised lag time using $\frac{t\,V_{\text{avg}}}{\delta_{\text{L}}}$. The longitudinal velocity auto-correlation function indicates a positive correlation over the range of Pe, whereas the transverse velocity auto-correlation function indicates no significant auto-correlation. Since fluid injection velocity is relatively high, advection plays the dominant role in nanoparticle migration, and most nanoparticles move along the flow directions. This leads to a positive correlation along longitudinal directions.

We determined the dispersion coefficient along the longitudinal and transverse directions by fitting a linear-part of the MSD curve to $2\text{D}_{\text{L,T}}\,t'$. We compared dispersion computed using MSD with a long-time dispersion coefficient estimated using a velocity auto-correlation function (VACF). We obtained a similar dispersion coefficient using the MSD method and a VACF with a difference of less than 10%. Fig 6.6f depicts dispersion coefficients over a range of Reynolds numbers estimated using the VACF method for non-Newtonian fluids and is comparable with the values estimated using the MSD method (Fig 6.5c).

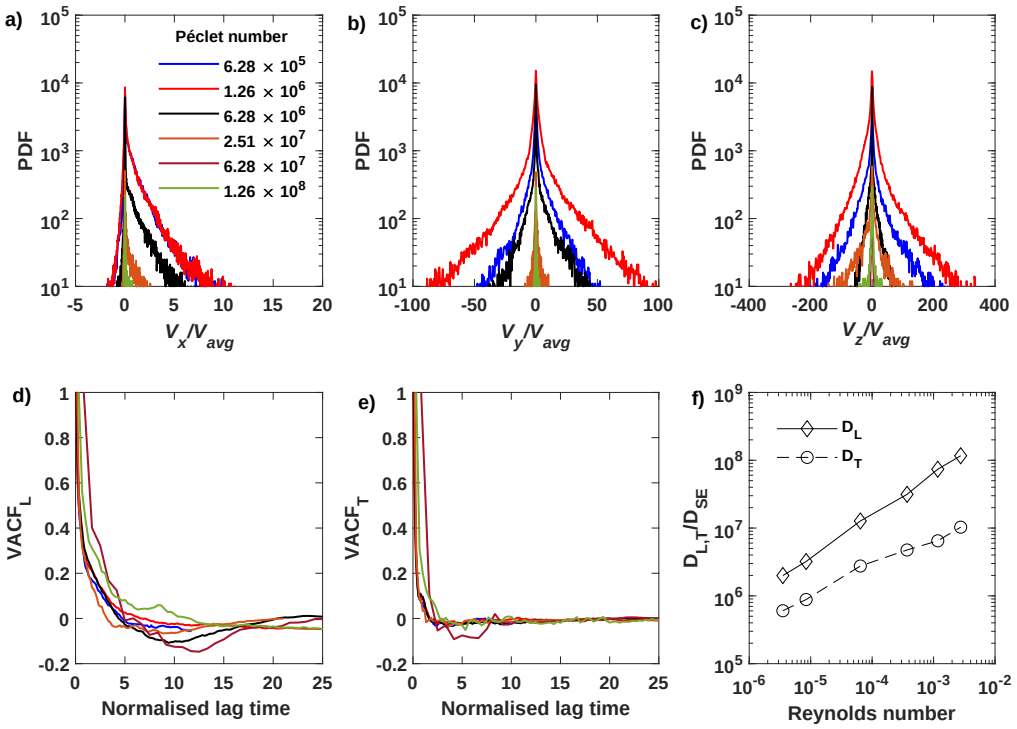

FIGURE 6.6: Probability density function (PDF) of nanoparticle velocity along (a) longitudinal X-direction, (b) transverse Y-direction, and (c) transverse Z-direction in a Mt. Simon sandstone. Velocity of particle is normalised by average velocity of the nanoparticle in that direction. Normalised velocity auto-correlation function along (d) longitudinal direction ($VACF_L$), (e) transverse direction ($VACF_T$). (f) Normalised longitudinal and transverse dispersion coefficient over a range of Reynolds number in non-Newtonian (NN) fluids and a Mt. Simon sandstone.

6.4.3 Effect of Brownian motion and nanoparticle concentrations

We injected 500 nanoparticles for 1 second in Mt. Simon sandstone over a range of Pe with and without Brownian force. Fig 6.7a,b shows spatial distribution of nanoparticles at normalised time of 60 and Pe of 1.26×10^6. The normalised resident concentration of nanoparticles (Fig 6.7c) in sandstone indicates that more than 58% of the nanoparticles are still trapped in the sandstone due to the absence of Brownian force. These results imply that the nanoparticles' Brownian motion helps migrate nanoparticles from the confined region to the fluid flow region. Furthermore, the Brownian motion of nanoparticles in the heterogeneous porous medium influences pore-accessibility. The mean square displacement of nanoparticles with Brownian force is much larger than nanoparticles without Brownian force (see Fig 6.7d). Fig 6.8 shows that the dispersion of nanoparticles (D_L, D_T) with Brownian force in the heterogeneous porous medium is

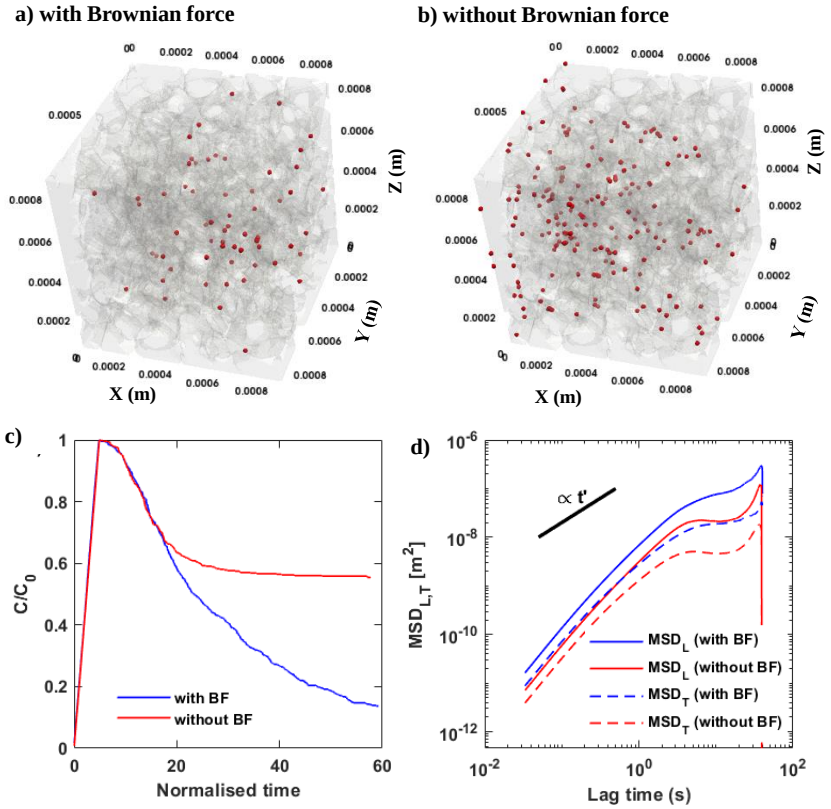

FIGURE 6.7: Spatial distribution of nanoparticles in Mt. Simon sandstone at normalised time of 60, (a) with and (b) without Brownian force. (c) Normalised resident concentration of nanoparticles as a function of dimensionless time. (d) Mean square displacement (MSD) along longitudinal direction and transverse direction with and without Brownian force in non-Newtonian fluid (Pe = 1.26×10^6).

1-2 orders of magnitude larger than the dispersion of nanoparticles without Brownian force over a range of Pe.

To evaluate the effect of nanoparticle concentration on dispersion, we injected 1000, 5000, and 10000 nanoparticles per second along with non-Newtonian fluid into Mt. Simon sandstone over a range of Pe. Fig 6.8a shows insignificant variation in D_L over a range of Pe and nanoparticle concentrations. However, Fig 6.8b indicates a significant increase in D_T with an increase in nanoparticle concentration at Pe higher than 10^7.

Contrary to the earlier experimental observation of [14, 15, 93], we did not observe the collapse of normalised dispersion coefficients on the single master curve over a range of Pe and porous medium geometries. These results imply that the gradient of shear stress affects the dispersion coefficient in three-dimensional space. Furthermore, although earlier experimental works [14, 15, 93] were carried out in 3D, the measurement of nanoparticle

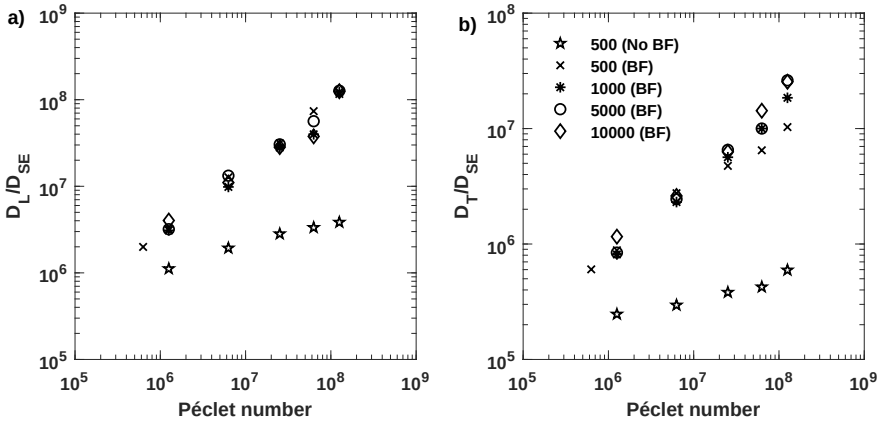

FIGURE 6.8: Effect of nanoparticles concentration and Brownian force (BF) on normalised dispersion coefficient along (a) longitudinal direction and (b) transverse direction in non-Newtonian (NN) fluid and Mt. Simon Simon sandstone. Each symbol represent number of nanoparticles injected per second.

displacement was carried out in 2D. Thus, the measurement of nanoparticle displacement in transverse z-direction was missing.

6.5 Conclusion

We have shown that the Euler-Lagrangian approach can be adopted to study nanoparticle transport and dispersion in an inelastic non-Newtonian fluid (described by the Meter model fluid) and heterogeneous porous media in 3D. Measurements of nanoparticle transport in 3D provide insights into nanoparticle dispersion in the longitudinal as well as the transverse direction. The gradient of shear stress formed in the pore-space of the porous medium dictates the transport behaviour, migration, pore-accessibility, and spatial distribution of nanoparticles in the porous medium. Nanoparticles adopt different flow paths in the porous medium at different Péclet numbers due to the porous medium's pore-scale spatial heterogeneity. The lower shear stress of the fluid in the stagnant zone creates resistance for nanoparticles to access pores in stagnant zones in heterogeneous porous media. The Brownian motion of nanoparticles increases the dispersion of nanoparticles in longitudinal and transverse directions.

Most non-Newtonian fluids are viscoelastic. Previous studies have shown that viscoelastic fluids exhibit elastic turbulence with low Reynolds number flows. Therefore, in the future, we will develop the Euler-Lagrangian method to simulate the transport of

nanoparticles in a non-Newtonian viscoelastic fluid modelled using the Phan-Thien-Tanner fluid model. This will help to understand the effect of pore-scale viscoelasticity on the dispersion of nanoparticles in 3D heterogeneous porous media.

Chapter 7

Summary and Future Work

The flow of fluid in a porous medium occurs on the scale of the pores. However, fluid flow measurements are made on a scale several orders of magnitude larger than the size of the pores, and that too, in an abstract way. Thus, upscaling fluid flow phenomena across different length scales (pore-scale to Darcy-scale to reservoir-scale) is necessary to design proper strategies for enhanced oil recovery and subsurface soil remediation. In addition, the fluid can show Newtonian or non-Newtonian (shear thinning, shear thickening, viscoelastic) behaviour depending on the presence of solutes (polymers, colloids) in a solvent, temperature, and molecular structural arrangement of the solute and solvent. Thus, the objective of the thesis is to develop a framework that can be used to upscale pore-scale non-Newtonian fluid flow to the Darcy scale based on an analytical and numerical approach. The major outcome of the thesis is as follows:

Most of the polymeric fluids used for enhanced oil recovery show an S-shape type of rheology. Upscaling non-Newtonian fluid flow from pore-scale to the Darcy scale was challenging due to the absence of an exact analytical solution through a circular capillary for these fluids. The exact analytical solution derived for the flow of a polymeric fluid (represented using the Meter model) in a circular capillary helped upscale pore-scale non-Newtonian fluid properties to the Darcy scale and determine effective viscosity and the Reynolds number.

The pore-correction and fluid-correction coefficient based capillary bundle model (BCM) for inelastic (Meter model) and viscoelastic (linear Phan-Thien-Tanner) non-Newtonian fluids could correctly upscale pore-scale flow to the Darcy scale. The pore-correction

coefficient considers variation in flow due to pore-geometry, and fluid-correction considers variation in fluid flow due to fluid rheology. Thus, the formulation proposed using BCM directly relates Darcy scale fluid flow properties (viscosity, shear rate, shear stress, velocity, and Reynolds number) to physical parameters (pore-morphology and fluid rheology).

The OpenFOAM-based direct numerical simulation using the inelastic Meter and viscoelastic linear Phan-Thien-Tanner (PTT) models was carried out in 2D and 3D heterogeneous porous media. The results showed that the upscaled parameters determined using the Meter model and the PTT model were similar. However, the viscoelastic PTT model gives a more realistic pore-scale description of non-Newtonian fluid flow compared to the Meter model. The mobile and immobile zones strongly affect pore-scale non-Newtonian fluid flow, and Darcy's viscosity represents viscosity in the active mobile zone of a porous medium.

OpenFOAM based two-phase simulations of non-Newtonian fluid displacing oil were carried out using the Meter model to study micro-heterogeneity and wettability-dependent stability of fluid flow in 2D and 3D porous media. The velocity and viscosity in the heterogeneous porous media were Beta and Gamma distributed, respectively. These spatial variations of velocity and viscosity and capillary/viscous forces controlled the stability of the two-phase fluid flow. Even after using a polymeric fluid with a higher viscosity value than the displaced oil, the heterogeneity of the porous medium leads to an unstable fluid flow front.

The Euler-Lagrangian approach developed for tracking spatio-temporal nanoparticle transport within the non-Newtonian and porous medium in 3D helps determine nanoparticles' dispersion in a longitudinal and transverse direction. The gradient of shear-stress that forms in an enclosed portions of a porous medium's pores and throats regulates the behaviour, migration, pore-accessibility and spatial distribution of nanoparticles. Furthermore, the observed non-Fickian behaviour of nanoparticle dispersion is related to the non-Gaussian distribution of particle migrations due to rheology and heterogeneity-dependent confinement.

The generalised Newtonian fluid model proposed for shear thickening fluid captures all regimes of typical shear thickening fluid and can be used to carry out single-phase simulations. The proposed equation predicts critical viscosity parameters of shear thickening

fluids such as η_0, η_{min}, η_{max}. The threshold shear stress parameters (τ_0, τ_p, τ_{d1}, τ_{d2}), the threshold shear rate parameters ($\dot{\gamma}_0$, $\dot{\gamma}_p$, $\dot{\gamma}_{d1}$, $\dot{\gamma}_{d2}$) and the threshold Péclet number parameters (Pe_p, Pe_{d1}, Pe_{d2}) of the proposed equations are parameters that modulate the effective transmutation of rheological characteristics (i.e. from Newtonian to shear-thinning, followed by a shear-thickening regime).

7.1 Future Work

This thesis provides a framework for upscaling non-Newtonian properties to the Darcy scale. But, there are many aspects that need careful consideration and improvement in the future. Some fundamental issues that can be considered are as follows:

1. The addition of nanoparticles or colloids imparts shear-thickening characteristics to some fluids. The shear thickening fluids have enormous potential to enhance oil recovery. However, previous studies on shear thickening fluids were carried out using the power-law model, which does not capture the complex behaviour of actual shear thickening fluids. Therefore, the GNF model proposed in chapter 3 can be used through the volume-of-fluid method of multiphase simulation to gain insight into the multiphase behaviour of the shear thickening fluid at the pore scale in porous media.

   To perform this investigation, an equation (Eq. 3.9) proposed in Chapter 3 for the shear-rate dependent viscosity of shear thickening fluids, can be implemented in the interFoam solver of OpenFOAM (Chapter 5). The effect of volume-fraction, wettability alteration, and heterogeneity of porous media on the displacement of Newtonian fluid (oil) when using shear thickening fluid can be investigated over a range of porosity, heterogeneity, and pressure gradient. The results can then be compared with the displacement of oil using shear-thinning fluid (e.g., as in Chapter 5). Along with a pore-scale evaluation of the two-phase displacement of shear thickening fluids, the above simulations will also help determine macroscopic parameters (i.e., relative permeability and capillary pressure) and their relationship with pore-scale displacement regimes. The hysteresis and energy dissipation during fluid-fluid displacements in porous media are due to an irreversible thermodynamic process, the memory of two-phase flow, and loss/imbalance of energy

[186]. The energy calculation for hysteresis in porous media is largely neglected in the literature. These simulations will help determine the spatial distribution of shear stress in porous media, which could help study the effects of the disorder of porous media on hysteresis involving shear thickening fluids.

2. The exact analytical solution could not be developed for the shear thickening fluid equation proposed in the present work. However, it would be possible to derive an analytical solution for the flow of shear thickening fluid through a circular capillary under certain limited conditions. For example, if we substitute $\eta_{\min} = 0$ and $\eta_0 = 0$ in Eq. 3.2 of chapter 3, we can derive an analytical solution for shear thickening fluid flow using the resulting equation and by following the procedure given in section 2.2.1 of Chapter 2. The analytical solution of shear thickening fluid can be implemented in a bundle-of-capillary model (BCM) proposed in chapter 4 for upscaling pore-scale properties of shear thickening fluids to Darcy's scale. Direct numerical simulation is computationally expensive and cannot be directly applied to field-scale applications, e.g. enhanced oil recovery. However, the upscaled macroscopic parameters using the BCM approach could be used for Darcy/reservoir scale simulation.

3. Most shear-thinning fluids exhibit viscoelasticity, which strongly affects the pore-scale displacement of non-Newtonian fluids and Newtonian fluids such as oil. In addition, wettability varies with space in subsurface porous media; therefore, more research is needed to understand how the interplay between wettability and viscoelasticity affects the two-phase displacement of non-Newtonian fluid using microfluidic experiments and viscoelastic PTT model-based numerical simulations. However, using the PTT model for two-phase simulation is challenging due to numerical stability issues.

   The OpenFOAM based RheoTool developed by [163] can be modified to perform two-phase simulations of viscoelastic Phan-Thien-Tanner fluid displacing oil over a range of wettability conditions. The hydrophobic and hydrophilic disordered glass micromodel can be fabricated to perform two-phase experiments of viscoelastic fluid displacing oil over a range of injection rates. Pore-scale displacement can be imaged using optical methods [59, 104] to determine pore-scale capillary pressure, static and dynamic contact angle, fluid-fluid interface curvature, Haines jump

instability and its effect on global displacement. These results, along with rheological parameters (relaxation time, storage and loss modulus etc.), can be used to validate two-phase simulations involving viscoelastic non-Newtonian fluids.

4. Direct numerical simulations are computationally expensive and thus cannot be used to study fluid flow behaviour on a larger scale. The exact analytic solution of the Meter model (chapter 2), on the other hand, has recently been used by [10] to develop a pore-network model [100, 101] to study the pore-scale fluid flow behaviour of shear-thinning fluid over a larger domain. Adopting a similar procedure [10], a pore-network model for viscoelastic PTT can be developed using an analytical solution of PTT fluid (i.e., Eq. 4.18 and Eq. 4.19 of chapter 4). Viscoelastic fluid flow using a pore-network model is not adequately studied in the literature, specifically if the porous medium is heterogeneous. A viscoelastic PTT fluid-based pore-network model can be used to identify the optimal flow conditions for viscoelastic fluid flow in real applications such as enhanced oil recovery.

Appendix A

Examination of the spatial (grid) convergence of simulations

The method proposed by Roache was adopted to evaluate the quality of the grid convergence [175]. In summary, the order of convergence (p) was estimated using $\mathrm{p} = \ln(\frac{\mathrm{f_3}-\mathrm{f_2}}{\mathrm{f_2}-\mathrm{f_1}})/\ln(\mathrm{h})$, where, h is the grid refinement ratio, f are the values of evaluated parameter at each grids. The Richardson extrapolation at h=0 was estimated using $\mathrm{f}_{h=0} = \mathrm{f_1} + \frac{\mathrm{f_1}-\mathrm{f_2}}{\mathrm{h^p}-1}$. The grid convergence index (GCI) at each refinement level was determined using $\mathrm{GCI} = \frac{\mathrm{F_s}\, e}{\mathrm{h^p}-1}$, where $\mathrm{F_s} = 1.25$ is factor of safety and $e = \frac{\mathrm{f_1}-\mathrm{f_2}}{\mathrm{f_1}}$ is error between two grids. The asymptotic range of convergence was examined using $\frac{\mathrm{GCI}_{2,3}}{\mathrm{h^p}\,\mathrm{GCI}_{1,2}}$.

The grid convergence study was performed on different grid resolutions (50,000 – 5,00,000) on a subsample of porous medium having a porosity of 54% (Figure A.1). To evaluate grid convergence of the numerical scheme described in the thesis for the single-phase flow of Meter model fluids (Chapter 4, section 4.4), a single-phase flow of shear thickening fluids (Chapter 3, section 3.3.6), and a two-phase flow of Meter model fluids (Chapter 5, section 5.2.1), we injected non-Newtonian fluid at an injection rate of 10^{-4} m/s and a time-step of 10^{-6} s. The convergence of velocity and viscosity was evaluated. Table A.1 shows the order of convergence (p), Richard extrapolation of velocity and viscosity values at zero-grid spacing values, the grid convergence index (GCI), and the asymptotic range of convergence for average velocity and average viscosity values. The error (%) in Fig A.1 shows the percentage of the average value attained for velocity and viscosity

TABLE A.1: Spatial grid-dependent convergence of the simulations

Parameter	Meter model (MM)		Shear thickening fluid		Two-phase model	
	U_{avg} (m/s)	η_{avg} (Pa·s)	U_{avg} (m/s)	η_{avg} (Pa·s)	U_{avg} (m/s)	η_{avg} (Pa·s)
p	1.26	1.18	1.07	1.13	1.2	1.3
f_0	1.73×10^{-4}	0.73	1.73×10^{-4}	274	1.73×10^{-4}	0.73
$GCI_{1,2}$	0.035	2.89	0.13	2.87	0.04	3.56
$GCI_{2,3}$	0.053	4.02	0.18	3.89	0.061	5.82
Asymptotic	1	0.98	1	1.01	1	1.02

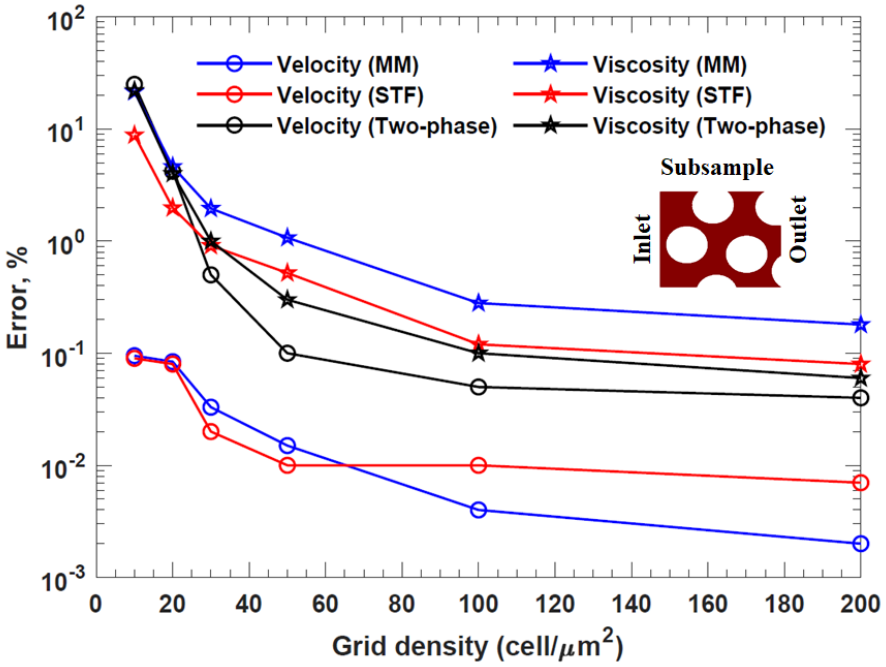

FIGURE A.1: Average velocities and average viscosity for each grid density. The error shows the percentage of the average value attained compared to the Richard extrapolation (i.e. highest grid resolution). [MM: Meter model, STF: shear thickening fluid.]

at each grid density compared to the average value at the zero-grid spacing values estimated using Richard extrapolation (*i.e.* at the highest grid resolution). This result indicates that average velocity and viscosity values approach an asymptotic zero-grid spacing value as the grid density increases. Figure A.1 shows an insignificant difference in the average velocity and viscosity after grid density 30 cells/μm^2. The Courant number was higher than 1 for a grid size lower than 20 cells/μm^2. Although computationally expensive, all simulations were carried out with a grid density higher than 50 cells/μm^2 to maintain convergence and accuracy. This resolution provided at-least 50 cells in the smallest pore-throat of the heterogeneous porous medium.

Appendix B

First page of published articles

Rheologica Acta (2021) 60:11–21
https://doi.org/10.1007/s00397-020-01248-y

ORIGINAL CONTRIBUTION

Effective viscosity and Reynolds number of non-Newtonian fluids using Meter model

Takshak Shende[1] · **Vahid J. Niasar**[1] · **Masoud Babaei**[1]

Received: 22 May 2020 / Revised: 30 September 2020 / Accepted: 3 October 2020 / Published online: 10 November 2020

Abstract

The Meter model (a four-parameter model) captures shear viscosity–shear stress relationship (S-shaped type) of polymeric non-Newtonian fluids. We devise an analytical solution for radial velocity profile, average velocity, and volumetric flow rate of steady-state laminar flow of non-Newtonian Meter model fluids through a circular geometry. The analytical solution converts to the Hagen–Posseuille equation for the Newtonian fluid case. We also develop the formulations to determine effective viscosity, Reynolds number, and Darcy's friction factor using measurable parameters as available rheological models do not correctly define these parameters for a given set of flow condition in circular geometry. The analytical solution and formulations are validated against experimental data. The results suggest that the effective Reynolds number and effective friction factor estimated using the proposed formulation help characterize non-Newtonian fluid flow through a circular geometry in laminar and turbulent flows.

Keywords Non-Newtonian fluid · Shear stress · Viscosity · Analytical solution · Shear-thinning fluid · Reynolds number · Micro-capillary fluid flow

Introduction

The laminar flow of a non-Newtonian fluid (described using generalized Newtonian fluid model) through a circular capillary/tube has broader engineering application (e.g., polymer fluid flow through pipes in industrial settings (Bird et al. 1987), capillary bundle model of porous media (Savins 1969), pore-network model (Sochi and Blunt 2008)). Among generalized Newtonian fluid models (Yilmaz and Gundogdu 2008), Cross (Cross 1965), Carreau (Yasuda 1979), Carreau–Yasuda (Yasuda 1979), Meter (Meter and Bird 1964; Meter 1964; Savins 1969; Tsakiroglou 2002; Tsakiroglou et al. 2003; Tsakiroglou et al. 2003), and Steller–Ivako (Steller and Iwko 2018) models can predict S-shaped rheological properties (i.e., constant viscosity at low and high shear values and decreasing viscosity at intermediate shear values) of many shear-thinning fluids.

Attempts have been made by many investigators to obtain an analytical solution for flow of non-Newtonian fluid through a circular tube. Matsuhisa and Bird derived an analytical solution for the laminar flow of a fluid obeying shear stress–dependent Ellis model (Matsuhisa and Bird 1965). Meter and Bird proposed the analytical solution for the flow of shear stress–dependent Meter model fluid in a circular capillary if $\frac{\eta_\infty}{\eta_0}$ is very small. Here, η_0 and η_∞ are zero and infinite shear viscosity, respectively (Meter and Bird 1964). Although Sochi (2015) and Kim (2018) proposed analytical solutions for Carreau and Cross fluid flow through a circular tube and Peralta et al. (2014, 2017) proposed analytical solution for flow over free-draining vertical plate, the exact analytical solution is absent for estimation of the radial velocity profile, average velocity, and volumetric flow rate of fluid flow in a circular tube/micro-capillary obeying Cross, Carreau, Meter, or Steller–Ivako model.

The Reynolds number of non-Newtonian fluids in a circular tube/capillary is commonly defined using the viscosity of the fluid at the wall (Escudier et al. 2005;

Electronic supplementary material The online version of this article (https://doi.org/10.1007/s00397-020-01248-y) contains supplementary material, which is available to authorized users.

✉ Masoud Babaei
masoud.babaei@manchester.ac.uk

[1] Department of Chemical Engineering and Analytical Science, The University of Manchester, Manchester, UK

Journal of Molecular Liquids 325 (2021) 115220

Contents lists available at ScienceDirect

Journal of Molecular Liquids

journal homepage: www.elsevier.com/locate/molliq

An empirical equation for shear viscosity of shear thickening fluids

Takshak Shende *, Vahid J. Niasar, Masoud Babaei *

The University of Manchester, Department of Chemical Engineering and Analytical Science, Manchester, UK

ARTICLE INFO

Article history:
Received 26 October 2020
Received in revised form 21 December 2020
Accepted 25 December 2020
Available online 29 December 2020

Keywords:
Colloidal suspension
Non-Newtonian fluid
Shear thickening fluid
Direct numerical simulation
OpenFOAM
Pore-scale simulation

ABSTRACT

Quantitative modelling of the rheology of non-Newtonian fluids requires significant empirical input due to very complex behaviour of the bulk fluid as a result of particle-scale physics of fluids. The existing rheology models are mainly limited to certain fluid dynamics conditions such as shear rate, shear stress, *etc*. Adopting Doolittle's free volume theory approach, we have proposed an empirical equation to describe the relative free volume-dependent viscosity, the shear stress-dependent viscosity, the shear rate-dependent viscosity, and the dimensionless Péclet number-dependent relative viscosity of shear thickening fluids. The proposed formulae predict all rheologically different behaving Newtonian, intermediate shear thinning, shear thickening and extreme shear thinning regimes of shear-thickening fluids. The proposed formulae have been validated against the experimental rheological data of various shear thickening fluids over a range of pH, volume fraction, electrolyte concentration, temperature, and magnetic field. The results suggest that the predicted threshold material parameters of shear thickening fluids help to quantitatively evaluate the effect of varying physico-chemical conditions on the rheology of shear thickening fluids. We simulated the flow of a shear thickening fluid, modelled using proposed shear rate-dependent equation, in a 2D staggered porous medium. We observed bimodal distribution of pore-scale shear rate, shear viscosity and velocity in a porous medium.

1. Introduction

The suspension shear-thickening behaviour (*i.e.* increase in the shear viscosity with an increase in the shear stress/rate showed by colloidal/non-colloidal suspension) [1] has wide applications starting from cement [2], woven fabrics [3], chocolates [4], cornstarch [5] to ceramics [6]. The shear-thickening fluids are excellent for shock-absorption due to their high elastic modulus and high dissipation energy [6,7]. Smart materials are being developed such as magnetorheological shear thickening fluids [8] which act as actuating fluids to maintain variable flow rate or force transfer scenario in many engineering applications such as artificial joints and breaks [7,9].

Mixing colloidal particles or polymers (*i.e.* solute) in a solvent (*e.g.* water) leads to an increase in the viscosity of the solution, and further increase in the concentration of solute/colloids makes fluid behave like a non-Newtonian fluid. At lower stress, shear thickening fluids show Newtonian behaviour [6]. The fluid shows shear-thinning characteristics once critical stress exceeds, *i.e.* viscosity of the fluid drops with an increase in stress. The fluid can flow under weak stress and still be able to behave like a gel at rest. The viscosity of the fluid suddenly rises once it reaches critical stress at higher stresses [6]. This behaviour of a fluid is defined as shear thickening, which mostly depends on properties of solute/colloids (shape and size of molecules, volume fraction, *etc.*) and solvents (viscosity, deformation *etc.*) [6,7,10,11]. Fig. 1 shows the typical rheological behaviour of a shear thickening fluid under varying shear stress or shear rate. The typical shear thickening behaviour can also be observed at low temperatures (*i.e.* temperature $> -40^{\circ}C$) [12].

Interparticle and intermolecular contact forces and hydrodynamic forces significantly contribute towards shear thickening of the suspension in the fluid [10,13–17], the external or internal forces in solution cause displacement of suspended colloid particles/solute. The force transmits from one colloid particle/solute molecule to the neighbouring colloid particle/solute molecule through intervening fluid. The hydrodynamic interaction between colloid particles/solute and solvent disturb local flow field of all colloids particles/solute molecules [17,18]. We note that the intervening fluid (solvent) acts as a lubricant between neighbouring colloids particles/solutes [1,11]. Hydrophobic or hydrophilic properties of the colloidal particles/polymer molecules along with hydrodynamic interaction between colloid/solute and solvent determines the relative motion of the particles and effectiveness of the solvent to act as a lubricant. The electrostatics [19,20] and van der Waals forces play a significant role in maintaining the viscosity of the solution [1,7,10]. Interparticle forces are dominant at lower stresses; on the contrary, hydrodynamic forces play a vital role at high stresses. Alteration of particles surface chemistry, ionic strength, shape and size affect the interparticle or intermolecular forces, thus viscosity of the solution. The

* Corresponding authors.
E-mail addresses: takshak.shende@manchester.ac.uk (T. Shende), masoud.babaei@manchester.ac.uk (M. Babaei).

https://doi.org/10.1016/j.molliq.2020.115220
0167-7322/

Chemical Engineering Science 239 (2021) 116638

Contents lists available at ScienceDirect

Chemical Engineering Science

journal homepage: www.elsevier.com/locate/ces

Upscaling non-Newtonian rheological fluid properties from pore-scale to Darcy's scale

Takshak Shende, Vahid Niasar, Masoud Babaei *

Department of Chemical Engineering and Analytical Science, The University of Manchester, Manchester, UK

HIGHLIGHTS

- Bundle-of-Capillaries model for viscoelastic linear PTT and Meter model fluids.
- Pore-correction and fluid-correction coefficients to account for pore-scale variability.
- Phan-Thien-Tanner (PTT) model fluid flow simulation in 3D heterogenous porous medium,
- Formulations to estimate upscaled Darcy viscosity, shear rate, and shear stress.

ARTICLE INFO

Article history:
Received 11 September 2020
Received in revised form 23 March 2021
Accepted 31 March 2021
Available online 21 April 2021

Keywords:
Upscaling
Non-Newtonian fluids
Polymeric fluids
Bundle-of-Capillaries model
Direct numerical simulation

ABSTRACT

Continuity and momentum equations govern the pore-scale flow properties of the fluid in the porous media, whereas Darcy's law governs Darcy scale properties of the fluid transport in porous media. The empirical shift factor relates the steady shear-dependent viscosity of non-Newtonian fluids to the Darcy viscosity in porous media. The reported values of the empirical shift factor cover three orders of magnitude depending on the considered fluid-medium configurations. This creates a challenge to upscale non-Newtonian rheology from pore-scale to Darcy's scale. We upscale Darcy viscosity based on pore-scale shear viscosity of Meter model fluid and viscoelastic linear Phan-Thien-Tanner fluid. We propose a Bundle-of-Capillaries model modified with pore-correction coefficient and fluid-correction coefficient. We numerically simulate the flow of polyacrylamide fluid, modelled using Meter model and linear Phan-Thien-Tanner model, through 3D symmetric micro-channel, 2D porous medium and 3D Mt Simon sandstone. Pore-scale direct numerical simulation using linear Phan-Thien-Tanner model showed viscoelastic instability in heterogeneous Mt Simon sandstone at low Reynolds number flow. Direct numerical simulations overestimate Darcy viscosity due to the presence of stagnant zones without active flow.

1. Introduction

Polymeric fluid flow in porous medium is of significant importance in many engineering applications such as enhanced oil recovery. Most of the polymeric solutions employed for the enhanced oil recovery applications show non-Newtonian behaviour (Bird et al., 1987; Savins, 1969; Sorbie, 2013; Xie et al., 2018). The commonly used non-Newtonian fluids (i.e. xanthan gum (Patel et al., 2020; Song et al., 2006) and polyacrylamide solution (Kawale et al., 2017; De et al., 2017)) for oil recovery show viscoelastic properties. The rheology of non-Newtonian fluids can be studied considering non-Newtonian fluid as a generalised Newtonian fluid (*e.g.* power-law, Bingham, Cross, Carreau, Elis, Meter model etc.) or viscoelastic fluid (*e.g.* Maxwell, Oldroyd-B, Giesekus, Phan-Thien–Tanner model etc.) (Alves et al., 2021; Bird and Carreau, 1968). These models are derived based on an empirical approach with many simplified assumptions; thus, each model has its own limitations and cannot universally be applied to all types of non-Newtonian fluids (Bird and Carreau, 1968).

The flow of polymeric solution in rheometer is remarkably different from that of the flow in porous medium. The reason could be (Afolabi et al., 2019) (i) the porous medium has complex geometry compared to rheometers; (ii) the presence of many expansion and contraction in the porous medium expose polymer to the various amount of shear stress (Sorbie, 2013); (iii) mechanical retention and adsorption of the polymer change the geometry of the porous medium. To describe polymeric fluid behaviour in porous medium, apparent viscosity or Darcy viscosity is a commonly used terms in the literature (Afolabi et al., 2019; Sorbie, 2013; Berg and van Wunnik, 2017; Rodríguez de Castro and Agnaou, 2019; Rodríguez de Castro et al., 2020). Darcy viscosity (η_{darcy}) is defined using

* Corresponding author.
E-mail address: masoud.babaei@manchester.ac.uk (M. Babaei).

https://doi.org/10.1016/j.ces.2021.116638
0009-2509/

Journal of Non-Newtonian Fluid Mechanics 296 (2021) 104628

Contents lists available at ScienceDirect

Journal of Non-Newtonian Fluid Mechanics

journal homepage: www.elsevier.com/locate/jnnfm

Pore-scale simulation of viscous instability for non-Newtonian two-phase flow in porous media

Takshak Shende, Vahid Niasar, Masoud Babaei *

Department of Chemical Engineering and Analytical Science, The University of Manchester, Manchester, United Kingdom

ARTICLE INFO

Keywords:
Non-Newtonian fluid
Meter model
Viscosity
Shear-thinning fluid
Weissenberg number
Heterogeneity
Porous media

ABSTRACT

The impact of micro-heterogeneity on non-Newtonian two-phase flow is the focus of the present study. The direct numerical simulation of non-Newtonian fluids (modelled using shear stress-dependent Meter model) displacing oil in 3D Mt. Simon sandstone and 2D heterogeneous porous media were considered over a range of wettabilities (strong imbibition to strong drainage), capillary numbers and viscosity ratios. This study suggests that heterogeneity of the porous medium can potentially lead to an unstable fluid flow front (even after use of polymer). Therefore along with capillary number and viscosity ratio, heterogeneity is the governing factor for controlling viscous and capillary fingering, and it is crucial to account for the microscale heterogeneity of porous media to design polymer solution injection.

1. Introduction

Immiscible multiphase flow in porous media involving polymeric solutions has many applications specifically for enhanced oil recovery [1–3], and remediation of subsurface non-aqueous phase liquid (NAPL) contaminants [3,4]. Polymeric solutions, which have non-Newtonian rheology, is commonly utilised to displace NAPL or crude oil in the subsurface. The heterogeneity of the porous medium and shear-dependent rheology of non-Newtonian fluids make the multiphase flow more complex. The effectiveness of polymeric solutions to displace oil depend on physical and chemical parameters of oil, polymeric solutions and subsurface materials which vary spatially with time [5]. Although coreflood experiments on larger samples have been used to study polymeric macroscopic sweep efficiency [1], these experiments can hardly be used to gain pore-scale insights on the microscopic displacement of invading and displacing fluids.

Wettability, which is the fluid's ability to adhere to the solid surface in the presence of another fluid, is one of the key factors in two-phase flow dynamics in the porous medium. The contact angle (θ) between the fluid–fluid interface and the solid surface determines which fluid (displaced or displacing) has a tendency to adhere to the solid surface. For example, in a porous medium wetted by water ($\theta < 90°$), the polymer fluid will adhere to the solid surface, while in a porous medium wetted by oil ($\theta > 90°$), the oil will adhere to the solid surface. Although fluid–fluid interactions during multiphase flow are influenced by the wettability of the solid surface [6], less attention is paid to the multiphase flow involving non-Newtonian fluids. Hatzignatiou et al. [7] conducted a polymer flood experiment on water and oil-wet Bentheim and Berea sandstone. They suggested that rock wettability strongly affects the polymer retention in the porous medium and influences the polymer front velocity. The authors postulated that the physical adsorption of polymer to the rock surface causes entrapment of polymer in the sandstone as they observed higher polymer retention in the water-wet Berea sandstone compared to the oil-wet Berea sandstone. Broseta et al. [8] reported reduction in the polymer adsorption in an oil-wet micromodel compared to a water-wet one. Jamaloei and Kharrat [9] reported that the displacement front's stability during polymer flooding depends on pore-morphology and wettability in a porous medium. Using magnetic resonance imaging technique, Romero-Zerón et al. [10] investigated the effects of wettability in water-wet and oil-wet rocks and reported higher oil recovery in strongly water-wet rocks using partially hydrolysed polyacrylamide solution. Ameli et al. [11] observed that salinity reduces the efficiency of oil recovery during polymer flooding, and the water-wet system gives favourable oil recovery compared to the oil-wet system. Eslami and Taghavi [12] demonstrated that the wettability affects the viscous fingering pattern formations and flow efficiency of the displacement using two-phase microfluidic experiments wherein Newtonian fluid was used to displace non-Newtonian fluid in a rectangular Hele-Shaw cell. Li et al. [13] visualised oil saturation in the oil-wet and water-wet rocks using magnetic resonance imaging and suggested that the polymer stripping mechanism dominates in an oil-wet rock.

* Corresponding author.
E-mail address: masoud.babaei@manchester.ac.uk (M. Babaei).

https://doi.org/10.1016/j.jnnfm.2021.104628
Received 28 May 2021; Received in revised form 26 July 2021; Accepted 2 August 2021
Available online 9 August 2021

Bibliography

[1] R. O. Afolabi, G. F. Oluyemi, S. Officer, and J. O. Ugwu. Hydrophobically associating polymers for enhanced oil recovery–part b: A review of modelling approach to flow in porous media. *Journal of Molecular Liquids*, page 111495, 2019.

[2] A. Agi, R. Junin, and A. Gbadamosi. Mechanism governing nanoparticle flow behaviour in porous media: insight for enhanced oil recovery applications. *International Nano Letters*, 8(2):49–77, 2018.

[3] J. Ahrens, B. Geveci, and C. Law. Paraview: An end-user tool for large data visualization. *The visualization handbook*, 717, 2005.

[4] C. Airiau and A. Bottaro. Flow of shear-thinning fluids through porous media. *Advances in Water Resources*, page 103658, 2020.

[5] T. Akai, M. J. Blunt, and B. Bijeljic. Pore-scale numerical simulation of low salinity water flooding using the lattice boltzmann method. *Journal of Colloid and Interface Science*, 566:444–453, 2020.

[6] F. Alcocer and P. Singh. Permeability of periodic arrays of cylinders for viscoelastic flows. *Physics of fluids*, 14(7):2578–2581, 2002.

[7] M. Alves, P. Oliveira, and F. Pinho. A convergent and universally bounded interpolation scheme for the treatment of advection. *International journal for numerical methods in fluids*, 41(1):47–75, 2003.

[8] M. Alves, P. Oliveira, and F. Pinho. Numerical methods for viscoelastic fluid flows. *Annual Review of Fluid Mechanics*, 53:509–541, 2021.

[9] F. Ameli, M. R. Moghbeli, and A. Alashkar. On the effect of salinity and nanoparticles on polymer flooding in a heterogeneous porous media: Experimental and

modeling approaches. *Journal of Petroleum Science and Engineering*, 174:1152–1168, 2019.

[10] S. An, M. Sahimi, T. Shende, M. Babaei, and V. Niasar. Enhanced thermal fingering in a shear-thinning fluid flow through porous media: Dynamic pore network modeling. *Physics of Fluids*, 34(2):023105, 2022.

[11] S. Aramideh, P. P. Vlachos, and A. M. Ardekani. Nanoparticle dispersion in porous media in viscoelastic polymer solutions. *Journal of Non-Newtonian Fluid Mechanics*, 268:75–80, 2019.

[12] R. Aziz, V. Joekar-Niasar, P. J. Martínez-Ferrer, O. E. Godinez-Brizuela, C. Theodoropoulos, and H. Mahani. Novel insights into pore-scale dynamics of wettability alteration during low salinity waterflooding. *Scientific reports*, 9(1): 1–13, 2019.

[13] R. Aziz, V. Niasar, H. Erfani, and P. J. Martínez-Ferrer. Impact of pore morphology on two-phase flow dynamics under wettability alteration. *Fuel*, 268:117315, 2020.

[14] F. Babayekhorasani, D. E. Dunstan, R. Krishnamoorti, and J. C. Conrad. Nanoparticle diffusion in crowded and confined media. *Soft Matter*, 12(40):8407–8416, 2016.

[15] F. Babayekhorasani, D. E. Dunstan, R. Krishnamoorti, and J. C. Conrad. Nanoparticle dispersion in disordered porous media with and without polymer additives. *Soft Matter*, 12(26):5676–5683, 2016.

[16] A. Bagdasaryan. A note on the 2f1 hypergeometric function. *arXiv preprint arXiv:0912.0917*, 2009.

[17] M. T. Balhoff and K. E. Thompson. A macroscopic model for shear-thinning flow in packed beds based on network modeling. *Chemical Engineering Science*, 61(2): 698–719, 2006.

[18] S. Berg and J. van Wunnik. Shear rate determination from pore-scale flow fields. *Transport in Porous Media*, 117(2):229–246, 2017.

[19] E. C. Bingham. *Fluidity and Plasticity*, volume 2. McGraw-Hill, 1922.

[20] R. B. Bird and P. J. Carreau. A nonlinear viscoelastic model for polymer solutions and melts—I. *Chemical Engineering Science*, 23(5):427–434, 1968.

[21] R. B. Bird, R. Armstrong, and O. Hassager. Fluid mechanics, dynamics of polymeric liquids, Vol. 1, 1987.

[22] R. B. Bird, W. E. Stewart, and E. N. Lightfoot. *Transport Phenomena*. John Wiley & Sons, 2007.

[23] G. S. Blair. The success of casson's equation. *Rheologica Acta*, 5(3):184–187, 1966.

[24] M. M. Błaszczyk, J. P. Sek, and Ł. Przybysz. Capillary bundle model for gravitational flow of emulsion through granular media and experimental validation. *Chemical Engineering Science*, 155:415–427, 2016.

[25] M. J. Blunt. *Multiphase flow in permeable media: A pore-scale perspective*. Cambridge University Press, 2017.

[26] S. C. Boothroyd, D. M. Hoyle, T. C. McLeish, E. Munch, R. Schach, A. J. Smith, and R. L. Thompson. Association and relaxation of supra-macromolecular polymers. *Soft Matter*, 15(26):5296–5307, 2019.

[27] A. Boromand, S. Jamali, B. Grove, and J. M. Maia. A generalized frictional and hydrodynamic model of the dynamics and structure of dense colloidal suspensions. *Journal of Rheology*, 62(4):905–918, 2018.

[28] J. F. Brady and J. F. Morris. Microstructure of strongly sheared suspensions and its impact on rheology and diffusion. *Journal of Fluid Mechanics*, 348:103–139, 1997.

[29] D. Broseta, F. Medjahed, J. Lecourtier, M. Robin, et al. Polymer adsorption/retention in porous media: Effects of core wettability and residual oil. *SPE Advanced Technology Series*, 3(01):103–112, 1995.

[30] E. Brown and H. M. Jaeger. The role of dilation and confining stresses in shear thickening of dense suspensions. *Journal of Rheology*, 56(4):875–923, 2012.

[31] E. Brown and H. M. Jaeger. Shear thickening in concentrated suspensions: phenomenology, mechanisms and relations to jamming. *Reports on Progress in Physics*, 77(4):046602, 2014.

[32] C. A. Browne, A. Shih, and S. S. Datta. Bistability in the unstable flow of polymer solutions through pore constriction arrays. *Journal of Fluid Mechanics*, 890, 2020.

[33] C. A. Browne, A. Shih, and S. S. Datta. Pore-scale flow characterization of polymer solutions in microfluidic porous media. *Small*, 16(9):1903944, 2020.

[34] L. Campagnolo, M. Nikolić, J. Perchoux, Y. L. Lim, K. Bertling, K. Loubiere, L. Prat, A. D. Rakić, and T. Bosch. Flow profile measurement in microchannel using the optical feedback interferometry sensing technique. *Microfluidics and Nanofluidics*, 14(1-2):113–119, 2013.

[35] S. Chandrasekhar. Stochastic problems in physics and astronomy. *Reviews of modern physics*, 15(1):1, 1943.

[36] O. Cheal and C. Ness. Rheology of dense granular suspensions under extensional flow. *Journal of Rheology*, 62(2):501–512, 2018.

[37] X. Chen, H. Marschall, M. Schäfer, and D. Bothe. A comparison of stabilisation approaches for finite-volume simulation of viscoelastic fluid flow. *International Journal of Computational Fluid Dynamics*, 27(6-7):229–250, 2013.

[38] Y. Chen, G. Zeng, and W. Liu. The effect of surface grafting polymer chains on the shear thickening of hard microsphere suspensions. *Colloids and Surfaces A: Physicochemical and Engineering Aspects*, 555:736–745, 2018.

[39] R. P. Chhabra and J. F. Richardson. *Non-Newtonian Flow and Applied Rheology: Engineering Applications*. Butterworth-Heinemann, 2011.

[40] H. C. Chu and R. N. Zia. The non-newtonian rheology of hydrodynamically interacting colloids via active, nonlinear microrheology. *Journal of Rheology*, 61 (3):551–574, 2017.

[41] A. Clarke, A. M. Howe, J. Mitchell, J. Staniland, L. Hawkes, and K. Leeper. Mechanism of anomalously increased oil displacement with aqueous viscoelastic polymer solutions. *Soft Matter*, 11(18):3536–3541, 2015.

[42] T. Clemens, K. Tsikouris, M. Buchgraber, L. M. Castanier, A. Kovscek, et al. Pore-scale evaluation of polymers displacing viscous oil–computational-fluid-dynamics simulation of micromodel experiments. *Spe Reservoir Evaluation & Engineering*, 16(02):144–154, 2013.

[43] M. M. Cross. Rheology of non-Newtonian fluids: a new flow equation for pseudoplastic systems. *Journal of Colloid Science*, 20(5):417–437, 1965.

[44] C. T. Crowe, J. D. Schwarzkopf, M. Sommerfeld, and Y. Tsuji. *Multiphase Flows with Droplets and Particles*. CRC Press, aug 2011. doi: 10.1201/b11103.

[45] D. Cruz, F. Pinho, and P. J. Oliveira. Analytical solutions for fully developed laminar flow of some viscoelastic liquids with a newtonian solvent contribution. *Journal of non-newtonian fluid mechanics*, 132(1-3):28–35, 2005.

[46] P. A. Cundall and O. D. Strack. A discrete numerical model for granular assemblies. *geotechnique*, 29(1):47–65, 1979.

[47] C. D. Cwalina and N. J. Wagner. Rheology of non-brownian particles suspended in concentrated colloidal dispersions at low particle reynolds number. *Journal of Rheology*, 60(1):47–59, 2016.

[48] C. D. Cwalina, K. J. Harrison, and N. J. Wagner. Rheology of cubic particles in a concentrated colloidal dispersion suspending medium. *AIChE Journal*, 63(3): 1091–1101, 2017.

[49] S. S. Datta, H. Chiang, T. Ramakrishnan, and D. A. Weitz. Spatial fluctuations of fluid velocities in flow through a three-dimensional porous medium. *Physical Review Letters*, 111(6):064501, 2013.

[50] G. D'Avino, G. Romeo, M. M. Villone, F. Greco, P. A. Netti, and P. L. Maffettone. Single line particle focusing induced by viscoelasticity of the suspending liquid: theory, experiments and simulations to design a micropipe flow-focuser. *Lab on a Chip*, 12(9):1638–1645, 2012.

[51] S. De, S. Das, J. Kuipers, E. Peters, and J. Padding. A coupled finite volume immersed boundary method for simulating 3d viscoelastic flows in complex geometries. *Journal of Non-Newtonian Fluid Mechanics*, 232:67–76, 2016.

[52] S. De, J. Kuipers, E. Peters, and J. Padding. Viscoelastic flow simulations in random porous media. *Journal of Non-Newtonian Fluid Mechanics*, 248:50–61, 2017.

[53] S. De, J. Kuipers, E. Peters, and J. Padding. Viscoelastic flow simulations in model porous media. *Physical Review Fluids*, 2(5):053303, 2017.

[54] S. De, J. A. Kuipers, E. A. Peters, and J. T. Padding. Viscoelastic flow past mono- and bidisperse random arrays of cylinders: flow resistance, topology and normal stress distribution. *Soft Matter*, 13(48):9138–9146, 2017.

[55] S. De, J. Van Der Schaaf, N. Deen, J. Kuipers, E. Peters, and J. Padding. Lane change in flows through pillared microchannels. *Physics of Fluids*, 29(11):113102, 2017.

[56] S. De, P. Krishnan, J. Van Der Schaaf, J. Kuipers, E. Peters, and J. Padding. Viscoelastic effects on residual oil distribution in flows through pillared microchannels. *Journal of colloid and interface science*, 510:262–271, 2018.

[57] P. de Anna, B. Quaife, G. Biros, and R. Juanes. Prediction of the low-velocity distribution from the pore structure in simple porous media. *Physical Review Fluids*, 2(12):124103, 2017.

[58] A. R. de Castro and M. Agnaou. Numerical investigation of the apparent viscosity dependence on darcy velocity during the flow of shear-thinning fluids in porous media. *Transport in Porous Media*, pages 1–28, 2019.

[59] A. R. de Castro, M. Oostrom, and N. Shokri. Effects of shear-thinning fluids on residual oil formation in microfluidic pore networks. *Journal of colloid and interface science*, 472:34–43, 2016.

[60] F. Del Giudice, G. Romeo, G. D'Avino, F. Greco, P. A. Netti, and P. L. Maffettone. Particle alignment in a viscoelastic liquid flowing in a square-shaped microchannel. *Lab on a Chip*, 13(21):4263–4271, 2013.

[61] F. Del Giudice, G. D'Avino, F. Greco, P. L. Maffettone, and A. Q. Shen. Fluid viscoelasticity drives self-assembly of particle trains in a straight microfluidic channel. *Physical Review Applied*, 10(6):064058, 2018.

[62] A. K. Doolittle. Studies in newtonian flow. ii. the dependence of the viscosity of liquids on free-space. *Journal of Applied Physics*, 22(12):1471–1475, 1951.

[63] J. L. Duda, S. A. Hong, and E. E. Klaus. Flow of polymer solutions in porous media: inadequacy of the capillary model. *Industrial & Engineering Chemistry Fundamentals*, 22(3):299–305, 1983.

[64] F. A. Dullien. *Porous media: fluid transport and pore structure*. Academic press, 2012.

[65] U. Eberhard, H. J. Seybold, M. Floriancic, P. Bertsch, J. Jiménez-Martínez, J. S. Andrade Jr, and M. Holzner. Determination of the effective viscosity of non-newtonian fluids flowing through porous media. *Frontiers in Physics*, 7:71, 2019.

[66] U. Eberhard, H. Seybold, E. Secchi, J. Jiménez-Martínez, P. Rühs, A. Ofner, J. Andrade, and M. Holzner. Mapping the local viscosity of non-newtonian fluids flowing through disordered porous structures. *Scientific Reports*, 10(1):1–12, 2020.

[67] E. M. Ekanem, S. Berg, S. De, A. Fadili, T. Bultreys, M. Rücker, J. Southwick, J. Crawshaw, and P. F. Luckham. Signature of elastic turbulence of viscoelastic fluid flow in a single pore throat. *Physical Review E*, 101(4):042605, 2020.

[68] R. Ellahi, A. Riaz, S. Nadeem, and M. Ali. Peristaltic flow of carreau fluid in a rectangular duct through a porous medium. *Mathematical problems in Engineering*, 2012, 2012.

[69] M. Escudier, R. Poole, F. Presti, C. Dales, C. Nouar, C. Desaubry, L. Graham, and L. Pullum. Observations of asymmetrical flow behaviour in transitional pipe flow of yield-stress and other shear-thinning liquids. *Journal of Non-Newtonian Fluid Mechanics*, 127(2-3):143–155, 2005.

[70] A. Eslami and S. Taghavi. Viscous fingering of yield stress fluids: The effects of wettability. *Journal of Non-Newtonian Fluid Mechanics*, 264:25–47, 2019.

[71] S. Fagbemi, P. Tahmasebi, and M. Piri. Interaction between fluid and porous media with complex geometries: a direct pore-scale study. *Water Resources Research*, 54 (9):6336–6356, 2018.

[72] A. Fall, F. Bertrand, G. Ovarlez, and D. Bonn. Shear thickening of cornstarch suspensions. *Journal of Rheology*, 56(3):575–591, 2012.

[73] C. Fernandes, D. Semyonov, L. L. Ferrás, and J. M. Nóbrega. Validation of the CFD-DPM solver DPMFoam in OpenFOAM® through analytical, numerical and experimental comparisons. *Granular Matter*, 20(4), aug 2018. doi: 10.1007/s10035-018-0834-x.

[74] V. A. Fernandes, A. J. Müller, and A. J. Sandoval. Thermal, structural and rheological characteristics of dark chocolate with different compositions. *Journal of Food Engineering*, 116(1):97–108, 2013.

[75] L. Ferrás, A. Afonso, M. Alves, J. Nóbrega, and F. Pinho. Newtonian and viscoelastic fluid flows through an abrupt 1: 4 expansion with slip boundary conditions. *Physics of Fluids*, 32(4):043103, 2020.

[76] J. H. Ferziger, M. Perić, and R. L. Street. *Computational methods for fluid dynamics*, volume 3. Springer, 2002.

[77] J. Fusier, J. Goyon, X. Chateau, and F. Toussaint. Rheology signature of flocculated silica suspensions. *Journal of Rheology*, 62(3):753–771, 2018.

[78] F. Galindo-Rosales, F. Rubio-Hernández, and A. Sevilla. An apparent viscosity function for shear thickening fluids. *Journal of Non-Newtonian Fluid Mechanics*, 166(5-6):321–325, 2011.

[79] F. J. Galindo-Rosales, F. J. Rubio-Hernández, A. Sevilla, and R. H. Ewoldt. How dr. malcom m. cross may have tackled the development of "an apparent viscosity function for shear thickening fluids". *Journal of Non-Newtonian Fluid Mechanics*, 166(23-24):1421–1424, 2011.

[80] F. J. Galindo-Rosales, L. Campo-Deaño, F. Pinho, E. Van Bokhorst, P. Hamersma, M. S. Oliveira, and M. Alves. Microfluidic systems for the analysis of viscoelastic fluid flow phenomena in porous media. *Microfluidics and nanofluidics*, 12(1-4): 485–498, 2012.

[81] B. Ghanbarian, A. G. Hunt, R. P. Ewing, and M. Sahimi. Tortuosity in porous media: a critical review. *Soil Science Society of America Journal*, 77(5):1461–1477, 2013.

[82] B. Gireesha, P. S. Kumar, B. Mahanthesh, S. Shehzad, and A. Rauf. Nonlinear 3d flow of casson-carreau fluids with homogeneous–heterogeneous reactions: a comparative study. *Results in physics*, 7:2762–2770, 2017.

[83] V. Gopalakrishnan and C. Zukoski. Effect of attractions on shear thickening in dense suspensions. *Journal of Rheology*, 48(6):1321–1344, 2004.

[84] C. J. Greenshields. Openfoam user guide. version 6. *OpenFOAM Foundation Ltd July*, 2017.

[85] F. Greifzu, C. Kratzsch, T. Forgber, F. Lindner, and R. Schwarze. Assessment of particle-tracking models for dispersed particle-laden flows implemented in openfoam and ansys fluent. *Engineering Applications of Computational Fluid Mechanics*, 10(1):30–43, 2016.

[86] D. Gupta and M. H. Peters. A brownian dynamics simulation of aerosol deposition onto spherical collectors. *Journal of Colloid and interface Science*, 104(2):375–389, 1985.

[87] S. Gürgen, M. C. Kuşhan, and W. Li. Shear thickening fluids in protective applications: a review. *Progress in Polymer Science*, 75:48–72, 2017.

[88] D. G. Hatzignatiou, H. Moradi, and A. Stavland. Polymer flow through water-and oil-wet porous media. *Journal of Hydrodynamics*, 27(5):748–762, 2015.

[89] D. Herman and J. Y. Walz. Adsorption and stabilizing effects of highly-charged latex nanoparticles in dispersions of weakly-charged silica colloids. *Journal of colloid and interface science*, 449:143–151, 2015.

[90] W. Herschel and R. Bulkley. The ostwald viscometer as a consistometer. *The Journal of Physical Chemistry*, 29(10):1217–1223, 1925.

[91] A. M. Howe, A. Clarke, and D. Giernalczyk. Flow of concentrated viscoelastic polymer solutions in porous media: effect of mw and concentration on elastic turbulence onset in various geometries. *Soft Matter*, 11(32):6419–6431, 2015.

[92] R. I. Issa. Solution of the implicitly discretised fluid flow equations by operator-splitting. *Journal of computational physics*, 62(1):40–65, 1986.

[93] J. D. Jacob, R. Krishnamoorti, and J. C. Conrad. Particle dispersion in porous media: Differentiating effects of geometry and fluid rheology. *Physical Review E*, 96(2):022610, 2017.

[94] P. P. Jagdale, D. Li, X. Shao, J. B. Bostwick, and X. Xuan. Fluid rheological effects on the flow of polymer solutions in a contraction–expansion microchannel. *Micromachines*, 11(3):278, 2020.

[95] S. Jamali, A. Boromand, N. Wagner, and J. Maia. Microstructure and rheology of soft to rigid shear-thickening colloidal suspensions. *Journal of Rheology*, 59(6): 1377–1395, 2015.

[96] B. Y. Jamaloei and R. Kharrat. Fundamental study of pore morphology effect in low tension polymer flooding or polymer–assisted dilute surfactant flooding. *Transport in porous media*, 76(2):199–218, 2009.

[97] K. Jang, W. Han, and K. Y. Huh. Simulation of a moving-bed reactor and a fluidized-bed reactor by dpm and mppic in openfoam®. In *OpenFOAM®*, pages 419–435. Springer, 2019.

[98] H. Jasak. Openfoam: open source cfd in research and industry. *International Journal of Naval Architecture and Ocean Engineering*, 1(2):89–94, 2009.

[99] H. Jasak, A. Jemcov, Z. Tukovic, et al. Openfoam: A c++ library for complex physics simulations. In *International workshop on coupled methods in numerical dynamics*, volume 1000, pages 1–20. IUC Dubrovnik Croatia, 2007.

[100] V. Joekar-Niasar and S. Hassanizadeh. Analysis of fundamentals of two-phase flow in porous media using dynamic pore-network models: A review. *Critical reviews in environmental science and technology*, 42(18):1895–1976, 2012.

[101] V. Joekar-Niasar, M. Prodanović, D. Wildenschild, and S. Hassanizadeh. Network model investigation of interfacial area, capillary pressure and saturation relationships in granular porous media. *Water Resources Research*, 46(6):W06526, 2010.

[102] D. Kalman, J. Schein, J. Houghton, C. Laufer, E. Wetzel, and N. Wagner. Polymer dispersion based shear thickening fluid-fabrics for protective applications. *Proceeding of SAMPE*, pages 3–7, 2007.

[103] W. Kang, X. Hou, C. Chen, S. Shao, X. Zhang, T. Zhu, T. Wang, and H. Yang. Study on rheological behavior and salt-thickening mechanism of a synthesized twin-tailed hydrophobically modified polyacrylamide. *Journal of Molecular Liquids*, 294:111619, 2019.

[104] N. K. Karadimitriou, H. Mahani, H. Steeb, and V. Niasar. Nonmonotonic effects of salinity on wettability alteration and two-phase flow dynamics in pdms micromodels. *Water Resources Research*, 55(11):9826–9837, 2019.

[105] D. Kawale, G. Bouwman, S. Sachdev, P. L. Zitha, M. T. Kreutzer, W. R. Rossen, and P. E. Boukany. Polymer conformation during flow in porous media. *Soft Matter*, 13(46):8745–8755, 2017.

[106] D. Kawale, E. Marques, P. L. Zitha, M. T. Kreutzer, W. R. Rossen, and P. E. Boukany. Elastic instabilities during the flow of hydrolyzed polyacrylamide solution in porous media: effect of pore-shape and salt. *Soft Matter*, 13(4):765–775, 2017.

[107] G. Kemmer and S. Keller. Nonlinear least-squares data fitting in excel spreadsheets. *Nature protocols*, 5(2):267, 2010.

[108] A. Khalifeh and J.-R. Clermont. Numerical simulations of non-isothermal three-dimensional flows in an extruder by a finite-volume method. *Journal of Non-Newtonian Fluid Mechanics*, 126(1):7–22, 2005.

[109] S. K. Kim. Flow-rate based method for velocity of fully developed laminar flow in tubes. *Journal of Rheology*, 62(6):1397–1407, 2018.

[110] A. H. Kohanpur, M. Rahromostaqim, A. J. Valocchi, and M. Sahimi. Two-phase flow of CO2-brine in a heterogeneous sandstone: Characterization of the rock and comparison of the lattice-boltzmann, pore-network, and direct numerical simulation methods. *Advances in Water Resources*, 135:103469, 2020.

[111] H. M. Laun. Rheological properties of aqueous polymer dispersions. *Die Angewandte Makromolekulare Chemie: Applied Macromolecular Chemistry and Physics*, 123(1):335–359, 1984.

[112] R. Lenormand, E. Touboul, and C. Zarcone. Numerical models and experiments on immiscible displacements in porous media. *Journal of Fluid Mechanics*, 189: 165–187, 1988.

[113] A. Li and G. Ahmadi. Dispersion and deposition of spherical particles from point sources in a turbulent channel flow. *Aerosol science and technology*, 16(4):209–226, 1992.

[114] D. Li, R. Wang, X. Liu, S. Fang, and Y. Sun. Shear-thickening fluid using oxygen-plasma-modified multi-walled carbon nanotubes to improve the quasi-static stab resistance of kevlar fabrics. *Polymers*, 10(12):1356, 2018.

[115] G. Li, G. H. McKinley, and A. M. Ardekani. Dynamics of particle migration in channel flow of viscoelastic fluids. *Journal of Fluid Mechanics*, 785:486–505, 2015.

[116] M. Li, L. Romero-Zeron, F. Marica, and B. J. Balcom. Polymer flooding enhanced oil recovery evaluated with magnetic resonance imaging and relaxation time measurements. *Energy & Fuels*, 31(5):4904–4914, 2017.

[117] S. Li, M. Dong, and P. Luo. A crossflow model for an interacting capillary bundle: Development and application for waterflooding in tight oil reservoirs. *Chemical Engineering Science*, 164:133–147, 2017.

[118] N. Y. Lin, B. M. Guy, M. Hermes, C. Ness, J. Sun, W. C. Poon, and I. Cohen. Hydrodynamic and contact contributions to continuous shear thickening in colloidal suspensions. *Physical Review Letters*, 115(22):228304, 2015.

[119] A. W. Liu, D. E. Bornside, R. C. Armstrong, and R. A. Brown. Viscoelastic flow of polymer solutions around a periodic, linear array of cylinders: comparisons of predictions for microstructure and flow fields. *Journal of Non-Newtonian Fluid Mechanics*, 77(3):153–190, 1998.

[120] S. Liu, Y. Zhang, W. Xing, W. Jian, Z. Liu, T. Li, and Y. Song. Laboratory experiment of co2–ch4 displacement and dispersion in sandpacks in enhanced gas recovery. *Journal of Natural Gas Science and Engineering*, 26:1585–1594, 2015.

[121] X. Lopez. *Pore-scale modelling of non-Newtonian flow*. PhD thesis, University of London, 2004.

[122] N. B. Lu, C. A. Browne, D. B. Amchin, J. K. Nunes, and S. S. Datta. Controlling capillary fingering using pore size gradients in disordered media. *Physical Review Fluids*, 4(8):084303, 2019.

[123] R. Lucas. Ueber das zeitgesetz des kapillaren aufstiegs von flüssigkeiten. *Kolloid-Zeitschrift*, 23(1):15–22, 1918.

[124] D. Macleod. On a relation between the viscosity of a liquid and its coefficient of expansion. *Transactions of the Faraday Society*, 19(July):6–16, 1923.

[125] R. S. Maier, D. M. Kroll, R. S. Bernard, S. E. Howington, J. F. Peters, and H. T. Davis. Pore-scale simulation of dispersion. *Physics of Fluids*, 12(8):2065–2079, 2000.

[126] R. Maitri, S. De, S. Koesen, H. Wyss, J. Van Der Schaaf, J. Kuipers, J. Padding, and E. Peters. Effect of microchannel structure and fluid properties on non-inertial particle migration. *Soft matter*, 15(12):2648–2656, 2019.

[127] O. Malaspinas, G. Courbebaisse, and M. Deville. Simulation of generalized Newtonian fluids with the lattice Boltzmann method. *International Journal of Modern Physics C*, 18(12):1939–1949, 2007.

[128] D. Mangal, J. C. Conrad, and J. C. Palmer. Nanoparticle dispersion in porous media: Effects of hydrodynamic interactions and dimensionality. *AIChE Journal*, 67(3):e17147, 2021.

[129] R. Mari, R. Seto, J. F. Morris, and M. M. Denn. Shear thickening, frictionless and frictional rheologies in non-brownian suspensions. *Journal of Rheology*, 58(6): 1693–1724, 2014.

[130] S. Matsuhisa and R. B. Bird. Analytical and numerical solutions for laminar flow of the non-Newtonian Ellis fluid. *AIChE Journal*, 11(4):588–595, 1965.

[131] C. Maus, R. Fayt, R. Jérôme, and P. Teyssie. Shear thickening of halato-telechelic polymers in apolar solvents. *Polymer*, 36(10):2083–2088, 1995.

[132] X. Meng. *Coupling of nanofluid flow, heat transfer and nanoparticles sedimentation using OpenFOAM*. PhD thesis, City, University of London, 2017.

[133] D. M. Meter. Tube flow of non-newtonian polymer solutions: Part II. turbulent flow. *AIChE Journal*, 10(6):881–884, 1964.

[134] D. M. Meter and R. B. Bird. Tube flow of non-newtonian polymer solutions: Part i. laminar flow and rheological models. *AIChE Journal*, 10(6):878–881, 1964.

[135] A. Metzner and J. Reed. Flow of non-newtonian fluids—correlation of the laminar, transition, and turbulent-flow regions. *AlChe Journal*, 1(4):434–440, 1955.

[136] J. Mewis and N. J. Wagner. *Colloidal suspension rheology*. Cambridge University Press, 2012.

[137] H. E. Meybodi, R. Kharrat, and M. N. Araghi. Experimental studying of pore morphology and wettability effects on microscopic and macroscopic displacement efficiency of polymer flooding. *Journal of Petroleum Science and Engineering*, 78 (2):347–363, 2011.

[138] J. Mitchell, K. Lyons, A. M. Howe, and A. Clarke. Viscoelastic polymer flows and elastic turbulence in three-dimensional porous structures. *Soft Matter*, 12(2): 460–468, 2016.

[139] P. Mohammadmoradi, A. Kantzas, et al. Pore scale investigation of wettability effect on waterflood performance. In *SPE Annual Technical Conference and Exhibition*. Society of Petroleum Engineers, 2016.

[140] A. F. Morais, H. Seybold, H. J. Herrmann, and J. S. Andrade Jr. Non-newtonian fluid flow through three-dimensional disordered porous media. *Physical review letters*, 103(19):194502, 2009.

[141] M. Moroni, N. Kleinfelter, and J. H. Cushman. Analysis of dispersion in porous media via matched-index particle tracking velocimetry experiments. *Advances in water resources*, 30(1):1–15, 2007.

[142] F. Moukalled, L. Mangani, M. Darwish, et al. *The finite volume method in computational fluid dynamics*, volume 6. Springer, 2016.

[143] S. Mueller, E. Llewellin, and H. Mader. The rheology of suspensions of solid particles. *Proceedings of the Royal Society A: Mathematical, Physical and Engineering Sciences*, 466(2116):1201–1228, 2010.

[144] D. Niblett, A. Mularczyk, V. Niasar, J. Eller, and S. Holmes. Two-phase flow dynamics in a gas diffusion layer-gas channel-microporous layer system. *Journal of Power Sources*, 471:228427, 2020.

[145] M. A. Nilsson, R. Kulkarni, L. Gerberich, R. Hammond, R. Singh, E. Baumhoff, and J. P. Rothstein. Effect of fluid rheology on enhanced oil recovery in a microfluidic sandstone device. *Journal of Non-Newtonian Fluid Mechanics*, 202:112–119, 2013.

[146] E. Nourafkan, Z. Hu, and D. Wen. Nanoparticle-enabled delivery of surfactants in porous media. *Journal of colloid and interface science*, 519:44–57, 2018.

[147] P. J. Oliveira and F. T. Pinho. Analytical solution for fully developed channel and pipe flow of phan-thien–tanner fluids. *Journal of Fluid Mechanics*, 387:271–280, 1999.

[148] W. Ostwald. About the rate function of the viscosity of dispersed systems. *Kolloid Z*, 36:99–117, 1925.

[149] P. Pálovics and M. Rencz. Investigation of the motion of magnetic nanoparticles in microfluidics with a micro domain model. *Microsystem Technologies*, pages 1–15, 2020.

[150] D. Parisi, J. Ahn, T. Chang, D. Vlassopoulos, and M. Rubinstein. Stress relaxation in symmetric ring-linear polymer blends at low ring fractions. *Macromolecules*, 2020.

[151] H. Park, M. Hawley, and R. Blanks. The flow of non-newtonian solutions through packed beds. *Polymer Engineering & Science*, 15(11):761–773, 1975.

[152] S. Parsa, E. Santanach-Carreras, L. Xiao, and D. A. Weitz. Origin of anomalous polymer-induced fluid displacement in porous media. *Physical Review Fluids*, 5 (2):022001, 2020.

[153] S. V. Patankar and D. B. Spalding. A calculation procedure for heat, mass and momentum transfer in three-dimensional parabolic flows. In *Numerical prediction of flow, heat transfer, turbulence and combustion*, pages 54–73. Elsevier, 1983.

[154] H. Patel, J. Kuipers, and E. Peters. Effect of flow and fluid properties on the mobility of multiphase flows through porous media. *Chemical Engineering Science*, 193:243–254, 2019.

[155] J. Patel, B. Maji, N. H. N. Moorthy, and S. Maiti. Xanthan gum derivatives: review of synthesis, properties and diverse applications. *RSC Advances*, 10(45): 27103–27136, 2020.

[156] J. M. Peralta, B. E. Meza, and S. E. Zorrilla. Mathematical modeling of a dip-coating process using a generalized Newtonian fluid. 1. Model development. *Industrial & Engineering Chemistry Research*, 53(15):6521–6532, 2014.

[157] J. M. Peralta, B. E. Meza, and S. E. Zorrilla. Analytical solutions for the free-draining flow of a Carreau-Yasuda fluid on a vertical plate. *Chemical Engineering Science*, 168:391–402, 2017.

[158] C. L. Perrin, P. M. Tardy, K. S. Sorbie, and J. C. Crawshaw. Experimental and modeling study of newtonian and non-newtonian fluid flow in pore network micromodels. *Journal of Colloid and Interface Science*, 295(2):542–550, 2006.

[159] G. W. Peters, J. F. Schoonen, F. P. Baaijens, and H. E. Meijer. On the performance of enhanced constitutive models for polymer melts in a cross-slot flow. *Journal of Non-Newtonian Fluid Mechanics*, 82(2-3):387–427, 1999.

[160] N. H. Pham and D. V. Papavassiliou. Nanoparticle transport in heterogeneous porous media with particle tracking numerical methods. *Computational particle mechanics*, 4(1):87–100, 2017.

[161] W. Philippoff. Zur Theorie der Strukturviskositaet. I. *Kolloid-Zeitschrift*, 71(1): 1–16, 1935.

[162] F. Pimenta and M. Alves. rheotool. https://github.com/fppimenta/rheoTool, 2016.

[163] F. Pimenta and M. Alves. Stabilization of an open-source finite-volume solver for viscoelastic fluid flows. *Journal of Non-Newtonian Fluid Mechanics*, 239:85–104, 2017.

[164] R. Poling-Skutvik, K. I. S. Mongcopa, A. Faraone, S. Narayanan, J. C. Conrad, and R. Krishnamoorti. Structure and dynamics of interacting nanoparticles in semidilute polymer solutions. *Macromolecules*, 49(17):6568–6577, 2016.

[165] R. Poole. The deborah and weissenberg numbers. *Rheol. Bull*, 53(2):32–39, 2012.

[166] M. Prodanovic, M. Esteva, M. Hanlon, G. Nanda, and P. Agarwal. Digital rocks portal: a repository for porous media images. 10.17612, 2015.

[167] A. Rabbani and S. Salehi. Dynamic modeling of the formation damage and mud cake deposition using filtration theories coupled with sem image processing. *Journal of Natural Gas Science and Engineering*, 42:157–168, 2017.

[168] H. S. Rabbani, V. Joekar-Niasar, T. Pak, and N. Shokri. New insights on the complex dynamics of two-phase flow in porous media under intermediate-wet conditions. *Scientific Reports*, 7(1):1–7, 2017.

[169] A. Q. Raeini, B. Bijeljic, and M. J. Blunt. Numerical modelling of sub-pore scale events in two-phase flow through porous media. *Transport in porous media*, 101 (2):191–213, 2014.

[170] A. Q. Raeini, M. J. Blunt, and B. Bijeljic. Direct simulations of two-phase flow on micro-ct images of porous media and upscaling of pore-scale forces. *Advances in water resources*, 74:116–126, 2014.

[171] J. M. Ramirez, E. A. Thomann, E. C. Waymire, J. Chastanet, and B. D. Wood. A note on the theoretical foundations of particle tracking methods in heterogeneous porous media. *Water Resources Research*, 44(1), 2008.

[172] M. Reddy and J. Reddy. Finite-element analysis of flows of non-Newtonian fluids in three-dimensional enclosures. *International Journal of Non-linear Mechanics*, 27(1):9–26, 1992.

[173] M. Reiner. In search for a general law of the flow of matter. *Journal of Rheology (1929-1932)*, 1(3):250–260, 1930.

[174] D. Richter, G. Iaccarino, and E. S. Shaqfeh. Simulations of three-dimensional viscoelastic flows past a circular cylinder at moderate reynolds numbers. *Journal of fluid mechanics*, 651:415, 2010.

[175] P. J. Roache. Quantification of uncertainty in computational fluid dynamics. *Annual review of fluid Mechanics*, 29(1):123–160, 1997.

[176] A. Rodríguez de Castro and G. Radilla. Non-Darcian flow experiments of shear-thinning fluids through rough-walled rock fractures. *Water Resources Research*, 52(11):9020–9035, 2016.

[177] A. Rodríguez de Castro and G. Radilla. Flow of yield stress and Carreau fluids through rough-walled rock fractures: Prediction and experiments. *Water Resources Research*, 53(7):6197–6217, 2017.

[178] A. Rodríguez de Castro, M. Agnaou, A. Ahmadi-Sénichault, and A. Omari. Numerical investigation of Herschel-Bulkley fluid flows in 2D porous media: yielding behaviour and tortuosity. *Computers & Chemical Engineering*, page 106922, 2020.

[179] G. Romeo, G. D'Avino, F. Greco, P. A. Netti, and P. L. Maffettone. Viscoelastic flow-focusing in microchannels: scaling properties of the particle radial distributions. *Lab on a Chip*, 13(14):2802–2807, 2013.

[180] L. Romero-Zerón, S. Ongsurakul, L. Li, and B. Balcom. Visualization of the effect of porous media wettability on polymer flooding performance through unconsolidated porous media using magnetic resonance imaging. *Petroleum science and technology*, 28(1):52–67, 2010.

[181] J. R. Royer, G. L. Burton, D. L. Blair, and S. D. Hudson. Rheology and dynamics of colloidal superballs. *Soft Matter*, 11(28):5656–5665, 2015.

[182] S. H. Sadek, H. H. Najafabadi, and F. J. Galindo-Rosales. Capillary breakup extensional magnetorheometry. *Journal of Rheology*, 64(1):55–65, 2020.

[183] T. J. Sadowski and R. B. Bird. Non-newtonian flow through porous media. i. theoretical. *Transactions of the Society of Rheology*, 9(2):243–250, 1965.

[184] J. Savins. Non-newtonian flow through porous media. *Industrial & Engineering Chemistry*, 61(10):18–47, 1969.

[185] J. Schindelin, I. Arganda-Carreras, E. Frise, V. Kaynig, M. Longair, T. Pietzsch, S. Preibisch, C. Rueden, S. Saalfeld, B. Schmid, et al. Fiji: an open-source platform for biological-image analysis. *Nature methods*, 9(7):676–682, 2012.

[186] C. Scholz, F. Wirner, J. R. Gomez-Solano, and C. Bechinger. Enhanced dispersion by elastic turbulence in porous media. *EPL (Europhysics Letters)*, 107(5):54003, 2014.

[187] S. Shahsavari and G. H. McKinley. Mobility and pore-scale fluid dynamics of rate-dependent yield-stress fluids flowing through fibrous porous media. *Journal of Non-Newtonian Fluid Mechanics*, 235:76–82, 2016.

[188] T. Shende, V. Niasar, and M. Babaei. Pore-scale simulation of viscous instability for non-newtonian two-phase flow in porous media. *Journal of Non-Newtonian Fluid Mechanics*, 296:104628, 2021.

[189] T. Shende, V. Niasar, and M. Babaei. Upscaling non-Newtonian rheological fluid properties from pore-scale to Darcy's scale. *Chemical Engineering Science*, 239: 116638, 2021.

[190] T. Shende, V. J. Niasar, and M. Babaei. Effective viscosity and reynolds number of non-newtonian fluids using meter model. *Rheologica Acta*, 60(1):11–21, 2021.

[191] T. Shende, V. J. Niasar, and M. Babaei. An empirical equation for shear viscosity of shear thickening fluids. *Journal of Molecular Liquids*, 325:115220, 2021.

[192] Y. Shi and G. Tang. Non-Newtonian rheology property for two-phase flow on fingering phenomenon in porous media using the lattice Boltzmann method. *Journal of Non-Newtonian Fluid Mechanics*, 229:86–95, 2016.

[193] A. Singh, R. Mari, M. M. Denn, and J. F. Morris. A constitutive model for simple shear of dense frictional suspensions. *Journal of Rheology*, 62(2):457–468, 2018.

[194] A. Skauge, N. Zamani, J. Gausdal Jacobsen, B. Shaker Shiran, B. Al-Shakry, and T. Skauge. Polymer flow in porous media: Relevance to enhanced oil recovery. *Colloids and Interfaces*, 2(3):27, 2018.

[195] A. H. Slim, R. Poling-Skutvik, and J. C. Conrad. Local confinement controls diffusive nanoparticle dynamics in semidilute polyelectrolyte solutions. *Langmuir*, 36(31):9153–9159, 2020.

[196] T. Sochi. Flow of non-newtonian fluids in porous media. *Journal of Polymer Science Part B: Polymer Physics*, 48(23):2437–2767, 2010.

[197] T. Sochi. Analytical solutions for the flow of Carreau and Cross fluids in circular pipes and thin slits. *Rheologica Acta*, 54(8):745–756, 2015.

[198] T. Sochi and M. J. Blunt. Pore-scale network modeling of ellis and herschel–bulkley fluids. *Journal of Petroleum Science and Engineering*, 60(2):105–124, 2008.

[199] K.-W. Song, Y.-S. Kim, and G.-S. Chang. Rheology of concentrated xanthan gum solutions: Steady shear flow behavior. *Fibers and Polymers*, 7(2):129–138, 2006.

[200] K. S. Sorbie. *Polymer-improved oil recovery*. Springer Science & Business Media, 2013.

[201] R. Steller and J. Iwko. New generalized newtonian fluid models for quantitative description of complex viscous behavior in shear flows. *Polymer Engineering & Science*, 58(8):1446–1455, 2018.

[202] M. Tembely, A. AlSumaiti, M. Jouini, and K. Rahimov. The effect of heat transfer and polymer concentration on non-newtonian fluid from pore-scale simulation of rock x-ray micro-ct. *Polymers*, 9(10):509, 2017.

[203] M. Tembely, W. S. Alameri, A. M. AlSumaiti, and M. S. Jouini. Pore-scale modeling of the effect of wettability on two-phase flow properties for newtonian and non-newtonian fluids. *Polymers*, 12(12):2832, 2020.

[204] N. P. Thien and R. I. Tanner. A new constitutive equation derived from network theory. *Journal of Non-Newtonian Fluid Mechanics*, 2(4):353–365, 1977.

[205] Y. Thomas Hu. Mechanisms of shear thickening in transient guar network. *Journal of Rheology*, 58(6):1789–1807, 2014.

[206] T. Tosco, D. L. Marchisio, F. Lince, and R. Sethi. Extension of the Darcy–Forchheimer law for shear-thinning fluids and validation via pore-scale flow simulations. *Transport in Porous Media*, 96(1):1–20, 2013.

[207] C. Tsakiroglou, M. Theodoropoulou, and V. Karoutsos. Fluid flow in fractured formations. In *New Paradigms in Subsurface Prediction*, pages 161–172. Springer, 2003.

[208] C. Tsakiroglou, M. Theodoropoulou, V. Karoutsos, D. Papanicolaou, and V. Sygouni. Experimental study of the immiscible displacement of shear-thinning fluids in pore networks. *Journal of Colloid and Interface Science*, 267(1):217–232, 2003.

[209] C. D. Tsakiroglou. A methodology for the derivation of non-darcian models for the flow of generalized newtonian fluids in porous media. *Journal of Non-Newtonian Fluid Mechanics*, 105(2-3):79–110, 2002.

[210] C. D. Tsakiroglou. Correlation of the two-phase flow coefficients of porous media with the rheology of shear-thinning fluids. *Journal of non-newtonian fluid mechanics*, 117(1):1–23, 2004.

[211] J. Van der Werff, C. De Kruif, and J. Dhont. The shear-thinning behaviour of colloidal dispersions: II. Experiments. *Physica A: Statistical Mechanics and its Applications*, 160(2):205–212, 1989.

[212] E. Vermolen, M. Van Haasterecht, S. Masalmeh, et al. A systematic study of the polymer visco-elastic effect on residual oil saturation by core flooding. In *SPE EOR Conference at Oil and Gas West Asia*. Society of Petroleum Engineers, 2014.

[213] M. Villone, G. D'Avino, M. Hulsen, F. Greco, and P. Maffettone. Simulations of viscoelasticity-induced focusing of particles in pressure-driven micro-slit flow. *Journal of non-newtonian fluid mechanics*, 166(23-24):1396–1405, 2011.

[214] N. J. Wagner and J. F. Brady. Shear thickening in colloidal dispersions. *Physics Today*, 62(10):27–32, 2009.

[215] E. W. Washburn. The dynamics of capillary flow. *Physical review*, 17(3):273, 1921.

[216] A. R. White and T. Ward. Constant pressure gas-driven displacement of a shear-thinning liquid in a partially filled radial hele-shaw cell: Thin films, bursting and instability. *Journal of Non-Newtonian Fluid Mechanics*, 206:18–28, 2014.

[217] M. L. Williams, R. F. Landel, and J. D. Ferry. The temperature dependence of relaxation mechanisms in amorphous polymers and other glass-forming liquids. *Journal of the American Chemical Society*, 77(14):3701–3707, 1955.

[218] H. Wu and D. K. Schwartz. Nanoparticle tracking to probe transport in porous media. *Accounts of Chemical Research*, 53(10):2130–2139, 2020.

[219] M. Wyart and M. Cates. Discontinuous shear thickening without inertia in dense non-brownian suspensions. *Physical Review Letters*, 112(9):098302, 2014.

[220] C. Xie, W. Lv, and M. Wang. Shear-thinning or shear-thickening fluid for better eor?—a direct pore-scale study. *Journal of Petroleum Science and Engineering*, 161:683–691, 2018.

[221] C. Yang, Z. Liu, M. Yu, and X. Bian. The influence of thixotropy on the magnetorheological property of oil-based ferrofluid. *Journal of Molecular Liquids*, page 114425, 2020.

[222] K. Yasuda. *Investigation of the analogies between viscometric and linear viscoelastic properties of polystyrene fluids*. PhD thesis, Massachusetts Institute of Technology, 1979.

[223] F. Yilmaz and M. Y. Gundogdu. A critical review on blood flow in large arteries; relevance to blood rheology, viscosity models, and physiologic conditions. *Korea-Australia Rheology Journal*, 20(4):197–211, 2008.

[224] D. Yuan, Q. Zhao, S. Yan, S.-Y. Tang, G. Alici, J. Zhang, and W. Li. Recent progress of particle migration in viscoelastic fluids. *Lab on a Chip*, 18(4):551–567, 2018.

[225] N. Zamani, I. Bondino, R. Kaufmann, and A. Skauge. Computation of polymer in-situ rheology using direct numerical simulation. *Journal of Petroleum Science and Engineering*, 159:92–102, 2017.

[226] F. Zami-Pierre, R. De Loubens, M. Quintard, and Y. Davit. Transition in the flow of power-law fluids through isotropic porous media. *Physical review letters*, 117 (7):074502, 2016.

[227] F. Zami-Pierre, R. de Loubens, M. Quintard, and Y. Davit. Polymer flow through porous media: numerical prediction of the contribution of slip to the apparent viscosity. *Transport in Porous Media*, 119(3):521–538, 2017.

[228] F. Zami-Pierre, R. de Loubens, M. Quintard, and Y. Davit. Effect of disorder in the pore-scale structure on the flow of shear-thinning fluids through porous media. *Journal of Non-Newtonian Fluid Mechanics*, 261:99–110, 2018.

[229] I. E. Zarraga, D. A. Hill, and D. T. Leighton Jr. The characterization of the total stress of concentrated suspensions of noncolloidal spheres in newtonian fluids. *Journal of Rheology*, 44(2):185–220, 2000.

[230] L.-j. Zhang and X.-a. Yue. Displacement of polymer solution on residual oil trapped in dead ends. *Journal of Central South University of Technology*, 15(1):84–87, 2008.

[231] M. Zhang, M. Prodanović, M. Mirabolghasemi, and J. Zhao. 3d microscale flow simulation of shear-thinning fluids in a rough fracture. *Transport in Porous Media*, 128(1):243–269, 2019.

[232] X. Zhang, W. Li, and X. Gong. Study on magnetorheological shear thickening fluid. *Smart Materials and Structures*, 17(1):015051, 2008.

[233] X. Zhang, H. Yang, P. Wang, T. Zhu, T. Wang, C. Chen, F. Wang, and W. Kang. Construction and thickening mechanism of amphiphilic polymer supramolecular system based on polyacid. *Journal of Molecular Liquids*, 286:110921, 2019.

[234] B. Zhao, C. W. MacMinn, and R. Juanes. Wettability control on multiphase flow in patterned microfluidics. *Proceedings of the National Academy of Sciences*, 113 (37):10251–10256, 2016.

[235] H. Zhong, W. Zhang, H. Yin, and H. Liu. Study on mechanism of viscoelastic polymer transient flow in porous media. *Geofluids*, 2017, 2017.

[236] H. Zhong, Y. Li, W. Zhang, H. Yin, J. Lu, and D. Guo. Microflow mechanism of oil displacement by viscoelastic hydrophobically associating water-soluble polymers in enhanced oil recovery. *Polymers*, 10(6):628, 2018.

[237] H. Zhong, Y. Li, W. Zhang, and D. Li. Study on microscopic flow mechanism of polymer flooding. *Arabian Journal of Geosciences*, 12(2):56, 2019.

[238] L. Zhong, M. Oostrom, T. W. Wietsma, and M. A. Covert. Enhanced remedial amendment delivery through fluid viscosity modifications: Experiments and numerical simulations. *Journal of contaminant hydrology*, 101(1-4):29–41, 2008.

[239] J. Zhou and I. Papautsky. Viscoelastic microfluidics: progress and challanges. *Microsystems & Nanoengineering*, 6(1):1–24, 2020.